UNIVERSITÀ DEGLI STUDI DELL'INSUBRIA
Dipartimento di Scienza e Alta Tecnologia
Dottorato di Ricerca in Astronomia e Astrofisica
XXV Ciclo

A MONTE CARLO APPROACH FOR THE SOLAR MODULATION

Stefano Della Torre

A Thesis submitted for the degree of
Doctor of Philosophy

Supervisor: P.G. Rancoita

November 2012

Nomenclature

ACE = Advanced Composition Explorer satellite
ACR = Anomalous Cosmic Ray
AMS = Alpha Magnetic Spectrometer
AU = Astronomical Unit = 149,597,870.700 km
BESS = Balloon-borne Experiment with a Superconducting Spectrometer
CR = Cosmic Ray
CRIS = Cosmic Ray Isotope Spectrometer
CME = Coronal Mass Ejection
COSPIN = Ulysses Cosmic and Solar Particle Investigation
FFM = Force Field Model
GCR = Galactic Cosmic Ray
GIS = Galactic Interstellar Spectrum
HCS = Heliospheric Current Sheet
HelMod = Heliosphere Modulation Code
HET = High Energy Telescope
IBEX = Interstellar Boundary Explorer
IMF = Interplanetary Magnetic Field
ISS = International Space Station
KET = Kiel Electron Telescope
LIS = Local Interstellar Spectrum
LISM = Local Interstellar Medium
NM = Neutron Monitor
NOAA = Nautical Oceanic and Atmospheric administration
PAMELA = Payload for Antimatter Matter Exploration and Light nuclei Astrophysics
RMS = Root Mean Square
SDE = Stochastic Differential Equation
SEP = Solar Energetic Particles
SSN = monthly Smoothed Sunspot numbers
UHECR = Ultra High Energy Cosmic Rays
WHCS = Wavy Heliospheric Current Sheet

c = Light speed

e = Unitary electric charge

J = Differential Intensity

$K_{i,j}$ = diffusion tensor

K_0 = diffusion parameter

P = Particle Rigidity = $pc/|Z|e$

p = Momentum of a particle

R = Normalized rigidity

T = Kinetic Energy

U = Number Density

Z = Atomic number

β = particle velocity in unit of light speed

γ = Spectral Index of a power low modeling J

ρ_k = ratio between the perpendicular and parallel diffusion coefficient

Contents

Chapter 1

Introduction to Cosmic Rays Observations and Heliosphere

Ground based Cosmic Ray (CRs) observations started 100 years ago with the historic discovery of Victor Hess that confirmed, using a pioneering ionization chamber, the extra-terrestrial origin of cosmic rays (e.g. Hess, 1912). It was only from 1950s, with the installation of a number of neutron monitors (NMs) all around the Earth surface, that CRs observations start to be continuous. Good results were also carried out from space-based observations, started in 1946 (e.g. Golian et al., 1946). Since then, a myriad of space-based detectors have been launched, continuously providing valuable observations and making new discoveries (see, e.g. Moses, 1987; Phillips et al., 1995; Marsden, 2001; Aguilar et al., 2002; Decker et al., 2005; Shikaze et al., 2007; McComas et al., 2009; Boezio et al., 2009; Battiston, 2010). This allows to continuously improve the knowledge of the space environment surrounding the Earth, our Galaxy and finally our Universe.

In this work we present a modeling of CR propagation through the Interplanetary magnetic field (IMF), originate from the Sun, down to Earth using a 2-D Monte Carlo code named HelMod. An overview about CRs and IMF based both on model and direct observation is presented in this Chapter. In particular we focused on the time variation related to Solar activity.
In Chapter 2 we discussed more in details the effect of solar activity on the CR intensity, named *solar modulation effects*, presenting the propagation model originally proposed by Parker (1965).
In Chapter 3 we presented the HelMod Monte Carlo solution for the solar modulation, discussing the model parameters and the sensitivity of the method.
Finally in Chapter 4 results for solar cycle 23 are presented, showing how the present model is able to describe both observation at Earth orbit, as well as outside ecliptic plane. We further discussed about the inclusion of magnetic drift into the propagation model, we showed how with this mechanism we are able to explain the observed positron ratio at low energies from PAMELA and the latitudinal gradients observed by Ulysses spacecraft.

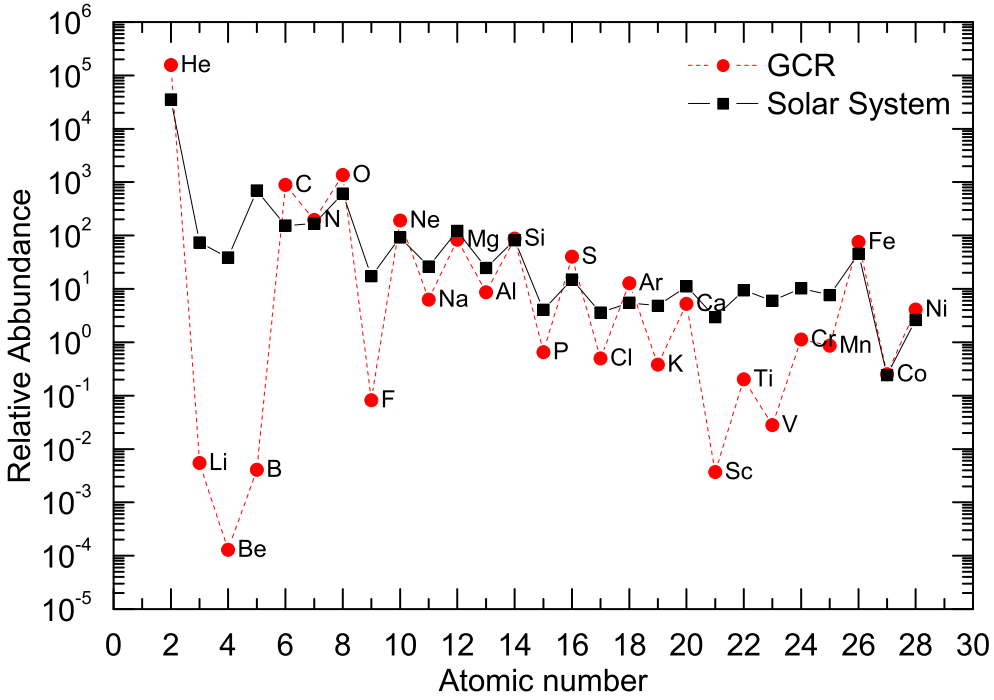

Figure 1.1: The relative abundance of He to Ni in cosmic rays (black square point), and in the Solar System (red round point) as a function of the atomic number Z (data from Schlaepfer, 2003).

1.1 Cosmic Rays

Cosmic Rays are energetic particles which, after being accelerated to very high velocities, propagate throughout the Galaxy. These particles were discovered by Victor Hess during the historic balloon flights in 1911 and 1912 (see, e.g. Hess, 1912) when it was shown that the origin of these particles was extraterrestrial. These particles were called *cosmic rays* by Millikan in 1925, after wrongly believing that they were high energy photons. By 1930, Compton and Clay had shown that these particles were electrically charged and mainly composed of hydrogen (Schein et al., 1941) and heavier nuclei (Freier et al., 1948) stripped of all their orbital electrons (for a review see e.g., Simpson, 1997). Extensive experimental investigations, using balloons and satellites, showed that the flux arriving on Earth is composed of ~ 98 % nuclei and ~ 2 % electrons and positrons. The nuclear component in the energy range 10^{-1}–10 GeV per nucleon[1] consists of ~ 87 % hydrogen, ~ 12 % helium, and ~ 1 % for all heavier nuclei. The most abundant heavier nuclei are Carbon, Nitrogen and Oxygen followed by Iron (see Fig. 1.1). This composition is similar to what is observed in the solar system from meteoritic samples and solar spectroscopic measurements. The largest discrepancy in this comparison is an overabundance of lighter nuclei as Lithium, Beryllium and Boron in cosmic rays. This feature can be accounted as a result of spallation collisions of primary heavier nuclei with interstellar gas.

The Differential Intensity of CRs, up to 10^9 GeV could be approximated in the form of a power law $J \propto T^{-\gamma}$, with $\gamma = 2.5 \sim 2.7$ the spectral index, T the kinetic energy in GeV/nuc and J the

[1]It is normal practice to determine the cosmic rays fluxes as a function of the kinetic energy divided for the number of nucleons.

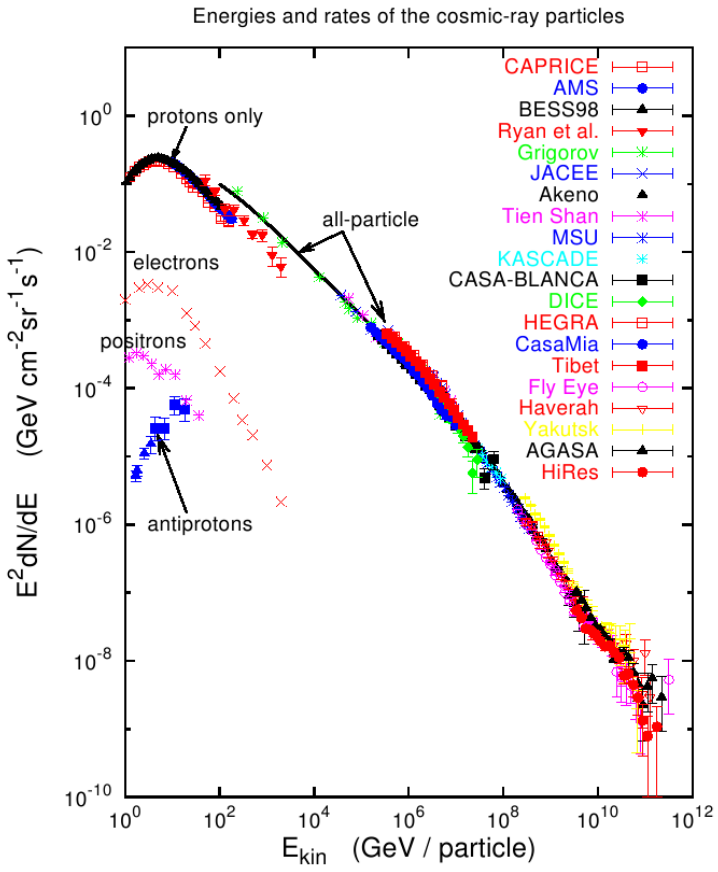

Figure 1.2: Compilation of measurements of the energy spectrum of charged cosmic rays. The observations can be described by a power-law with spectral breaks at 4×10^6 GeV, referred to as the knee, a second knee at 4×10^8 GeV and the ankle at 10^9 GeV. [Figure from (Hillas, 2006)]

differential intensity typically in units of particles $\mathrm{m}^{-2}\mathrm{s}^{-1}\mathrm{sr}^{-1}\mathrm{GeV}^{-1}$ (e.g., Longair, 1990; Jokipii and Kóta, 1997). For $T > 10^6$ GeV the CR proton spectrum exhibits a break (see Fig. 1.2) and becomes steeper with $\gamma = 3.1$. This break is known as the "knee" of the spectrum. The reason for the occurrence of this "knee" is believed to be a less efficient mechanism of CRs acceleration in supernova shocks: at these energies the particle's gyro-radius starts to exceed the thickness of the shock resulting in an less efficiency in the acceleration process (Fermi, 1949). At very high energy $T > 10^9 \sim 10^{10}$ GeV the CR spectrum show a flatness, called *ankle*, probably due to possible nearby sources of Ultra High Energy Cosmic Rays (UHECR) producing cosmic rays with energies over so-called GZK cutoff. GZK cutoff is limit on the energy of cosmic rays set by the interaction of CR particles with the microwave background radiation.
Observations show that in the range $10^2 \sim 10^5$ GeV, the distribution of arrival directions of cosmic rays is remarkably uniform, anisotropy at energies $10^4 \sim 10^5$ GeV only being detected at the level less than 1 part in 10^3 (Rochester and Turver, 1981). For $T < 10 - 30$ GeV, CRs measurement at Earth deviate from the power low because of solar modulation effects in the heliosphere (see Sect. 2.1).

As reported in Strauss et al. (2012b), CRs can generally be grouped into different populations,

i.e., Galactic Cosmic Rays (GCRs), Anomalous Cosmic Rays (ACRs), Jovian Electrons and Solar Energetic Particles (SEPs). GCRs are the dominant species, and consisting mostly of protons. They are believed to be accelerated at astrophysical sources, like supernovae (see, e.g. Axford, 1981), pulsars and pulsar wind nebulae (see, e.g. Gaensler and Slane, 2006); then, as calculated with galactic CR propagation models (e.g. Strong and Moskalenko, 2001; Büsching and Potgieter, 2008), they are transported through the Galaxy, to reach the Local Interstellar Medium. Here the CR intensity form the so-called Local Interstellar Spectrum (LIS). This component is the main topic in this work.

ACR (Garcia-Munoz et al., 1973) are interstellar neutral atoms which get singly ionized relatively close to the Sun, transported with the Solar Wind till the Heliosphere Termination Shock (see Sect. 1.2.4), and there they are accelerated mainly through diffusive shock (e.g. Fisk et al., 1974; Pesses et al., 1981; Potgieter and Moraal, 1988). One should note however that recent Voyager measurements (e.g. Decker et al., 2005) have led to a re-visitation of this paradigm (e.g. Ferreira et al., 2007; Jokipii and Kóta, 2008; Fisk and Gloeckler, 2009; Lazarian and Opher, 2009; Strauss et al., 2010).

Jovian Electrons were discovered during the Pioneer 10 Jovian encounter (e.g. Teegarden et al., 1974). Subsequent modelling of this species has shown that it is the dominant electron population at very low energies (few MeV) in the inner heliosphere (see, e.g. Fichtner et al., 2000; Ferreira et al., 2001b; Ferreira, 2005; Lange et al., 2006; Heber and Potgieter, 2007; Dunzlaff et al., 2010).

Finally SEPs originate from solar flares (e.g. Forbush, 1946), coronal mass ejections (CMEs) and shocks in the interplanetary medium. SEPs may have energies up to several hundred MeV but are usually observed at Earth orbit only for several hours when a solar event occurs. These particles are not taken into account for the purpose of this study. For a review see (Cliver, 2000; Dröge et al., 2010).

There are convincing evidences that the bulk of nuclear radiation below $\sim 10^6$ GeV has its origin and is confined within the Galaxy. Measurements of the flux and distribution of gamma rays with energies ∼70 MeV, arising from the interaction of cosmic ray protons with the interstellar hydrogen[2], reveal a γ-ray intensity distribution roughly proportional to the distribution and density of matter and cosmic rays in the Galaxy, indicating that cosmic rays are present throughout the Galaxy. An indication of CR confinement within the Galaxy is that if CRs streamed freely out of the Galaxy, they would come preferably from the center of the Galaxy where their density is higher, and this is in conflict with the observed isotropy (Rochester and Turver, 1981).

The lifetime for confinement in interstellar magnetic fields is $\sim 10^7$ years. This could be estimated measuring the surviving fraction of the radioactive secondary nuclei ^{10}Be (with half-life $\sim 1.5 \times 10^6$ years and produced in significant quantities in the spallation of carbon and oxygen) with respect to the stable ^{9}Be.

The bulk of cosmic ray nuclear flux at energies $\leq 10^6$ GeV must be continuously renewed in the Galaxy to compensate the loss of nuclei by nuclear and electronic collisions or escape from the Galaxy (Simpson, 1983). In fact studies on cosmic ray bombardment in meteorites reveals that

[2]follow the reactions p + H $\rightarrow \pi_0$ + nucleons $\rightarrow \gamma + \gamma$ + nucleons.

the average cosmic ray flux entering the solar system has been constant within approximately a factor of 2 over the past $\sim 4 \times 10^9$ years and, from the amount of ^{10}Be in deep sea sediments, to within $\pm 30\%$ over the past $\sim 10^6$ years. These observations led to the assumption of a steady-state condition at a galactic scale. The renewal of the cosmic rays requires an average energy input of $\sim 10^{39}$ erg s^{-1}, i.e., for example the same order of the average energy input from Supernovae. Acceleration mechanisms are usually invoked to justify the relativistic energy and the power law spectrum of cosmic rays. Theories of cosmic-ray acceleration in the Galaxy have been focused on the Fermi acceleration mechanism (Fermi, 1949), but also specific models have been proposed to describe the acceleration process together with the propagation within the Galaxy and to predict the spectra of particles arriving at the solar system (see e.g. Blandford and Ostriker, 1980; Kota and Owens, 1980; Fransson and Epstein, 1980; Stephens and Golden, 1990).

1.1.1 Cosmic Rays Measurements

The first CRs observation was performed during the famous hydrogen balloon flights of V. Hess in 1912, using a simple electroscope. Since that experiment the technology improved getting more and more precise. Although based on similar technologies, the detectors could be divided in 3 main categories: ground-based, "in atmosphere" and space detectors. The most used detectors are scintillators, photo-multipliers and Cherenkov detectors. Additionally also other technologies from particle physics are successful applied also to astroparticle physics, such as magnetic spectrometers (magnetic field with a tracker) and electromagnetic calorimeters.

As we already mentioned, the CR flux decreases of about 30 orders of magnitude from the MeV/nucleon region to the 10^{12} GeV/nucleon: different experimental approaches are then needed to measure CR energy spectra and composition at different energies.

Ground-based experiment measure the secondary component of CR, i.e. the one that interact with the atmosphere. These experiments are, for example, devoted to study of UHECR where wide surface and high altitude are required to collect all the secondary product of a single particle interaction. Combining all informations, like the total energy, the dispersion and the direction, one is able to re-construct the vertex of reaction and so the initial energy of the incident particle. On ground is also possible get information about the overall quantity of space radiation by mean of Neutron Monitor (NM) detector. Neutrons are produced at high altitude by primary CRs colliding with atmosphere atoms, a measurement of variation in Neutron radiation give an estimation of the primary radiation. A Magnetic field shield the Earth from the cosmic radiation with different efficient depending from altitude and geographic latituded; the combination of both gives the minimum energy detectable due to geomagnetic and atmospheric cut-off of primary particles. Neutron Monitor could be uses alone or combining information from several NM (see e.g. Usoskin et al., 2005). Recently a network of several Neutron Monitor observatory is born allowing for a easier access to this data[3].

Increasing with altitude it is possible to observe the primary component before that this interact with the atmosphere. Here only magnetosphere deviate or trap particles with no sufficient energy

[3]The access to the Neutron Monitor database could be done online via: http://www.nmdb.eu/ (NMDB, 2012)

to pass through our "magnetic shield"; proper corrections depending on altitude (for "in atmosphere" detectors) and geomagnetic position (for "in atmosphere" and space detectors) have to be account for such observations (see e.g. Bobik et al., 2006). Usually such detectors have limitations on collecting area and energy resolution due to structural limitations of the transport vector for very high altitude or space.

Direct measurements of CRs, before their interaction with the atmosphere, are carried out by compact detectors on board of high altitude balloons or spacecrafts. The strict requirements on weight and power consumption for flying equipment constraint the size, and therefore the acceptance, of such experiments which are limited by the collectible statistics at energies of TeV/n. At very low energies (<GeV/nucleon) the flux is intense enough to allow even relatively small detectors, with acceptances of ~ 100 cm^2 sr, to directly measure chemical composition and isotopic abundances of GCR with good statistical accuracy. As example the High Energy Telescope (HET) on Ulysses spacecraft (Simpson et al., 1992) or the Cosmic Ray Isotope Spectrometer (CRIS) on board of the Advanced Composition Explorer (ACE) satellite (Stone et al., 1998), have performed accurate measurements of chemical and isotopic composition of GCR using the full absorption technique in solid state compact detectors. In the GeV–TeV energy domain, much larger exposures are required in order to reach the statistical sensitivity for direct measurements of light (Z = 1, 2) and heavier (Z > 2) CR energy spectra and composition. Light nuclei energy spectra and isotopic composition studies in this energy range have been performed by means of magnetic spectrometers on board of stratospheric balloons as the Balloon-Borne Experiment with a Superconducting Spectrometer (BESS) (Shikaze et al., 2007), the Alpha Magnetic Spectrometers AMS-01 and AMS-02 (Aguilar et al., 2002) flown on the shuttle Discovery and the Payload for Antimatter Matter Exploration and Light nuclei Astrophysics (PAMELA) (Adriani et al., 2011).

A clear advantage of the magnetic spectrometric technique is the simultaneous measurement of the absolute value and the sign of the charge, allowing the study of anti-matter CR components. The drawback of such spectrometric approach is the intrinsic limits of its geometrical acceptance, typically < 1 m^2 sr. In fact, large bending power BL^2 is needed to extend the spectrometric measurement to high rigidities, where B in the magnetic field magnitude and L the length over which the bent track is measured. For a given effective area of the tracking device, an increase in the length L directly translates on a limit on the tracker angular acceptance, whose typical values are $\sim 40°$. For what concerns the B intensity, either light-weight magnet are used to generate intense B field in a reduced volume (hence reducing the geometrical acceptance) or much heavier equipment is needed (at the expenses of a critical mass budget for the whole instrument). AMS-02 (Battiston, 2010) represent the state-of art of this type of space-detectors. Successful installed on the International Space Station (ISS) on 19$^{\text{th}}$ may, with his 8.5 ton for 64 m^3 of volume and 2.5 KWatt of power consumption is the biggest particle detector in space, allowing for acceptance of ~ 0.45 m^2 sr.

At higher energies, up to 10^5 GeV, the extreme rigidity of the CR tracks and the need of large exposure factors effectively prohibit the use of magnetic spectrometers and satellite experiments. Detection techniques based either on calorimetry, as the Advanced Thin Ionization Calorimeter

(ATIC) (Chang et al., 2008), or on transition radiation emission as the Transition Radiation Array for Cosmic Energetic Radiation (TRACER) (Ave et al., 2008) or on both techniques as in the Cosmic-Ray Energetics and Mass (CREAM) experiment (Yoon et al., 2011) are used. At higher energies, only ground based experiments can actually reach the required exposures for CR detection: the properties of energetic CRs are inferred from the characteristics of Energetic Air Showers (EAS) produced in their interactions with the atmosphere. Large arrays of detectors disposed on areas up to 3000 km^2 are used to reconstruct the shower shape and composition, measuring either the charged shower components as KASKADE (Antoni et al., 2005) or the emitted radiation accompanying the shower as HiRes (Abbasi et al., 2004), or both as the Pierre Auger Observatory (PAO) (Abraham et al., 2004). Monte Carlo techniques are then used to extract the original CR identity and energy from the differences in the expected interactions with the atmosphere. EAS could also observed by mean of observatories in space, based on the detection of UV light accompanying the shower as in the Extreme Universe Space Observatory (EUSO) or as in JEM-EUSO (Takahashi and JEM-EUSO Collaboration, 2009).

1.1.2 Cosmic Rays Detectors

For the purpose of this study only experiments that operate in the energy range $0.1 \approx 100$ GeV are considered. The data used for comparison in Sect. 4 are those at Earth orbit from BESS, AMS-01 and PAMELA which cover and entire solar cycle from 1997 to 2009. Additionally, we consider also the measurements outside ecliptic plane given by Ulysses Spacecraft. In this Section a brief description of such experiment is given, for completeness also the AMS-02 detector is presented, that is expected to provide great accuracy measurements of cosmic ray intensity near the Earth.

The *Ulysses* spacecraft is one of the most important missions in the way to study the heliosphere and in particular the CR modulation (e.g. Heber et al., 1997). This was the first spacecraft to undertake measurements far from the ecliptic and over the polar regions of the Sun, thus obtaining first-hand knowledge concerning the high latitudes of the inner heliosphere. The Ulysses mission, with his nine scientific instruments, has been described by Simpson et al. (1992); Wenzel (1993); Ferrando et al. (1996); Heber et al. (1997). Of particular interest of this work is the Kiel Electron Telescope (KET) which was part of the Ulysses Cosmic and Solar Particle Investigation (COSPIN), that provided a wide range of proton and electron flux up to 2 GeV. The Ulysses spacecraft was launched on 6^{th} October 1990. It used the gravitational encounter with Jupiter to get a out-of-ecliptic orbit and reached the higher solar latitudes never get by a spacecraft ($\sim 80°$ from solar equator). Detail of the trajectory of the Ulysses spacecraft can be found on the Ulysses website[4]. The Ulysses mission was highly successful and contributed significantly to the current knowledge regarding the heliosphere. On 30^{th} June 2009, after 19 year of data taking, Ulysses was switched off on its way returning towards the heliographic equator at a radial distance of 5.3 AU. For a review see Sanderson et al. (1995); Marsden (2001); Balogh et al. (2001).

The detector *Balloon-borne Experiment with a Superconducting Spectrometer* (BESS) is a high-resolution rigidity spectrometer with a large geometrical acceptance. It was designed and developed

[4]http://helio.esa.int/ulysses/

as a multipurpose spectrometer to perform precise flux measurements of various components of cosmic rays (see, e.g. Yamamoto et al., 1994; Shikaze et al., 2000; Sanuki et al., 2000; Abe et al., 2003; Haino et al., 2004; Shikaze et al., 2007), as well as highly sensitive searches for rare cosmic rays (see, e.g. Yoshimura et al., 1995; Orito et al., 2000; Sasaki et al., 2002). The large acceptance is realized with a cylindrical structure and makes it possible to perform precise flux measurements with high statistics and small systematic errors. The spectrometer consists of a superconducting solenoid coil, a JET type drift chamber, two inner drift chambers, Time-of-Flight (ToF) plastic scintillation hodoscopes and an aerogel Cerenkov counter (see, e.g. Asaoka et al., 1998; Shikaze et al., 2000). A uniform magnetic field of 1 Tesla is produced by the thin superconducting coil which allows particles to pass through with small interaction probability. The magnetic field variation is less than 2.5% along a typical trajectory. The magnetic field region is filled with the central tracking detectors. Tracking of incident charged particles results in a rigidity resolution of 0.5% at 1 GV. The continuous, redundant, and three-dimensional tracking makes it possible to recognize background events with interaction or scattering. The upper and lower ToF counters measure the velocity (β) with $1/\beta$ resolution of 1.4%, and provide two independent ionization energy loss measurements in the scintillators. Particle identification by mass is performed with these measurements. The balloon flights to measure cosmic-ray spectra with the BESS spectrometer were carried out at Lynn Lake, Manitoba, Canada (56°5' N, 101°3' W), where the geomagnetic vertical cut-off rigidity is low, approximately 0.4 GV. The balloons reached a level float altitude of 37 km. The residual atmosphere above the spectrometer was typically around 5 g/cm^2 . The data collected are referred to 1997,1998,1999, 2000 and 2002 (see table 1 of Shikaze et al., 2007). In the 2002 balloon-flight experiment, the observation was made with an upgraded detector developed for precise measurement of high energy particles up to 500 GeV (Haino et al., 2004).

The *Alpha Magnetic Spectrometer* (AMS) is a particle physics instrument designed for the high precision and long duration measurement of CRs in space. The AMS-01 precursor experiment operated successfully during a 10 days flight on the space shuttle Discovery (mission STS-91). The spectrometer was composed of a cylindrical permanent magnet, a silicon micro-strip tracker, time-of-flight (TOF) scintillator planes, an Aerogel Cerenkov counter and anti- coincidence counters. The performance of AMS-01 is described in Aguilar et al. (2002). Data collection started on June 3^{th} 1998. The orbital inclination was 51.7° and the geodetic altitude ranged from 320 to 390 km. The data were collected in four phases: (a) 1 day of check out before docking with the MIR space station, (b) 4 days while docked to MIR, (c) 3.5 days with AMS pointing directions within 0°, 20° and 45° of the zenith and (d) 0.5 days before descending, pointing toward the nadir. The acceptance criterion of the trigger logic in the AMS-01 instrument was a four-fold coincidence between the signals from the four TOF planes. Only particles traversing the silicon tracker were accepted. Events crossing the anti-coincidence counters or producing multiple hits in the TOF layers were rejected. The AMS-01 mission provided results on cosmic ray protons, helium, electrons, positrons and light nuclei (Aguilar et al., 2002, 2007, 2010, 2011). During the flight, a total of 99 million triggers were recorded by the spectrometer, with 2.85×10^6 helium nuclei and nearly 200,000 nuclei with charge $Z > 2$.

The *Payload for Antimatter Matter Exploration and Light nuclei Astrophysics* (PAMELA) is designed to perform high-precision spectral measurement of charged particles of galactic, heliospheric and trapped origin over a wide energy. PAMELA was mounted on the Resurs DK1 satellite launched the 15^{th} of June 2006, on an elliptical and semi-polar orbit, with an altitude varying between 350 km and 600 km, at an inclination of 70°. At high latitudes, the low geomagnetic cutoff allows low-energy particles (down to 50 MeV) to be detected and studied. The apparatus comprises a number of high performance detectors, capable of identifying particles through the determination of charge (Z), rigidity (P) and velocity (β) over a wide energy range. The device is built around a permanent magnet with a six-plane double-sided silicon micro-strip tracker, providing absolute charge information and track-deflection information. A scintillator system, composed of three double layers of scintillators, provides the trigger, a time-of-flight measurement and an additional estimation of absolute charge. A silicon-tungsten imaging calorimeter, a bottom scintillator and a neutron detector are used to perform lepton-hadron discrimination. An anti-coincidence system is used off-line to reject spurious events generated by particles interacting in the apparatus. A more detailed description of PAMELA and the analysis methodology can be found in Casolino et al. (2008).

The second *Alpha Magnetic Spectrometer* (AMS-02) is a large acceptance instrument conceived to perform accurate measurements of the cosmic radiation on board the International Space Station (ISS). The AMS-02 detector has been designed and built taking advantages from the experience of the high energy particle physics experiments. In its final design, AMS-02 has an acceptance of ~ 0.45 m^2 sr and has been successfully installed on May 19^{th} on board of the ISS (with space shuttle mission STS–134). Requirements for a space-borne high energy physics experiment are extremely challenging. Several constraints in the AMS-02 design have been imposed by the transport on the Space Shuttle and the long term operation on the ISS, in vacuum and at ambient temperatures varying in time between -80°C and 50°C. A weight limit of 8.5 tons, a maximum allowed power consumption of 2.5 KWatt and an average data transmission rate of 9 Mb per second have been the requirements imposed to the detector design. In the design and constructions of each sub-system prototypes have produced to both qualify the physics performances and the space safety compliance. All the electronic components have been certified against radiation damage and the electronic boards produced in engineering, qualification and flight models, tested against mechanical and thermal stress in vacuum. A thermal test in vacuum of the whole AMS-02 detector and calibration with particle beams have been performed to verify the whole system in space-like operating conditions and to calibrate its sub-detectors.
The core of the detector is the magnetic spectrometer: nine layers of double sided silicon microstrip detectors are used to reconstruct the trajectory of charged particles bent by the 0.15 Tesla magnetic field provided by a permanent magnet. With a $\sim 10\mu$m position resolution on the bending coordinate, the Tracker system is able to measure the charged particle rigidity in the GV - TV range. At both ends of the magnet two pairs of segmented scintillator planes are placed to measure the Time Of Flight of the impinging particles and provide the main trigger of the experiment. An Anti-Coincidence scintillator Counter system surrounds the Tracker planes

installed within the magnet volume: it provides the veto signal to the trigger in order to reject multi-particle events generated in the interaction of cosmic rays entering the detector through the sides. The AMS-02 detector is completed by other three sub-detectors which provide redundant measurements of the particle charge magnitude and complete the particle identification: the Ring Image Cherenkov detector dedicated to the precise measurement of the particle velocity and absolute charge magnitude; the Transition Radiation Detector and the Electromagnetic Calorimeter to ensure an accurate separation between leptons and hadrons. The Calorimeter allows to determine electron and photon energy at the percent level providing also a dedicated trigger for photons.

1.2 The Heliosphere

The Sun is a typical star of intermediate size and luminosity with radius $r_\odot \simeq 696\,000$ km $\simeq 0.005$ Astronomical Unit (AU, i.e. the average Earth–Sun distance[5]). It has a differential rotational period that increases with latitude from an average of 25 days at the equator up to even 32 days near the poles in the sidereal frame (e.g., see pag. 77 of Aschwanden, 2006; Brajsa et al., 2001; Ruždjak et al., 2005). This behavior is because the Sun is not a solid body like the Earth but rather a *sphere of plasma* that is gravitationally bound and compressed. The compression causes high temperatures and densities in the core; this sustained a thermonuclear reaction, producing a great amount of energy. Energy from the core radiates and convects out to the solar atmosphere where it escapes into space, where we can observe as electromagnetic radiation and neutrinos. The Sun is composed of mostly Hydrogen (∼90%) and Helium (∼10%) with traces of heavier elements such as Carbon, Nitrogen and Oxygen. The visible solar surface over the convective zone is called the photosphere. With a temperature of 5.700°C (i.e. the peak of solar radiation emission) this is the common observable part of the Sun. The photosphere divide the inner thick region from the more rarefied outer regions: the *chromosphere*, which extends some 10 000 km above the photosphere, and the *solar corona* which is observable beyond the chromosphere for more than 10^6 km.

Visible on the photosphere there are dark areas of irregular shape that are cooler than the rest of the surface, the so called *sunspots*. Strong magnetic fields are also associated with them. Continuous daily observations were started at the Zurich Observatory in 1849 and earlier observations have been used to extend the records back to 1610. The sunspot number, which are direct indications of the level of solar activity, is calculated by first counting the number of sunspot groups and then the number of individual sunspots (Hathaway, 2010). The *sunspot number* is then given by the sum of the number of individual sunspots and ten times the number of groups. Since most sunspot groups have, on average, about ten spots, this formula for counting sunspots gives reliable numbers even when the observing conditions are less than ideal and small spots are hard to see. Monthly averages of the sunspot numbers (see Fig. 1.3) show that the number of sunspots visible on the sun rises and wanes with an approximate 11-year cycle, which is called a solar activity cycle (see Sect. 1.3). There are actually at least two "official" sunspot numbers reported: the *International Sunspot Number*, that is compiled by the Solar Influences Data Analysis Center in

[5] 1 A.U. = 149,597,870.700 km

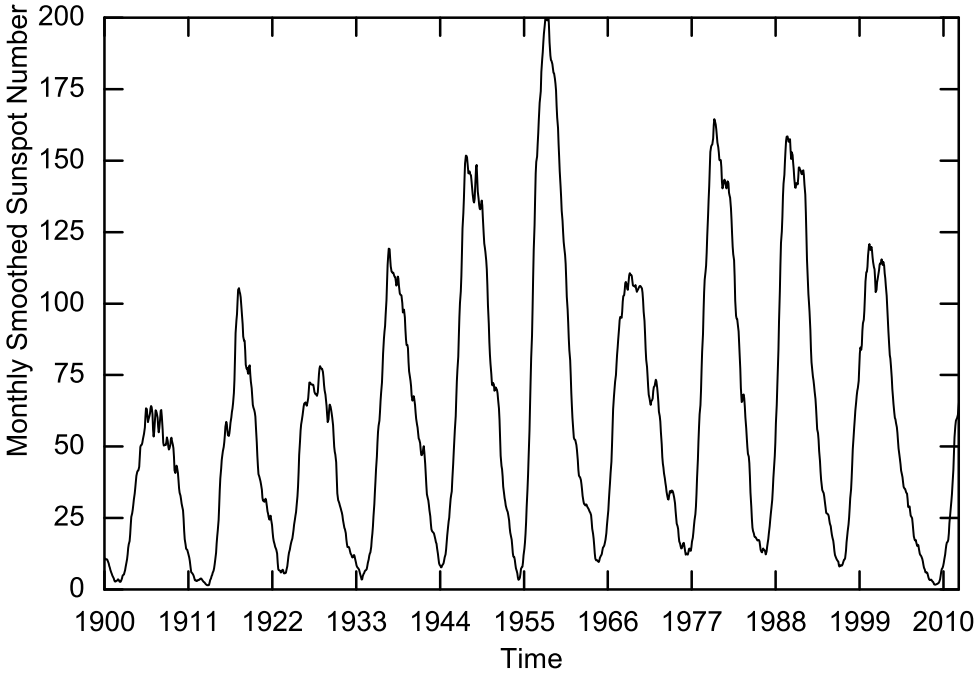

Figure 1.3: Monthly averages (updated monthly) of the sunspot numbers from 1900 up to 2012. (Data computed by SIDC-team, 2012)

Belgium (SIDC-team, 2012), and the *NOAA sunspot number*, that is compiled by the US National Oceanic and Atmospheric Administration.

The plasma atmosphere of the Sun constantly blows away from its surface to maintain equilibrium (See Sect. 1.2.2). This is possible because temperatures in the corona are so high that the solar material is not gravitationally bound to the Sun. The escaping hot coronal plasma from the Sun is called the *solar wind* and is discussed in more detail in Sect. 1.2.2. Convective motions, along with solar rotation, create the Sun's magnetic field. The solar wind carries the solar magnetic field into interplanetary space, forming the Interplanetary Magnetic Field (IMF) which is mostly responsible for the modulation of CRs in the heliosphere as discussed in Chap. 2.

1.2.1 The Interplanetary Magnetic Field

As already mentioned because of a continuous exchange of energy, from inner to outer part of the Sun, some clouds of gas could escape from Sun's gravity and flow out in the Solar System, taking the name of *Solar Wind* (SW). Nowadays, we know that the SW is a plasma that permeates the interplanetary space and constitutes the interplanetary medium. It is, as discussed in Sect. 1.2.2, the outer part of the Sun's corona streaming through the solar system and creating the so-called *heliosphere*. It carries an embedded weak magnetic-field, which results in modulating the fluxes of GCRs entering the heliosphere (see Chap. 2).

After some works of Biermann and Chapman in the early 1950s, that exploited the property of the solar corona and the particles emission from the Sun, Parker (1958) demonstrate as is not possible for solar corona to be in complete hydrostatic equilibrium out to large distance. Parker

(1960) consider the possibility of a steady adiabatic expansion of the plasma from the solar corona that was termed the *solar wind* for the Sun and the *stellar wind* for the other star. The existence of a solar wind had been known from comet observations but the properties predicted by Parker were confirmed by the satellites Lunik III and Venus I in 1959 and by Mariner II in the early 1960s.

In IMF's models the magnetic-field lines are supposed to be embedded in the streaming particles of the SW, that causes the large scale structure of the IMF and the heliosphere. The notion of *frozen-in* magnetic field originates from the work on electromagnetic hydrodynamic waves by Alfvén (1942) and plays a relevant role in the description of IMF (Parker, 1957, 1958) and planets' magnetosphere (see, e.g. Section 4.1.2.1 of Leroy and Rancoita, 2011).

The basics approach, presented in this Section, to define the IMF follow from Parker (1958) (see also Parker, 1957, 1960, 1961, 1963 and Sect. 4.1.2.2 of Leroy and Rancoita, 2011). He suggested that the solar magnetic field is frozen-in to the flow of the SW non-relativistic plasma, which carries the field with it into interplanetary space and generates the IMF. As remarked in Sect. 4.1.2.2 of Leroy and Rancoita (2011), Parker assumed i) a constant solar rotation with angular velocity Ω not depending on solar latitude, ii) a simple spherically symmetric emission of the SW and iii) a constant (or approaching an almost constant) wind speed at larger radial distances (r), e.g., for $r > r_b \approx 10\mathrm{R}_\odot$ (where $\mathrm{R}_\odot$ is the Solar radius), since beyond r_b the wind speed varies slowly with the distance (see, e.g. figure 4.5 of Leroy and Rancoita, 2011). This latter assumption is justified because both the solar gravitation and the outward acceleration by high coronal temperature may be neglected or affect marginally the wind speed for $r > r_b$. Thus, in a spherical system of coordinates (r, θ, ϕ) rotating with the Sun, the outward velocity of a fluid element carrying the magnetic field is approximately given by (Parker, 1958):

$$V_r = V_{sw} \quad , \qquad V_\theta = 0 \quad , \qquad V_\phi = \Omega(r - r_b)\sin\theta, \tag{1.1}$$

where Ω is the angular velocity of the sun. Since, as already noted, the magnetic field is frozen into the solar wind, this allow to compute the magnetic field streamline for an initial azimuth ϕ_0 at $r = r_b$ (e.g. see Parker, 1958 and discussion in Section 4.1.2.2 of Leroy and Rancoita, 2011, and reference there in)

$$\frac{r}{r_b} - 1 - \ln\left(\frac{r}{r_b}\right) = \frac{V_{sw}}{r_b\Omega}(\phi - \phi_0) \tag{1.2}$$

Thus a magnetic-field line has the shape of an Archimedes spiral also termed the *Parker spiral*. In this model, the IMF field-line wraps around a cone, whose surface has an angle θ with respect to the solar rotation axis; i.e., equivalently the expected spiral pattern consists of field lines on cones of constant heliographic latitude (see Fig. 1.4).

Babcock and Babcock (1955) observed the Sun magnetic-field over a two years period (1952–1954) using an solar magnetograph [6] and established that the Sun has a general magnetic dipole field of $\sim 10^{-4}$ Tesla distributed over the visible photosphere. The magnetic-dipole tilt with respect to the rotation axis varies and depends on the solar cycle: apparently the magnetic polarity is reversed (e.g., see Jones et al., 2003, and references therein) about every 11 years with the evolution of the

[6] i.e. an instrument utilizing the Zeeman effect to study an external Magnetic field

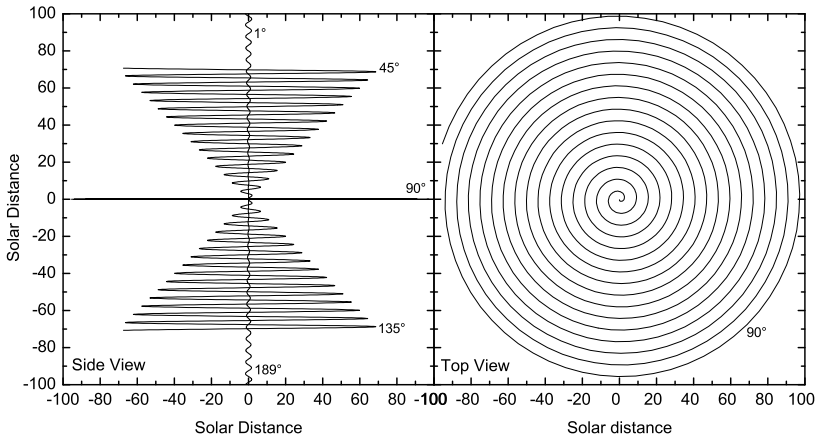

Figure 1.4: Magnetic streamline resulting from a single outflow of plasma from a rotating star emitted near poles, at 45°, at 135° of solar co-latitude and at equator. The right panel show a single streamline emitted at equator as see from north side of Heliosphere, the shape is a Archimedes spiral up to the heliosphere boundary, that in the picture we located at 100 AU, as described by Eq. (1.2).

solar cycle, i.e., a similar magnetic configuration is found about every 22 years (the so-called Hale cycle or solar magnetic cycle). Example of field configuration on the Sun surface could be found e.g. in figure 3a of Sanderson et al. (2003). Furthermore, McComas et al. (2000) observed that during the Sun's approach to solar maximum the coronal structure becomes increasingly complex and the magnetic field becomes less dipolar.

An analytical equation for the IMF can be described by (e.g. see Hattingh and Burger, 1995)

$$\mathbf{B}_p = \frac{A}{r^2}(\mathbf{e}_r - \Gamma \mathbf{e}_\phi)[1 - 2H(\theta - \theta')] \tag{1.3}$$

where A is a coefficient that determines the field polarity and allows $|\mathbf{B}_p|$ to be equal to $B_\oplus$, i.e., the value of the IMF at Earth's orbit as extracted from NASA/GSFC's OMNI data set (King and Papitashvili, 2005; NASA-OMNIweb, 2012); $\mathbf{e}_r$ and $\mathbf{e}_\phi$ are unit vector components in the radial and azimuthal directions, respectively; θ is the colatitude (polar angle); θ' is the polar angle determining the position of the Heliospheric Current Sheet (HCS, Jokipii and Thomas, 1981, see also Sect. 1.2.3); H is the Heaviside function: thus, $[1 - 2H(\theta - \theta')]$ allows $\mathbf{B}_p$ to interchange the sign in the two regions above and below the HCS of the heliosphere (see Sect. 1.2.3); finally,

$$\Gamma = \tan \Psi = \frac{\Omega(r - r_b)\sin\theta}{V_{sw}} \tag{1.4}$$

with Ψ the spiral angle and Ω is assumed to be independent of the heliographic latitude and equal to the sidereal rotation at the Sun's equator. The magnitude of Parker field is thus:

$$B_p = \frac{A}{r^2}\sqrt{1 + \Gamma^2} \tag{1.5}$$

Although this model well describes the IMF on ecliptic plane, several studies (Jokipii and Kota, 1989, and reference therein) found that entry of GCRs over the poles is extremely rapid

because of the low magnitude field intensity and radial field orientation. Jokipii and Kota (1989) noted that the radial field lines at the poles are in a state of unstable equilibrium. Therefore, the smallest perturbation can cause the collapsing of the field line. They have argued that the solar surface, where the *feet* of the field lines occur, is not a smooth surface, but a granular turbulent surface that keeps changing with time, especially in the polar regions. This turbulence may cause the *footpoints* of the polar field lines to wander randomly, creating transverse components in the field, thus causing temporal deviations from the smooth Parker geometry (Jokipii and Kota, 1989). The net effect of this is a highly irregular and compressed field line. Thus, the magnitude of the mean magnetic field at the poles is greater than in the case of the smooth magnetic field of a pure Parker spiral. Jokipii and Kota (1989) have therefore suggested that the Parker spiral field may be generalized by the introduction of a parameter ($\delta(\theta,\phi)$) which amplifies the field strength at large radial distances. With this modification the magnitude of Parker spiral field, Eq.(1.5), becomes (Jokipii and Kota, 1989)

$$B_{JK} = \frac{A}{r^2}\sqrt{1+\Gamma^2+\left(\frac{r}{r_b}\right)^2\delta(\theta,\phi)^2} \tag{1.6}$$

this reflect in a modification of the Parker IMF, Eq. (1.3), as proposed by Langner (2004):

$$\mathbf{B}_{JK} = \frac{A}{r^2}\left[\mathbf{e}_r + \left(\frac{r\delta(\theta,\phi)}{r_b}\right)^2 - \Gamma\mathbf{e}_\phi\right][1-2H(\theta-\theta')] \tag{1.7}$$

The effect of this modification is to increase the field in the polar regions in such a way that for larger distance it decreases as $1/r$ instead of $1/r^2$. In the ecliptic region of the outer heliosphere, where $1+\Gamma^2 \gg 1$, this modification has little effect on the field and it becomes in essence a Parker spiral field. It should be noted, however, that this leaves the field divergence free ($\nabla\cdot\mathbf{B}_{JK}=0$) only if $\delta(\theta,\phi)\propto 1/\sin\theta$. Thus, Langner (2004) parametrized this turbulence as:

$$\delta(\theta,\phi) = \frac{\delta_m}{\sin\theta}, \tag{1.8}$$

where $\delta_m = 8.7\times10^{-5}$, so that $\delta(\theta,\phi)=0.002$ near the poles (at $\theta=2.5°$) and $\delta(\theta,\phi)\sim 0$ in the ecliptic plane. Qualitatively this modification is supported by measurements made of the IMF in the polar regions of the heliosphere by Ulysses (e.g. Balogh et al., 1995). For applications and implications of a modification where $\delta(\theta,\phi)=0.002$ in the whole heliosphere, see e.g. Langner (2004) and reference there in. In this work a parametrization similar to those proposed by Langner (2004) is used and is described afterward in this Section.

Moraal (1990) suggested that the Jokipii & Kóta modification could be improved by the introduction of an arbitrary function $\Theta(\theta)$ in the Parker field, to incorporate the same physical effects that their modification compensated for, thus giving

$$\mathbf{B}_{Moraal} = \frac{A}{r^2}\Theta(\theta)(\mathbf{e}_r - \Gamma\mathbf{e}_\phi)[1-2H(\theta-\theta')]. \tag{1.9}$$

This function is chosen to be symmetric about $\theta=90°$, with $\Theta(90°)=1$, and increasing towards the poles. This modification keeps the field divergence free for all forms of $\Theta(\theta)$. Note, however,

that if $\Theta(\theta)$ is not a function of only θ, but also of r and ϕ, then $\nabla \cdot \mathbf{B}_{Moraal} \neq 0$.

Another modification was proposed by Smith and Bieber (1991) who based their work on magnetic field observations on ecliptic plane between 0.7 to 15.9 AU. They proposed that the magnetic field is not fully radial below the Alfvén radius[7], suggesting an initial nonzero azimuthal field components, arising from differential solar rotation, that may be convected into the corona to provide a steady source of azimuthal magnetic fields at the source point of the solar wind. This causes a different initial spiral angle, depending on the magnetic field component on the solar surface. The modification is parametrized by the ratio of the tangential (azimuthal, B_T) component of the magnetic field to that of the radial component as is found at the Alfvén radius, thus the spiral angle is given by

$$\Gamma = \tan \Psi = \frac{\Omega(r - r_b) \sin \theta}{V_{sw}(r)} - \frac{B_T(r_b) V_{sw}(r_b) r}{B_r(r_b) V_{sw}(r) b} \tag{1.10}$$

where $r_b = 20 r_\odot$ and $B_T(r_b)/B_r(b) \approx 0.02$ according to an estimate by Smith and Bieber. At solar high-latitude this modification may lead to significantly greater winding of the hight-latitude IMF than Parker theory predicts. For an implementation of this modification in a numerical model see e.g. Haasbroek and Potgieter (1995); Haasbroek et al. (1995). Although this approach has particular merit, it is not further utilized in this study.

However, also Fisk (1996) has pointed out that a correction to Parker's IMF needs to be made to the Parker spiral model for the simple reason that the Sun does not rotate rigidly but differentially, with the solar poles rotating $\sim 20\%$ slower than the solar equator (Snodgrass, 1983). The interplay between the differential rotation of the footprints of the IMF lines in the photosphere of the Sun, and the subsequent non radial expansion of the field lines with the solar wind from coronal holes, can result in excursions of the field lines with heliographic latitude. This effect can account for observations from the Ulysses spacecraft of recurrent energetic particle events at higher latitudes. In the Fisk model the magnetic field lines at high latitudes can be connected directly to co-rotating interaction regions in the solar wind at lower latitudes. When the footpoint trajectories on the source surface can be approximated by circles offset from the solar rotation axis with an angle β_A, an analytical expression for the Fisk IMF is obtained (Zurbuchen et al., 1997):

$$B_r = \frac{A}{r^2}, \tag{1.11}$$

$$B_\theta = B_r \frac{r}{V_{sw}} \omega \sin \beta_A \sin\left(\phi + \frac{\Omega r}{V_{sw}}\right), \tag{1.12}$$

$$B_\phi = B_r \frac{r}{V_{sw}} \left[\omega \sin \beta_A \cos\theta \cos\left(\phi + \frac{\Omega r}{V_{sw}}\right) + \sin\theta(\omega \cos \beta_A - \Omega)\right], \tag{1.13}$$

with ω the differential rotation rate and β_A is the angle between the axis formed by the field-line originating at the heliographic poles, which suffers no differential rotation, and the rotational axis of the Sun (Hitge and Burger, 2010). The existence of such a IMF may be supported by a tilt angle (discussed in Sect. 1.2.3) varying in time which can cause a regular meridional component

[7] taken to be in the order of $10 \sim 30\, r_\odot$, below which the magnetic field and the solar corona co-rotate in phase

in the IMF (Kóta and Jokipii, 1997, 1999). The properties of this type of IMF have been studied extensively by e.g., Burger and Hattingh (2001) and Burger et al. (2001), but because of the complexity of this field it is not incorporated in the numerical modulation model that is used in this work. So in conclusion, although the Jokipii-Kóta modification to the IMF is to some extend unsatisfactory, it is still well motivated and the most convenient to apply (Langner, 2004).

In present work we use a *hybrid IMF description* that use the standard Parker Field in the equatorial region, hence we use the Jokipii-Kóta modification in the polar regions:

$$\mathbf{B} = \begin{cases} \frac{A}{r^2}\left[\mathbf{e}_r + \frac{r}{r_b}\delta(\theta)\mathbf{e}_\theta - \Gamma\mathbf{e}_\phi\right]\left[1 - 2H\left(\theta - \theta'\right)\right] & \text{Polar regions} \\ \frac{A}{r^2}\left[\mathbf{e}_r - \Gamma\mathbf{e}_\phi\right]\left[1 - 2H\left(\theta - \theta'\right)\right] & \text{elsewhere} \end{cases} \tag{1.14}$$

Where A, Γ, r_b and θ' defined before. To guaranteed the divergence-Free of the field, the perturbation factor is taken to be:

$$\delta(\theta) = \frac{\delta_m}{\left[1 - 2H\left(\theta - \theta'\right)\right]\sin\theta}. \tag{1.15}$$

The field-line in polar region of this description could be obtained as the solution of the differential equations

$$\frac{dr}{B_r} = \frac{rd\theta}{B_\theta} = \frac{r\sin\theta d\phi}{B_\phi},$$

leading to the follow:

$$\begin{cases} \dfrac{r}{r_b} - 1 - \ln\left(\dfrac{r}{r_b}\right) = \dfrac{V_{sw}}{r_b\omega}(\phi - \phi_0) \\ \theta = \arccos\left\{-\left[\left(\dfrac{r}{r_b} - 1\right)\delta_m - \cos\theta_0\right]\right\} \end{cases}. \tag{1.16}$$

Although the polar latitudinal field (B_θ) in Eq. (1.14) do not reverse his polarity changing the solar hemisphere. this leads to a the streamline in the form of Eq. (1.16) that is symmetric for both solar hemisphere. The polar field in Eq. (1.14) began of the same magnitude of equatorial field with increasing the colatitude towards the solar equator (see Fig. 1.5). At large distance, i.e. greater than 10 AU, the percentage difference between the two formula is $\sim 1\%$ for colatitude angle greater than 20°. The definition of the polar region of Eq. (1.14), i.e. the colatitude angles at which the polar correction is no longer needed and the IMF is described by the Parker Field, is discussed in Sect. 4.3.1. It is remarked that in literature other works attempt to use hybrid field in order to combine Parker Field on equatorial region, with polar modifications, such as Fisk field (see, e.g. Burger et al., 2008; Hitge and Burger, 2010) .

1.2.2 Solar Wind

The solar wind (originally called the *solar corpuscular radiation*) was first proposed by Biermann (1951, 1957, 1961) to account for the behavior of comet tails that always pointed directly away from the Sun regardless of the position of the comet. Biermann has found that the pressure of the solar radiation alone can not explain his observation and has suggested that the solar wind, in the form of ionized particle flowing out from the Sun, always exists and effects the formation of comet tails. Estimation by Biermann of the solar wind speed, ranged between 400 – 1000 km

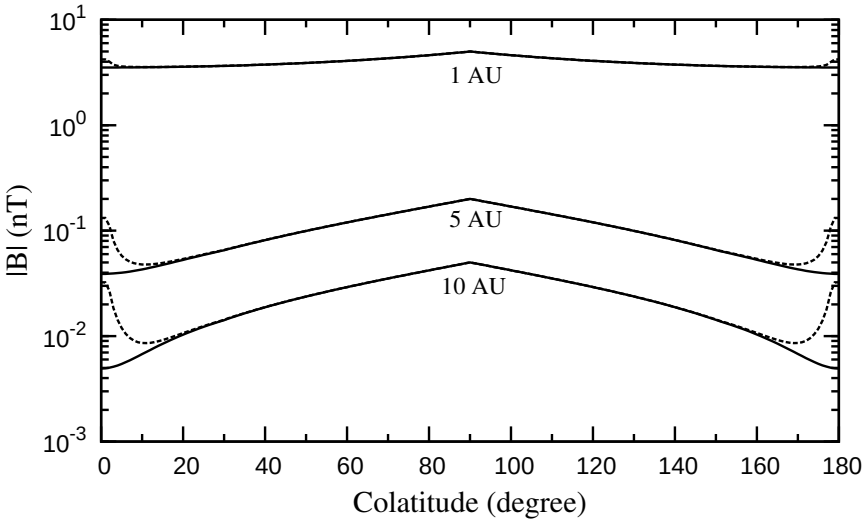

Figure 1.5: Magnitude ($|B|$) of the IMF (dashed line) from Jokipii and Kota (1989) – computed using Equations (1.6) – compared with that from Parker (solid line; Equation (1.5)) at 1, 5, and 10 AU as a function of the colatitude. For the purpose of this calculation, at 1 AU and 90°$|B| = 5\,\mathrm{nT}$ (figure from Bobik et al., 2012a).

s^{-1} which was subsequently confirmed by *in-situ* observation. However, the name *solar wind* was first introduced by Parker (1958, 1963) when he showed that the atmosphere of the Sun could only be in equilibrium if the atmosphere was expanding at supersonic speeds (For a review see Marsch et al., 2003).

The SW is highly variable in both time and space; it consists of protons (about 95% of the positively charged particles), double charged helium ions, a very small number of other positively charged particles and electrons, so that the plasma is electrically neutral (see e.g. Sect. 4.1.2.1 Leroy and Rancoita, 2011). At the orbit of Earth, i.e., at 1 AU from the Sun, experimental observations of SW allowed one to determine that the proton density and temperature are $\approx (8-9)$ proton/cm^3 and $\sim 1.2 \times 10^5$ K, respectively. The mean wind speed is ~ 470 km/s, while the mean speed of sound in the interplanetary medium is (50–63) km/s and, thus, the SW speed is supersonic as predicted by Parker (see e.g. Sect. 4.1.2.1 Leroy and Rancoita, 2011, and reference therein).

Observations over many years have revealed that the intensity of the Solar wind speed is not uniform over all latitudes and can be divided into the fast solar wind and the slow solar wind. The basic reason is that the Sun's magnetic field dominates the original outflow of the solar wind (Langner, 2004): if the solar magnetic field is perpendicular to the radial outflow of the solar wind it can prevent the outflow. This is usually the case at low solar latitudes where the near Sun magnetic field lines are parallel to the Sun's surface (Langner, 2004). These field lines are in the form of loops which begin and end on the solar surface and stretch around the Sun to form the streamer belts. These streamers belts are regarded as the most plausible sources of the slow solar wind speed which have typical velocities of up to $V_{\mathrm{sw}} \simeq 400\,\mathrm{km\,s}^{-1}$ (Schwenn, 1983; Marsch, 1991). Other indications are that the slow solar wind speed may arise from the edges of large coronal holes or from smaller coronal holes (e.g., Hundhausen, 1977, and references therein). In regions where the solar magnetic field is directed radially outward, such as at the solar polar regions,

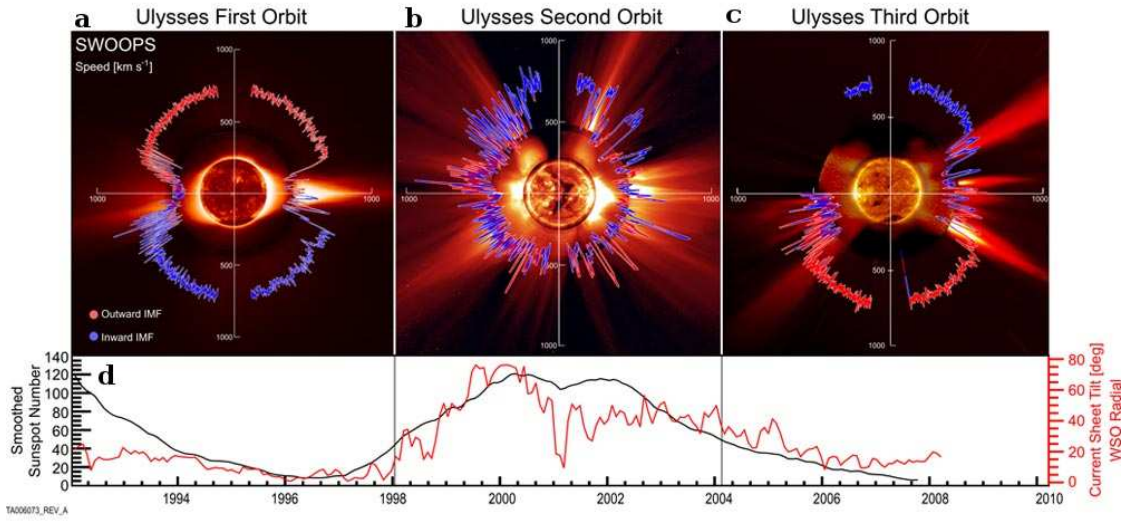

Figure 1.6: (a – c) Polar plots of the solar wind speed, colored by IMF polarity for Ulysses' three polar orbits colored to indicate measured magnetic polarity. In each, the earliest times are on the left (nine o'clock position) and progress around counterclockwise. (d) Contemporaneous values for the smoothed sunspot number (black) and heliospheric current sheet tilt (red), lined up to match Figures 1a – 1c. In Figures 1a – 1c, the solar wind speed is plotted over characteristic solar images for solar minimum for cycle 22 (8/17/96), solar maximum for cycle 23 (12/07/00), and solar minimum for cycle 23 (03/28/06). [figure from McComas et al. (2008)].

the magnetic field will assist the coronal outflow. The fast solar wind speed with characteristic velocities of up to 800 km s^{-1} are associated with polar coronal boles which are located at the higher heliographic latitudes (Krieger et al., 1973; Zirker, 1977, and references therein). In these regions the magnetic field lines are carried off by the solar wind and their connection to the Sun at the one end of the field line is lost. It is these open magnetic field lines which affect the transport of CRs in the heliosphere. The fast solar wind from the polar regions can sometimes extend close to the equator and overtake the earlier emitted slow stream, resulting in a corotating interaction region (CIR). For a review see Odstrcil (2003).

The latitude dependence of SW has been confirmed by Ulysses spacecraft and is shown in Fig. 1.6 in function of the heliolatitude and Solar activity (see, e.g. Phillips et al., 1995). It is evident from Figs. 1.6a,c the significant variations of SW with heliolatitude. This confirms the existence of the fast and slow solar wind streams during solar minima. At latitude $> 20°$ S Ulysses observed a high solar wind speed, 700 - 800 km s^{-1}. In the $\sim 20°$ S to the $\sim 20°$ N band it observed medium to slow speeds, to increase again to a speed between km s^{-1} at $> 20°$ N. For solar maxima (Fig. 1.6b) no well-defined high speed solar wind is observed (e.g. Richardson et al., 2001)

The radial dependence of SW between 0.1 AU and 1.0 AU was studied by e.g., Kojima et al. (1992) and Sheeley et al. (1997). They have found that both the low and high speed winds accelerate within 0.1 AU of the Sun and become a steady flow at 0.3 AU. Using measurements from e.g. Pioneer 10 and 11 and Voyagers 1 and 2, Gazis et al. (1994) and Richardson et al. (2001) have

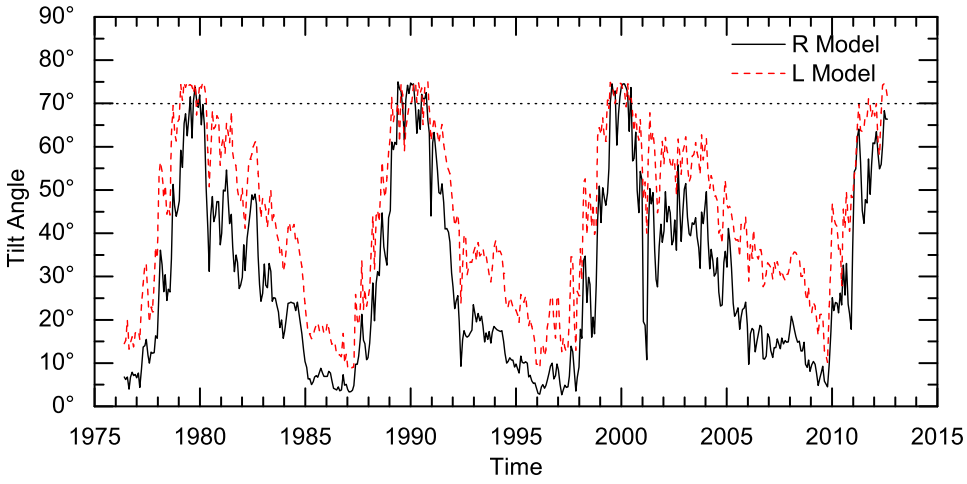

Figure 1.7: Maximum extent in latitude reached by the computed heliospheric current sheet, i.e. tilt angle, in function of time. The maximum latitudinal extent of the HCS was computed using two potential field models applied to photospheric magnetic field observations from WSO (2012). Values above 70 degrees should be considered lower limits as the model is not computed above 70 degrees. The "classic" model uses a line-of-sight boundary condition at the photosphere and includes a significant polar field correction (L-model). A newer, possibly more accurate, model uses a radial boundary condition at the photosphere, and requires no polar field correction (R-Model).(Tilt angle values computed by Hoeksema, 1995; WSO, 2012)

found that the slow averaged solar wind speed does not vary with distance at least up to 50 AU. Measurements of Voyager spacecrafts extend this limits till the SW termination (see Fig. 1.9). However, SW does show a solar cycle dependence with values about 20% higher during solar minimum than during solar maximum. It is remarked that at solar maximum there is a mixture of high speed and low speed winds in the region of the equator (Gazis et al., 1992) so that the picture is not as clear as during solar minima.

1.2.3 Heliospheric current sheet

The major corotating structure in the heliosphere is the heliospheric current sheet (HCS) which divides the IMF into hemispheres of opposite polarity[8]: an hemisphere where the IMF is directed inward and a hemisphere where the IMF is directed outward. The transition between these hemispheres is necessarily made within a thin neutral sheet region, known as the *heliospheric current sheet* (see e.g. figure 1 of Smith, 2001). The HCS has a wavy structure and is rooted in the coronal magnetic field. Since the magnetic axis of the Sun is tilted relative to the rotational axis, the magnetic equator of the Sun does not coincide with the heliographic equator. This tilt angle is denoted by α_t. The waviness of the HCS is correlated to the solar activity of the Sun. During high levels of activity, the tilt angle increases to as much as $\alpha_t \sim 75°$. During times of low solar activity the axis of the magnetic equator and the heliographic equator become nearly aligned, causing relative small current sheet waviness with $\alpha_t \sim 5°$ to $10°$ (see Fig. 1.7) . The wavy structure of the HCS is carried, together with the IMF, radially outwards by the solar wind forming the so

[8]The IMF reverse the sign of the magnetic polarity every ∼11 years

called *Ballerina skirt* (for a review see Smith, 2001). For a constant and radial solar wind speed, the HCS according to Jokipii and Thomas (1981) is

$$\theta' = \frac{\pi}{2} + \arcsin\left\{\sin\alpha_t \sin\left[\phi + \frac{\Omega(r - r_b)}{V_{\rm sw}}\right]\right\} \tag{1.17}$$

The derivation of such formula could be found in Langner (2004).
For periods of high levels of solar activity the dipole-like appearance of the Sun's magnetic field changes. The dipole configuration is replaced by quadrupole moments and therefore even multiple HCSs are possible (Crooker et al., 1993; Kota and Jokipii, 2001). The discovery of the HCS is related to attempts in explaining the sector structure of the IMF. A surprising feature of the earliest IMF measurements in space was their organization into magnetic "sectors" in which the fields alternated between inward and outward (Wilcox and Ness, 1965). It was Alfvén (1977) who made the connection that the magnetic sectors were separated by a current sheet enclosing the Sun (see also Davis, 1972; Schulz, 1973; Levy, 1976). Because of the out-blowing solar wind, the HCS is carried together with the IMF into the heliosphere, having been observed to be present in the most distant IMF observations of Pioneer 10 (Smith, 1989) and Voyager 1 and 2 (Burlaga and Ness, 1993). The wavy structure of the HCS, which has been first suggested by Thomas and Smith (1981), plays an important role in CR modulation affecting the drift motions. Because the IMF above and below the HCS is oppositely directed, CRs experience particle drifts along the HCS (See Sect. 2.2.2). Fully three dimensional simulations of CR transport with a three-dimensional HCS and a two-dimensional approximation to the HCS have been done by e.g. Kota and Jokipii (1983) and Hattingh and Burger (1995). Moreover connection between α_t and CR solar modulation are studied e.g. by Alanko-Huotari et al. (2007a).

1.2.4 Dimension of the heliosphere

A heuristic understanding of the heliosphere is that the solar wind flows radially outward from the Sun and blows a spherical "bubble" that continuously expands. However, the interstellar space is not empty and contains matter in the form of the local interstellar medium (LISM). If there is a significant pressure in the LISM, the expansion of the solar wind must eventually stop, resulting is a quasi-static "bubble" (See, e.g. Fichtner and Scherer, 2000). The heliosphere can be seen as a giant laboratory, provided by nature where we can directly observe and measure physical parameters revealing phenomena that cannot be scaled down to terrestrial laboratories.

A schematic representation of the heliosphere is shown in Fig. 1.8. It is a view of the heliospheric equatorial plane with respect to which the ecliptic plane, wherein most of the major planets rotate around the Sun, is tilted. As the heliosphere moves through the LISM, it forces the LISM to flow around it. The solar wind must merge with the LISM surrounding the heliosphere. At large radial distances the LISM pressure causes the supersonic solar wind plasma to decrease to subsonic speeds (see Fig. 1.9) in order for the solar wind ram pressure to match the interstellar thermal pressure (e.g., see Sections 4.1.2.3, 4.1.2.4 of Leroy and Rancoita, 2011). A heliospheric shock is created, which is called the solar wind termination shock (TS), because the internal wave speed

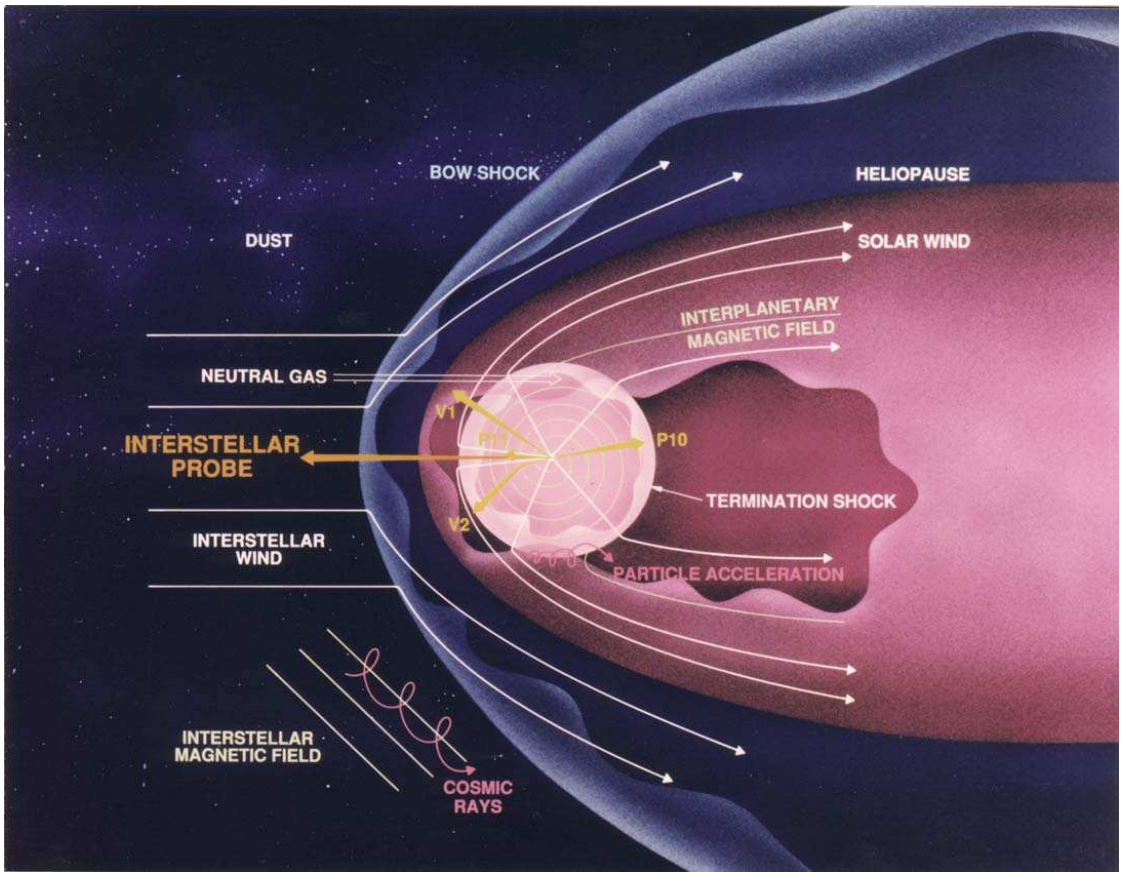

Figure 1.8: Schematic view of Heliosphere adapted from Jokipii (1989)

suddenly becomes larger than the plasma propagation speed as has first been suggested by Parker (1961). Estimates for the position of the TS vary between ∼70 AU and ∼100 AU (e.g. Stone et al., 1996; Whang and Burlaga, 2000), Whang and collaborators (e.g., see Whang and Burlaga, 2000; Whang et al., 2003, 2004) could estimate the radial position of the TS on and outside the ecliptic plane (see, e.g. figure 2 of Whang et al., 2004). They found that (a) on the ecliptic the radial distance of the TS is about 80 AU on average (without large variation between low and high solar activities), (b) near the ecliptic the radial distance varies by less then 20 AU, and (c) outside the ecliptic plane (e.g., at a latitude of 35°) the location of the TS increases by more than or about 50 AU (Whang et al., 2003). In addition, Whang and collaborators estimated that the averaged value over a 26-year period of the radial distance of the TS increases with latitude (see Table 2 of Whang et al., 2003).

From inspection of figure 2 in Whang et al. (2004), one note that the distance of the TS also varies over the solar cycle because of change in the dynamic pressure of the solar wind, with the maximum distance predicted to occur near solar minimum (e.g., see Whang and Burlaga, 2000; Whang et al., 2003, 2004). This distance could be calculated using various methods that include: Extrapolating observed CR gradients, pressure balance calculations, modulation models, gas-dynamic models of the interaction of the solar wind and the LISM, radio emissions from the heliopause triggered by the dissipation of large CR decreases in the heliopause, comparing Lyman-a light scattering from neutral Hydrogen in the upwind and downwind direction, solar wind velocity

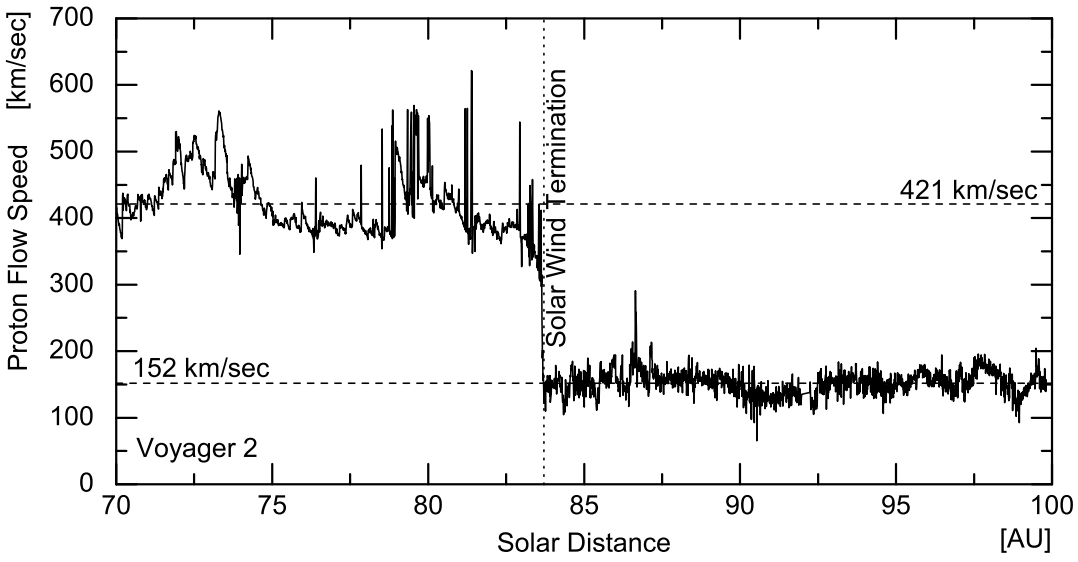

Figure 1.9: Solar Wind Speed observed by Voyager–2 spacecraft from 2003 to 2012 (NASA-COHOweb, 2012). During 2007 the spacecraft reach the Solar Wind termination locate at 83.7 AU, the transition could be seen in the graph when the SW speed from $\sim$ 421 km/s becomes subsonic $\sim$ 152 km/s.

observations and finally observations of the ACRs. It is worth noting that $\sim$100 AU is the averaged value over the corresponding solid angle of the TS location, which can be obtained from Table 2 of (Whang et al., 2003). Furthermore, Voyager 1 and 2 reached the TS in 2004 and 2007 located at about 94.0 AU and 83.7 AU, respectively, in agreement with the predictions from Whang and collaborators (e.g., see Stone et al., 2005, 2008). Langner and Potgieter (2005) treated symmetric and asymmetric TS models and concluded that for the $A > 0$ cycle for solar minimum no significant difference occurs; for the $A < 0$ cycle differences remain insignificant in the nose direction while, approaching the tail direction, some differences can be appreciated at proton energies below (1–1.5) GeV. Beyond the TS, the position of the outer boundary/heliopause is uncertain, probably at least 30-50 AU far from the solar wind termination. Finally recent measurement with IBEX (Interstellar Boundary Explorer) satellite show that there is no bow shock forming ahead of the heliosphere, as was widely expected in the past (McComas et al., 2012). For a review on the heliosphere structure see e.g. Strauss et al. (2012b).

1.3 Solar Cycle

The solar cycle has been observed since the 1600s when Galileo started observing sunspots (irregular, dark spots on the Sun's photosphere, indicative of intense magnetic fields). By examining the corresponding sunspot number, a long term record of solar activity is obtained, showing a quasi 11 year periodicity: periods of large sunspot numbers correspond to *solar maximum* conditions, while periods of fewer sunspots correspond to *solar minimum* condition (Smith and Marsden, 2003). Since sunspot are clearly correlated with the solar activity (higher number of sunspot higher is the solar activity) is possible to use it as a parameter of this activity and numbering the variation in

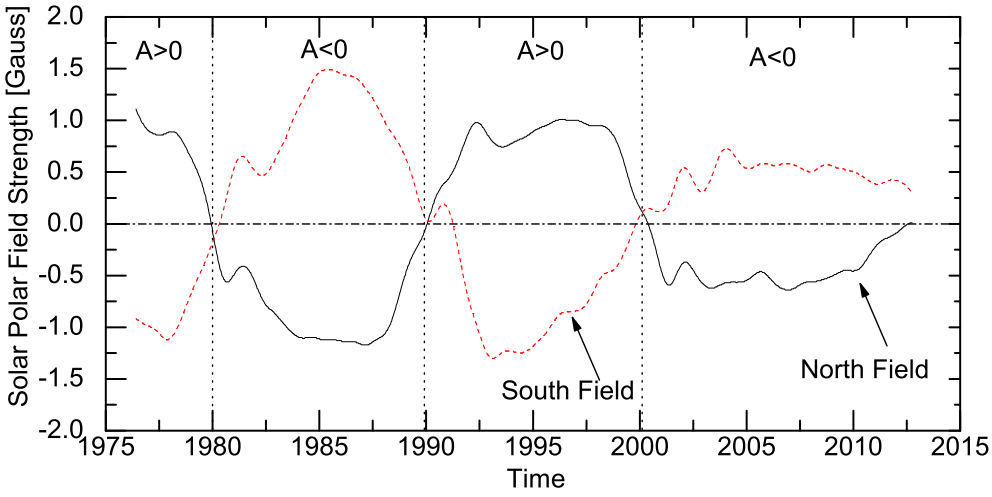

Figure 1.10: Sun's Polar Field strength is measured in the polemost 3' apertures at WSO each day, north (Solid Black line) and south (Dashed red line). The polemost aperture measures the line-of-sight field between about 55 and the poles. Each 10 days the usable daily polar field measurements in a centered 30-day window are averaged. A 20nhz low pass filtered values eliminate yearly geometric projection effects. Dot line divided the periods with opposite overall IMF Polarity (Data computed by WSO, 2012).

cycles, e.g. the period from the quiet sun in 1996 to quiet period in 2008 is called cycle 23. During solar maximum, an increase in the Sun's magnetic field is observed, along with its variability and the amount of transient events observed (e.g. solar flares, coronal mass ejections and co-rotating interaction regions). An other parameter that account for solar activity is the HCS tilt angle (α_t) that increases to maximum values during solar maximum, thereafter decreases to lower values during solar minimum conditions. all this cycles are correlated together also with the ≈22 year cycle in the IMF polarity; dubbed the *Hale cycle*. This is shown, e.g., in Fig. 1.10: by observing both the northern and southern solar magnetic field strength, we note that their polarity switches every ≈11 years. Periods when the northern IMF points away from the Sun are referred to as A $>$ 0 periods (e.g. centered at 1976, 1997), while A $<$ 0 periods (e.g. centered at 1965, 1987, 2010) refer to times when this field points inwards. Finally, as pointed out in Sect. 1.2.2, the solar wind speed also has a solar cycle related dependence, due to the time dependent latitudinal distribution of coronal holes on the solar surface. During solar minimum conditions, when the coronal holes are confined to the solar polar regions (e.g. Cranmer et al., 1999), two distinct solar wind distributions are observed (e.g. Phillips et al., 1995), namely the slow solar wind stream near the equatorial regions (with an average speed of Vsw ∼400 km s^{-1}) and two fast steams near the polar regions ($V_{\rm sw} \sim$ 800 km s^{-1}). During solar maximum conditions, the coronal holes are smaller and distributed uniformly over solar latitude (e.g. Harvey and Recely, 2002) and only a slow stream (albeit more variable) is observed over all latitudes (e.g. Strauss et al., 2012b).

Chapter 2

Solar Modulation

If we consider a distribution of charged particles moving through a medium of electromagnetic field that permeate space, i.e. the heliosphere (see Sect. 1.2), its time evolution is described by the Parker Transport Equation. It was initially treated by Parker (1965) who demonstrated that, in the framework of statistical physic, the random walk of the cosmic-ray particles is a Markov process, describable by a Fokker-Planck Equation (Sect. 2.2). During this propagation CR loose energy with greater efficiency at energy lower than 10–30 GeV/nucleon. This causes a decreasing of differential intensity of CRs depending on Solar Activity, the so called *solar modulation effect* described in Sect. 2.1. The most widely used solution of Parker equation uses the so-called Force Field approximation. In Sect. 2.3 a critical discussion of this kind of solutions is presented, including its intrinsic limitation to reproduce properly all modulated effects observable with modern detectors.

2.1 Particle Modulation Effects

The long term variation of the cosmic ray intensity is commonly studied at Earth orbit by mean of Neutron Monitors (NM). The measured NM counting rate at ground level (see e.g. Fig. 2.1) provides an indication of the GCR flux reaching Earth (Krüger et al., 2008; Krüger and Moraal, 2010). It is evident from Fig. 2.1 that the GCR flux at Earth has a strong anti-correlation with the solar activity cycle, with lower rate observed during solar maximum conditions, leading to the ∼11 years cycle. From inspection of Fig. 2.1 one note also different shape in the time variation on NM counting rate related to the *Hale cycle*, with peaked profiles observed during A < 0 periods and flat profiles during A > 0 periods. A discussion on this ~ 22 years cycle in CR intensities could be found e.g. in Strauss et al. (2012b), in Usoskin et al. (2011) (that evaluate the solar modulation parameter[1] since 1936 using Neutron monitors data) as well in McCracken et al. (2004) that extend the study of cosmic radiation since over the past 1150 years using the abundance of ^{10}Be in Greenland and South Pole ice.

Using the Neutron Monitor database (NMDB, 2012), that collect data from 35 station in Asia, Europe and Antarctica, one note that the time dependence in CR intensities is observed at all geographic latitude. This is equivalent to say that this behavior affect at least particles from 0.01

[1] see definition in Sect. 2.3

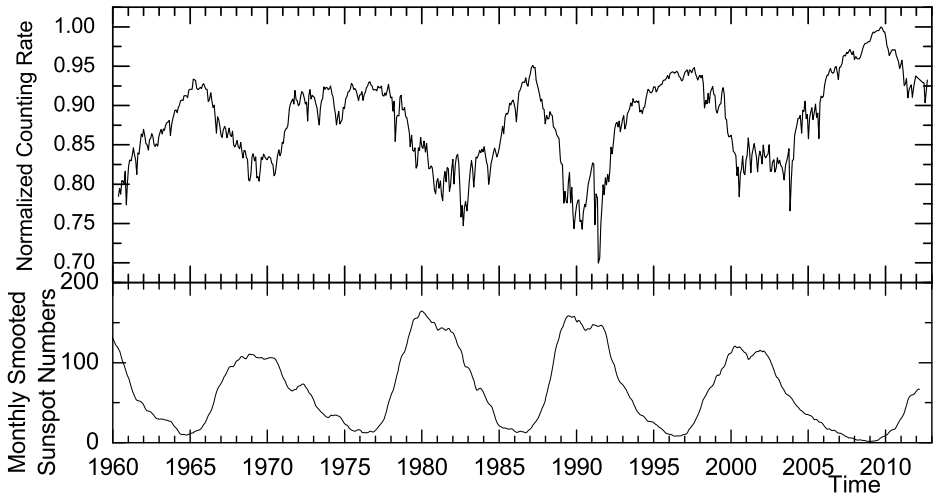

Figure 2.1: Relation between the solar cycle and CR Intensity. The top panel shown the normalized NM counting rate from McMurdo Neutron Monitor in function of the time (McMurdo, 2012; NMDB, 2012), data are normalized to September 2009. The bottom panel shown Monthly averages (updated monthly) of the sunspot numbers from 1960 up to 2012 (Data computed by SIDC-team, 2012).

to 10.75 GV (i.e. the minimum and the maximum lower rigidity cutoff values of stations recorded in the database[2]).

During the last two decades, using balloon flights and space-borne missions, the fluxes of galactic cosmic rays (GCRs) and their energy distributions were observed in different phases of solar activity. In particular the results of balloon flights campaign by BESS collaboration (see e.g. Shikaze et al., 2007, and fig 2.2) allowed to get GCRs fluxes with the same instrument from 0.2 up to 20 GeV almost once per year from 1997, solar minimum, to 2002, descending phase after solar maxima. In the near future even more accurate and systematic data will be available from AMS-02. This spectrometer is operational on board the International Space Station from 2011 May and is expected to collect data for more than a solar cycle (Battiston, 2010; Bobik et al., 2010). These observations will allow one to obtain accurate spectra with different solar activity conditions from some hundreds of MeV up to very high energy (a few TeV); in addition, using the same experimental apparatus, systematic errors on measured fluxes are expected to be minimized.

The interaction of charged particle with the IMF causes a magnetic drift in different direction for both particles and anti-particles or for opposite IMF polarity periods (see Sect. 2.2.2). Evidences of the solar modulation dependence on the sign of CR particles was observed at solar minimum by Garcia-Munoz et al. (1986); Potgieter et al. (1993a); Boella et al. (2001); the latter authors in particular, by mean of IMP8 satellite data during the period 1973–1995, notice that the charge dependence becomes gradually ineffective with increasing solar activity (see e.g. discussion in Section 4.1.2.6 of Leroy and Rancoita, 2011).

[2] since a neutron monitor has different cutoff rigidities for different incoming directions here we consider the lowest cutoff for each station; moreover this values should be corrected by an atmospheric cutoff (related to the so called yield function, see e.g. Clem and Dorman, 2000), that for a typical ground station is about 300 MeV (see, e.g. Flückiger et al., 2008).

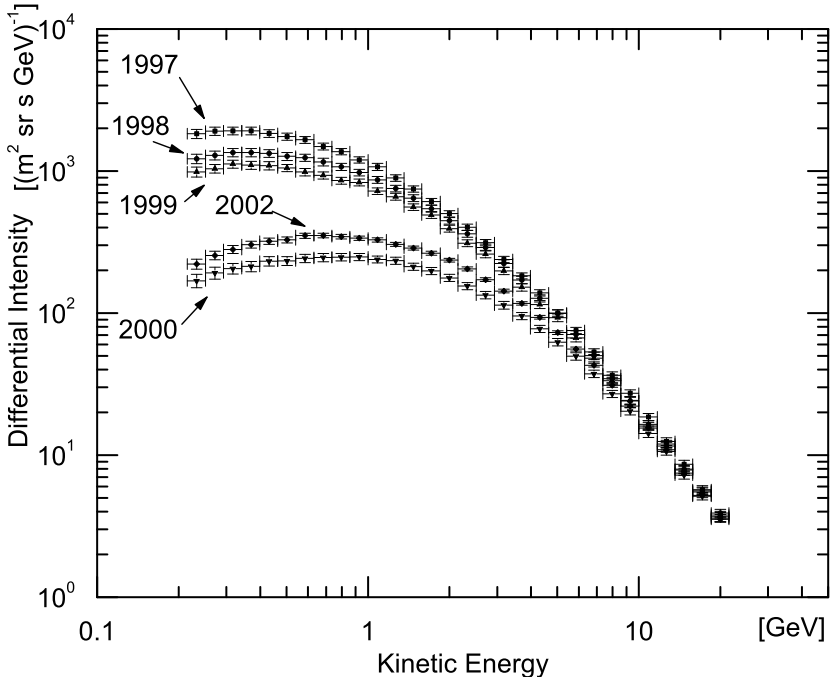

Figure 2.2: Proton Differential Intensity at the top of the atmosphere from 1997 through 2002 measured by BESS balloon. (Data from Shikaze et al., 2007)

The Ulysses collaboration performed the first-ever CR observations outside the ecliptic plane. The special orbit of this spacecraft allow them to study the heliosphere from $\sim -80°$to $\sim +80°$of solar latitude Simpson et al. (1992); Heber et al. (1997). Of particular interest are the so called *fast-scan*, i.e. the part of the orbit that allow to observe from south solar pole region up to north solar pole region in about one year. During the whole duration of the mission Ulysses perform 3 *fast-scan*, two of them during a period of solar minimum, one in the 1995 and the latter in 2007 (see Fig 2.3). During the first *fast-scan* they determine a latitudinal dependence of galactic protons intensity with an equatorial southward offset minimum and a north polar excess and a more homogeneous latitudinal distribution of electrons (Heber et al., 1996; Simpson, 1996; Simpson et al., 1996; Heber et al., 1997, 1998) during the last *fast scan* was observed the opposite behavior: the presence of a latitudinal gradient for electrons, of the same order of proton in the previous minimum, and a very small negative latitudinal gradient for protons Heber et al. (2008); De Simone et al. (2011). In Sect. 4.3.1 we discussed this results as due to magnetic drift effect. Finally, it has be remarked that modulation phenomena were observed also at low energies (i.e., lower than 500 MeV/nucleon) in the outer heliosphere (e.g. see Webber et al., 2008) and are currently being investigated, for instance, by Langner et al. (2003), Langner and Potgieter (2004), Bobik et al. (2008), Potgieter (2008) and references therein.

2.2 Transport Particle Equation

During '60s, E.N. Parker developed the basis of the theory for the general properties of the propagation of charged particles through the interplanetary space, considering the energy loss, and

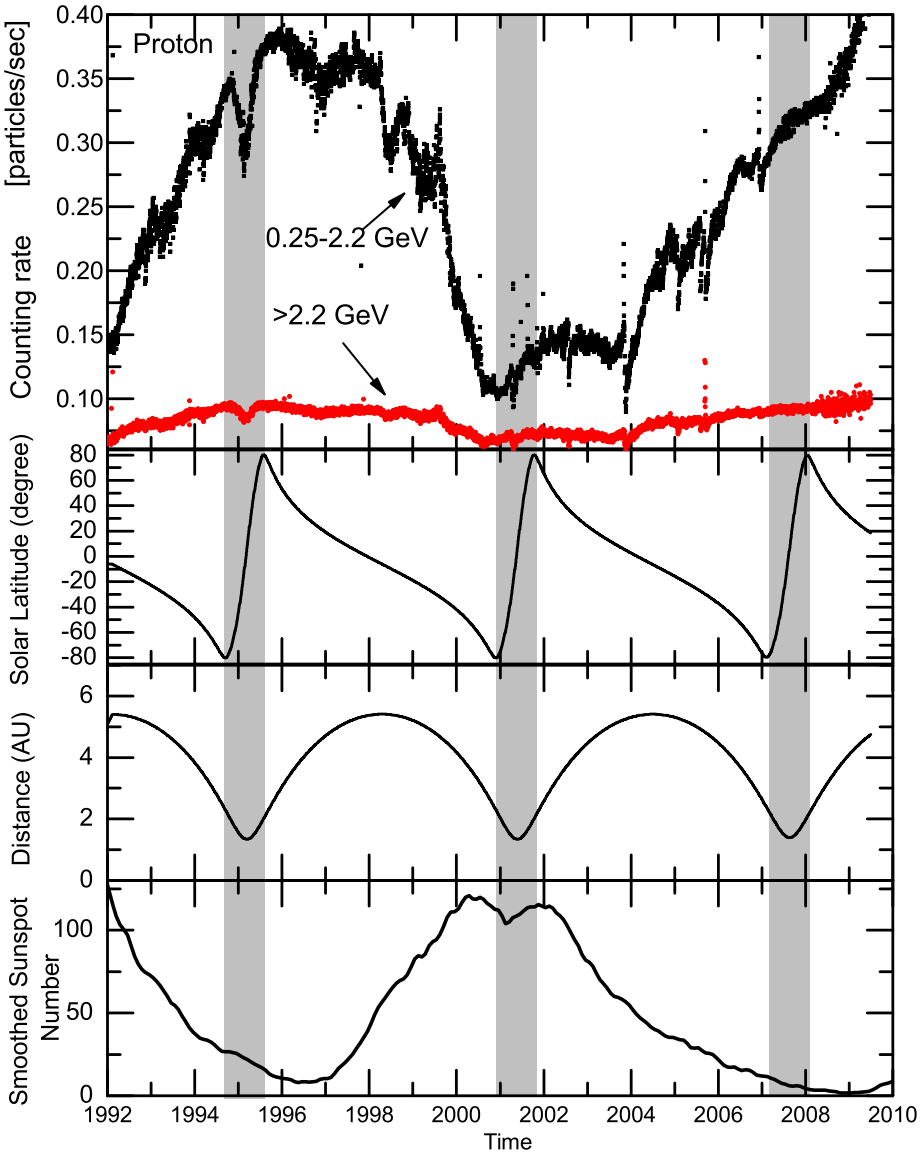

Figure 2.3: Ulysses daily averaged count rates of 0.25–2.2 GeV (black point) and $>$ 2.2 GeV (red point) protons from 1992 to 2009. Ulysses' distance from the Sun and its heliographic latitude are shown in the middle and bottom panel. The three *fast latitude scans* are marked by shaded bands. (data from NASA-COHOweb, 2012; CDAweb, 2012)

the outward convection of solar particles. In 1964 he showed that a charged particle, moving in a large-scale field with small-scale irregularity, is most effectively scattered by irregularity which have a scale comparable to the radius of gyration of the particle. Observation made by the IMP 1 spacecraft[3] shown spatial irregularity of the scale of 10^5–10^7 km in the magnetic field transported rigidly with the solar wind[4]. Than Parker (1965) conclude that this continuous scattering, in the reference frames of the magnetic irregularities, causes the charged particles to a random walk, which can be considered as a Markov process. Previously, Chandrasekhar (1943) demonstrated that for such process, the Boltzmann equation describing the evolution of the (normalized) phase-space distribution[5], can be treated using the so called *Fokker-Planck approximation*, leading to the so called Fokker-Planck equation. Starting from this arguments, using a non rigorous demonstration, Parker (1965) combined the major physical process in a time-dependent transport equation (also known as *Parker Equation*). To verify all the transport process present, this equation has been re-derived by Gleeson and Axford (1967) and it has been refined by Gleeson and Axford (1968b) and Jokipii and Parker (1970), correcting and better clarifying some details not included in the early work (see e.g. Section 4.1.2.4 of Leroy and Rancoita, 2011). Other works in literature also derived the Parker equation from a generic particles transport equation then applying the *Fokker-Planck approximation* (see e.g. Schlickeiser (1989), Chapter 3 and 8 of Stawicki (2003)). In the heliocentric system the Parker equation is expressed (e.g. see Jokipii et al. 1977, Equation (4.47) in Section 4.1.2.4 of Leroy and Rancoita 2011 and references therein):

$$\frac{\partial \mathrm{U}}{\partial t} = \frac{\partial}{\partial x_i}\left(K_{ij}\frac{\partial \mathrm{U}}{\partial x_j}\right) - \frac{\partial}{\partial T}\left(\mathrm{U}\frac{\partial T}{\partial t}\right) - \frac{\partial}{\partial x_i}(V_{\mathrm{sw},i}\mathrm{U}) \tag{2.1}$$

where U is the number density of Galactic Particles per unit of particle kinetic energy T, at the time t. $V_{\mathrm{sw},i}$ is the solar wind velocity along the axis x_i (described in Sect. 1.2.2), K_{ij} is the diffusion tensor discussed below (see also Sect. 2.2.1 and 2.2.2) and $\frac{\partial T}{\partial t}$ is the energy loss term treated in Sect. 2.2.3. The equivalent expression in terms of the omnidirectional distribution function (f) of CR particles with momentum $\mathbf{p}$ at the position $\mathbf{x}$ and time t can be found, for instance, in Equation (1) of Potgieter (1998) and Equation (4.59) of Leroy and Rancoita (2011). The differential intensity J is thus obtained as (Gleeson and Axford, 1968a; Pei et al., 2010b; Bobik et al., 2012a):

$$J = \frac{v\mathrm{U}}{4\pi} = p^2 f \tag{2.2}$$

where v is the speed of CR particle.

In his fundamental work, (Parker, 1958) describes the physical process occurring the GCR diffusion using the tensor representation K_{ij}. This is completely described in a reference system co-moving with the IMF irregularities; e.g. if we consider one axis parallel to the average magnetic field and

[3] also called *Explorer XVIII* (Ness et al., 1964)

[4] which, for instance, are comparable with the radius of gyration of protons with kinetic energies larger than ≈ 100 MeV and lower than ≈ 10 GeV moving perpendicular to a typical interplanetary magnetic field of ≈ 5 nT(Parker, 1964).

[5] e.g. see Section 2.1.2 of Cravens (1997), Section 2.2 of Gombosi (1998) and Section 5.2.1 of Kallenrode (2004)

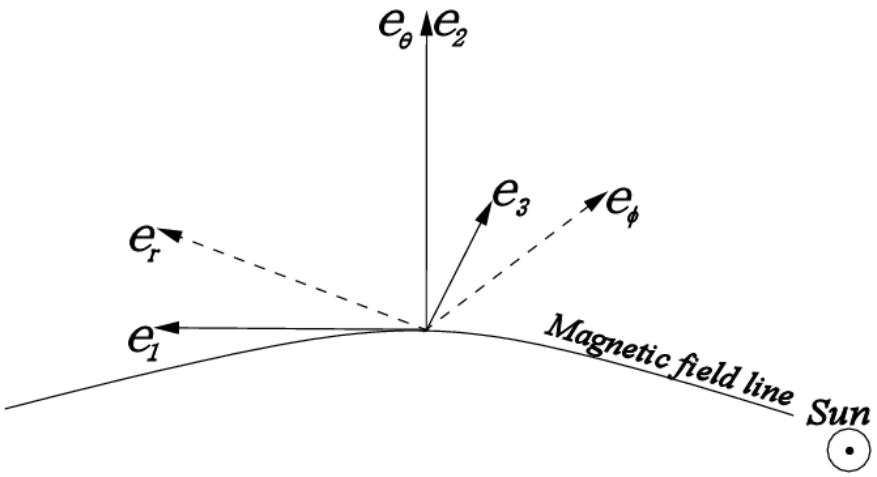

Figure 2.4: Schematic view of field line reference system (solid arrow) and heliocentric reference system (dashed arrow); in this schema $\mathbf{e}_2$ and $\mathbf{e}_\theta$ has the same direction

the other two perpendicular to this as in Fig. 2.4 (see e.g. Jokipii, 1971):

$$K_{ij} = \begin{bmatrix} K_{||} & 0 & 0 \\ 0 & K_{\perp,2} & K_A \\ 0 & -K_A & K_{\perp,3} \end{bmatrix} \tag{2.3}$$

with $K_{||}$ the diffusion coefficient describing the diffusion parallel to the average magnetic field; $K_{\perp,3} = K_{\perp,r}$ and $K_{\perp,2} = K_{\perp,\theta}$ are the diffusion coefficient describing the diffusion perpendicular to the average magnetic field in the radial and polar directions respectively, and finally K_A is the so-called antisymmetric diffusion coefficient described afterward. It is possible to divide this description in two parts, one represented by a symmetric tensor K_{ij}^S that describes the GCRs diffusive transport parallel and perpendicular to the mean magnetic field; the second, represented by a antisymmetric tensor K_{ij}^A, that includes drift effects:

$$K_{ij} = K_{ij}^S + K_{ij}^A = \begin{bmatrix} K_{||} & 0 & 0 \\ 0 & K_{\perp,2} & 0 \\ 0 & 0 & K_{\perp,3} \end{bmatrix} + \begin{bmatrix} 0 & 0 & 0 \\ 0 & 0 & K_A \\ 0 & -K_A & 0 \end{bmatrix} \tag{2.4}$$

Although the diffusion tensor is a compound of Symmetric and Antisymmetric, it is possible to divide the two effect, deriving and treating them in separate way in a generic reference frame, where the description is not so simple as in Eq. (2.3) and includes also nonzero off diagonal values (see e.g. App. A).

In the Parker theory, diffusion process is introduced as due to scattering on the magnetic irregularity that causes a random walk of the particles. The description of K_{ij}^S and K_{ij}^A here presented follow the approach close to Parker (1965). If a particle density gradient (∇n) is produced, this causes a proportional flux (S_{ij}) in the reference system of the irregularity,

$$S_{ij} = K_{ik}^S \nabla n, \tag{2.5}$$

where K_{ik}^S, that has the same meaning of the one in Eq. (2.1), represent the rate at which a diffusing substance (i.e. cosmic particle) is transported between opposite faces of a unit cube of a system when there is unit concentration difference between them. If the scattering is infrequent (compared to the cyclotron frequency) then the particles random walk back and forth along the magnetic field lines of force with little diffusion across them; in this case the particle motion between scatterings is describable by the well known guiding center approximation. If, on the other hand, significant scattering occurs frequently as once each cyclotron period, then diffusion across lines of force becomes important too. To compute the form of K_{ij}, Parker (1965) define L as the length of the step the particles makes along the magnetic field B_i, ν represent the number of steps taken in unit time, so that $\nu \simeq w_{||}/L$, where w_i is the particle velocity and $w_{||}$ denotes the component of w_i along B_i. This lead to diffusion coefficient along the field described as (Parker, 1965):

$$K_{||} \approx \nu L^2. \tag{2.6}$$

To define the diffusion coefficient across the field $K_\perp$, Parker (1965) define first the radius of gyration of the particle across the field as $S = w_\perp/\Omega$, where Ω is the cyclotron frequency of the particle in the field; if the particle is closely tied to the line of force, so that $\nu \ll \Omega$ (i.e. if $S \ll L$) then this gives $K_\perp \approx \nu S^2$; if on the other hand $L \ll S$, i.e. if the particle is scattered many times in one cyclotron period ($\nu \gg \Omega$) then $K_\perp \approx K_{||}$. The tensor representation combining $K_{||}$ and $K_\perp$ in a frame co-moving with the irregularities is (Parker, 1965):

$$K_{ij}^S \approx \nu L^2 \left(\frac{\nu^2 \delta_{ij} + \Omega_i \Omega_j}{\nu^2 + \Omega^2} \right) \tag{2.7}$$

where $\Omega_i = \frac{qB_i}{Mc}$, q particle charge, M particle mass and δ_{ij} is the well-known *Kronecker's delta* that is 1 if $i = j$ and 0 otherwise. The actual description about the symmetric part of diffusion tensor is discussed more in details in Sect. 2.2.1.

The complete treatment of the diffusion tensor did by Parker (1965) included the possibility of a net streaming as a consequence of a pressure gradient in the particle density, i.e. a drift of the guiding center. For most circumstance in the Heliosphere it is possible to assume no cosmic rays anisotropy, and to neglect the changes in particle energy during a single gyro-rotation (Parker, 1965). It follows that the net particle streaming u_i at a point in a large-scale field can be written (equation (8) of Parker, 1965) :

$$n u_i \sim \frac{v^2}{3\Omega^2} \epsilon_{ijk} \Omega_j \frac{\partial n}{\partial x_k} \tag{2.8}$$

where v is the particle velocity and ϵ_{ijk} is the usual permutation tensor, equal to ± 1 according as ijk is even or odd permutation of 1,2,3 and zero otherwise. To included Eq. (2.8) into Eq. (2.5) Parker (1965) represented this pressure drift by the artifice of an antisymmetric diffusion tensor:

$$K_{ij}^A = \frac{v^2}{3\Omega^2} \epsilon_{ijk} \Omega_k. \tag{2.9}$$

The antisymmetric elements of the diffusion-tensor matrix could be then rewritten as:

$$K_{ij}^{A} = K_{A}\epsilon_{ijk}\frac{B_k}{|\mathbf{B}|} \tag{2.10}$$

where is introduced the *antisymmetric diffusion coefficient* (Potgieter and Moraal, 1985; Burger and Hattingh, 1995):

$$K_{A} = \frac{pv}{3Ze|\mathbf{B}|} \tag{2.11}$$

with p, v, and Ze the momentum, velocity and charge of the cosmic-ray particle, respectively. As pointed out by Jokipii et al. (1977) and Jokipii and Levy (1977), the includes of Eq. (2.10) inside the Parker equation, Eq. (2.1), link directly the antisymmetric part of the diffusion tensor, $\frac{\partial}{\partial x_i}\left(K_{ij}^{A}\frac{\partial U}{\partial x_j}\right)$, to the drift velocity[6], $-\frac{\partial}{\partial x_i}\left(v_{d,i}U\right)$, so that:

$$\frac{\partial K_{ij}^{A}}{\partial x_j} = \frac{\partial}{\partial x_j}\epsilon_{ijk}K_{A}\frac{B_k}{|\mathbf{B}|} = \frac{pv}{3Ze}\nabla\times\frac{\mathbf{B}}{B^2} = \mathbf{v}_d, \tag{2.12}$$

That is endorsed in the well know guiding center approximation, where the motion of a particle is describable by the motion of the center of his gyro-rotation along the magnetic field.

We stressed that the drift velocity is determined by the antisymmetric part of the diffusion tensor which accounts for gradient, curvature and current sheet drifts of particles in the IMF, i.e. it depends on the charge sign of the particles (Bobik et al., 2012a). Furthermore, as discussed by Jokipii and Levy (1977), one can rewrite Eq. (2.1) enclosing Eq. (2.4) and (2.12) (see also equation (4.75) of Leroy and Rancoita, 2011 and equation (4) of Bobik et al., 2012a): :

$$\frac{\partial \mathrm{U}}{\partial t} = \frac{\partial}{\partial x_i}\left(K_{ij}^{S}\frac{\partial \mathrm{U}}{\partial x_j}\right) + \frac{1}{3}\frac{\partial V_{\mathrm{sw},i}}{\partial x_i}\frac{\partial}{\partial T}\left(\alpha_{\mathrm{rel}}T\mathrm{U}\right) - \frac{\partial}{\partial x_i}[(V_{\mathrm{sw},i}+v_{d,i})\mathrm{U}] \tag{2.13}$$

where α_{rel} is defined in eq (2.24).

Thus, one obtains that drift effects are accounted for a convection velocity in which the drift velocity is added to the solar wind velocity. In this way, as remarked by Bobik et al. (2012a), the resulting effective convection velocity may non-negligibly differ from that due to the solar wind; but noting that $\nabla\cdot\overline{v}_d = 0$, one finds that drift effects do not contribute to the adiabatic energy changes, i.e. second right-hand term of Equations (2.13) (see also Jokipii and Levy, 1977). Even if drift motions can affect modulated GCR spectra by redirecting particles within the heliosphere (Jokipii et al., 1977) and this mechanism was included in the Parker equation, some modulation models neglected it, like, for istance the so called Force Field model described in Sect. 2.3 (see discussion in Parker (1965); Jokipii and Parker (1970); Jokipii and Levy (1977); Jokipii et al. (1977); Potgieter (1998)).

[6] for the complete calculation: apply the common rules for derivation of derivative (like the Leibniz derivative rules), and than note that the divergence of a curl is identically zero.

2.2.1 Parallel and Perpendicular Transport

In (Bobik et al., 2012a) the Parker equation was solved using the $K_{||}$ suggested by Potgieter et al. (1993b); Potgieter and Le Roux (1994):

$$K_{||} \approx \beta k_1(r,t) K_P(P,t) \frac{B_\oplus}{3B} \tag{2.14}$$

with $\beta = v/c$, v the particle velocity and c the speed of light; the diffusion parameter k_1 accounts for the dependence on the solar activity and is treated in Sect. 3.2.2; $B_\oplus$ (typically ≈ 5 nT) is the value of the IMF at Earth's orbit but it varies as a function of time; B is the magnitude of the large-scale IMF (discussed in Sect. 1.2) and thus depends on the heliospheric region (Sect. 3) through which GCRs are transported; finally, the term K_P takes into account the dependence on the rigidity P of the GCR particle and is usually expressed in GV. To a first approximation, (Bobik et al., 2012a) assumed that

$$K_P \approx P \tag{2.15}$$

for particle rigidities above a threshold value $P_{\rm th}$ within the rigidity range (0.4–1.015) GV, as commonly supposed by many authors (e.g., see Gloeckler and Jokipii, 1966; Gleeson and Axford, 1968a; Perko, 1987; Potgieter and Le Roux, 1994; Strauss et al., 2011). In this work this formulation is modified in order to reproduce also GCR data outside the ecliptica as seen by Ulysses (see Sects. 4.2.2 and 4.3.1). We use the spatial dependence of $K_{||}$ proposed by Strauss et al. (2011) on base of diffusion coefficients used previously in electrons studies (e.g., Potgieter and Ferreira, 2002) and observations of electron mean free paths near Earth (e.g., Palmer, 1982; Dröge, 2005). The Energy depence is the same of Eq. (2.14), but differ in the spatial dependence:

$$K_{||} = \frac{\beta}{3} K_0 \frac{P}{1\text{GV}} \left(1 + \frac{r}{1\text{ AU}}\right); \tag{2.16}$$

and $k_1(r,t)$ is substituted by the diffusion parameter K_0 as discussed in Sect. 3.2.2. K_P is assumed to be equal to the value of the rigidity (P) above the upper limit of the $P_{\rm th}$ range, i.e. $P_{\rm th} = 1\text{GV} \simeq 0.444$ GeV for proton kinetic. In this new form $K_{||}$ has no latitudinal dependence and a radial dependence $\propto r$, i.e. the same radial dependence at large distance and on ecliptic of Eq. (2.14); as also discussed in McDonald et al. (1997) this spatial dependence of $K_{||}$ affect the latitudinal gradients at high latitude and is consistent with the original suggestion of Jokipii and Kota (1989).

The perpendicular diffusion coefficient is taken to be proportional to $K_{||}$ (Bobik et al., 2012a), with $K_{\perp,r} = K_{\perp,\theta} = \rho_k K_{||}$ (e.g., see Potgieter, 2000, and references therein).

In the present model, the value of ρ_k is tuned on observational data for the whole solar cycle 23 (see Sect. 4.2.1). Potgieter (2000) (see also Burger et al., 2000; Heber and Potgieter, 2006; Bobik et al., 2012a), suggested the usage of an enhanced $K_{\perp,\theta}$ in the polar regions in order to reproduce the observed GCR latitudinal gradients for protons and electrons (e.g., see Potgieter, 1997; Heber et al., 1998). He introduced a sharp transition (via a transition function, e.g., see Figure 7 in that article) in the colatitude regions $120^\circ < \theta < 130^\circ$ and $60^\circ < \theta < 50^\circ$, that increased $K_{\perp,\theta}$ by a

factor of about (or larger than) 10, while later Ferreira and Potgieter (2004) used a factor of 8. Strauss et al. (2012b) anyway underline as the theoretical basis for this enhancement however still remains elusive (e.g. Jokipii et al., 1995; Ruffolo et al., 2008). In Section 4.2.1 the case with and without enhancement are compared.

As remarked in Strauss et al. (2012b) the derivation of the diffusion tensor remains a great challenge for CR modulation studies. Quasi-linear theory (QLT, Jokipii, 1966) remains the preferred scattering theory to derive $K_{||}$, while non-linear guiding center theory (NLGC, Matthaeus et al., 2003) is widely used to calculate the perpendicular components. For a review on the current status of diffusion theory, see e.g. Shalchi (2009). By using these theories, and recent advances in modeling turbulent transport (e.g. Pei et al., 2010a), tractable expressions for the diffusion coefficients, based on fundamental turbulence parameters, are available (e.g. Shalchi and Schlickeiser, 2004), and has been implemented in numerical modulation models with some success (e.g. Engelbrecht and Burger, 2010; Strauss and Potgieter, 2010). Strauss et al. (2012b) note, however, that some of these advenced studies accounts for observations carried out on data of low-energy electrons collected using spacecraft (for instance, (3–10) MeV from Ulysses in Ferreira et al. (2001a) and 16 MeV from Pioneer 10 in Potgieter and Ferreira (2002)), so are not considered for the purpose of this work.

2.2.2 Magnetic Drift

As pointed out in Parker (1957) drift velocity in Eq. (2.12) accounts for effects due to gradient and curvature drifts experienced by cosmic-ray particles transported through the IMF ($\mathbf{v}_{d,\mathrm{regular}}$, see also Parker, 1957; Isenberg and Jokipii, 1979; Burger et al., 1985; Armstrong et al., 1985); moreover, as summarize in Fig. 2.5, this account also for the net drift effects occurring close to the Heliospheric Current Sheet[7] (HCS, Parker, 1957; Burger et al., 1985; Potgieter and Moraal, 1985; Pei et al., 2012). For general purpose is convenient consider the drift velocity as a combination of two drift velocity (Burger and Hattingh, 1995):

$$\mathbf{v}_d = \mathbf{v}_{d,\mathrm{regular}} + \mathbf{v}_{d,\mathrm{HCS}}, \tag{2.17}$$

and treat the two term separately. The 3D analytical expression of both $\mathbf{v}_{d,\mathrm{regular}}$ and $\mathbf{v}_{d,\mathrm{HCS}}$ was evaluated starting from Eq. (2.12) by Hattingh and Burger (1995) and Langner (2004) for the special case of pure Parker Field, during a low activity period of the Sun. A modulation model of GCRs for steady-state conditions with relevant drift effects including that due to a wavy HCS (WHCS) could be found e.g. in Potgieter and Moraal (1985).

In the 2D approximation, treated in this work and presented here following the approach close to (Bobik et al., 2012a), the drift velocity ($\mathbf{v}_d$) is integrated over a complete solar rotation (i.e. over the azimuthal angle ϕ); this causes $\mathbf{v}_{d,\mathrm{HCS}} \neq 0$ in the latitudinal region spanned by the neutral sheet and for $\mathbf{v}_{d,\mathrm{regular}}$ is introduced a scaling function that varies from +1 ($\theta \sim 0$) to –1 ($\theta \sim \pi$) (see e.g. Hattingh and Burger, 1995). Analytical solution of this integral was computed by

[7] i.e. the region where the IMF changes polarity, see Sect. 1.2.3

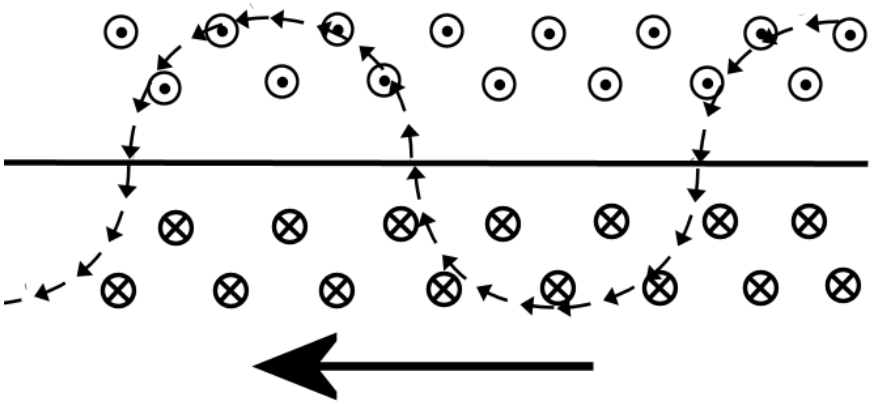

Figure 2.5: Schematic view of drift effect along a neutral sheet plane (central line), a particle in the upper part of the picture, moving along the magnetic field, experienced a counter-clockwise rotation due to Lorentz magnetic force, while in the bottom part, since the direction of the magnetic field is reversed, the particle experienced a clockwise rotation; the continuous passage between the two side, causes the particle drift from right to left side of the picture.

Hattingh and Burger (1995) (see also Langner, 2004) under the assumption of an analytical shape of the neutral sheet as the one modeled in Burger and Potgieter (1989). Potgieter and Moraal (1985) succeeded in formulating a 2D description of the WHCS, which –as discussed by Burger and Hattingh (1995)– is equivalent to the treatment of transport in a three-dimensional heliosphere with the assumption of an axis-symmetric particle distribution. In this description, the presence of a wavy neutral sheet is approximated via an appropriate modification of K_{ij}^{A}, i.e. multiply the antisymmetric part of the diffusion tensor (K_A) by a scaling factor $f[\mu(\theta)]$, that account for the change of polarity of the magnetic field in the different heliospheric hemisphere (see Section 4 of Bobik et al., 2012a):

$$f(\mu) = \begin{cases} 1 - 2H[\mu(\theta)] & \text{if } c_h \geq \frac{\pi}{2} \\ \frac{1}{a_f} \arctan\left\{ \left[1 - 2 \arccos \frac{\mu(\theta)}{\pi} \right] \tan(a_f) \right\} & \text{if } c_h < \frac{\pi}{2} \end{cases} , \tag{2.18}$$

where

$$a_f = \arccos\left(\frac{\pi}{2\theta_{1/2}} - 1 \right), \qquad \mu(\theta) = \cos(\theta),$$

and finally c_h is a parameter that define the smoothness or sharpness of the transition function. The relationship between c_h and the tilt angle (α_t, described in sect 1.2.3) is given by Burger and Potgieter (1989):

$$c_h = \begin{cases} \frac{\pi}{2} - 0.5 \sin(\frac{\pi}{2}) & \text{if } \alpha + \Delta\theta_{HCS} \geq \frac{\pi}{2} \\ \frac{\pi}{2} - 0.5 \sin(\alpha + \Delta\theta_{HCS}) & \text{if } \alpha + \Delta\theta_{HCS} < \frac{\pi}{2} \end{cases} , \tag{2.19}$$

where

$$\Delta\theta_{HCS} = \frac{2r_p}{r} = \frac{2A_{at}\sqrt{T(T+2T_0)}}{Zr|B|}, \tag{2.20}$$

r_p is the particle gyro-radius (e.g., see Hattingh and Burger, 1995; Burger and Hattingh, 1995),

A_{at} and Z are respectively the Mass number and the Atomic number of the particle, and finally $f(c_h) = 0.5$ and $f(\pi/2) = 0$. $\Delta\theta_{HCS}$ is determined from the maximum distance that a particle drifting along the neutral sheet can be away from this sheet (Burger and Potgieter, 1989). In present model we adopt the approach of Potgieter and Moraal (1985), with a magnetic filed defined in Eq. (1.14). The complete expression (i.e. including HCS drift) for the drift velocity become:

$$\mathbf{v}_d = \nabla \times \left[f(\theta) \frac{pv}{3qB_N^2} \mathbf{B}_{\rm P} + \frac{pv}{3qB_N^2} \mathbf{B}_{\rm L} \right] + \frac{\partial f(\theta)}{\partial \theta} \frac{pv}{3qrB} \mathbf{e}_\theta \times \left(\frac{\mathbf{B}_{\rm P}}{B} \right); \tag{2.21}$$

where

$$\mathbf{B}_{\rm P} = \frac{A}{r^2} \left[\mathbf{e}_r - \Gamma \mathbf{e}_\varphi \right]$$

is the Parker Field expression valid on the whole heliosphere, while

$$\mathbf{B}_{\rm L} = \frac{A}{r} \frac{\delta(\theta)}{r_b} \mathbf{e}_\theta$$

is the polar correction factor as introduced at pag. 22.

For completeness has to be considered that studies focused to the lower part of GCR spectra (up to few hundred MeV) introduces a *drift suppression factor*,

$$f_s = \frac{(\omega_g \tau)^2}{1 + (\omega_g \tau)^2} \tag{2.22}$$

with ω_G the ion gyro-frequency and τ a time scale defined by scattering (e.g. Bieber and Matthaeus, 1997). Burger et al. (2000) showed that by approximating the scattering parameter as $\omega_g \tau \propto P$, results in reasonable agreement with CR observations. More fundamentally, Minnie et al. (2007) showed explicitly that the drift speed is indeed suppressed by scattering. Strauss et al. (2012b) comments that analytical approximations of f_s remain elusive, but continues to be an avenue of further study (e.g. Burger and Visser, 2010).

2.2.3 Adiabatic Energy Loss

In Eq. 2.1 the second term of right side accounts for the energy changes experienced by cosmic particles during the propagation inside the heliosphere. If Fermi acceleration is neglected (Parker, 1965) the only energy loss contribution (dT/dt) comes from the *adiabatic compression and expansion* of the cosmic radiation due to spatial divergence of the solar wind (Jokipii and Parker, 1970, and pag. 366 of Leroy and Rancoita, 2011):

$$\frac{dT}{dt} = -\frac{T}{3} \alpha_{\rm rel} \frac{\partial V_{{\rm sw},i}}{\partial x_i} = -\frac{T}{3} \alpha_{\rm rel} (\nabla \cdot \mathbf{V}_{\rm sw}), \tag{2.23}$$

where

$$\alpha_{\rm rel} = \frac{T + 2m_r c^2}{T + m_r c^2} \tag{2.24}$$

is $\alpha_{\rm rel} = 2$ for non relativistic particles, and $\alpha_{\rm rel} = 1$ for ultra-relativistic particles (Parker, 1965). Thus, for a radial solar wind speed, as the one described in Sect. 1.2.2, the energy loss is (see e.g.

Parker, 1965, and pag. 366 of Leroy and Rancoita, 2011):

$$\frac{dT}{dt} = -T\frac{\alpha_{\rm rel}}{3r^2}\frac{\partial r^2 V_{\rm sw}}{\partial r} = -T\frac{\alpha_{\rm rel}V_{\rm sw}}{3r}; \tag{2.25}$$

If we exclude phenomena of re-acceleration, due to the heliosphere's border effects or related to impulsive and local events from the Sun, inside the heliosphere this is the main way for galactic particles to modify their energy. This is true for proton and heavier particles while for electron and positron, due to their small mass, this assumption could be no more valid. For this reason other energy loss process are accounted by Bobik et al. (2011a), such inverse-Compton, Ionization, Bremsstrahlung and Synchrotron. In Appendix C we showed that the global effect of this enclosure is under the percent level in the most optimistic case, and this confirm that adiabatic cooling associated to particle diffusion is the only way for galactic particles at GeV energies to modify their energy.

2.3 Force Field Approximation

It is worthwhile to note that Equations (2.1) and (2.13) can be solved analytically only by treating a simplified transport of GCRs through the heliosphere. The most used solution is the so called *Force Field Model* (FFM), presented in this Section. Here we follow the approach close to Gleeson and Axford (1968a) and Section 4.1.2.4 of Leroy and Rancoita (2011). The *Force Field Model* (FFM) assumed that, at the time t, (a) modulation effects can be expressed with a spherically symmetric modulated differential number density U of GCRs, (b) the diffusion coefficient reduces to a scalar given by a separable function of r (the radial distance from the Sun) and P (the particle rigidity in GV):

$$\kappa(r,t) = \beta k_1(r,t) K_P(P,t) \tag{2.26}$$

with K_P from Sect. 2.2.1 for particle rigidities above ≈1 GV, and (c) the modulation occurs in a steady-state condition, i.e., the relaxation time of the distribution is short with respect to the solar cycle duration so that one can assume that the partial derivative of U with respect to time is zero. The conditions (a) and (b) leads to rewrite Eq. (2.1) is a pure radial and diffusive-convective equation (see equation 4.40 of Leroy and Rancoita, 2009):

$$\frac{\partial U}{\partial t} = \frac{1}{r^2}\frac{\partial}{\partial r}\left(r^2\kappa\frac{\partial U}{\partial r}\right) - \frac{1}{r^2}\frac{\partial}{\partial r}(r^2 V_{\rm sw} U) + \frac{1}{3r^2}\frac{\partial(r^2 V_{\rm sw})}{\partial r}\frac{\partial}{\partial T}(T\alpha_{\rm rel}U). \tag{2.27}$$

Condition (c) of steady-state condition, require that:

$$\frac{\partial U}{\partial t} = 0. \tag{2.28}$$

Using Eq. (2.28) it is possible rewrite Eq. (2.27) (Gleeson and Axford, 1968a):

$$\frac{1}{r^2}\frac{\partial}{\partial r}(r^2 S) = -\frac{V_{\rm sw}}{3}\frac{\partial^2}{\partial r \partial T}(\alpha T U), \tag{2.29}$$

$$S = V_{\rm sw} U - \kappa \frac{\partial U}{\partial r} - \frac{V_{\rm sw}}{3}\frac{\partial}{\partial T}(\alpha T U). \tag{2.30}$$

Where S is the radial current density (or streaming) of the cosmic-ray particles in the kinetic energy range $(T, T + dT)$; Gleeson and Axford (1968a) noted that for reasonable values of coefficients in Eq. (2.29), S is negligible when $T \geq 400$ MeV for protons. At lower energies S becomes significant. In the energy range where S could be considered negligible, it is possible to rewrite Eq. (2.30) in term of the total particle energy ($E_t = T + m_r c^2$) and rest mass (m_r) (Gleeson and Axford, 1968a, and equation 6.61 of Leroy and Rancoita, 2011):

$$\begin{aligned}
\kappa\frac{\partial U}{\partial r} &\approx V_{\rm sw}\left[U - \frac{1}{3}\frac{\partial}{\partial T}(T\alpha_{\rm rel}U)\right] \\
\kappa\frac{\partial U}{\partial r} &= V_{\rm sw}\left[U - \frac{1}{3}\frac{\partial}{\partial E_t}\left(\frac{E_t^2 - m_r^2c^4}{E_t}U\right)\right] \\
&= V_{\rm sw}\left\{U - \frac{1}{3}\frac{\partial}{\partial E_t}\left[\frac{U}{E_t(E_t^2 - m_r^2c^4)^{1/2}}(E_t^2 - m_r^2c^4)^{3/2}\right]\right\} \\
&= -\frac{V_{\rm sw}}{3}(E_t^2 - m_r^2c^4)^{3/2}\frac{\partial}{\partial E_t}\left[\frac{U}{E_t(E_t^2 - m_r^2c^4)^{1/2}}\right].
\end{aligned} \tag{2.31}$$

The solution of this equation together with Eq. (2.29) can be regarded as an asymptotic solution of the correct Eq. (2.29) and (2.30) valid at high energies. Gleeson and Axford (1968a) introduce the quantities:

$$\zeta = \int_{m_r c^2}^{E_t} \frac{K_P}{(E_t'^2 - m_r^2c^4)^{1/2}} dE', \tag{2.32}$$

$$\phi_s = \int_r^{r_{tm}} \frac{V_{\rm sw}}{3k_1} dr', \tag{2.33}$$

where r_{tm} is the termination distance of the solar wind. ϕ_s is the so-called *modulation strength* (or modulation parameter) that is independent of the species of GCR particles and it is usually expressed in units of GV (or MV): for instance, a typical weak modulation condition at 1 AU occurs for ϕ_s(1 AU) = (0.32–0.35) GV (pag. 370 of Leroy and Rancoita, 2011).
With a diffusion coefficient given by Eq. (2.26), Eq. (2.31) can be integrated to give:

$$\frac{U}{E_t(E_t^2 - m_r^2c^4)^{1/2}} = H(\zeta - \phi_s, t) \tag{2.34}$$

here $H(\zeta - \phi_s, t)$ is an arbitrary function to be determined from the boundary conditions or by matching observations. In general $H(\zeta - \phi_s, t)$ will be different for each species (Gleeson and Axford, 1968a). Then lets introduce the *Differential intensity* as (Gleeson and Axford, 1968a).

$$J(r, E_t, t) = \frac{vU(r, E_t, t)}{4\pi} = \frac{c}{4\pi}E_t(E_t^2 - m_r^2c^4)^{1/2}U(r, E_t, t) \tag{2.35}$$

and apply the boundary conditions

$$H(\zeta, t) = \frac{4\pi}{c} \frac{J(\infty, E_t)}{(E_t^2 - m_r^2 c^4)} \tag{2.36}$$

to Eq. (2.34) that give (Gleeson and Axford, 1968a):

$$\frac{J(r, E_t, t)}{(E_t^2 - m_r^2 c^4)} = \frac{J(\infty, E_t + \Phi_p)}{(E_t + \Phi_p)^2 - m_r^2 c^4}; \tag{2.37}$$

This equation specifies the differential intensity at (r, E_t, t) in term of undisturbed intensity at infinity, $J(\infty)$, i.e. the Local Interstellar Spectrum outside the SW termination. Φ_p is defined in a way that given the inverse function $E_t = \psi(\zeta, Z, t)$, with Z particle charge in unit of electron charge e, is valid the expression $\Phi_p = \psi(\zeta + \phi_s, Z, t) - \psi(\zeta, Z, t)$. We remark that Φ_p is completely determined by $\phi_s(r, t)$, but (i) depends on E_t, (ii) may be different for each species, (iii) accounts for mean energy-losses experienced by particles coming from outside the heliosphere down to radial distance r and, thus, (iv) may be interpreted as similar to a "potential energy". This approximated solution for obtaining modulated differential intensities is termed *force-field solution*, while Φ_p is called *force-field energy-loss* (see, e.g. pag. 370 of Leroy and Rancoita, 2011, and reference therein). We underline that the *force-field solution* is obtained with a spherical approximation of the heliosphere and does not accounts any drift effects. Although this solution could easily describe the solar modulation of a particular species with a single parameter, it could not describe the actual solar modulation in general. 2D effects related to the large scale magnetic field, e.g. like the latitudinal gradient observed by Ulysses (see Sect. 4.2.2), could not be reproduced by FFM. In a similar way a compound study on different particles specie, like e.g. the anti-proton over proton rate (Sect. 3.2.6) and positron ratio (Sect. 4.3.2), is hard to handle with this simple solution since each species require an independent solution. For a more general discussion on the limitation of *force-field solution* see Caballero-Lopez and Moraal (2004). In this work we will show how a numerical solution, using the Monte Carlo technique could reproduce observed data, at Earth orbit as well outside ecliptic plane, using a limited number of observation parameters mainly dependent by heliosphere environment.

Chapter 3

HelMod Monte Carlo Code

Due to the complexity of the Parker Transport Equation described in Sec. 2.2, an analytical solution could be obtained only by treating a simplified transport of GCRs through the heliosphere (see Sect. 2.3). For this reason this transport equation is typically solved numerically, for example employing a finite difference methods (Jokipii and Kopriva, 1979; Kota and Jokipii, 1983; Potgieter and Moraal, 1985; Burger and Hattingh, 1995) or with the standard implicit difference technique (Fisk, 1971; Kota and Jokipii, 1991). These methods have several disadvantages, most notoriously numerical instability problems when solving differential equation in higher dimensions (Pei et al., 2010b; Kopp et al., 2012). An alternative method is to reduce the problem from Parker's differential equation, which is a Fokker-Planck type equation, to a set of ordinary differential equations that can be solved using the stochastic simulation technique. As underlined by Strauss et al. (2011), this methods has several advantages, most notably unconditional numerical stability and independence of a spatial grid. Additionally, the Monte Carlo approach allow to evaluate more physical insights than simply the modulated spectra Bobik et al. (e.g. see 2012b); Strauss et al. (e.g. see 2011). A stochastic motion do not allow for a particle by particle study, but one can only explore how the system evolve in average, considering all particles as ensemble. When the particles stochastic behavior is studied from probabilistic point of view, the theory of Markov stochastic process may provide very powerful mathematical tools (Zhang, 1999).
An early attempt to use individual particle transport to study cosmic-ray modulation problems was given by Jokipii and Owens (1975) and Jokipii and Levy (1977), but their approach has very limited applications, because the stochastic particle motion part was treated in an unconventional way that is only valid for special choices of the diffusion coefficients (Zhang, 1999). Recently a stochastic method similar to the pioneering Monte Carlo method has been proposed to solve the Fokker-Planck equation which appear in various astrophysical settings like model the transport of pick-up ions in the heliosphere (Fichtner et al., 1996), the study the CR acceleration in astrophysical systems (Kruells and Achterberg, 1994) and modeling the CR propagation in the heliosphere (Yamada et al., 1998; Gervasi et al., 1999; Zhang, 1999; Alanko-Huotari et al., 2007b; Pei et al., 2010b; Strauss et al., 2011; Bobik et al., 2012a). As pointed out by Pei et al. (2010b), it is interesting to note that, since each random process have to be independent of all others, one big advantage of the stochastic method is that it is very easy to parallelize so that it can runs

on many CPUs of a local cluster which can reduce the computation time and lower the hardware costs dramatically. In this Chapter we present the *Heliosphere Modulation code* (HelMod – Version 2.0) developed for this work, that represent an improvement with respect the HelMod version 1.5 already presented in Bobik et al. (2012a). In Sect. 3.1 we presented the Stochastic Differential Equation technique from a mathematical point of view, their properties and their relationship with the particles transport equation. In Sect. 3.2 we present the actual implementation of HelMod code with some general results that gives the feeling of the powerful of this technique. Discussion on the model through comparison with experimental data is postponed to chap. 4.

3.1 Stochastic Differential Equation

Stochastic Differential Equation (SDE) models play a prominent role in a range of application areas, including biology, chemistry, epidemiology, mechanics, microelectronics, economics, and finance. As explained by Higham (2001), a complete understanding of SDE theory requires familiarity with advanced probability and stochastic processes, however, it is possible to appreciate the basics of how to simulate SDEs numerically with just a background knowledge of Euler's method for deterministic ordinary differential equations and an intuitive understanding of random variables. The SDE theory is described in specialized textbook like e.g. Gardiner (1985, chap. 4) or Klöden and Platen (1999). For a more practical approach is suggested to read the work done by Higham (2001) that use a numerical approach and practical example to explain SDE Monte Carlo technique and also contain a good index of reference for further understanding of the numerical methods associated. In this Section we first introduce the concept of Brownian motion and the link with the SDE, then we present the connection of SDE with a Fokker-Planck like equation and how to integrate them using the Euler-Majorana method.

3.1.1 Brownian Motion and Evolution of a Stochastic Process

A scalar *standard Brownian motion*, or *standard Wiener process*, over $[0, T]$ is a random variable $W(t)$ that depends continuously on $t \in [0, T]$ and satisfies the following three conditions (as defined by Higham, 2001):

1. $W(0) = 0$ (with probability 1);

2. For $0 \leq s < t \leq T$ the random variable given by the increment $W(t) \sim W(s)$ is normally distributed with mean zero and variance $t - s$; equivalently, $W(t) - W(s) \sim \sqrt{t-s}N(0, 1)$, where $N(0, 1)$ denotes a normally distributed random variable with zero mean and unit variance.

3. For $0 \leq s < t < u < v \leq T$ the increments $W(t) - W(s)$ and $W(v) - W(u)$ are independent.

For computational purposes it is useful to consider discrete Brownian motion, where $W(t)$ is specified at discrete t values. We thus set $\delta t = T/N$ for some positive integer N and let W_j denote $W(t_j)$ with $t_j = j\delta t$. the first condition says $W_0 = 0$ with probability 1, while the second and the

third conditions tell us that

$$W_j = W_{j-1} + dW_j, \qquad j = 1, 2, ..., N, \tag{3.1}$$

where each dW_j is an independent random variable of the form $\sqrt{\delta t}N(0,1)$.

A scalar, autonomous *Stochastic Differential Equation* for a stochastic quantity $x(t)$ can be written in integral form as (Gardiner, 1985; Higham, 2001)

$$x(t) = x(t_0) + \int_{t_0}^{t} dt' a[x(t'), t'] + \int_{t_0}^{t} dW(t') b[x(t'), t'] \tag{3.2}$$

Here, a and b are scalar functions and the initial condition $x(t_0)$ is a random variable. While the first integral has a deterministic solution, the second integral on the right-hand side of (3.2) is the so called *stochastic integral* (see Higham, 2001) to be taken with respect to Brownian motion. There are mainly two different approach to solve this integral, the Ito and the Stratonovich rules (Zhang, 1999). The Ito Stochastic integral evaluate $b[x(t'), t']$ at the pre-point, i.e. one of the border of the interval dt, while in the Stratonovich integral $b[x(t'), t']$ is evaluate in the mid point of the interval dt. For infinite small increments the two methods converge, while this is no more true in discrete approximation (like e.g. Euler-Maruyana method, see Higham, 2001, Sect.4). In many natural physical systems, Stratonovich rules would be more appropriate because the midpoint is close to the actual time when random forces are applied. Unfortunately Stratonovich differential equations subject to the Stratonovich integration has properties which are hard to handle in mathematics (Zhang, 1999). For this reason they are often transformed into stochastic differential equation of the Ito type. The differential form of (3.2) can be written (see, e.g. chap. 4 of Gardiner, 1985; Zhang, 1999; Higham, 2001)

$$dx(t) = a[x(t), t]dt + b[x(t), t]dW(t). \tag{3.3}$$

This is the so-called *Ito Stochastic Differential Equation*, we refer to this in the text as the SDE general form. The solution of an SDE given the initial condition $x(t_0)$ is again a Markov process[1], hence an SDE describes the time evolution of a stochastic process.

3.1.2 Fokker Planck Equation

In our approach we used Eq. (3.3) to describe the evolution of pseudo-particles inside the Heliosphere. the fundamental of this approach, described afterward, has been taken by Kopp et al. (2012). One we can understand the path of the pseudo particles as a Markov process and define a transition density, $G(s, y; t, x)$, describing the probability density for a transition from the "old" point (s, y) to the "new" one (t, x), and vice-versa. The integration over a set of all possible new (old) states gives the actual probability measure. Due to the fact that we are dealing with a Markov process, all states of the particle prior to time $\tau = s$ (after time $\tau = t$) are unimportant regarding the probability, unless they define the fixed initial (final) state. Time-forward and time-backward

[1] a mathematical proof of that could be found in Section 4.3.2 of Gardiner (1985, and reference therein).

integrations of SDEs exactly do this: after having defined an initial and a final state, respectively, they compute the transition density for a particle to reach the current state (τ, z) (Kopp et al., 2012):
The time-forward integration, thus, fixes the "old" variables $(s, y) = (s_0, y_0)$, and the associated SDE solves the transport equation:

$$\frac{\partial G(s_0, y_0; t, x)}{\partial t} = -\frac{\partial}{\partial x}[a(t, x)G(s_0, y_0; t, x)] + \frac{1}{2}\frac{\partial^2}{\partial x^2}[b^2(t, x)G(s_0, y_0; t, x)] \tag{3.4}$$

in addition, an initial condition in the form $G(s_0, y_0; \tau_{min}, x) = G_{min}(x)$ can be formulated.
The time-backward integration, in contrast, fixes the "new" variables to $(t, x) = (t_0, x_0)$, so the transport equation is solved by the associated SDE in the variables s and y:

$$\frac{\partial G(s, y; t_0, x_0)}{\partial t} = a(s, y)\frac{\partial}{\partial y}[G(s, y; t_0, x_0)] + \frac{1}{2}b^2(s, y)\frac{\partial^2}{\partial y^2}[G(s, y; t_0, x_0)] \tag{3.5}$$

the initial condition of the time-forward integration now becomes a "final" condition of the form $G(\tau_{max}, y; t_0, x_0) = G_{max}(y)$.

Equations (3.4) and (3.5) are transport equations know in literature as *Kolmogorov equation Forward-in-time and Backward-in-time*, respectively, and they describes the same process but with different time evolution approach (see e.g. Chapter 1 of Klöden and Platen, 1999). The *Forward-in-time* equation is usually know also with the name of Fokker-Planck equation (Gardiner, 1985). In this work we use the *Forward-in-time* approach, since it allows one to reproduce rigorously processes occurring inside the heliosphere, a *Backward-in-time* approach compared with the forward ones is presented in Kopp et al. (2012).

The equivalence between SDE in the form of Eq. (3.3) and a Fokker-Planck equation in the form of Eq. (3.4), is here showed following the treatment discussed in Section 4.3–4.3.5 of Gardiner (1985). Let's write the SDE related to an arbitrary function of $f[x(t)]$, where $x(t)$ is a stochastic quantity, this could be obtained expanding $df[x(t)]$ at the second order in $dW(t)$

$$\begin{aligned} df[x(t)] &= f[x(t) + dx(t)] - f[x(t)] \\ &= f'[x(t)]dx(t) + \frac{1}{2}f''[x(t)]dx(t)^2 + ... \\ &= f'[x(t)]\{a[x(t), t]dt + b[x(t), t]dW(t)\} + \frac{1}{2}f''[x(t)]b[x(t), t]^2[dW(t)]^2 + ... \end{aligned} \tag{3.6}$$

where f' and f'' are respectively the first and the second derivative of the function f. Now using $[dW(t)]^2 = dt$ (see Section 4.3.3 of Gardiner, 1985) it is possible to obtain the *Ito's formula* for the change of variable:

$$df[x(t)] = a[x(t), t]f'[x(t)] + \frac{1}{2}b[x(t), t]^2 f''[x(t)]dt + b[x(t), t]f'[x(t)]dW(t). \tag{3.7}$$

We now consider the time evolution of the arbitrary function $f[x(t)]$. Using the *Ito's formula*,

Eq. (3.7), and consider the average value, we get:

$$\frac{\langle df[x(t)]\rangle}{dt} = \left\langle \frac{df[x(t)]}{dt} \right\rangle = \frac{d}{dt}\langle f[x(t)]\rangle$$
$$= \langle a[x(t),t]\frac{\partial}{\partial x}f + \frac{1}{2}b[x(t),t]^2\frac{\partial^2}{\partial x^2}f\rangle. \tag{3.8}$$

However, since $x(t)$ is a stochastic quantity, we can associate a conditional probability density $G(t_0, x_0; t, x)$ as defined before and rewrite Eq. (3.8) as:

$$\frac{d}{dt}\langle f[x(t)]\rangle = \int dx f(x)\frac{\partial}{\partial t}G(x_0, t_0; x, t) \tag{3.9a}$$
$$= \int dx \left[a(x(t),t)\frac{\partial}{\partial x}f + \frac{1}{2}b(x(t),t)^2\frac{\partial^2}{\partial x^2}f\right] G(x_0, t_0; x, t). \tag{3.9b}$$

Using Eq. (3.9a) with (3.9b), we integrate by part and discard surface terms to obtain

$$\int dx f(x)\frac{\partial}{\partial t}G = \int dx f(x)\left\{-\frac{\partial}{\partial x}[a(x,t)G] + \frac{1}{2}\frac{\partial^2}{\partial x^2}[b(x,t)^2 G]\right\} \tag{3.10}$$

and hence, since $f(x)$ is arbitrary:

$$\frac{\partial}{\partial t}G(x,t|x_0,t_0) = -\frac{\partial}{\partial x}\left[a(x,t)G(x,t|x_0,t_0)\right] + \frac{1}{2}\frac{\partial^2}{\partial x^2}[b(x,t)^2 G(x,t|x_0,t_0)] \tag{3.11}$$

We have thus a complete equivalence to a diffusion process defined by a drift coefficient $a(x,t)$ and a diffusion coefficient $b(x,t)^2$ (Gardiner, 1985).

3.1.3 Integration Methods

In sects. 3.1.1 and 3.1.2 we have treated the 1-Dimensional case, where the evolution in time of the process is only along one spatial coordinate. Eqs. (3.3) and (3.4) could be generalized to a N-dimension phase space allows one to express the Fokker-Planck equation involving the generic function F – which, in turn, is a function of phase space vector $\mathbf{q}$ – as (Zhang, 1999; Bobik et al., 2012a; Kopp et al., 2012):

$$\frac{\partial}{\partial t}F = -\sum_i \frac{\partial}{\partial q_i}[A_i(\mathbf{q},t)F] + \frac{1}{2}\sum_{i,j}\frac{\partial}{\partial q_i}\frac{\partial}{\partial q_j}\{[\tilde{\mathbf{D}}(\mathbf{q},t)]_{ij}F\} \tag{3.12}$$

with $\tilde{\mathbf{D}} = \tilde{\mathbf{L}}\tilde{\mathbf{L}}^{\mathrm{T}}$ and then obtain the equivalent set of differential equations (Zhang, 1999; Bobik et al., 2012a; Kopp et al., 2012)

$$d\mathbf{q} = \mathbf{A}(\mathbf{q},t)dt + \tilde{\mathbf{L}}(\mathbf{q},t)d\mathbf{W}(t) \tag{3.13}$$

where $\mathbf{A}(\mathbf{q},t)dt$ accounts for the so-called advective processes (e.g., Kruells and Achterberg, 1994), $\tilde{\mathbf{L}}(\mathbf{q},t)d\mathbf{W}(t)$ is the *stochastic term* containing $d\mathbf{W}(t)$ which is the increment of the so-called *Wiener process* (e.g., Section 4.3 of Gardiner, 1985).

For a more general description, the transport function (3.12) should also account with *sink* and *source* term; in this case Kopp et al. (2012) demonstrated that the equivalent SDEs does not change with respect (3.13), but the algorithm of numerical resolution will need some refinement. For the Parker equation, in the *forward-in-time* approach, this is not necessary: this because Parker equation does not account loss term once transformed in the form of Fokker-Planck[2] (see App. B), while the case of local sources (e.g. Jovian electron) is not treated in this work because of their low energy influence (up to few hundred MeV). As shown in appendix B of Pei et al. (2010b) the matrix $\tilde{\mathbf{L}}$ is not unique. Since for diffusive process the matrix $\tilde{\mathbf{D}}$ is definite positive (Gardiner, 1985; Kopp et al., 2012) there are several methods to evaluate the square root $\tilde{\mathbf{L}}$ of $\tilde{\mathbf{D}}$ (Pei et al., 2010b; Kopp et al., 2012). As discussed in Kopp et al. (2012) in the case of matrix $\tilde{\mathbf{D}}$ not *always* positive definite, it is usually nevertheless possible to compute the square root using alternative approaches. Present approach to calculate the matrix $\tilde{\mathbf{L}}$ is described in App. B.

Gardiner (1985, see Section 4.3.1 therein) demonstrated that, following a Euler–Cauchy procedure, the SDEs can be approximated in terms of the increments $\Delta\mathbf{q}$ occurring after a time Δt has elapsed. The corresponding increment of the Wiener process is given by $\omega\sqrt{\Delta t}$, where ω is a vector of random number following a Gaussian distribution with a mean of zero and a standard deviation of one (e.g. see Kruells and Achterberg, 1994; Pei et al., 2010b). As a consequence, the SDEs can be approximated by equation (8) of Pei et al. (2010b):

$$\Delta\mathbf{q} = \mathbf{A}(\mathbf{q}, t)\Delta t + \tilde{\mathbf{L}}(\mathbf{q}, t)\omega\sqrt{\Delta t} \tag{3.14}$$

The general procedure to solve a transport equation of the form (3.12) with the SDE method, could be summarize in the following (see e.g. Kopp et al., 2012): we solve Eqs. (3.14) for a large number of pseudo-particles and apply a binning procedure to the resulting set of pseudo-particle trajectories, leading to values for $G(t_0, \mathbf{q}_0; t, \mathbf{q})$ for a particular region on a phase-space grid.
Pei et al. (2010b) underline that a pseudo-particle is not a real particle nor a test particle, but a point in phase space; a real particle or a test particle moves around in the planetary field obeying Lorentz equation and following field lines (Pei et al., 2006). A pseudo-particle, instead, has a tendency to follow field lines according to Eqs. (3.13) provided that parallel diffusion dominates, but it does not in general follow them rigorously owing to the random Wiener process present in the equation (Pei et al., 2010b). If no limit on the time evolution of the pseudo particle is applied, one get the steady-state solution for all pseudo-particle because this is equivalent to set $t \to \infty$ (Pei et al., 2010b). A time dependent solution could be get specifying at which particular time do you want to evaluate the solution.

The transition probability density $G(t_0, \mathbf{q}_0; t, \mathbf{q})$, as defined in Sect. 3.1.2 and computed from Eqs. (3.14), is then calculated on the trajectories collected and should be normalized as:

$$\int_{\Omega_d} G(t_0, \mathbf{q}_0; t, \mathbf{q}) d\mathbf{q} = 1 \tag{3.15}$$

where Ω_d denotes the whole domain in phase-space. G can also be interpreted as Green Func-

[2] note that energy loss term in the Parker equation began a convective term in Fokker Planck like formulation.

tion (see, e.g. discussion in Webb and Gleeson, 1977; Li et al., 2009). The steady state solution for the modulated distribution function F in a particular position $(\mathbf{r}_e, \mathbf{p}_e)$ of the spatial($\mathbf{r}$)-momentum(p) is determined by (Pei et al., 2010b):

$$F(\mathbf{r}_e, \mathbf{p}_e) = \oint_{\mathbf{r}\in S} \int F_b(\mathbf{r}, \mathbf{p}) G(\mathbf{r}, \mathbf{p}; \mathbf{r}_e, \mathbf{p}_e) d\mathbf{p} d\mathbf{r} \tag{3.16}$$

where S denotes the boundaries which generally are closed surfaces of a multiply connected domain and F_b denotes boundary conditions (i.e. the un-modulated solution). Eq. (3.16) is a general form for steady state solutions and for general boundaries. If the outer boundary condition is independent of position (e.g. isotropic flux outside the heliosphere), the integral over the outer boundary of $G(\mathbf{r}, \mathbf{p}; \mathbf{r}_e, \mathbf{p}_e)$ gives $G'(\mathbf{p}; \mathbf{r}_e, \mathbf{p}_e)$ due to the normalization, i.e., $G'(\mathbf{p}; \mathbf{r}_e, \mathbf{p}_e) = \oint_{\mathbf{r}\in S} G(\mathbf{r}, \mathbf{p}; \mathbf{r}_e, \mathbf{p}_e) d\mathbf{r}$. For simplicity, here after we drop the prime. Thus if at the same time, the inner boundary is a reflecting boundary or an absorbing boundary, Eq. (3.16) reduces to (Pei et al., 2010b):

$$F(\mathbf{r}_e, \mathbf{p}_e) = \int F_b(\mathbf{p}) G(\mathbf{p}; \mathbf{r}_e, \mathbf{p}_e) d\mathbf{p}, \tag{3.17}$$

which is a 3-D generalization of equation (6) in Yamada et al. (1998), and equation (8) in Li et al. (2009) which both are for 1-D and for special inner boundaries only. Pei et al. (2010b) remark that as long as the boundary condition is independent of position, we don't need to know the details of the initial[3] positions of pseudo-particles on that boundary for any shape of the boundary. For example, even if the heliosphere has an irregular shape, such as a bullet shape, it is sufficient to know the pseudo-particle momentum when it start from the boundary (or when it encounters the boundary if traced backward from the Earth). Thus, in such case, the integral in equation Eq. (3.17) can be computed directly, with no need to form the complicated function $G(\mathbf{r}, \mathbf{p}; \mathbf{r}_e, \mathbf{p}_e)$ as an intermediate step.

3.2 Monte Carlo Model Description

In our Monte Carlo approach we rewrite the Parker equation, here rewritten for convenience,

$$\frac{\partial \mathrm{U}}{\partial t} = \frac{\partial}{\partial x_i}\left(K_{ij}^S \frac{\partial \mathrm{U}}{\partial x_j}\right) + \frac{1}{3}\frac{\partial V_{\mathrm{sw},i}}{\partial x_i}\frac{\partial}{\partial T}\left(\alpha_{\mathrm{rel}} T \mathrm{U}\right) - \frac{\partial}{\partial x_i}[(V_{\mathrm{sw},i} + v_{d,i})\mathrm{U}], \tag{3.18}$$

into a set of fully equivalent SDEs. The convective ($\mathbf{A}$) and diffusive ($\tilde{\mathbf{D}}$) terms of equivalent Fokker-Planck equation in the form of Eq. (3.12), for a 3D transport equation in heliocentric spherical coordinates $[r, \mu = \cos(\theta), \phi]$, in a generic magnetic field (and consequentially a generic diffusion tensor) and pure radially solar wind speed (the apex S of the symmetric part of the

[3] final position for backward-in-time approach

diffusion tensor is removed to simplify the reading):

$$\mathbf{A} = \begin{bmatrix} \frac{1}{r^2}\frac{\partial}{\partial r}(r^2 K_{rr}) - \frac{\partial}{\partial \mu}\left(\frac{K_{r\mu}\sqrt{1-\mu^2}}{r}\right) + \frac{1}{r^2}\frac{\partial}{\partial \phi}\left(\frac{rK_{r\mu}}{\sqrt{1-\mu^2}}\right) + V_{\rm sw} + v_{d,r} \\ -\frac{1}{r^2}\frac{\partial}{\partial r}\left(rK_{\mu r}\sqrt{1-\mu^2}\right) + \frac{\partial}{\partial \mu}\left(K_{\mu\mu}\frac{1-\mu^2}{r^2}\right) - \frac{1}{r^2}\frac{\partial}{\partial \phi}\left(K_{\mu\phi}\right) - \frac{1}{r}v_{d,\mu}\sqrt{1-\mu^2} \\ \frac{1}{r^2}\frac{\partial}{\partial r}\left(\frac{rK_{\phi r}}{\sqrt{1-\mu^2}}\right) + \frac{\partial}{\partial \mu}\left(-K_{\phi\mu}\right) + \frac{1}{r^2}\frac{\partial}{\partial \phi}\left(\frac{K_{\phi\phi}}{1-\mu^2}\right) + \frac{1}{r}\frac{v_{d,\phi}}{\sqrt{1-\mu^2}} \\ -\frac{\alpha_{\rm rel}T}{3r^2}\frac{\partial V_{\rm sw} r^2}{\partial r} \end{bmatrix} \tag{3.19}$$

$$\tilde{\mathbf{D}} = \begin{bmatrix} 2K_{rr} & -\frac{2K_{r\mu}\sqrt{1-\mu^2}}{r} & \frac{2K_{r\phi}}{r\sqrt{1-\mu^2}} \\ -\frac{2K_{\mu r}\sqrt{1-\mu^2}}{r} & \frac{2K_{\mu\mu}(1-\mu^2)}{r^2} & \frac{-2K_{\mu\phi}}{r^2} \\ \frac{2K_{\phi r}}{r\sqrt{1-\mu^2}} & \frac{-2K_{\phi\mu}}{r^2} & \frac{2K_{\phi\phi}}{r^2(1-\mu^2)} \end{bmatrix}. \tag{3.20}$$

The symmetric part of diffusion tensors K_{ij} is evaluated into heliocentric spherical coordinates (r,μ,ϕ) (see e.g. Equation (17) of Burger et al., 2008; Kobylinski, 2001; Alania, 2002)):

$$K_{rr} = K_{\perp,2}\,\sin^2\zeta + \cos^2\zeta\,(K_{||}\,\cos^2\Psi + K_{\perp,3}\,\sin^2\Psi), \tag{3.21}$$

$$K_{\theta\theta} = K_{\perp,2}\,\cos^2\zeta + \sin^2\zeta\,(K_{||}\,\cos^2\Psi + K_{\perp,3}\,\sin^2\Psi), \tag{3.22}$$

$$K_{r\theta} = +\sin\zeta\cos\zeta\,(K_{||}\cos^2\Psi + K_{\perp,3}\,\sin^2\Psi - K_{\perp,2}), \tag{3.23}$$

$$K_{\theta r} = +\sin\zeta\cos\zeta\,(K_{||}\cos^2\Psi + K_{\perp,3}\,\sin^2\Psi - K_{\perp,2}). \tag{3.24}$$

Where $\tan\Psi = -B_\phi/(B_r^2 + B_\theta^2)^{1/2}$ and $\tan\zeta = B_\theta/B_r$. In appendix A, the interested reader, could found the mathematical demonstration of eqs. (3.21)–(3.24). Since we are interested on long term modulation effects, i.e. greater than the time of a solar rotation, in this work we downgrade the problem to the 2D, solar radial distance (r) and cosine of solar co-latitude ($\mu = \cos(\theta)$), approximation that is equivalent to integrate the solar modulation effects for a complete solar rotation (i.e. $\sim$25 days in sidereal frame). The choice of $\mu = \cos\theta$ allows to easily compute a 2D spatial grid that in 3D leads to latitudinal regions of the same surface. We note as all index θ could be substitute with the index μ with the variable change, without loosing the physical meaning behind that. Then it is possible to compute the square root of matrix $\tilde{\mathbf{D}}$ to get the diffusion element $\tilde{\mathbf{L}}$ of Eq. (3.14) using the Cholesky decomposition (Pei et al., 2010b; Kopp et al., 2012, e.g., see). The equivalent set of SDEs for the 2D approximation of Parker equation is:

$$\begin{aligned} \Delta r &= \frac{1}{r^2}\frac{\partial}{\partial r}(r^2 K_{rr})\Delta t - \frac{\partial}{\partial \mu(\theta)}\left(\frac{K_{r\mu}\sqrt{1-\mu^2(\theta)}}{r}\right)\Delta t \\ &\quad + (V_{\rm sw} + v_{d,r})\Delta t + (2K_{rr})^{1/2}\omega_r\sqrt{\Delta t}, \end{aligned} \tag{3.25a}$$

$$\begin{aligned}\Delta\mu(\theta) &= -\frac{1}{r^2}\frac{\partial}{\partial r}\left[rK_{\mu r}\sqrt{1-\mu^2(\theta)}\right]\Delta t + \frac{\partial}{\partial\mu(\theta)}\left[K_{\mu\mu}\frac{1-\mu^2(\theta)}{r^2}\right]\Delta t \\ &\quad -\frac{1}{r}v_{d,\mu}\sqrt{1-\mu^2(\theta)}\Delta t - \frac{2K_{r\mu}}{r}\left[\frac{1-\mu^2(\theta)}{2K_{rr}}\right]^{1/2}\omega_r\sqrt{\Delta t} \\ &\quad +\frac{1}{r}\left\{[1-\mu^2(\theta)]\frac{K_{\mu\mu}K_{rr}-K_{r\mu}^2}{0.5K_{rr}}\right\}^{1/2}\omega_\mu\sqrt{\Delta t}, \qquad (3.25b)\end{aligned}$$

$$\Delta T = -\frac{\alpha_{\rm rel}T}{3r^2}\frac{\partial V_{\rm sw}r^2}{\partial r}\Delta t, \qquad (3.25c)$$

where $\mu(\theta)=\cos\theta$, K_{ij} is the symmetric part of diffusion tensor in Heliocentric spherical coordinates described by Eqs. (3.21)–(3.24), $v_{d,i}$ follow the definition of Eq. (2.17), $V_{\rm sw}$ is treated in Sect. 1.2.2 and ω_i is a random number following a Gaussian distribution with a mean of zero and a standard deviation of one. The whole procedure from Eq. (3.18) down to the equivalent SDE set in Eq. (3.25) is described in App. B.

As discussed in the previous Section, the vector $\mathbf{q}=[r,\mu(\theta),T]$ represents a so-called pseudo-particle which time evolution is simulated by mean of Eqs. (3.25) from the outer boundary down to the inner heliosphere. As treated by Achterberg and Krulls (1992), the number density U – and equivalently the differential intensity J defined in Eq. (2.35) – can be obtained from the density of pseudo-particles by averaging over many realizations of the SDEs.

The procedure used to integrate the SDEs *Forward-in-time* is the one described in Section 6 of (Bobik et al., 2012a): (a) events are isotropically generated on the outer border of the effective heliosphere; (b) each event is integrated over the time evolution of a pseudo-particle (see e.g. Fig. 3.1) and is processed forward in time until it reaches either the outer (or inner) border of the effective heliosphere located at 100 AU (r_b) or the pseudo-particle energy becomes lower than a minimum threshold (which depends on the set of experimental data taken into consideration), then a new particle is generated; (c) when a pseudo-particle reaches a particular region (for instance that corresponding to Earth position) its injection energy, statistical weight, etc., are recorded; (d) finally, the number density U results from the normalized distribution function obtained using the procedure described in Sect. 3.2.4.
In Fig. 3.1 we report four example pseudo-particle time evolution, as obtained by Eqs. 3.1.

In the present code Δt varies as r^2/K_{rr}, this allowed an increase of the accuracy in the inner heliosphere, but kept the appropriate precision up to regions close to the outer border of the effective heliosphere. Furthermore, this condition ensures that the diffusion process is dominant (see Section 4.1 of Kruells and Achterberg, 1994).
The present model depends on few parameters most of them obtained from *in-situ* measurements of heliosphere environment. Description of the model parameters in Sect. 3.2.1 and 3.2.2 follow the approach close to Bobik et al. (2012a), while the discussion of IMF parameters (Sect. 3.2.3) has been taken by Bobik et al. (2012d).

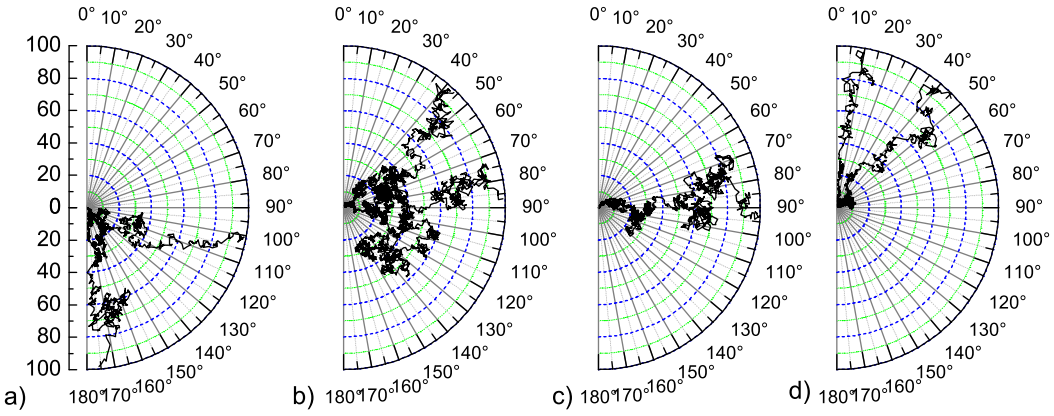

Figure 3.1: Common examples of spatial evolution of 1 GeV pseudo-particles. Pseudo-particles are generated at 100 AU and propagated following the time evolution described by Eqs. (3.25). Pseudo-Particle history is termed when it reach the spatial border of heliosphere (case a,b,d) or the energy go below a minimum threshold (case c).

3.2.1 Parameters

As discussed by Potgieter (2008, see also references therein), until recently the heliosphere was assumed to be spherical in most modulation models with an outer boundary at radial distances beyond ∼100 AU. Presently, the heliospheric structure is considered latitudinally asymmetric (particularly) during solar minimum conditions mostly because the SW depends on the latitude and solar activity (see Sect. 1.2.4). However, Langner and Potgieter (2005) and Potgieter (2008) suggested that, in general, a symmetric Solar Wind termination with a radial distance of ∼100 AU is still a reasonable assumption. In the present model, the effect of the modulation is obtained for GCR propagation through a symmetric effective heliosphere with a radius of 100 AU.

The time spend by the SW to cover the distance from the outer corona up to the boundary of the effective heliosphere ($R_{\rm tm}$) can be expressed in units of the time needed for a sidereal rotation on the equator of the Sun ($\tau_{\rm rot}$, i.e. $\simeq$ 25 days, see page 77 of Aschwanden, 2006 and also Brajsa et al., 2001):

$$N_{\rm rot} = \frac{R_{\rm tm}}{V_{\rm sw} \cdot \tau_{\rm rot}} \tag{3.26}$$

[4] For instance on the ecliptic the SW, to reach the outer boundary, spends the corresponding amount of time needed to complete from 12 up to 20 sidereal solar rotations, for a SW speed of 500 Km/s and 300 Km/s respectively. In the present code, the effective heliosphere (with a radius of 100 AU) was subdivided into 15 spherical regions (see Fig. 3.2) equivalent to an average SW speed of 400 Km/s. In each region, the parameters (e.g., SW speed, K_0 , $B_\oplus$, α_t , etc.) are determined at the time of the SW ejection from the Sun (see Bobik et al., 2012a). The parameters (which depend on the solar activity) are the diffusion parameter K_0, the tilt angle α_t of the HCS,

[4]The Sideral rotation of the Sun is respect a external fixed frame (e.g. fixed star in the sky). This shouldn't confused with the Sinodic rotation (e.g. Carrington rotation,$\simeq$ 27 days) that is a complete rotation of the Sun as seen from the Earth (Ruždjak et al., 2005).

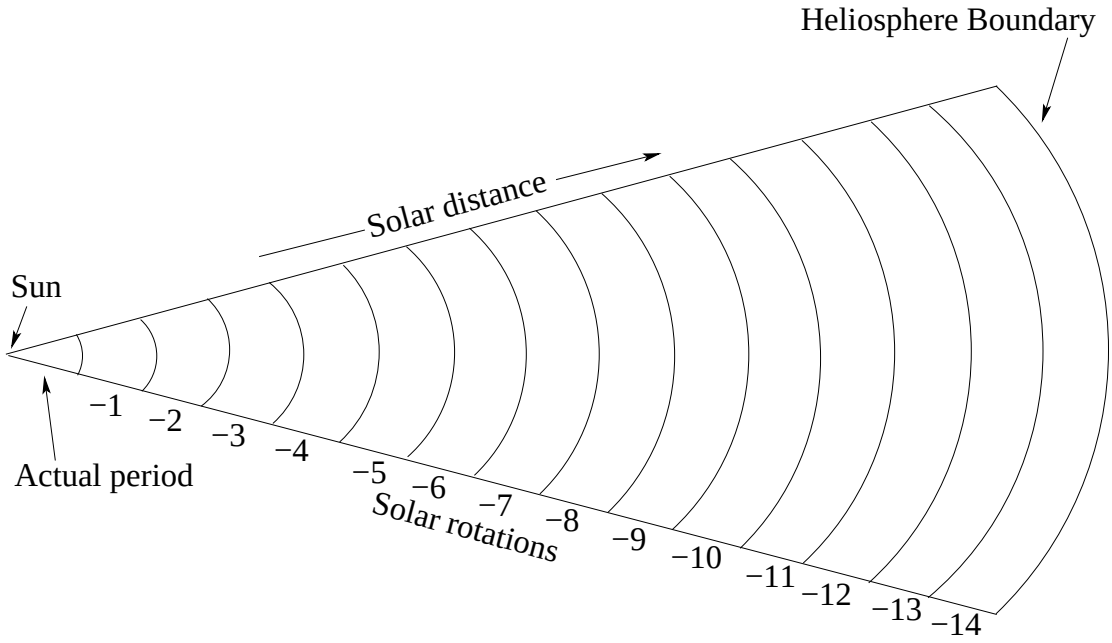

Figure 3.2: The effective heliosphere is divided in 15 regions, each one referred from 1 to 14 solar rotation before the simulated period.

the magnetic field polarity – related to the sign of the coefficient A in Eq. (1.14) –, the magnetic field magnitude ($B_{\oplus}$), and the solar wind velocity ($V_{\rm sw}$). The latter two parameters are measured at Earth's orbit using specialized spacecraft like Wind (Kasper, 2002) and ACE (McComas et al., 1998); this data are collected by NASA and available through the NASA-OMNIweb (2012) online database hourly, daily or 27-days averaged. The diffusion parameter K_0 is determined (following the procedure described in Sect. 3.2.2) using the values of the modulation strength, SSN values[5], and radius of the effective heliosphere. Actual choose of K_0 also imply that present model is valid only for particle with rigidity greater than 1 GV ($\sim$ 444 MeV for proton) (see discussion in Sect. 3.2.2 and Bobik et al., 2012a). Extension of the present model to lower energy was explored in Sect. 4.4 through including the heliosphere dimension as additional parameter into the parallel diffusion coefficient.

α_t and the field polarity are used to deal with the drift velocity (as discussed in Sect. 2.2.2), which modifies the overall convection velocity in Equation (3.25). α_t values are obtained from Wilcox Solar Observatory (Hoeksema, 1995; WSO, 2012) and are calculated using two different models called "R" and "L". Ferreira and Potgieter (2003, 2004) suggested that the "R" model accounts for GCR observations during periods of increasing solar activity (for instance, 1987.4–1990.0 and 1995.5–2000.0), while the "L" model accounts for periods of decreasing solar activity (for instance, 1990.0–1995.5 and 2000.0–2010.0). The implementation of the "R" and "L" models in the current code is further treated in Sect. 4.

To represent the observed SW speeds, Fichtner et al. (1996) suggested that the solar wind speed

[5] In this work we use the *International Sunspot Number* that is compiled by the Solar Influences Data Analysis Center in Belgium; (SIDC-team, 2012)

may be proportional to $(1 + cos^2\theta)$. In the present model we use (Bobik et al., 2012a)

$$V_{\rm sw}(\theta) = \begin{cases} V_{\rm sw,max} & \text{, for } \theta \leq 30^\circ \text{ and } \theta \geq 150^\circ, \\ V_{\rm sw,min} \times (1 + |cos\theta|) & \text{, for } 30^\circ < \theta < 150^\circ \end{cases} \tag{3.27}$$

with $V_{\rm sw,max} = 760$ km s^{-1} (e.g., see McComas et al., 2000) and $V_{\rm sw,min}$ is the corresponding value extracted from NASA/GSFC's OMNI data set (King and Papitashvili, 2005; NASA-OMNIweb, 2012). Eq. (3.27) exhibits a slightly better agreement with observed data than that proposed by Fichtner et al. (1996). Jokipii and Kóta (1995) and Pommois et al. (2001) proposed other functions for such periods. However, these functions depends on an additional parameter related to the latitudinal extension of the region with a slow solar wind. This parameter can be determined only using measurements to be performed largely outside the ecliptic plane, like those made by the Ulysses spacecraft. Thus, Eq. (3.27) has the advantage of allowing one to more generally treat periods of low solar activity. In the present model, for the solar wind we assume a speed independent of the colatitude in periods characterized by high solar activity. As previously, the value of the speed is extracted from NASA/GSFC's OMNI data set through OMNIWeb (King and Papitashvili, 2005). Other Parameters of the model are the ratio ρ_k of the diffusion coefficients, introduced in Sect. 2.2.1, the perturbation factor δ_m of the magnetic field, discussed in Sect. 1.2.1, and the magnitude of an enhancement of $K_{\perp,\mu}$ (see Sect. 2.2.1). The implementation of such parameters with respect experimental data is described in Sect. 4.

3.2.2 Diffusion Parameter in the Framework of the Force Field Model

In present model the diffusion parameter is initially estimated using the FFM. In the FFM (Gleeson and Axford, 1968a) the differential intensity (J) at a radial distance r is given by (see Sect. 2.3):

$$J(r, E_t, t) = J(R_{tm}, E_t + \Phi_p)\frac{E_t^2 - m_r^2c^4}{(E_t + \Phi_p)^2 - m_r^2c^4}; \tag{3.28}$$

where $J(R_{tm}, Et + \Phi_p)$ is the undisturbed intensity beyond the solar wind termination located at a radial distance R_{tm} from the Sun, E_t is the total energy of the particle with rest mass m_r , and, finally, Φ_p is the so-called force-field energy loss (Gleeson and Axford, 1968a; Gleeson and Urch, 1971, 1973). When modulation is small, i.e. $\phi_p \ll m_rc^2$ and $\phi_p \ll T$, Gleeson and Axford (1968a) determines that

$$\Phi_p = \frac{ZeP}{K_P}\phi_s \approx Ze\phi_s \tag{3.29}$$

where Ze is the particle charge, K_P defined in Eq. (2.15) and ϕ_s is defined in Eq. (2.33). Assuming that $V_{\rm sw}$ and k_1 are almost constant, Eq. 2.33 reduces to (e.g., see Equation (4.64) of Leroy and Rancoita (2011)):

$$\phi_s(r, t) \approx \frac{V_{\rm sw}(R_{tm} - r)}{3k_1(t)} \tag{3.30}$$

from which the diffusion parameter can be re-expressed as:

$$k_1(t) \approx \frac{V_{\rm sw}(R_{tm} - r)}{3\phi_s(r,t)} \tag{3.31}$$

$k_1(t)$ is then linearly depend on $(R_{tm}-r)$ and independent of the species of GCR particles as $\phi_s(r,t)$ (see e.g. equation 4.68 of Leroy and Rancoita, 2011, and reference therein). The values of the modulation strengths at Earth, $r_{\rm Earth} = 1$AU, was determined e.g. by Usoskin et al. (2005, 2011) monthly for the time period from 1936 up to 2009 using CR measurements obtained from neutron monitors. The values of SW speed $V_{\rm sw}$ are available through the NASA-OMNIweb (2012). Bobik et al. (2012a) notice that although k_1 depends on the value of the solar wind termination (R_{tm}) one can re-express Eq. (3.31) in terms of the diffusion coefficient (K_0) in a *effective heliosphere* with a solar wind termination fixed at 100 AU as

$$K_0 \approx k_1 \frac{99\text{AU}}{R_{\rm tm} - r_{\rm Earth}} = 99\text{AU}\frac{V_{\rm sw}}{3\phi_s(r_{\rm Earth})} \tag{3.32}$$

where 99 AU is the distance of the Earth from the border of the effective heliosphere used in the current simulation code.

In this work we related K_0 with the corresponding value of SSN (SIDC-team, 2012). The K_0 data are subdivided into four sets, i.e., ascending and descending phases for both negative and positive solar magnetic-field polarities (see table 3.1). The criteria to divide the different periods

	Period	Years
I)	$A < 0$ Ascending	1964.79–1968.87, 1986.70–1989.54, 2008.95–2009.95
II)	$A < 0$ Descending	1964.53–1964.79, 1979.95–1986.70, 2000.28–2008.95
III)	$A > 0$ Ascending	1976.20–1979.95, 1996.37–2000.28
IV)	$A > 0$ Descending	1968.87–1976.20, 1989.54–1996.37

Table 3.1: Definition of Ascending and Descending periods

is to look for the local minimum and maximum value of SSN within a period of ∼11 year. When a minimum (or maximum) occurs a new period is defined. Period where SSN increase (decrease) are defined Ascending (Descending). After each maximum the sign of the magnetic field, i.e. the parameter A in Eq. (1.14), is reversed (see figs. 1.10 and 3.3).

For each set, the data could be fitted with a practical relationship (see Fig. 3.4) between K_0 and SSN values for 1.4 ≤SSN≤ 165. i.e., finding (Bobik et al., 2012d)

$$\text{I)} \quad K_0 = 0.000297 - 2.9\cdot10^{-6}\text{SSN} + 8.1\cdot10^{-9}\text{SSN}^2 + 1.46\cdot10^{-10}\text{SSN}^3 - 8.4\cdot10^{-13}\text{SSN}^4 \tag{3.33}$$

$$\text{II)} \quad K_0 = \begin{cases} 0.000304846 - 5.8\cdot10^{-6}\text{SSN} & \text{if SSN} <= 20 \\ \frac{0.00195}{\text{SSN}} - 2.3\cdot10^{-10}\text{SSN}^2 + 9.1\cdot10^{-5} & \text{if SSN} > 20 \end{cases} \tag{3.34}$$

$$\text{III)} \quad K_0 = 0.0002391 - 8.453\cdot10^{-7}\text{SSN} \tag{3.35}$$

$$\text{IV)} \quad K_0 = 0.000247 - 1.175\cdot10^{-6}\text{SSN} \tag{3.36}$$

In addition, the data were found to exhibit a Gaussian distribution of percentage differences ($R_{\rm perc}$)

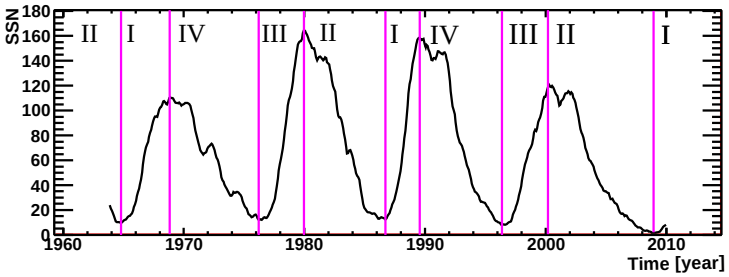

Figure 3.3: Smoothed Sunspot numbers in function of times, for the period considered during the evaluation of Diffusion parameter. The vertical lines indicates the time at the values on SSN is a local maximum or minimum.

of K_0 values from the corresponding fitted values K_F , with (see equation (14) of Bobik et al., 2012a)

$$R_{\rm perc} = \frac{K_F - K_0}{K_F}. \tag{3.37}$$

The RMS values of the Gaussian distributions were found to be 6%, 10.1%, 7% and ∼13.2% for the period Ascending with $A < 0$ (I), Descending with $A < 0$ (II), ascending with $A > 0$ (III) and descending with $A > 0$ (IV), respectively.

Present analysis is an improvement of such presented in Bobik et al. (2012a), and allow to have a better estimation of periods with very low SSN, like the last solar minimum. From the practical relationship found in this Section, we can use the estimated SSN values to obtain the diffusion parameter K_0 at times beyond 2009. Bobik et al. (2012a) remarked that this procedure allows one to extend the ~ 44 year period by exploiting the practical relationship between the fitted K_0 values and the SSN values (one of the main parameters related to the solar activity). In addition, as in Bobik et al. (2012a) we introduced in our code a Gaussian random variation of K_0 with RMS corresponding to those found for each subset of data. Results of the simulation with and without the Gaussian variation are consistent within the uncertainties of the code.

Bobik et al. (2012a) note that, to determine $\phi_s(r_{\rm Earth})$, Usoskin et al. (2005, 2011) used an expression of the LIS for protons compatible with those from Burger et al. (2000). In practice, their spectrum differs from that due to Burger et al. (2000) by about or more than 5% at kinetic energies lower than about 117 MeV. Usoskin et al. (2005, see Appendix A in that article) also found that using other commonly adopted LISs their corresponding values of the modulation strengths follow a linear relation with respect to $\phi_s(r_{\rm Earth})$ (see also Herbst et al., 2010). In Section 4.1 we show that the error-weighted average of the differential spectral index of the high energy proton differential intensity is compatible, within one standard deviation, with the LIS introduced by Burger et al. (2000), while the differential spectral indexes of spectra tested by Usoskin et al. (2005) are not compatible within three or more standard deviations with that found in Sect 4.1.

Moreover, Bobik et al. (2012a) also noted that the response of neutron monitors has to be evaluated by combining (a) the effects of both the geomagnetic cutoff rigidity (Usoskin et al., 2005) which results in a reduced sensitivity of detection apparatus and (b) the so-called atmospheric yield function (Clem and Dorman, 2000). Thus, they finds that (i) the contribution of the GCRs with

rigidities below 2 GV amounts to about or less than 1.1% of the total neutron monitor counts due to particles with energies up to about 50 GV and (ii) the maximum neutron monitor sensitivity – the maximum of the response function (see Figure 7 of Clem and Dorman, 2000) – occurs in the rigidity interval (3–15) GV. This lead to the conclusion that this diffusion parameter is valid only for the rigidity above ≈ 1 GV. Scherer et al. (2011) shown how at such rigidities the contribution of the outer heliosphere (i.e. the Heliopause) is practically negligible, while is more and more important at lower rigidities. In (Bobik et al., 2012c) are shown how is possible to extend the range of validity of present model considering an effective heliosphere with a different dimension just for particle a lower rigidities, this preliminary study will be reported in Sect. 4.4.

3.2.3 IMF Parameter

For the purpose of this work we use a *hybrid IMF description* presented in Sect. 1.2.1. In this description we divide the heliosphere into *polar* regions and a *equatorial* region where different description of IMF are applied. In the *equatorial* region the Parker's IMF, Eq. (1.5), is used, while in the *polar* regions we used an IMF that allow for the magnitude as in Eq. (1.6):

$$\begin{cases} \mathbf{B}_{Pol} = \dfrac{A}{r^2}\left(\mathbf{e}_r + \dfrac{r}{r_b}\delta(\theta)\mathbf{e}_\theta - \dfrac{\omega(r-r_b)\sin\theta}{V_{sw}}\mathbf{e}_\varphi\right)\left[1-2H\left(\theta-\theta'\right)\right] & \textit{Polar regions} \\ \mathbf{B}_{Par} = \dfrac{A}{r^2}\left(\mathbf{e}_r - \dfrac{\omega(r-r_b)\sin\theta}{V_{sw}}\mathbf{e}_\varphi\right)\left[1-2H\left(\theta-\theta'\right)\right] & \textit{Equatorial region} \end{cases} \tag{3.38}$$

where the *equatorial* region is that with colatitude $X^\circ \leq \theta \leq (180^\circ - X^\circ)$. The complementary parts are the *polar* regions indicated with the symbol θ_{X°. The difference between the magnitude of B_{Par} and B_{Pol} is less then $\sim$1.2% at solar distance greater than 10-20 AU for colatitudes $20^\circ < \theta < 160^\circ$ (see Fig. 3.5a) and increase for colatitudes approaching the polar regions (see e.g. Fig. 1.5).

In Sect. 1.2.1 we already pointed out that in order to have a divergence free magnetic field we require that the perturbation factor $\delta(\theta)$ is parametrized by the Eq. (1.15). The intensity of such perturbation depends by δ_m i.e. the minimum perturbation factor of the field. The perturbation parameter is let growing with decreasing of the co-latitude. However but in their original work, Jokipii and Kota (1989), estimated the value of δ parameter between 10^{-3} and $3 \cdot 10^{-3}$.

Since the polar field have to be a perturbation of the Parker field, it is a reasonable assumption that the stream line of the magnetic field (described by Eq. (1.16)) do not cross the equatorial plane, remaining completely contained in the solar hemisphere of injection (see Fig 3.6). This allows one to estimate an upper limit on the possible values of δ_m in function of colatitude as shown in Fig. 3.5b. In Sect. 4.2.1 we exploit the effect on modulation changing δ_m values from 0, i.e. a Parker IMF with out correction, up to 3×10^{-5}. Furthermore in Sect. 4.2.2 we study how the extension in latitude of *Polar* regions influence the latitudinal gradients of GCR intensity.

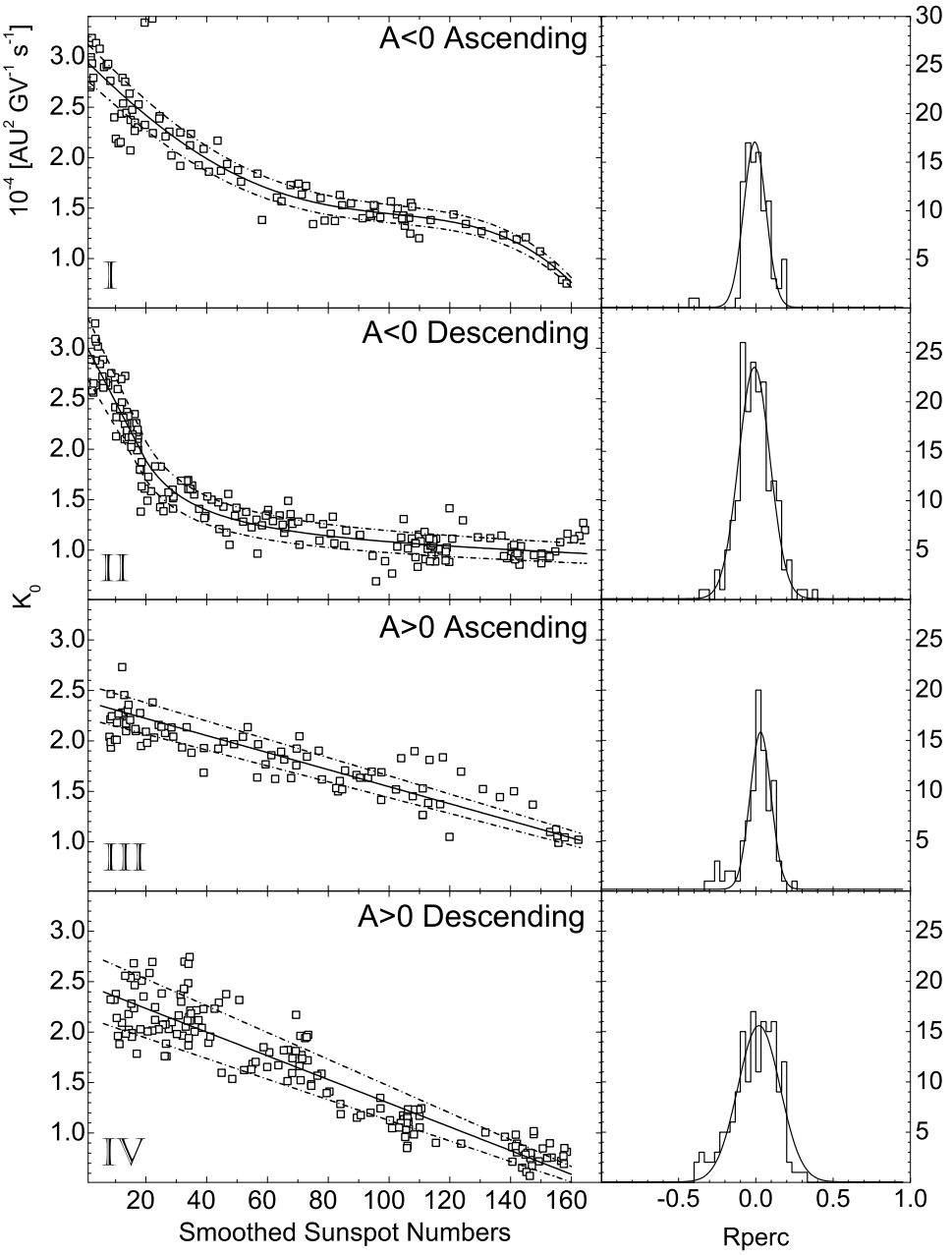

Figure 3.4: Diffusion parameter K_0 (left side) and percentage differences $R_{\rm perc}$ (Eq. (3.37); right side) as a function of the SSN value; the central continuous lines are obtained from a fit of K_0 with respect to SSN values in the range $1 \lesssim \text{SSN} \lesssim 165$; the dashed and dotted lines are obtained adding (top) or subtracting (bottom) one standard deviation from the fitted values.

3.2.4 Evaluation of Differential Intensity

As discussed in Sect. 3.1.3 the modulated differential intensity is obtained by solving the integral of Eq. (3.17), that could be easily transposed in function of energy:

$$F(\mathbf{r}_e, T_e) = \int F_b(T) G(T; \mathbf{r}_e, T_e) dT. \tag{3.39}$$

Here $G(T; \mathbf{r}_e, T_e)$ is a *transmission function* that describe the probability of a particle with initial Energy T to reach the $\mathbf{r}_e$ position with energy T_e. $F(\mathbf{r}, T)$ is a generic function that is related

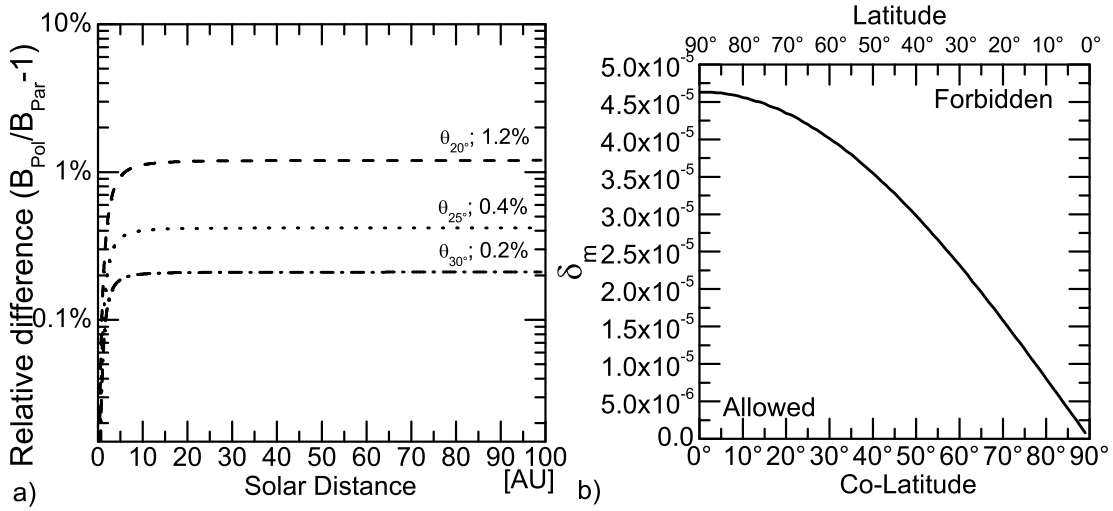

Figure 3.5: a) maximum percentage difference between B_{Pol} and B_{Par} in function of solar distance for Polar regions θ_{20° , θ_{25° and θ_{30°. b) Maximum value allowed of δ_m in function of co-latitude, since Eq. (3.38) is symmetric with respect the solar equatorial plane, values greater of 90° of Co-latitude lead to same results of those presented.(figure from Bobik et al., 2012d)

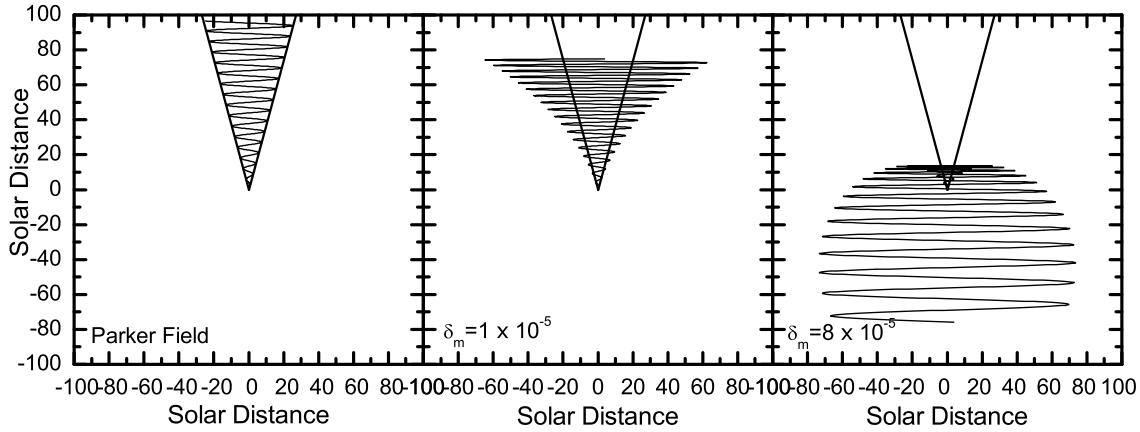

Figure 3.6: Stream line calculated with Eq. (1.16) for $\delta_m = 0$ (Parker Field), $\delta_m = 1 \times 10^{-5}$ and $\delta_m = 8 \times 10^{-5}$; The solid line represented the initial emission inclination plane at $\theta_0 = 20^\circ$.

with the number density U of the Parker Equation (see appendix B); moreover U is related to the differential intensity by means of Eq. (2.35), so that:

$$J(T) \propto U(T)\beta(T) \tag{3.40}$$

so the modulated differential intensity at given position could be obtained:

$$J(\mathbf{r}_e, T_e) = \beta^{-1}(T_e) \int_{T_{min}}^{T_{max}} J_{LIS}\beta(T)(T)G(T; \mathbf{r}_e, T_e)dT. \tag{3.41}$$

where $J_{LIS}(T)$ is the local interstellar spectrum evaluated at the Termination Shock, and discussed in Sect. 4.1. For the numerical evaluation a spatial/energy grid is created. The transmission function $G(T^c; \mathbf{r}_e^c, T_e^c)$ then is proportional to the ratio between the number of pseudo-particles with initial Energy in the bin T^c that reach the $\mathbf{r}_e^c$ grid position with energy inside the bin T_e^c, i.e. $N(T^c; \mathbf{r}_e^c, T_e^c)$, and the total number of pseudo-particles with initial Energy T^c, $N_{tot}(T^c)$:

$$G(T^c; \mathbf{r}_e^c, T_e^c) \sim \frac{N(T^c; \mathbf{r}_e^c, T_e^c)}{N_{tot}(T^c)}. \tag{3.42}$$

If pseudo-particles are not generated with a flat distribution (in energy), but with a particular probability distribution $p_g(T)$, the number of pseudo-particles (N and N_{tot}) have to be corrected by a *generation weight* that is proportional to $p_g^{-1}(T)$. Different choose of $p_g(T)$ are motivated to increase the statistic significance in particular energy range; for example a flat in log-scale generation, as the one used in this work (see App. B.3), allow one to increase the statistical precision in the low energy part of the spectra (< 10 GeV), where the modulation act, with a good statistical precision in the high energy part of the spectra, that is used to normalize the results with respect to experimental data. Using Eq. (3.42) into (3.41) is it possible to obtain,

$$J(T_e^c) = C_n \cdot \beta^{-1}(T_e^c) \cdot \sum_{T_{min}^c}^{T_{max}^c} J_{LIS}(T^c)\beta(T^c)\frac{N(T^c; \mathbf{r}_e^c, T_e^c)}{N_{tot}(T^c)} \tag{3.43}$$

where C_n is a normalization factor that allow the integral of high energy part of the modulated to be equal to the integral of the same energy range of LIS. The summation is on the initial energy bin, while T_{max}^c and T_{min}^c are considered the maximum and the minimum Energy bin.

As concluded in Sect. 3.1.3, it is possible to compute directly the modulated spectra without the intermediate step of evaluating the G function. If we define $\sum_{(T^c;T_e^c)}$ as the summation of the pseudo-particles that get the $\mathbf{r}_e^c$ grid point with energy T_e in the bin T_e^c, that were injected with initial energy T in the bin T^c, and with $\sum_{(tot,T^c)}$ the summation of all the pseudo-particles generated with initial energy T in the bin T^c, it is possible to compute:

$$J^{LIS}(T^c)\beta(T^c)\beta^{-1}(T_e^c)G(T^c; \mathbf{r}_e^c, T_e^c) \sim \frac{\sum_{(T^c;T_e^c)} J(T)\beta(T)\beta^{-1}(T_e)p_g^{-1}(T)}{\sum_{(tot,T^c)} p_g^{-1}(T)} \tag{3.44}$$

and thus the modulated spectra in the grid position $\mathbf{r}_e^c$ is:

$$J(T_e^c) = C_n \cdot \sum_{T_{min}^c}^{T_{max}^c} \frac{\sum_{(T^c;T_e^c)} J_{LIS}(T)\beta(T)\beta^{-1}(T_e)p_g^{-1}(T)}{\sum_{(tot,T^c)} p_g^{-1}(T)}, \tag{3.45}$$

with

$$C_n = \frac{\sum_{(tot,>30\text{GeV})} p_g^{-1}(T)}{\sum_{(T^c;>30\text{GeV})} p_g^{-1}(T)}. \tag{3.46}$$

The normalization factor that accounts for un-modulated part of the spectra. The two summations in Eq. (3.44) are easily computable by computer program; moreover this allow also to parallelize the computation since each pseudo-particle history is (and have to be) different from the others, and the only relevant informations are the one represented by the summations in Eq. (3.44).

3.2.5 Sentitivity of the Method

The error associated to our Monte Carlo solution could be seen as a composition of both Statistical and Systematic error. The statistical error decreases as the number of pseudo-particles (N, see e.g. Klöden and Platen, 1999; Strauss et al., 2011) and could be treated using the Central Limit Theorem (see e.g. Weisstein, 2012, and reference therein) so that $\propto 1/\sqrt{N}$ of each energy bin. The Systematic error is related to the Monte Carlo methods itself. This method utilizes the approximation $dt \approx \Delta t$ (see Sect. 3.1.3) where dt is the infinitesimal time change, and Δt, defined in Sect. 3.2, is the time step used in the model. As pointed out in Strauss et al. (2011), this approximation gives $dx_i \approx \Delta x_i$, when evaluated the stochastic evolution in Eq. (3.25) for each phase space component x_i. The resolution of phase-space is thus determined by the size of the time increment Δt, with smaller values leading to enhanced integration accuracy, but longer integration times. So, using the *Convergence Theorems of SDE integration* (see e.g. Section 4.3 of Gardiner, 1985; Higham, 2001) one can relate that the systematic error depends on the time step $\propto \sqrt{\Delta t}$ like e.g. in Strauss et al. (2012b). This approach could not be used directly in our model since Δt is chosen to be space dependent increasing the accuracy in the inner part of heliosphere but optimizing the computational integration time in the outer part of heliosphere. Moreover other effects such as computation precision could not be accounted in such parametrization. For this reason the sensitivity of our Monte Carlo approach was estimated computing the differences of the "best results" (f_{Best}, i.e. those in Sect. 4.2.1 that minimize the difference with experimental data) with the other simulated intensities for energies above 30 GeV, i.e., for an energy region in which the spectrum is unaffected by modulation and, thus, no difference is expected. For this purpose, we defined the quantities:

$$\hat{\eta}_{\text{rms,h}} = \sqrt{\frac{\sum_i (\hat{\eta}_{i,\text{h}}/\sigma_{\hat{\eta},i,\text{h}})^2}{\sum_i 1/\sigma^2_{\hat{\eta},i,\text{h}}}} \tag{3.47}$$

with

$$\hat{\eta}_{i,\text{h}} = \frac{f_{\text{h}}(T_i) - f_{\text{Best}}(T_i)}{f_{\text{Best}}(T_i)} \tag{3.48}$$

where $f_{\rm h}(T_i)$ is the differential intensity of the ith energy bin (above 30 GeV), $\sigma_{\hat{\eta},i,{\rm h}}$ is the statistical uncertainties for the ith energy bin, and, finally "h" indicates one of the simulation considered in Sect. 4.2.1. The computed average $\hat{\eta}_{\rm rms,h}(\%)$ for each Simulated data-set, reported in table 3.2, are then averaged to get the estimation of our Monte Carlo sensitivity of about $\sim 2\%$. This value is comparable with previous estimation of 2.3%, presented in Bobik et al. (2012a) and obtained with the same procedure but varying the dimension of the heliosphere from 80 up to 120 AU.

1997	1998	1999	2000	2002	2006/08	Average
3.3	2.0	2.3	1.3	1.8	1.1	2.0

Table 3.2: Average $\hat{\eta}_{\rm rms,h}(\%)$ calculated for each data-set considered in this work (see Sect. 4.2.1), and the "Average" global value that gives global estimation of Monte Carlo Sensitivity.

3.2.6 Simple Applications

The, Monte Carlo Technique allows to get additional information beside the modulated spectra. In this Section we present few example applications of SDE technique studies that we explored during the development of the code. In Bobik et al. (2012b) we study the propagation time, from the boundary down to the Earth, of GCR Protons as a function of energy and solar activity. We simulated mono-energetic pseudo-particles during a low activity period (i.e. 1998) and an high activity period (i.e. 2002). The Time could be obtained with the summation of all Δt step from the generation up to reach the Earth position ($\sim$ 1AU). In Fig 3.7 results for the low (on the left) and high (on the right) activity period. Is possible to see how propagation time is generally higher during higher activity periods at all energy. More over the population of particle generated with low energy that reach the Earth orbit is overall greater during low activity period. This results

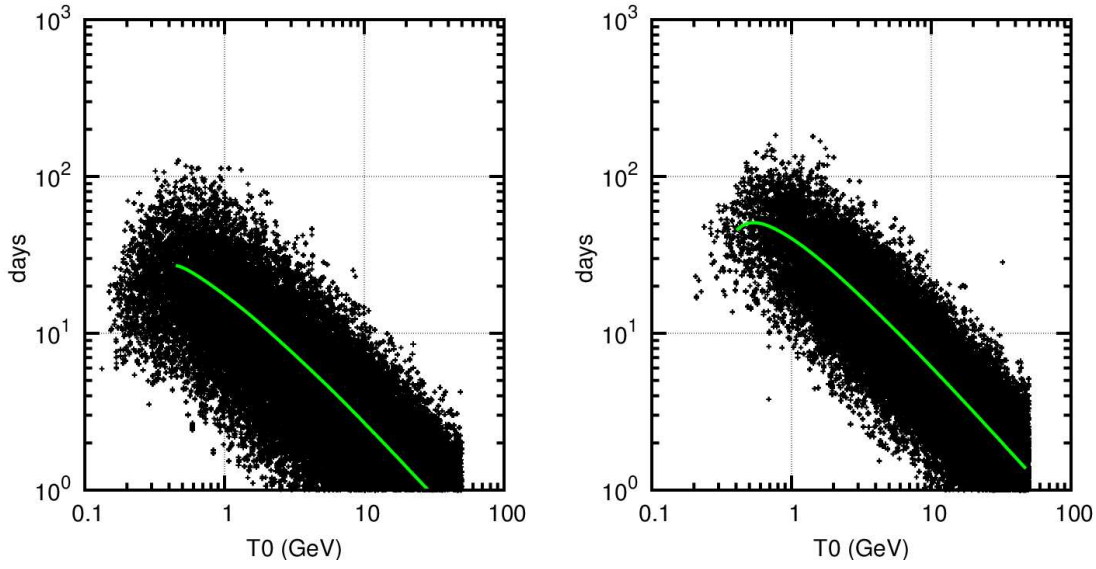

Figure 3.7: Propagation time (in days) of particle with initial energy T0 from the Heliosphere boundary down to Earth, the point are se single pseudo-particle, the green line is the average value. Left panel is for the Low activity period, while right panel is for the high activity period.

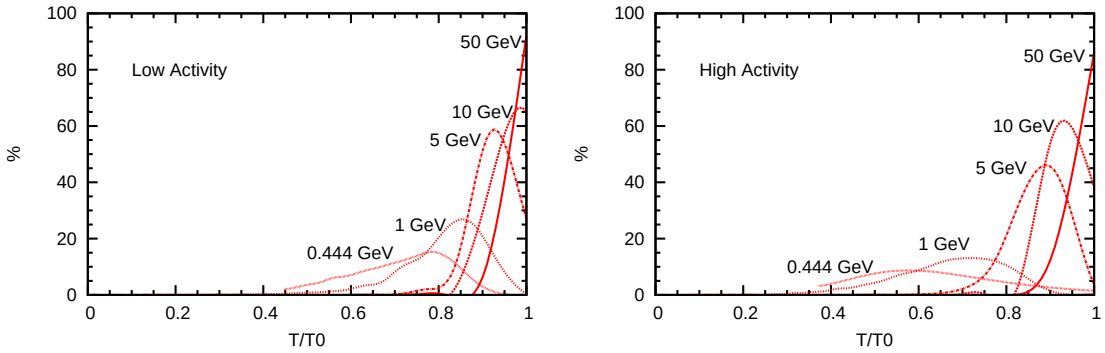

Figure 3.8: Energy distribution at Earth for injected energy T0. Left panel is for the Low activity period, while right panel is for the high activity period. (images from Bobik et al., 2012b)

are strictly related to the the energy distribution. Indeed, from Eq. (3.25c) one can see that much longer a pseudo-particle remain inside the heliosphere, greater is the energy lost, with an efficient directly proportional to the time. In Fig. 3.8 we show the energy distribution (in percentage) at the Earth for pseudo-particles injected with energy T0 equal to 0.444 ($\sim$ 1 GV), 1, 5, 10 and 50 GeV, for both low and high activity periods. It is possible to note that, during the propagation inside the heliosphere, high energy pseudo-particle lost a small fraction of their energy, while 0.444 GeV pseudo-particle can lost more than half of their energy (Bobik et al., 2012b). This effect depends also from the solar activity and is less efficient during the low activity period. This agrees with the experimental evidence of a larger modulation effect during solar maximum, as discussed in Sect. 2.1 (see also Bobik et al., 2012b), and gives the possibility to describe the long term variation of the solar modulation as a change in the environmental effect, due to sun activity, that affect the particle path get it longer or shorter.

The HelMod code is also able to reproduce modulation of GCR of any kind of particles. An example could be find in the preliminary study presented in Bobik et al. (2011b). In this preliminary work, HelMod code (version 1.4)[6] was applied to Antiproton ($\bar{p}$) over Proton (p) rates (see Fig. 3.9) showing a qualitatively good agreement with experimental data. For this study was used the LIS computed online via GALPROP WebRun service[7] (Vladimirov et al., 2011).
Examples of other studies carried out with the Monte Carlo technique could be found e.g. also in Strauss et al. (2011),

[6] that does not contain yet the optimization on LIS, Diffusion Parameter and IMF discussed in Sect. 3.2, Sect. 4.1 and Sect. 4.2.1

[7] http://galprop.stanford.edu/webrun/

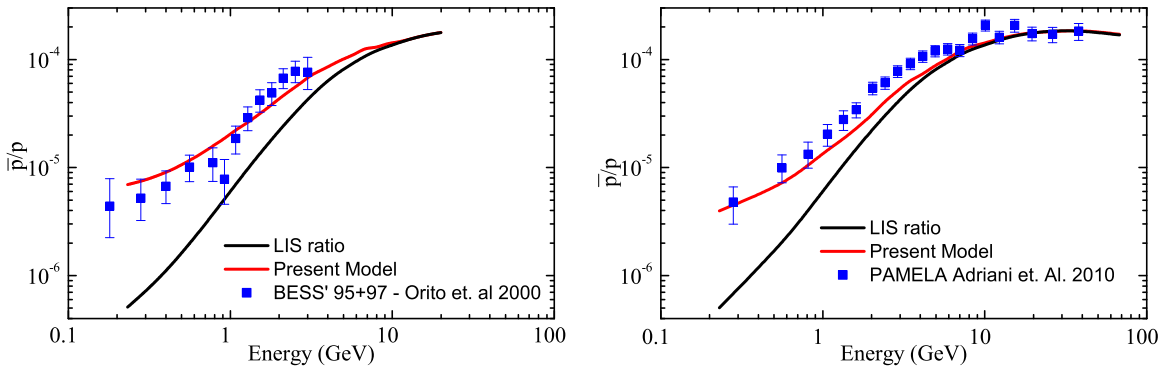

Figure 3.9: Comparison of simulated $\bar{p}/p$ ratio at 1 AU and experimental data from BESS–1997 (left panel Orito et al., 2000) and PAMELA–2006/08 (right panel Adriani et al., 2010). The the LIS was computed online via GALPROP WebRun service (Vladimirov et al., 2011). [images from Bobik et al. (2011b)]

Chapter 4

Results for solar cycle 23

The HelMod code described in Sect. 3.2 allows one to solve the Parker equation discussed in Sect. 2.2. This allow one, given a LIS as hypothesis (see Sect. 4.1), to obtain modulated GCR intensity in the inner heliosphere. In particular we compare our results at Earth orbit with proton differential intensities observed at Earth during solar cycle 24 (see Sect. 4.2.1). Furthermore in Sect. 4.2.2 we tune our model using Ulysses data outside ecliptic plane, using the 2D-approximation to explore the effects of polar IMF on the Solar Modulation and latitudinal gradient in the inner heliosphere. HelMod is also able to reproduce any kind of species of GCR particle, this features was used to study the effects of Solar Modulation also for positrons and electrons. In particular in Sect. 4.3 we study the Ulysses latitudinal gradient asymmetry between protons and electrons and between different IMF polarity. We also present the positron ratio for different IMF polarity. Finally in Sect. 4.4 we show how the dimension of the dynamic heliosphere affects the low energy part of GCR spectrum, allowing for a possible extension of Present Model to rigidity lower than 1 GV. Results presented in this Chapter are consistent to those presented in Bobik et al. (2011b, 2012a); Della Torre et al. (2012a) and Bobik et al. (2012d).

4.1 Proton Local Interstellar Spectrum

LIS are commonly predicted by mean of numerical methods for CR propagation model into the galaxy (see e.g. Strong and Moskalenko, 2001). This method could also takes into account the large scale structure of the galaxy (e.g. the spiral arms source distribution) as well including possible local sources within a few parsec from the Sun Strauss et al. (2012b). Recently, Herbst et al. (2010) reviewed different proton LISs published in the literature and determined that these spectra agree well with each other for proton energies above 10 GeV. Over the past years, Moskalenko, Strong, and collaborators, using GALPROP, provided many protons LIS for different propagation model within the galaxy (e.g., see Strong and Moskalenko, 2001; Moskalenko et al., 2002; Strong et al., 2004; Trotta et al., 2011) but latest calculation agrees above 1 GV with the LIS of Burger et al. (2000, BPH-LIS) used in this work (e.g., see Fig. 4.1). Moreover Scherer et al. (2011) shown as the presence of the heliopause affect the propagation of particles, resulting to modulation effects already in the outer heliosphere. This suggest to distinguish the “Galactic” Interstellar spectrum

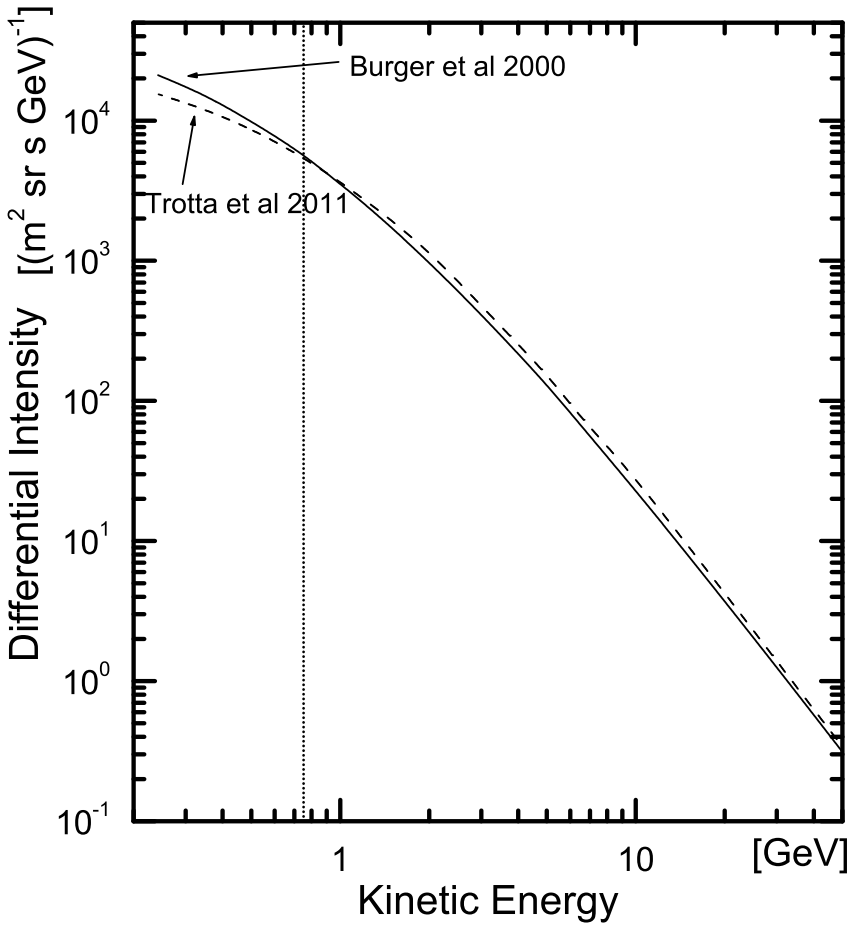

Figure 4.1: Comparison between the Proton LIS from GALPROP (dash line, Trotta et al., 2011) and BPH-LIS (Solid line, Burger et al., 2000). The short-dot line correspond to 1 GV.

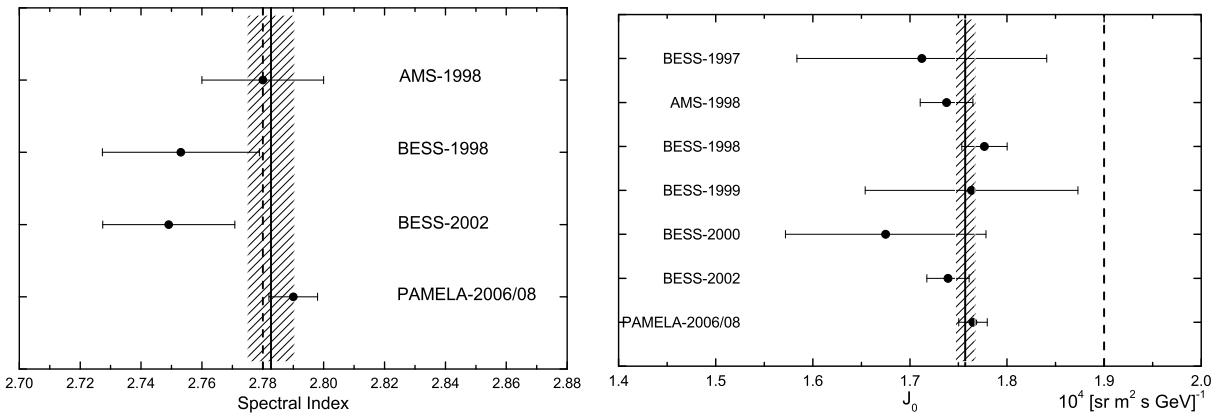

Figure 4.2: Left: spectral index (γ) obtained (see the text) for AMS–1998, BESS–1998, BESS–2002, and PAMELA–2006/08. Right: normalization constant (J_0) for BESS–1997, AMS–1998, BESS–1998, BESS–1999, BESS–2002, and PAMELA–2006/08. The dotted lines represent the values of the spectral index ($\gamma_{\rm BPH}$) and normalization constant ($J_{0,\rm BHP}$) of the BPH-LIS, respectively; the continuous lines represent the error-weighted averages of spectral index ($\gamma_{\rm wa}$) and normalization constant ($J_{0,\rm wa}$) (figure from Bobik et al., 2012a).

(GIS), above the Heliopause, from the LIS at Solar Wind Termination. These effects are important at very low energy (10 MeV∼100 MeV) but it is of the order of few percent at energy below 1 GV, so that heliopause modulation effects are not accounted in this work and the LIS is taken to be the GIS at the boundary of the effective heliosphere. We focus our attention on the BPH-LIS that in units of $(srm^2sGeV)^{-1}$ is expressed as (see equation (30) of Bobik et al., 2012a):

$$J_{\rm BHP}(T) = \begin{cases} J_{0,\rm BPH} R^{-\gamma_{\rm BPH}}, \text{ for } R \geq 7, \\ \exp[9.472 - 1.999 \ln R - 0.6938 (\ln R)^2 \\ +0.2988 (\ln R)^3 - 0.04714 (\ln R)^4], \text{ for } R < 7 \end{cases} \tag{4.1}$$

with

$$R \equiv R(T) = \frac{P(T)}{P_0} \tag{4.2}$$

where (e.g., see Equation (4.94) in Leroy and Rancoita, 2011)

$$P(T) = \frac{\sqrt{T(T + 2m_p c^2)}}{e}$$

is the proton rigidity in GV with m_p is the rest mass of the proton in GeV/c^2, T is the proton kinetic energy in GeV, e is the electron charge, c is the speed of light, $\gamma_{\rm BPH} = 2.78$ is the spectral index, $J_{0,\rm BPH} = 1.9 \times 10^4$ (sr m^2 s GeV)$^{-1}$ is a normalization constant, and, finally, P_0 =1 GV.

Above (10–20) GeV the differential proton intensities are slightly or marginally affected by modulation. The high energy part of BPH-LIS was compared to experimental spectra available in the literature and collected during solar cycle 23 i.e., AMS–1998 (Aguilar et al., 2002), BESS–1998 (with data only in the range 20–117 GeV Sanuki et al., 2000), BESS–2002 (Haino et al., 2004), and PAMELA–2006/08 (Adriani et al., 2011). In Figure 3, the spectral indexes (γ) of

AMS–1998 and PAMELA–2006/08 are those from Aguilar et al. (2002) and Adriani et al. (2011), respectively, while for BESS–1998 and BESS–2002 the spectral indexes were obtained from a fit to the published data of the differential proton intensities. Bobik et al. (2012a) noted that Adriani et al. (2011) found a spectral index in the range 30–320 GV dependent on rigidity

$$J = J_0 R^{-\Gamma} = J_0 R^{-\gamma_{\rm PAMELA} - \alpha_p \frac{R-R_0}{R_0}}$$

with R as defined in Eq. (4.2) and $R_0 = 100$ GV. The rigidity-independent part of the spectral index found by PAMELA–2006/08 is $\gamma_{\rm PAMELA} = 2.790 \pm 0.008({\rm stat}) \pm 0.001({\rm syst})$, while $\alpha_p = (1.07 \pm 0.25({\rm stat}) \pm 0.05({\rm syst})) \cdot 10^{-2}$ is the rigidity dependent part with a maximum variation of the order of the previously quoted uncertainties. Furthermore, the spectral index (2.79 ± 0.08) found by Caprice–1994 (Boezio et al., 1999) is in agreement with those found by the experiments discussed in this Section, but the quoted errors are larger. Bobik et al. (2012a) also considered the normalization constant J_0 (Fig. 4.2 right). This were obtained from a fit using $\gamma_{\rm BPH}$ as spectral index to the experimental data. The J_0 constant was evaluated for the set of experimental observation considered in this work, i.e., BESS–1997 (Shikaze et al., 2007), BESS–1998 (Shikaze et al., 2007; Sanuki et al., 2000), AMS–1998 (Aguilar et al., 2002), BESS–1999 (Shikaze et al., 2007), BESS–2002 (Haino et al., 2004), and PAMELA–2006/08 (Adriani et al., 2011). The weighted averages of both the spectral index (γ) and normalization constant (J_0) and their errors were determined following the procedure indicated on pages 14–15 of Nakamura et al. (2010). The error-weighted averages found are

$$\gamma_{\rm wa} = 2.783 \pm 0.009 \tag{4.3}$$

and

$$J_{0,{\rm wa}} = (1.76 \pm 0.01) \times 10^4 ({\rm sr\ m^2 s\ GeV})^{-1} \tag{4.4}$$

$\gamma_{\rm wa}$ is in good agreement with that ($\gamma_{\rm BPH}$) suggested by Burger et al. (2000). $J_{0,{\rm wa}}$ and $\gamma_{\rm wa}$ are represented with the continuous lines in Fig. 4.2; in the same figure the dotted lines refer to the values of the BPH-LIS. We note that the value of J_0 found from a fit to Caprice–1994 data above 20 GeV (Boezio et al., 1999) is 1.44 ± 0.02: this value differs by more than 5 standard deviations from $J_{0,{\rm wa}}$.

To allow a direct comparison of simulated intensities with experimental data, in this work we use the BPH-LIS as parametrized in equation (33) of Bobik et al. (2012a):

$$J_{\rm HelMod}(T) = J_{\rm BPH}(T) \left(\frac{J_0}{J_{0,{\rm BPH}}} \right) ({\rm sr\ m^2 s\ GeV})^{-1}. \tag{4.5}$$

$J_{\rm HelMod}(T)$ keeps the same spectral index for $P(T) \geq 7$ GV as in Eq. (4.1) and depends linearly on J_0 , which accounts for the slight variations in absolute fluxes between the observations. The normalization factor $\left(\frac{J_0}{J_{0,{\rm BPH}}} \right)$ is evaluated for each data-set and reported in table 4.1. For BESS–2000 (Shikaze et al., 2007), the experimental observations did not exceed 21.5 GeV, i.e., an energy region of proton differential intensity which might (marginally) still be affected by modulation in a period of high solar activity; thus, the normalization constant used for these data was the one

	$\frac{J_0}{J_{0,\mathrm{BPH}}}$
BESS-1997	0.9012
AMS-98	0.9145
BESS-1999	0.9281
BESS-2000	0.9153
BESS-2002	0.9153
PAMELA	0.9289

Table 4.1: Normalization factor $\frac{J_0}{J_{0,\mathrm{BPH}}}$ of BPH-LIS to experimental data, as defined in Eq. (4.5), for BESS–1997, AMS–1998, BESS–1999, BESS–2002, and PAMELA–2006/08. The normalization factor for BESS-2000 is the one obtained from BESS-2002 (see text).

obtained from BESS–2002 (Haino et al., 2004) data.

4.2 Comparison with data

We used the present code for quantitative comparisons, using Eqs. (4.6) and (4.7), with experimental data collected during solar cycle 23.

The HelMod Code presented in Sect. 3.2 allowed us to investigate how the simulated modulated differential intensities are affected by the particle drift effect (Sections 2.1 and 2.2.2), and the polar enhancement of the diffusion tensor along the polar direction ($K_{\perp,\theta}$. The effects related to particle drift were investigated via the suppression of the drift velocity, i.e., under the assumption that in Eq. (2.12) $K_A = 0$ and so only symmetric component of diffusion tensor are considered. This also accounts for the hypothesis that magnetic drift convection is almost completely suppressed during solar maximum. Results using the parallel diffusion coefficient in Eq. (2.14) were presented in Bobik et al. (2012a) where the authors exploited also the latitudinal dependence of GCR intensity. They found a qualitatively agreement with observation of Ulysses spacecraft during the 1995 *fast scan* (see Section 7.4 of Bobik et al., 2012a) but not for 2007 *fast scan*. In current analysis we improve the analysis using the parallel diffusion coefficient described in Eq. (2.16), whose elements depend on the actual value of the diffusion parameter K_0, leading to similar conclusion on ecliptic plane to those presented previously but opening a new vision on drift effects on latitudinal intensity, as shown in Sect. 4.3.

The polar enhancement is evaluated from 1, i.e. no enhancement, up to 10, as described in Bobik et al. (2012a). These differential intensities were calculated for a polar-increased value of $K_{\perp,\mu} = \rho_E K_{\perp,r}$ (see discussion in Sect. (2.2.1)) with values of ρ_E of 1, 8 and 10, i.e. no enhancement, those suggested by Ferreira and Potgieter (2004) and those suggested by Potgieter (2000) and Bobik et al. (2012a, and reference there in). In addition the differential intensities were calculated accounting for particles inside an heliospheric region where solar latitudes are lower than $|5.7°|$. Although in (Bobik et al., 2012a) also an heliosphere region where solar latitudes are lower than $|30°|$ was considered for period of solar maximum, present analysis does not found any advances for this choose. The results presented in this Sections follow the approach close to (Bobik

et al., 2012d).

4.2.1 Ecliptic effects

Since the structure of the heliosphere is different between high and low solar activity, passing from a quasi chaotic structure to a magnetic field more dipolar (see Sect. 1.3), we analyze the two periods separately. For period of high activity we select data from the BESS collaboration in the years 1999, 2000, and 2002 (Shikaze et al., 2007). while for period not dominated by high solar activity we consider those in solar cycle 23, i.e., BESS–1997 (Shikaze et al., 2007), AMS–1998 (Aguilar et al., 2002), and PAMELA–2006/08 (Adriani et al., 2011). As done in Bobik et al. (2012a), these data were compared with those obtained by means of the HelMod code using the error-weighted root mean square ($\eta_{\rm rms}$) of the relative difference (η) between experimental data ($f_{\rm exp}$) and those resulting from simulated differential intensities ($f_{\rm sim}$), as in equations (34)-(35) of Bobik et al. (2012a):

$$\eta_{\rm rms} = \sqrt{\frac{\sum_i (\eta_i/\sigma_{\eta,i})^2}{\sum_i 1/\sigma_{\eta,i}^2}} \tag{4.6}$$

with

$$\eta_i = \frac{f_{\rm sim}(T_i) - f_{\rm exp}(T_i)}{f_{\rm exp}(T_i)} \tag{4.7}$$

where T_i is the average energy of the ith energy bin of the differential intensity distribution and $\sigma_{\eta,i}$ are the errors including the experimental and Monte Carlo uncertainties; the latter account for the Poisson error of each energy bin. The simulated differential intensities are interpolated with a cubic spline function. Since PAMELA data accounts for nearly 3 years periods, we simulated the solar condition for 33 solar rotation from 2006 to 2008, then, thanks to the peculiarity of Monte Carlo approach, we combine this results simulating a 3 years uniform observation.

The modulation results are studied varying the parameters δ_m (from 0, i.e. pure Parker IMF, up to 3×10^{-5}, see Sect. 3.2.3), ρ_k (from 0.10 up to 0.14) and ρ_E (from 1 up to 10) looking for the set that minimize $\eta_{\rm rms}$. The resulting $\eta_{\rm rms}$ obtained for both low and high solar activity are presented respectively in App. D.1 and D.2. In tables 4.2 we consider the averages $\eta_{\rm rms}(\%)$ between the low activity periods; they were obtained in the energy range [1] from 444 MeV up to 30 GeV, without any enhancement of the diffusion tensor along the polar direction ($K_{\perp,\mu}$), using the "L" and "R" models for the tilt angle α_t and for the no drift approximation (discussed previously in this Section); results with enhancement of the diffusion tensor along the polar direction are shown in App. D.1. This shown that simulations for $\rho_E = 8$ and 10 lead to a $\eta_{\rm rms}$ that is from 1.5 up to 3 time greater with respect the case without enhancement [2]. From inspection of Tables 4.2, one can remark that the drift mechanisms leads to a better agreement with experimental data. Furthermore the "R" and "L" models for tilt angles are comparable within the precision of the method (discussed in Sect. 3.2.5). The minimum difference with the experimental data occurs when $\rho_k = 0.12 \sim 0.13$ and $\delta_m = 1.0 \times 10^{-5}$ for both "R" and "L" model.

[1] Above 30 GeV the differential intensity is marginally (if at all) affected by modulation.

[2] For a comparison, the *scalar* approximation presented in (Bobik et al., 2012a), i.e., assuming that the diffusion propagation is independent of magnetic structure, leads to an average$\eta_{\rm rms}$ of $\sim 15\%$.

Parameters	"R" model	"L" model	No Drift
$\delta_m = 0.0 \times 10^{-5}$; $\rho_k = 0.10$;	14.1	11.0	33.4
$\delta_m = 1.0 \times 10^{-5}$; $\rho_k = 0.10$;	11.7	8.7	33.2
$\delta_m = 2.0 \times 10^{-5}$; $\rho_k = 0.10$;	11.6	8.3	33.7
$\delta_m = 3.0 \times 10^{-5}$; $\rho_k = 0.10$;	11.6	8.3	33.7
$\delta_m = 1.0 \times 10^{-5}$; $\rho_k = 0.11$;	6.4	9.0	27.7
$\delta_m = 2.0 \times 10^{-5}$; $\rho_k = 0.11$;	7.8	9.0	28.3
$\delta_m = 3.0 \times 10^{-5}$; $\rho_k = 0.11$;	7.5	8.8	29.2
$\delta_m = 1.0 \times 10^{-5}$; $\rho_k = 0.12$;	6.3	7.1	23.5
$\delta_m = 2.0 \times 10^{-5}$; $\rho_k = 0.12$;	6.3	7.3	24.7
$\delta_m = 3.0 \times 10^{-5}$; $\rho_k = 0.12$;	7.1	6.9	24.4
$\delta_m = 1.0 \times 10^{-5}$; $\rho_k = 0.13$;	6.3	6.4	20.1
$\delta_m = 2.0 \times 10^{-5}$; $\rho_k = 0.13$;	6.6	7.6	20.4
$\delta_m = 3.0 \times 10^{-5}$; $\rho_k = 0.13$;	6.7	7.7	20.5
$\delta_m = 1.0 \times 10^{-5}$; $\rho_k = 0.14$;	7.3	7.0	15.9
$\delta_m = 2.0 \times 10^{-5}$; $\rho_k = 0.14$;	7.3	7.2	16.4
$\delta_m = 3.0 \times 10^{-5}$; $\rho_k = 0.14$;	7.2	6.5	16.8

Table 4.2: Average $\eta_{\rm rms}(\%)$ between BESS–1997, AMS–1998, PAMELA-2006/08, obtained from Eq. (4.6) without any Enhancement of the Diffusion Tensor along the polar direction ($\rho_E = 1$), using "R" and "L" Models for the tilt angle and No Drift Approximation; the differential intensities were calculated accounting for particles inside two heliospheric regions where solar latitudes are lower than $|5.7°|$.

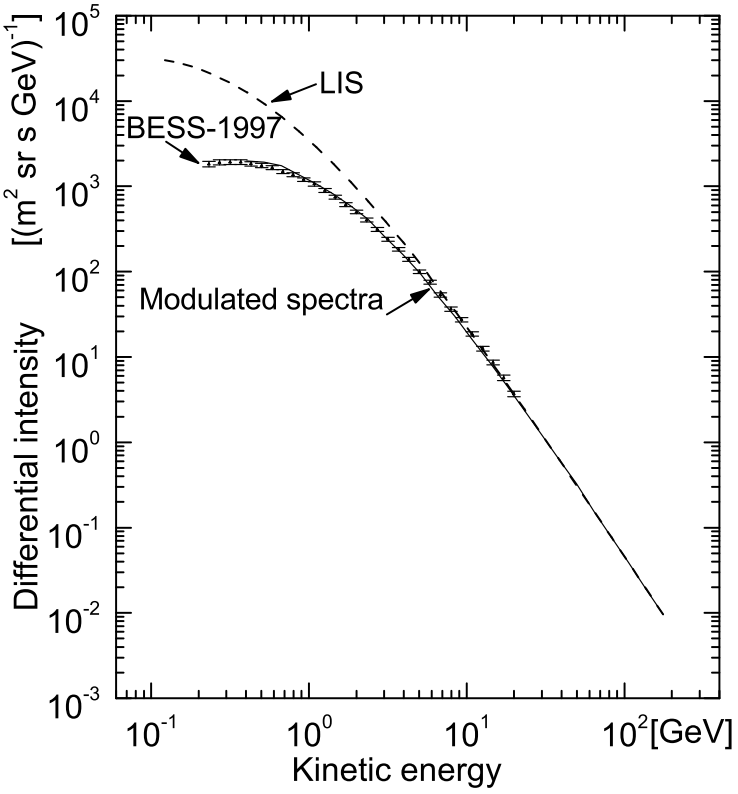

Figure 4.3: Figure 4. Differential intensity determined with the HelMod code (continuous line) compared to the experimental data of BESS–1997; the dashed line is the LIS (see the text).

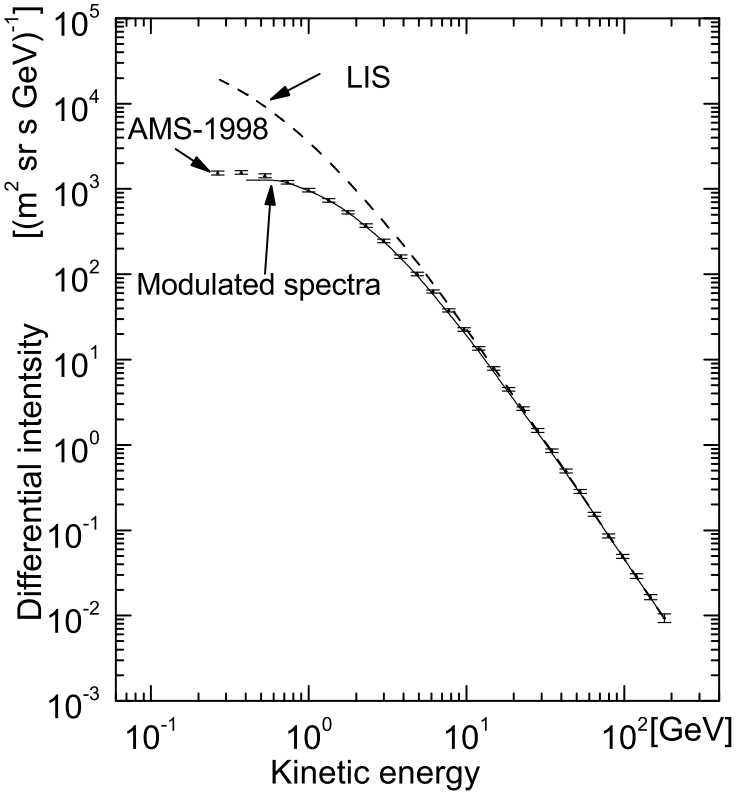

Figure 4.4: Figure 4. Differential intensity determined with the HelMod code (continuous line) compared to the experimental data of AMS-1998; the dashed line is the LIS (see the text).

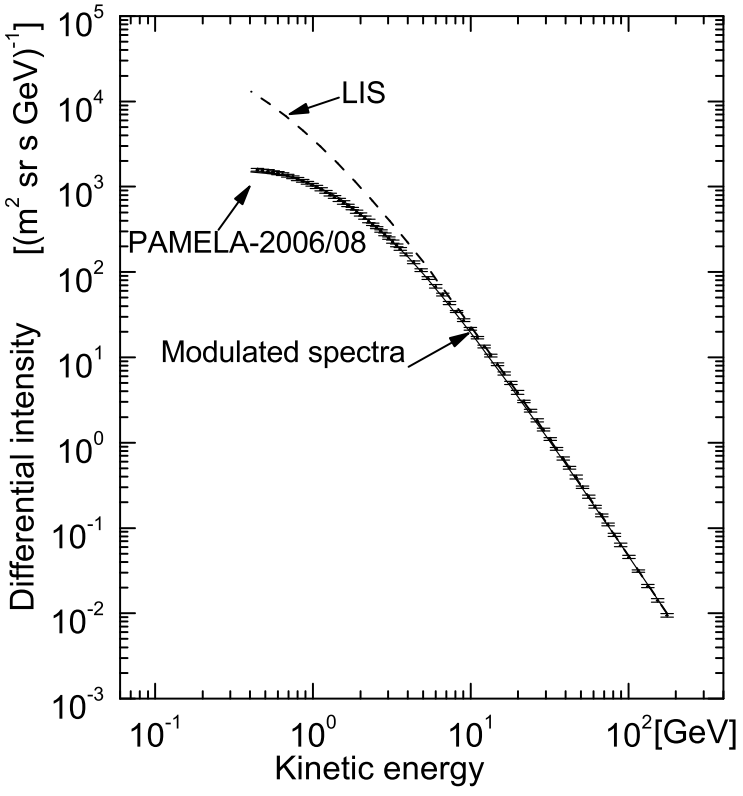

Figure 4.5: Figure 4. Differential intensity determined with the HelMod code (continuous line) compared to the experimental data of PAMELA 2006/08; the dashed line is the LIS (see the text).

The same analysis was done for periods dominated by high solar activity; Results without any enhancement of the diffusion tensor along the polar direction ($K_{\perp,\mu}$) are reported in table (4.3). Results with enhancement of the diffusion tensor along the polar direction, reported in App. D.2, shown that simulations with $\rho_E = 8$ and 10 lead to $\eta_{\rm rms}$ comparable with those presented in Table (4.3) but solutions with $\rho_E = 1$ carried to better agreement with data at lower energy. From inspection of Table (4.3), one can note that "R" and "L" models for tilt angles are comparable within the precision of the method; furthermore the minimum difference with the experimental data occurs when $\rho_k = 0.10 \sim 0.11$ and $\delta_m = 2.0 \times 10^{-5}$ for both "R" and "L" model. The HelMod parameters configuration which minimize the difference with the experimental data is reported in Table 4.4: one may notice that the No Drift description is (almost) comparable to drift descriptions for both BESS–2000 and BESS–2002 data, which are collected during and after the maximum of the solar activity. Apparently the Drift treatment is needed in order to describe BESS-1999 data, which observed during a period approaching the solar maximum.

In Figs. 4.3–4.5, the differential intensities determined with the HelMod code are shown and compared to the experimental data of BESS–1997, AMS–1998, and PAMELA–2006/08, respectively. These modulated intensities are the ones calculated for a heliospheric region where solar latitudes are lower than $|5.7°|$, using $\rho_k = 0.13$, $\delta_m = 1.0 \times 10^{-5}$, without any enhancement of diffusion tensor (i.e. $\rho_E = 1$) and including particle drift effects with values of the tilt angle from the "L" model. In Figs. (4.6)–(4.8) the differential intensities determined with the HelMod code are shown and compared with the experimental data of BESS–1999, BESS–2000, and BESS–2002, respectively. These modulated intensities are the ones calculated for a heliospheric region where solar latitudes are lower than $|5.7°|$, using $K_{\perp,\mu} = K_{\perp,r}$ independently of the latitude and including particle drift effects with the values of the tilt angle from the "L" model. In all figures the dashed line is the LIS (Eq. (4.1) and (4.5)) with normalization constants $\frac{J_0}{J_{0,\rm BPH}}$ as in table 4.1.

4.2.2 Polar Region Effects

As discussed in Sect. 1.2.1 the standard Parker field fails to correctly reproduce the polar IMFand, in turn, the GCR transport through polar direction. This is related to the solar differential rotation that lead to a more complex magnetic field description in the vicinity of sun poles, as discussed in Sect. 3.2.3 (see e.g. Jokipii and Kota, 1989; Balogh et al., 1995; Moraal, 1990; Smith and Bieber, 1991; Fisk, 1996; Hitge and Burger, 2010). Moreover Ulysses spacecraft (see Sect. 1.1.2) explored the heliosphere outside the ecliptic plane up to $\pm 80°$ of solar latitude observing a latitudinal gradient in the Proton intensity (see e.g. first *fast scan* in Fig. 2.3, and Heber et al., 1996; Simpson, 1996). Data collected during the *latitudinal fast scan* (from September 1994 up to August 1995), show a nearly symmetric latitudinal gradient with the minimum near ecliptic plane, a southward shift of the minimum and the intensity in the north polar region at 80° exceeds the south polar intensity. Simpson (1996) estimate a latitudinal gradient of $\sim 0.3\%$/degree for proton with kinetic energy > 0.1 GeV. While in Heber et al. (1996) the analysis was extended to higher energy estimating $\sim 0.22\%$/degree for proton with kinetic energy > 2 GeV. The minimum of the proton intensity occurs $\sim 10°$ south of the heliographic equator (Simpson, 1996). In addition an

Parameters	"R" model	"L" model	No Drift
$\delta_m = 0.0 \times 10^{-5}$; $\rho_k = 0.10$;	11.2	10.8	15.4
$\delta_m = 1.0 \times 10^{-5}$; $\rho_k = 0.10$;	11.0	10.1	15.8
$\delta_m = 2.0 \times 10^{-5}$; $\rho_k = 0.10$;	9.6	10.0	16.7
$\delta_m = 3.0 \times 10^{-5}$; $\rho_k = 0.10$;	9.6	10.0	16.7
$\delta_m = 1.0 \times 10^{-5}$; $\rho_k = 0.11$;	13.4	13.1	16.0
$\delta_m = 2.0 \times 10^{-5}$; $\rho_k = 0.11$;	12.7	12.9	15.4
$\delta_m = 3.0 \times 10^{-5}$; $\rho_k = 0.11$;	12.7	12.5	16.2
$\delta_m = 1.0 \times 10^{-5}$; $\rho_k = 0.12$;	18.7	17.7	13.4
$\delta_m = 2.0 \times 10^{-5}$; $\rho_k = 0.12$;	18.3	16.9	12.8
$\delta_m = 3.0 \times 10^{-5}$; $\rho_k = 0.12$;	18.1	17.3	12.8
$\delta_m = 1.0 \times 10^{-5}$; $\rho_k = 0.13$;	23.3	23.5	14.3
$\delta_m = 2.0 \times 10^{-5}$; $\rho_k = 0.13$;	25.0	24.7	13.3
$\delta_m = 3.0 \times 10^{-5}$; $\rho_k = 0.13$;	24.3	24.2	13.1
$\delta_m = 1.0 \times 10^{-5}$; $\rho_k = 0.14$;	32.3	30.7	18.0
$\delta_m = 2.0 \times 10^{-5}$; $\rho_k = 0.14$;	32.8	30.8	17.1
$\delta_m = 3.0 \times 10^{-5}$; $\rho_k = 0.14$;	31.5	30.7	17.9

Table 4.3: Average $\eta_{\rm rms}(\%)$ between BESS–1999, BESS–2000, BESS–2002, obtained from Eq. (4.6) without any Enhancement of the Diffusion Tensor along the polar direction ($\rho_E = 1$) , using "R" and "L" Models for the tilt angle and No Drift Approximation; the differential intensities were calculated accounting for particles inside two heliospheric regions where solar latitudes are lower than $|5.7°|$.

Observations	"R" model	"L" model	No Drift
BESS–1999	9.3	10.6	25.7
BESS–2000	12.5	12.6	16.7
BESS–2002	6.9	6.7	7.7

Table 4.4: $\eta_{\rm rms}(\%)$ For BESS–1999, BESS–2000, BESS–2002, obtained from Eq. (4.6) without any Enhancement of the Diffusion Tensor along the polar direction ($\rho_E = 1$), $\delta_m = 2.0 \times 10^-5$, $\rho_k = 0.10$ and using "R" and "L" Models for the tilt angle and No Drift Approximation; the differential intensities were calculated accounting for particles inside two heliospheric regions where solar latitudes are lower than $|5.7°|$.

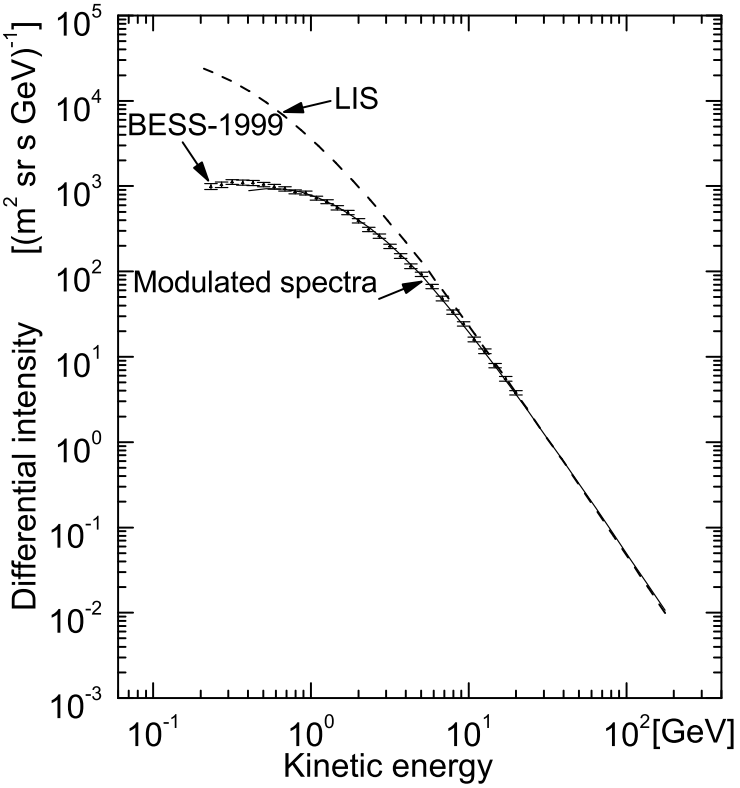

Figure 4.6: Figure 4. Differential intensity determined with the HelMod code (continuous line) compared to the experimental data of BESS–1999; the dashed line is the LIS (see the text).

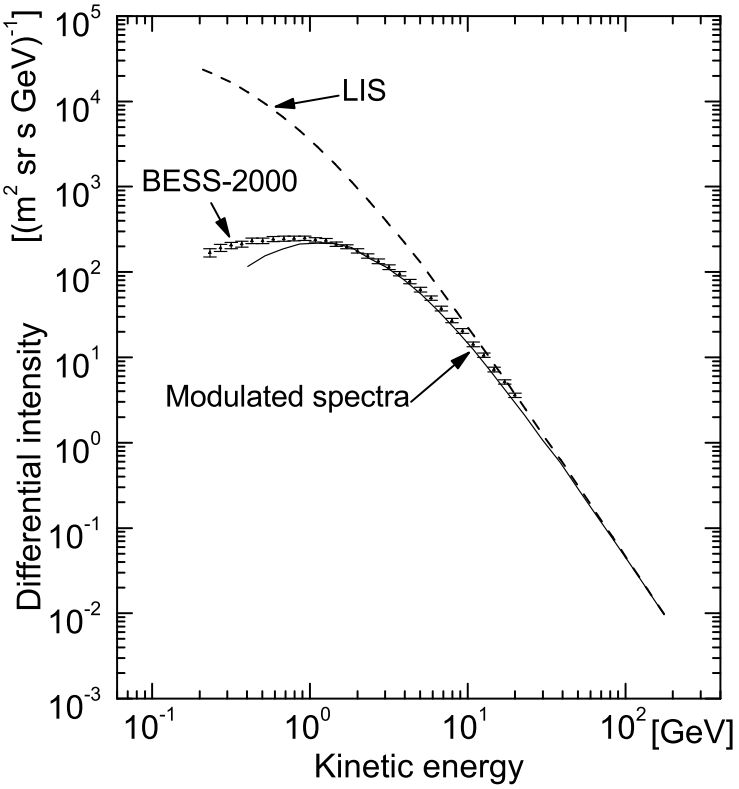

Figure 4.7: Figure 4. Differential intensity determined with the HelMod code (continuous line) compared to the experimental data of BESS–2000; the dashed line is the LIS (see the text).

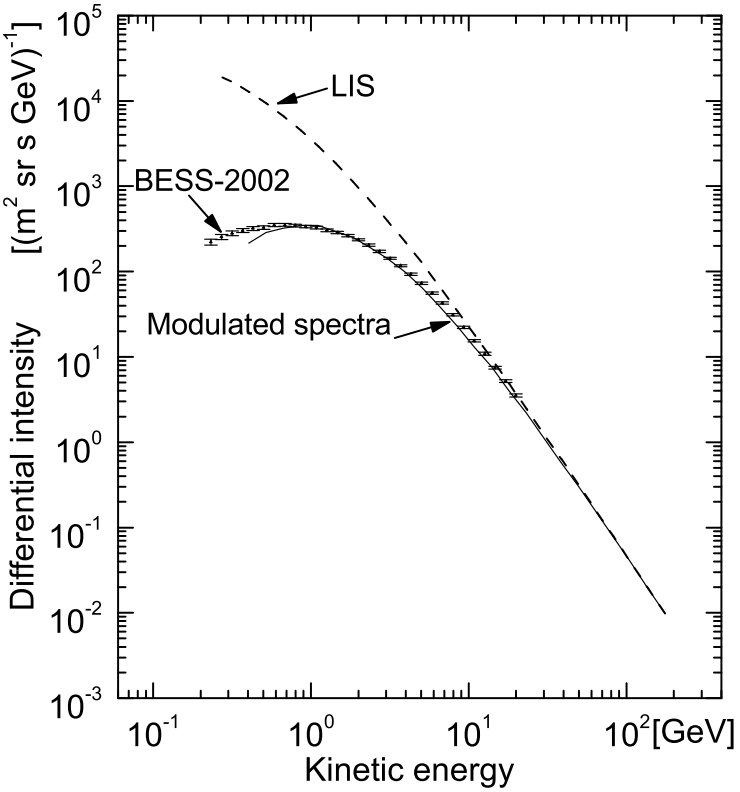

Figure 4.8: Figure 4. Differential intensity determined with the HelMod code (continuous line) compared to the experimental data of BESS–2002; the dashed line is the LIS (see the text).

independent analysis that takes into account the latitudinal motion of Earth and IMP 8 confirms a significant ($\sim 8^\circ \pm 2^\circ$) southward offset of the intensity minimum for $T > 100$ MeV proton (Simpson, 1996). Furthermore Heber et al. (1996) estimate a southward offset of about $\approx 7^\circ$ that is independent of particle energy up to 2 GeV. Finally Simpson (1996) estimate that the intensity in the north polar region at 80° exceeds the south polar intensity of $\sim 6\%$ for $T > 100$ MeV proton. Similar study was performed both for electrons and for the successive *fast scan* in 2007, this results are discussed in Sect. 4.3.

Using the present HelMod code (version 2.0) we study the effect of the solar modulation on GCR latitudinal gradient. As defined in Sect. 3.2.3 we denote with θ_{X° a polar region of amplitude X° from polar axis, i.e. $\theta < X^\circ$ and $\theta > 180^\circ - X^\circ$. Three regions $X^\circ = 20^\circ$, 25° and 30° are investigated. These regions allows for a smooth transition between $\mathbf{B}_{Pol}$ and $\mathbf{B}_{Par}$ in Eq. 3.38 and leads to results consisted with those presented in previous Section within the accuracy of the Monte Carlo. For the purpose of this study we consider an energy binning closer to those presented in Heber et al. (1996). The KET instrument, considered for this analysis, collect proton data in five "channel" from 0.038 GeV up to > 2 GeV A successive re-analysis of collected data allows the Heber and collaborators to subdivide the 0.25–2 GeV channel in 3 sub-channel of intermediate energies. Since the Present Model is optimized for particle with rigidity greater than 1GV (≈ 0.444 GeV) we compare our result only with channels reported in table 4.5.

At 1 AU and as a function of the solar colatitude, the GCR intensities for protons are shown

HelMod Energy Bins	KET channel
0.35 – 0.98 GeV	0.4 – 1.0 GeV
0.76 – 2.09 GeV	0.8 – 2.0 GeV
2.09 – 200 GeV	> 2 GeV

Table 4.5: Energy Bins in kinetic energy selected with HelMod Code and the corresponding Proton Energy channel for KET instruments on board the Ulysses spacecraft (Heber et al., 1996).

in Fig. 4.9. For a comparison with Ulysses observations, the modulated intensities of protons - resulting from HelMod code - were investigated from 80° (North) and down to −80° (South). They were obtained using the HelMod code and selected using the energy bins reported in table 4.5. In Fig. 4.9, the latitudinal intensity distribution is normalized to the corresponding South Pole intensity. The quoted errors include statistical and systematic errors. The distributions were interpolated using a parabolic function expressed as:

$$I(\theta) = a + c(\theta_{\rm lat} + d)^2 \tag{4.8}$$

where $I(\theta_{\rm lat})$ is the normalized intensity, $\theta_{\rm lat}$ is the latitudinal angle[3] and a, b and c are parameters determined from the fitting procedure. The so obtained fitted curves are shown as continuous lines in Fig. 4.9. Furthermore, the latitudinal positions of minimum intensity ($\theta_{\rm lat,min}$), percentages of North-South asymmetry of intensities ($\Delta_{\rm N\text{-}S}$) and differences in percentage between the maximum and minimum intensities ($\Delta_{\rm max}$) were also determined from the fitting procedure and are listed in Table 4.6, Table 4.7 and Table 4.8, respectively. The quoted errors are obtained considering all curves that gives a $\eta_{\rm rms,lat}$ not greater than 2 times the $\eta_{\rm rms,lat}$ obtained with best fit ($I_{\rm best}$). $\eta_{\rm rms,lat}$ is defined in similar way of Eqs (4.6) and (4.7):

$$\eta_{\rm rms,lat} = \sqrt{\frac{\sum_i (\eta_{i,lat}/\sigma_{\eta,i,lat})^2}{\sum_i 1/\sigma^2_{\eta,i,lat}}} \tag{4.9}$$

with

$$\eta_{i,lat} = \frac{I(\theta_i) - I_{\rm best}(\theta_i)}{I_{\rm best}(\theta_i)} \tag{4.10}$$

where θ_i is the central value of the ith latitudinal bin of the differential intensity distribution and $\sigma_{\eta,i,lat}$ are the errors including the experimental and Monte Carlo uncertainties;

Energy range	$\theta_{\rm lat,min}$ (°)		
	θ_{20°	θ_{25°	θ_{30°
0.35 – 0.98 GeV	-5^{+4}_{-5}	-8^{+4}_{-4}	-9^{+3}_{-3}
0.76 – 2.09 GeV	-5^{+6}_{-7}	-6^{+5}_{-6}	-10^{+4}_{-4}
2.09 – 200 GeV	-3^{+7}_{-7}	-7^{+7}_{-7}	-9^{+5}_{-6}

Table 4.6: latitudinal position of minimum intensity $\theta_{\rm lat,min}$ (°) evaluated in the same energy range of Heber et al. (1996), using three alternative definition of *polar regions*.

[3] defined as $\theta_{\rm lat} = 90^\circ - \theta$.

Energy range	$\Delta_{\text{N-S}}$ (%)		
	θ_{20°	θ_{25°	θ_{30°
0.35 – 0.98 GeV	-8^{+6}_{-6}	-11^{+5}_{-4}	-13^{+4}_{-4}
0.76 – 2.09 GeV	-5^{+5}_{-6}	-6^{+5}_{-5}	-9^{+3}_{-3}
2.09 – 200 GeV	-1^{+3}_{-1}	-3^{+3}_{-3}	-4^{+2}_{-2}

Table 4.7: percent North-South asymmetry ($\Delta_{\text{N-S}}$) evaluated in the same energy range of Heber et al. (1996), using three alternative definition of *polar regions*.

Energy range	Δ_{max} (%)		
	θ_{20°	θ_{25°	θ_{30°
0.35 – 0.98 GeV	-34^{+5}_{-5}	-35^{+4}_{-4}	-36^{+4}_{-3}
0.76 – 2.09 GeV	-22^{+6}_{-7}	-23^{+5}_{-4}	-25^{+3}_{-3}
2.09 – 200 GeV	-8^{+4}_{-3}	-9^{+3}_{-3}	-10^{+2}_{-2}

Table 4.8: percentage difference between the maximum and the minimum intensity along the solar latitude (Δ_{max}) evaluated in the same energy range of Heber et al. (1996), using three alternative definition of *polar regions*.

For θ_{30°, i.e., assuming a modified polar magnetic-field for $\theta < 30^\circ$ and $\theta > 150^\circ$, we found a general agreement with Ulysses observations. The position of $\theta_{\text{lat,min}}$ is compatible between the errors with one observed in Ref. Heber et al. (1996), as well as the values of $\Delta_{\text{N-S}}$ and Δ_{max} (Bobik et al., 2012d). The HelMod code allows one to investigate the relevance of the treatment of the polar region magnetic-field with respect to the resulting modulation of GCR. Thus, the latitudinal normalized intensities were obtained excluding a few (small) regions nearby the poles. This was determined from reducing the latitudinal spatial phase-space admissible for *pseudo-particles* (see Ref. Bobik et al. (2012a)) - i.e., the latitudinal extension of GCR particles taken into account - to $1^\circ < \theta < 179^\circ$ ($\theta_{\text{R,1}}$), $2^\circ < \theta < 178^\circ$ ($\theta_{\text{R,2}}$) and $10^\circ < \theta < 170^\circ$ ($\theta_{\text{R,10}}$). The so obtained latitudinal gradients are compared with the full latitudinal extension, $\theta_{\text{R,0}}$ ($0^\circ < \theta < 180^\circ$), in Fig. 4.10. By an inspection of Fig. 4.10, one may lead to the conclusion that the GCR diffusion nearby the polar axis has a large impact to the latitudinal gradients in the inner heliosphere and, as a consequence, the relevance of IMF description in the polar regions in order to reproduce the observed modulated GCR spectra.

4.3 Drift Effects

There are evidences that particle with different charge sign does not propagate in the same way into the inner heliosphere, e.g. those from Ulysses spacecraft and PAMELA and will be discussed later in this Section. Although the overall modulation process is dominated by diffusion, results summarized in Sect. 4.2.1 remark that drift mechanisms are need in order to reproduce correctly the modulated data at Earth orbit. The magnetic drift act as a convective velocity which direction depends from the product Aq, where A is the IMF polarity defined in Sect. 1.2.1 and q is the particle charge in unit of electron charge (see Sect. 2.2.2); For this reason the introduction of

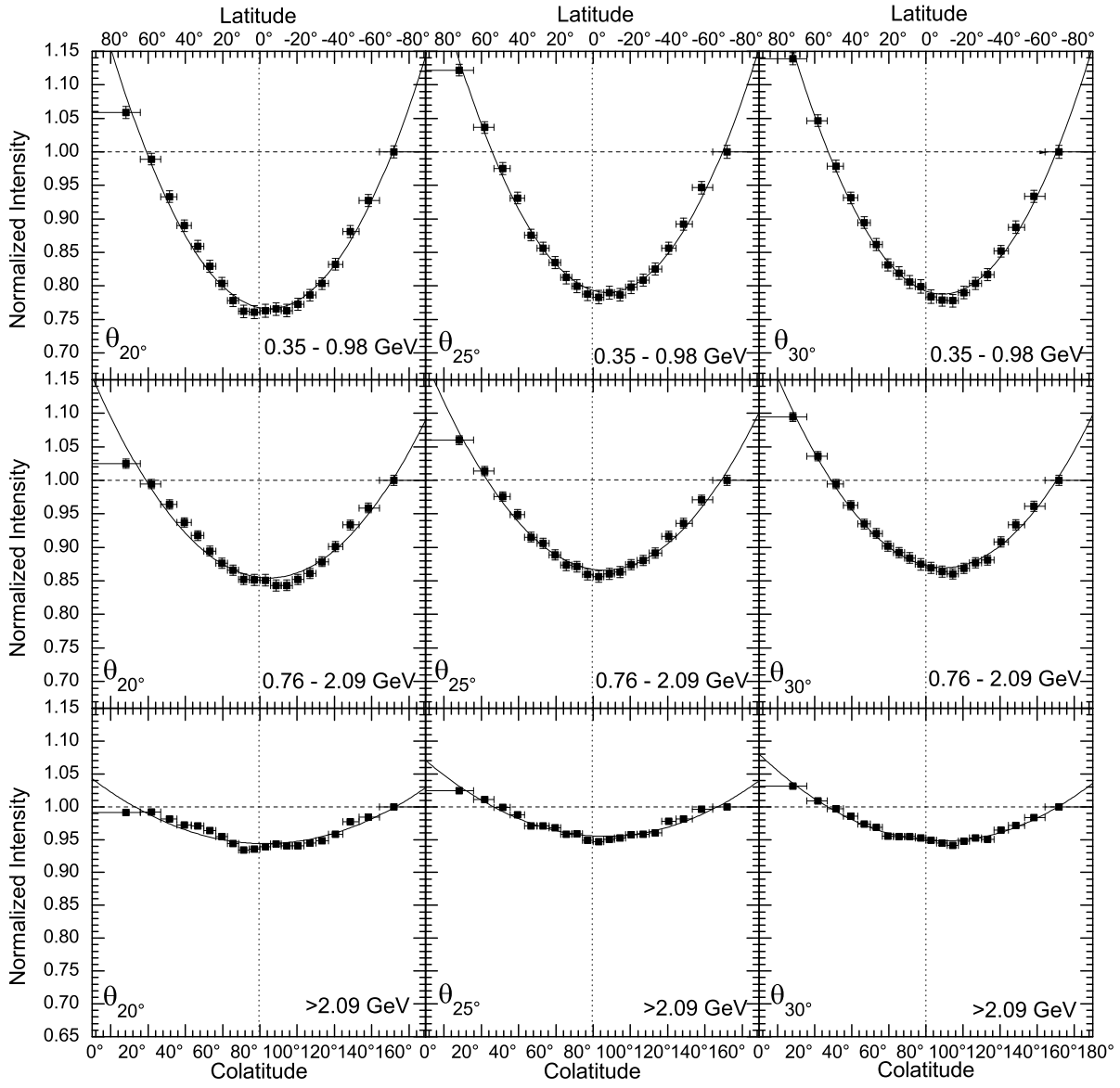

Figure 4.9: Latitudinal relative intensity at r =1AU, obtained at different solar co-latitude for proton with energy > 1.8 GeV using *polar regions* with ρ equal to 20°, 25° and 30°.

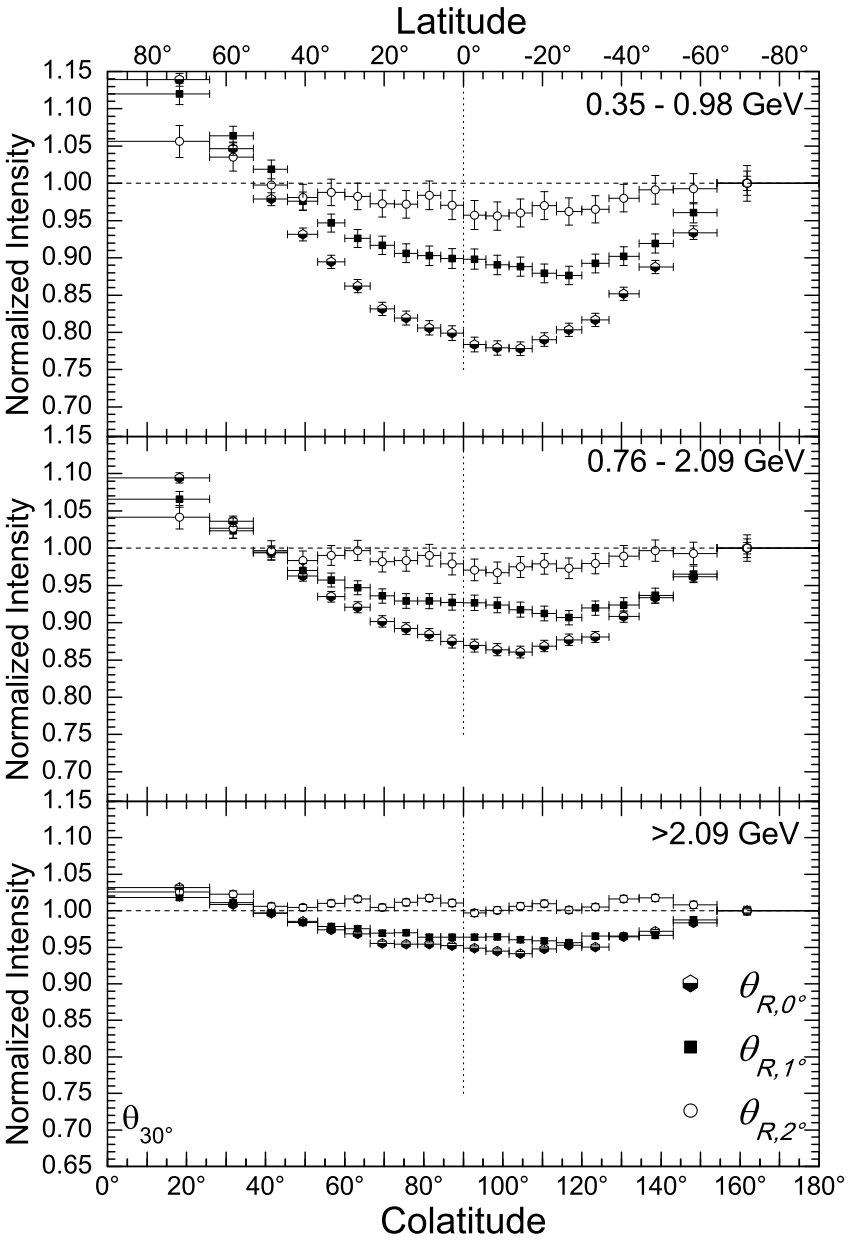

Figure 4.10: Latitudinal relative obtained for proton with energy > 1.8 GeV using Polar region with $\rho = 30°$ and κ equal to 1°,2° and 10°.

magnetic drift process makes the modulation model to be dependent from the particle species. In practice this means that the model allows one to describes the solar modulation of anti-particle and electron using hte same parameters tuned on proton data. This could not be done using analytical approximation like, e.g., the Force Field model where modulation potentials is different for each GCR species (Gleeson and Axford, 1968a).

With HelMod Code we are able to change arbitrary the IMF magnitude and the sign of particle charge, as well neglecting the drift effects for a qualitatively comparison. Test are done using the same seed for the random number generator. This allow us to compare the different configuration assuming same systematic error. In Figs. 4.11 and 4.12 we present modulated intensities at Earth orbit for a typical low activity solar condition. In this figures we inverted the IMF polarity, the sign of particle charge and we compare the results to the *no drift* solution. One can note that the drift process is sensible to the Aq product. Moreover $Aq > 0$ leads to a less pronounced modulation with respect $Aq < 0$ case. This justified ones to expect different effects on solar modulation, for different IMF polarity and Particle/Antiparticle.

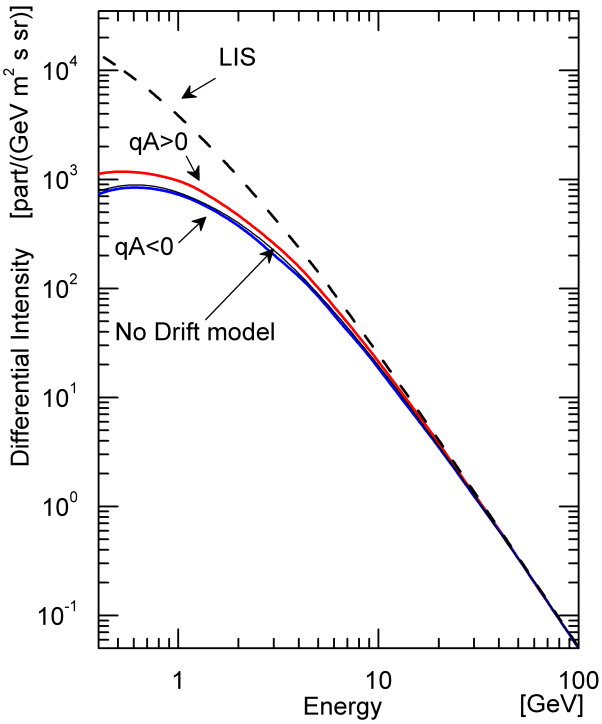

Figure 4.11: Proton differential intensity evaluated for a typical low solar activity period, changing the sign of A and of the particle charge q. The dash line is the LIS defined in Sect.4.1. The red line represent $qA > 0$ configurations, Blu line represent $qA < 0$ configurations. Finally the black solid line represent the reference "No drift" configuration.

4.3.1 Cosmic Rays Intensity Outside Ecliptic Plane

For many decades the Earth orbit was the only place accessible for GCR *in-situ* measurements. Voyager and Pioneer spacecraft launched in '70 explore the radial distribution found that the overall intensity of GCR increase with the distance from the Sun, leading to the idea that solar modulation

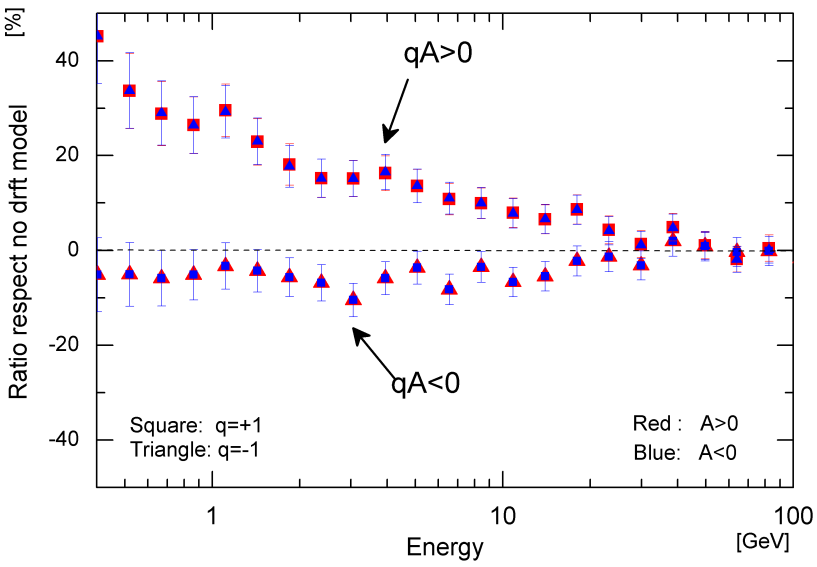

Figure 4.12: Proton differential intensity evaluated for a typical low solar activity period, changing the sign of A and of the particle charge q. The Red points represent $A > 0$ IMF, Blu points represent $A < 0$ configurations, Square point are obtained for $q = +1$ charge particles, while Triangle points are obtained with $q = -1$ charge particle. Finally the black dash line represent the reference "No drift" configuration.

is more effective in the inner heliosphere. Proton observation carry out by Ulysses spacecraft during his first *fast scan*, corresponding to a period with $A > 0$ IMF, show a nearly symmetric latitudinal gradient with the minimum near ecliptic plane, as already discussed in Sect. 4.2.2. The observations performed during the third Ulysses *fast scan*, from May to December 2007 corresponding to an IMF with $A < 0$, found almost zero Proton intensity latitudinal gradient (see, e.g. Heber et al., 2008; De Simone et al., 2011). Heber et al. (2008) estimate that the latitudinal gradient of 2.5 GV protons ($\sim$ 1.7 GeV) is consistent with zero, while De Simone et al. (2011) founds that for 1.6–1.8 GV Protons ($\sim$ 1 GeV) the latitudinal gradient during the same period is $(-0.024 \pm 0.005)\%$/degree. The same study on electron leads to opposite conclusion: Ferrando et al. (1996) concludes that, during the $A > 0$ *fast scan*, electron intensity do not show any sign of latitudinal dependence, at least up to 2.5 GV; in their analysis they results in a latitudinal gradient of 0.2%/degree$\pm$0.05%/degree for electrons.

In Fig. 4.14a we show the $\sim$ 1.7 GV Proton intensity measured by PAMELA (located at Earth orbit) and KET instrument on board the Ulysses spacecraft (red point) in function of time (De Simone et al., 2011) during the 3rd Ulysses *fast scan*. The data are normalized to the intensity measured when the spacecraft passed through ecliptic plane, i.e. the closer distance to Earth. To study the latitudinal variations the KET data should be corrected for the time variation using proton measurements at Earth. For the first Ulysses *fast scan* Heber et al. (1996) used the proton measurements from IMP–8 satellite. while for the 3rd *fast scan* Heber et al. (2008) used the carbon measurements by CRIS (Stone et al., 1998) spectrometer, on board the ACE satellite, while De Simone et al. (2011) used PAMELA protons intensity at the same time (see Fig. 4.14). In Fig. 4.14b

is showed the proton 1.7 GV KET intensity normalized to PAMELA.
In this work we compute the GCR intensity at the same time and spatial position of Ulysses spacecraft to reproduce their observations. We compare Ulysses results with our HelMod solution in the rigidity range 1.67–1.98 GV and with a frequency of one simulation every 27 day, i.e. a Carrigton Rotation. In Fig. 4.14a we use blue lines to indicate simulations at 1AU, i.e. PAMELA position, and with red for results at the Ulysses position indicated in Fig. 4.14c. The blue and red shadow represents the uncertainties of our model, accounting both statistical and systematic error presented in Sect. 3.2.5. In Fig. 4.14b we compare the KET/PAMELA proton rate with the same obtained from HelMod; the simulations are corrected to be ~ 1 at the time of closest approach. In this analysis we do not correct our results for the KET efficiency response as done by De Simone et al. (2011). Nevertheless Figs. 4.14 show good agreement of present model with the observed intensities allowing us to extend the results in Sect. 4.2.2 to a period of $A < 0$ IMF.

In this work we then consider either proton and electron intensities during the first and third Ulysses *fast scan* (i.e. $A > 0$ and $A < 0$ solar minimum periods). The computed intensities in Fig. 4.14, along the Ulysses orbit, are then divided by the intensities computed at the same time at Earth orbit and subsequently normalized to average intensity at solar South pole. For this analysis we compare our results with analysis of Heber et al. (2008) and De Simone et al. (2011), performed at 1.7 GV and 2.5 GV respectively, considering Protons with equivalent rigidity within 1.67–1.99 GV and 2.38–2.88 GV, while for electrons we consider the equivalent rigidity bin 1.62–2.09 GV and 2.09–2.69 GV. From inspection of Fig. 4.14 one can note that when $qA < 0$ the access of GCR particles is more symmetric with respect when $qA > 0$. This observations could be explained assuming effects related to particle charge interacting with the IMF polarity. We test this idea with HelMod code to evaluate the pure effects of magnetic drift process with different IMF polarities. In Fig. 4.15 we compare the normalized GCR intensity at Earth orbit for Proton with energy ~ 1.7 GeV obtained with the same solar condition but changing the IMF polarity ($A > 0$ Black point, $A < 0$ Red Point) compared with those obtained from the model not including drift effects. The GCR intensity are normalized to South Pole. The model not including the drift effects show a small presence of latitudinal gradient of GCR intensity, but it is not enough to reproduce Ulysses observation in 1995. The introduction of drift effects create two opposite picture, depending on IMF polarity: with $A > 0$ IMF the GCR intensity varies strongly with the latitude, as already presented in Sect. 4.2.2. On contrary, with $A < 0$ IMF there is no evidence of latitudinal distribution of GCR intensity, leading to a more uniform distribution. This enforce the idea that $A > 0$ IMF enhance the enter of Proton into the inner heliosphere passing through the poles, while $A < 0$ IMF enhance the Proton arriving from HCS region (see e.g. Figure 8 of Strauss et al., 2012a). Since the drift mechanism is related to the product qA, for electron we observe the opposite situation, with no special entry point of electrons over the poles for $A > 0$ IMF and a preferred electron transport toward higher latitudes when $A < 0$ that is in agreement with the results of (Ferrando et al., 1996) and Strauss et al. (2011).

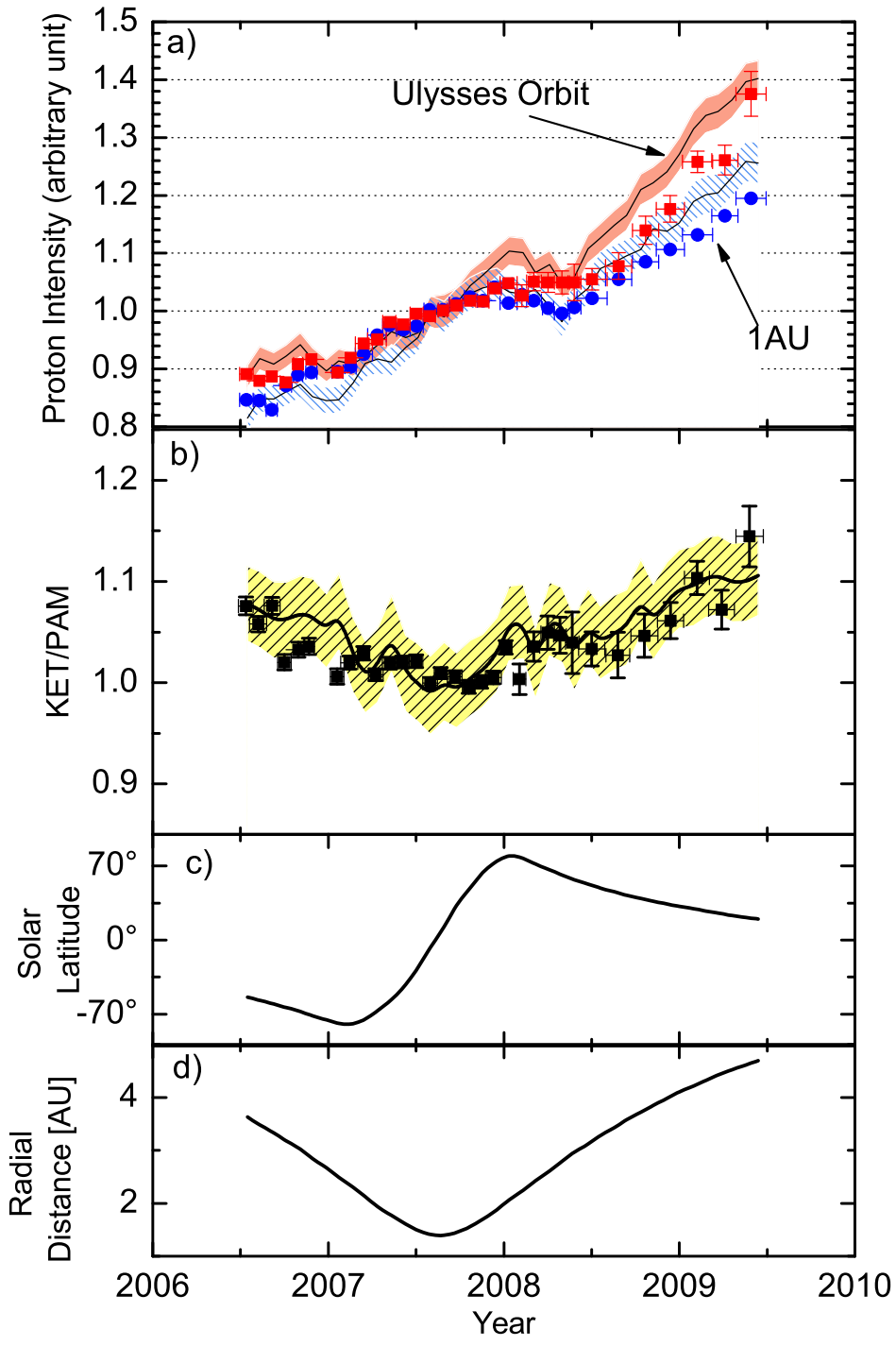

Figure 4.13: Panel (a): Comparison of HelMod results (blue and red shadow) with Ulysses (red square) and PAMELA (blue point) proton intensities at rigidity$\sim$ 1.7GV; the proton intensities are normalized to the value corresponding to the closest approach of Ulysses spacecraft to Earth orbit. Panel (b): Proton intensity rate between Ulysses (KET) and PAMELA (PAM), compared with the HelMod solution (light yellow shadow). The experimental data in panel (a) and (b) data are taken from De Simone et al. (2011). The HelMod intensity are evaluated at 1 AU and along the Ulysses orbit reported in panel (c) and (d).

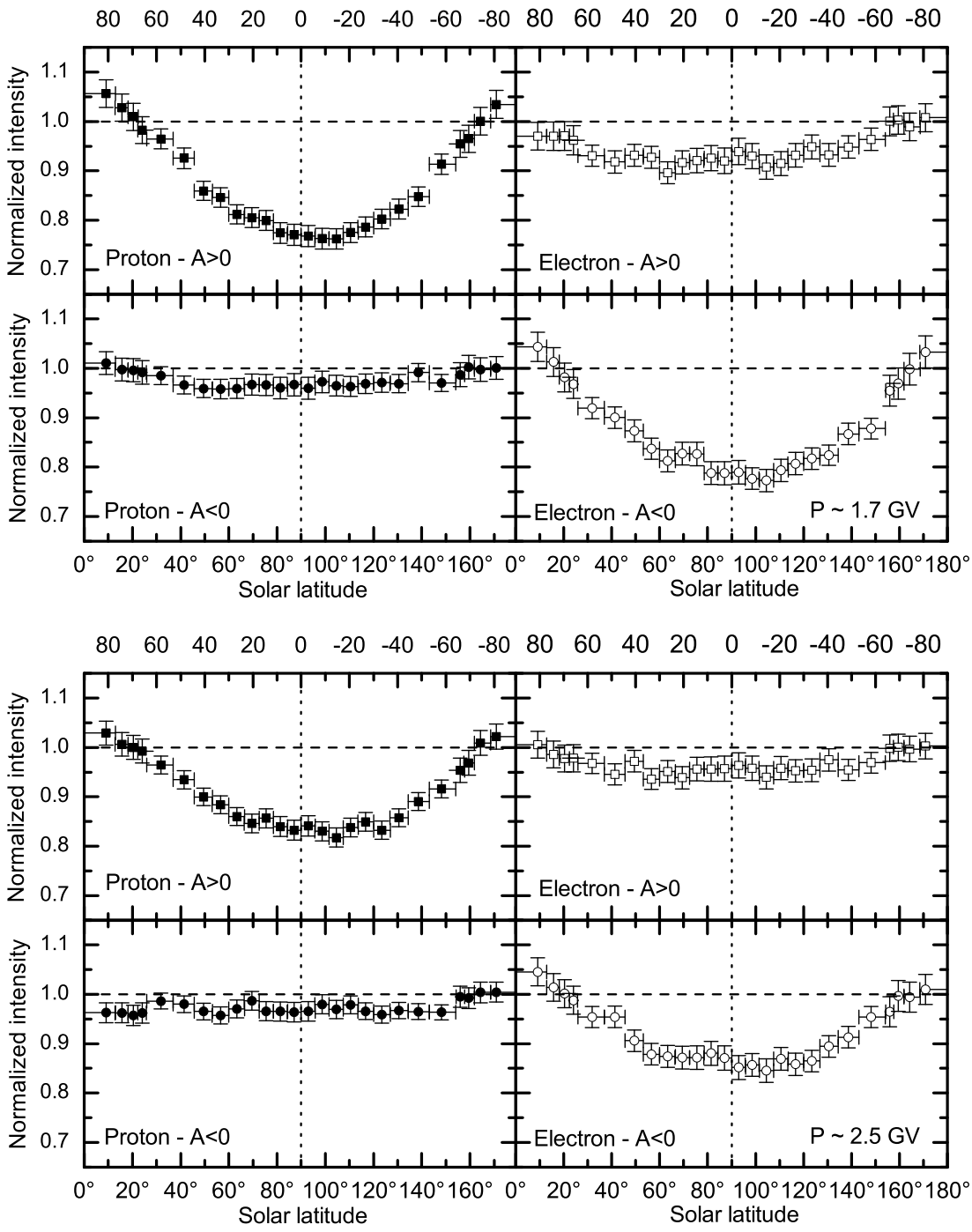

Figure 4.14: Latitudinal relative intensity along the Ulysses orbit, obtained at different solar co-latitude for proton and electron with particle rigidity 1.7 GV (top) and 2.5 GV (bottom). Intensity are divided by the solution at Earth orbit at the same time, then normalized to the average values at south pole. Solution with $A > 0$ IMF are evaluated during the Ulysses *fast scan* in 1995, while Solution with $A < 0$ IMF are evaluated during the Ulysses *fast scan* in 2007.

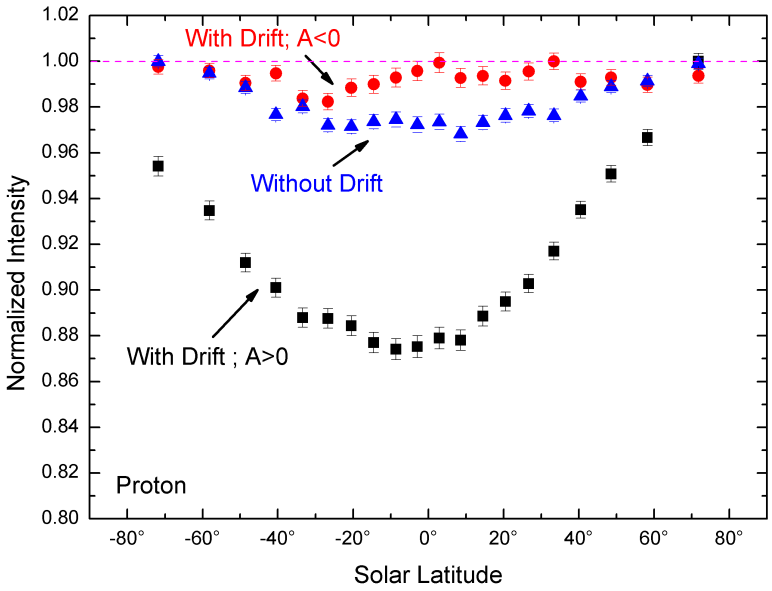

Figure 4.15: Normalized GCR intensity at Earth orbit for Proton with energy $\sim$ 1.7 GeV, the normalized GCR intensity presented are obtained with the same solar condition but changing the IMF polarity ($A > 0$ Black point, $A < 0$ Red Point) compared with those obtained from the model not including Drift effects. The GCR intensity are normalized to South Pole.

4.3.2 Positron Ratio

Ulysses observations remark how propagation of both protons and electrons is different at the same observation time. Since as we conclude in the latter Section this is due particle charge effects, one is justified to extend this remark also for positron and electrons. In this Section we apply the HelMod code to explore the effects of modulation on positron ratio. For this study we use the version 1.5 of the code, presented in Bobik et al. (2012a), that was optimized for GCR observed at Earth orbit only[4]. This Section has been taken from Della Torre et al. (2012a). The recent accurate measurements of cosmic positrons and electrons, performed by PAMELA (Adriani et al., 2009), show an anomalous positron excess at energies $>$ 10 GeV in comparison with the models of secondary production (see Zhang, L. and Cheng, K. S., 2001; Moskalenko and Strong, 1998). In the last years many papers discussing the nature of this excess have been published. Some of them suggest a dark matter signature (Yin et al., 2009); other authors invoke a primary production of electron/positron pairs by local astrophysical sources like Pulsars (Grasso et al., 2009). In this Section we do not discuss this cosmic ray positron fraction excess, since we focused on the energy interval $\leq$ 10 GeV where the same observations of GCR positron fraction made by PAMELA experiment are systematically below previous measurements, like e.g. AMS–1998 observations (Aguilar et al., 2007), as well as below the models of galactic secondary production. The LIS of electrons is mainly due to the primary component of particles diffusing in the galaxy.

[4] As discussed in Sect.4.3, version 2.0, presented in Sect. 3.2 improve this picture comparing data outside the ecliptic plane.

The LIS of positrons is, on the contrary, a secondary production due to GCR interactions with the interstellar medium. We used the model proposed by Zhang, L. and Cheng, K. S. (2001) (here expressed in unit of GeV^{-1} s^{-1} sr^{-1} m^{-2}) based on calculation by (Moskalenko and Strong, 1998):

$$\phi_{e^-} = \frac{1600 \cdot T^{-1.1}}{1 + 11 \cdot T^{0.9} + 1.92 \cdot T^{2.45}} \tag{4.11}$$

$$\phi_{e^+} = \frac{45000 \cdot T^{0.7}}{1 + 650 \cdot T^{2.3} + 1500 \cdot T^{4.2}} \tag{4.12}$$

We corrected the lower-right term in Eq. (4.11), in order to fit AMS–1998 observations at energy > 20 GeV, but we leave unmodified the low energy terms. Recent measurements of AMS–1998 and PAMELA have shown an excess in the cosmic ray positron fraction, which cannot be accounted for by the usual galactic production models. Here we include in the positron LIS an additional term like the one proposed by Grasso et al. (2009), that simulates the possible contribution of local Pulsars. This term helps to adapt LIS to observations at energy > 10 GeV, but does not affect modulated spectra at lower energy. The charge sign dependence of GCR propagation in the heliosphere is due to the particle drift term of the Parker equation. The fundamental parameter setting the direction of particle drift is qA, where q is the particle charge and A is a coefficient that accounts for the field polarity. We made a simulation of propagation of electrons and positrons during a solar minimum, reproducing the solar activity conditions occurred in June 1998, assuming both the solar field polarities. We found, in agreement with theory, that the flux for $qA < 0$ is systematically lower than the flux for $qA > 0$ (see e.g. Potgieter and Langner, 2004; Alanko-Huotari et al., 2007b, for similar results). Results are shown in Fig. 4.16, where positron and electron spectra are compared. In Fig. 4.17 we show the modulated cosmic ray positron fraction above 1 GeV: for $A > 0$ modulated positron fraction is comparable with the LIS positron fraction; while for $A < 0$ a reduction of the cosmic ray positron fraction is expected and it is even more relevant going to low kinetic energy.

We selected two experiments in similar solar conditions but opposite magnetic field polarity. AMS–1998 (Alcaraz et al., 2000; Aguilar et al., 2007) operated on board of the Space Shuttle in June 1998, at the end of a solar minimum occurred during a period with $A > 0$. PAMELA (Adriani et al., 2009) is a space born experiment working since July 2006. Published data have been taken between 2006 and December 2008, therefore during the last long solar minimum with $A < 0$. We mainly reproduce, within the error bars, the AMS–1998 observations for electrons and positrons (see figs. 4.18 and 4.19). We find a good agreement between simulations and observations also for the cosmic ray positron fraction. Despite the large solar modulation of both electrons and positrons, for AMS–1998 the modulated ratio is very close to the interstellar ratio (see Fig. 4.20), as obtained in previous results for $A > 0$. We used the same model of propagation to reproduce PAMELA observations for the period 2006/08. Due to the wide time interval covered by the analysis, we performed several simulations using parameters related to the full period of observations and taking their average value. In Fig. 4.20 it is shown that, for PAMELA, the modulated cosmic ray positron fraction is lower than the interstellar one, as expected. We conclude that observations can be well explained with a polarity-dependent effect of solar modulation, due to the particle drift.

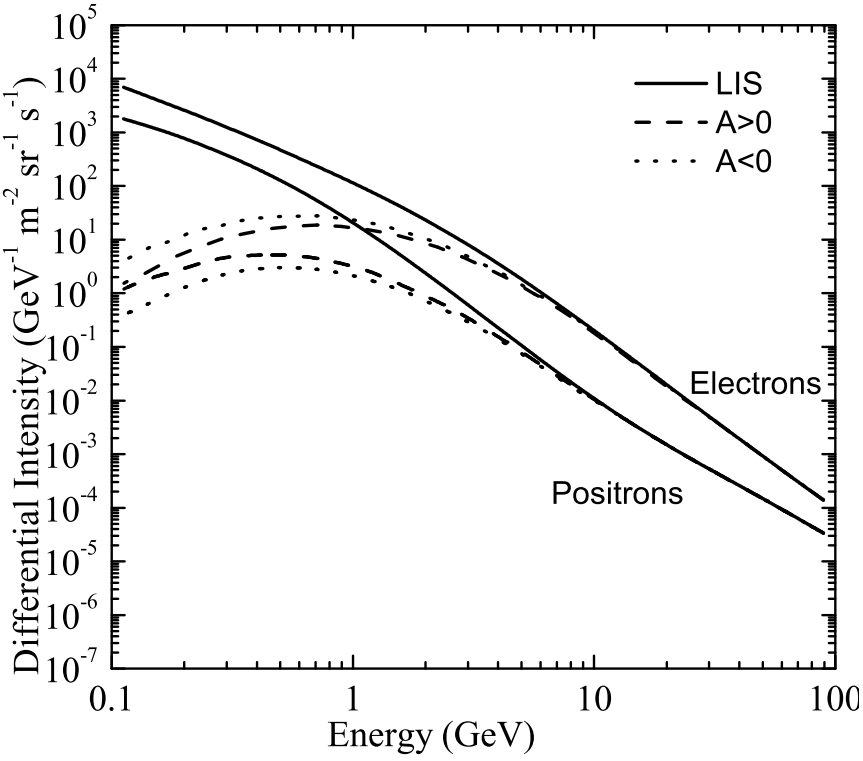

Figure 4.16: e^- and e^+ modulation for a period corresponding to a typical solar minimum (we used the conditions occurred in June 1998) with both magnetic field polarities. Short-dotted lines at high energy represent the two LIS due to only Eq. (4.11) and (4.12). (figure from Della Torre et al., 2012a)

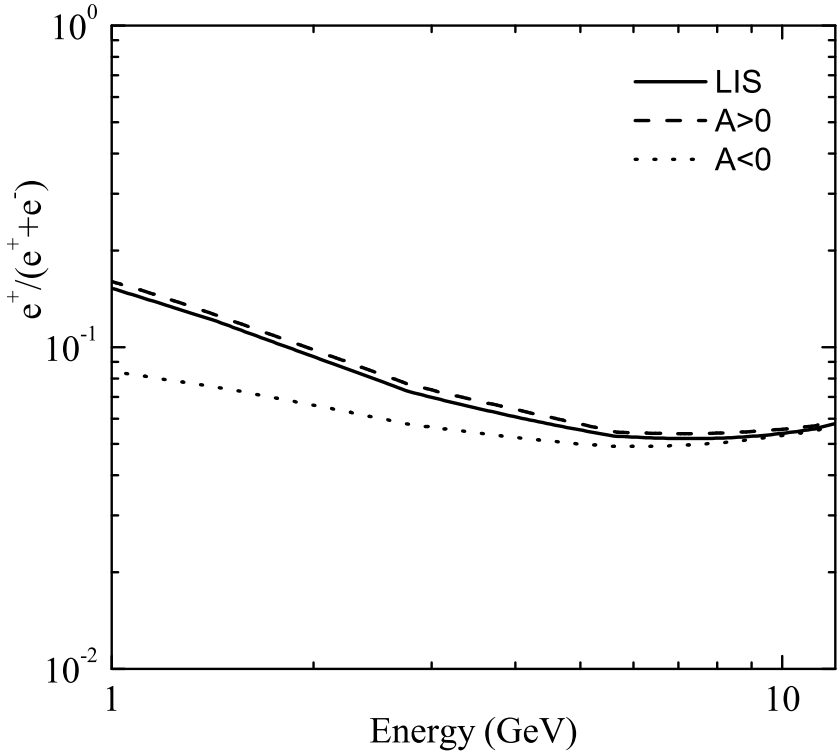

Figure 4.17: The cosmic ray positron fraction evaluated for a period corresponding to a typical solar minimum with both magnetic field polarities. We used the results shown in Fig. 4.16. (figure from Della Torre et al., 2012a)

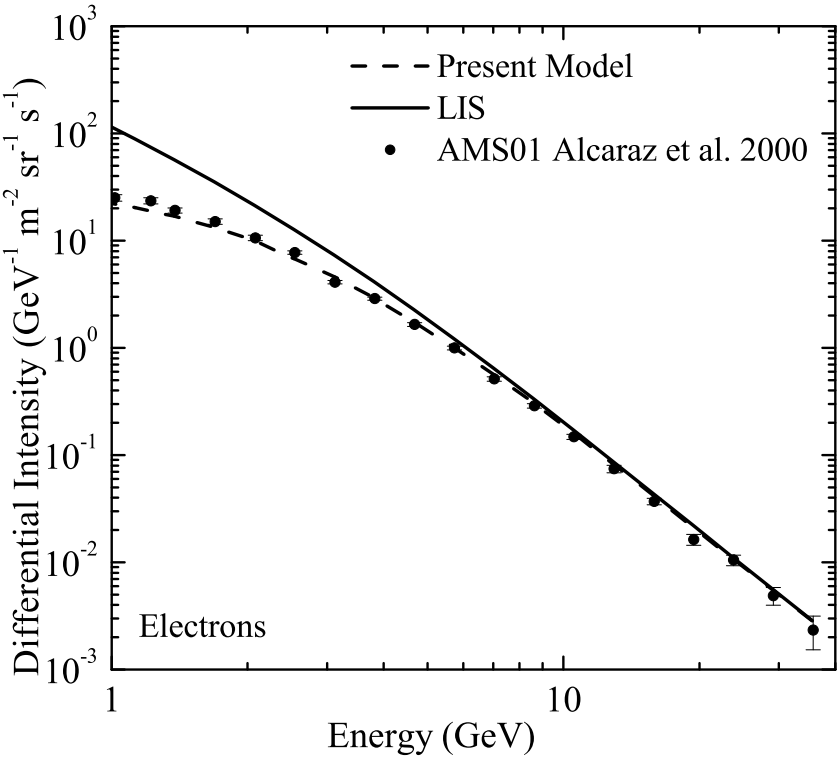

Figure 4.18: Simulated electron spectrum for AMS–1998 mission. (figure from Della Torre et al., 2012a)

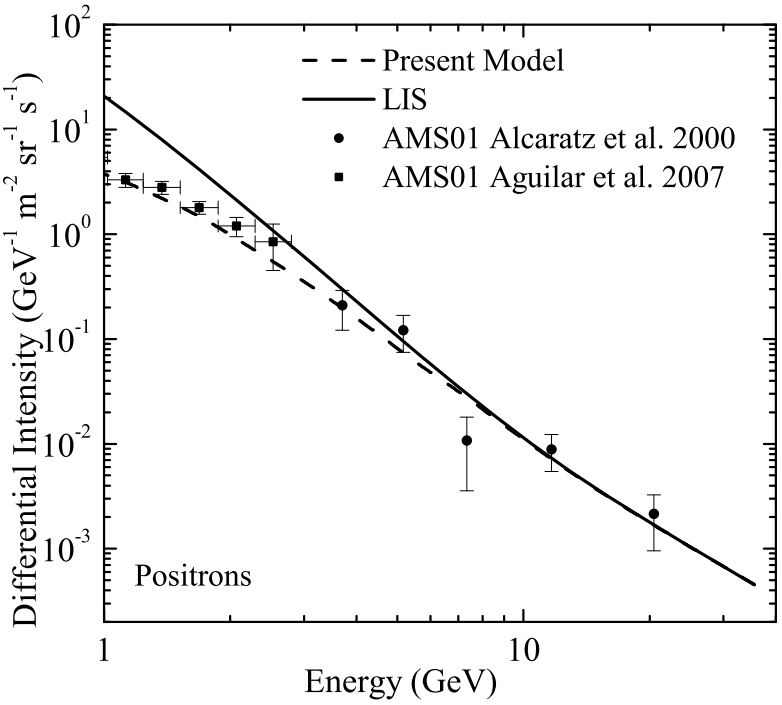

Figure 4.19: Simulated positron spectrum for AMS–1998 mission. (figure from Della Torre et al., 2012a)

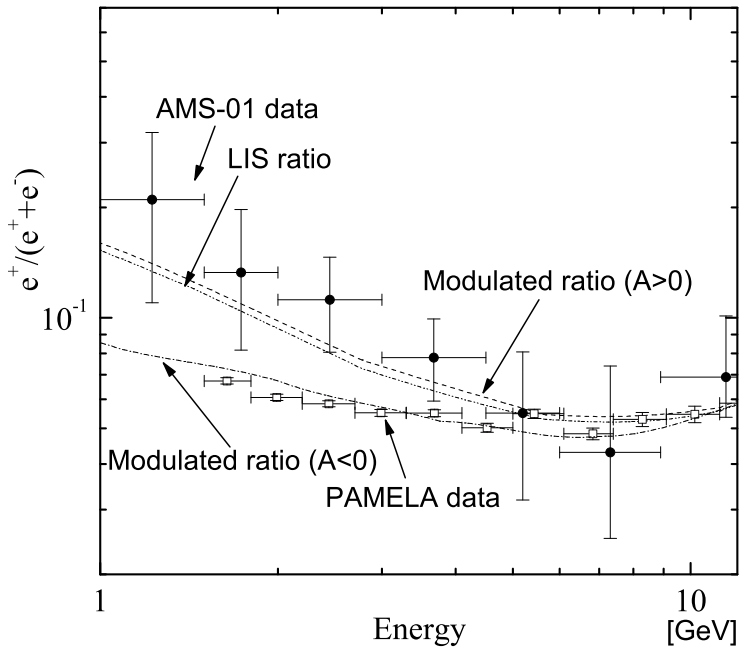

Figure 4.20: Simulated cosmic ray positron fraction for AMS–1998 and PAMELA–2006/08. (figure from Della Torre et al., 2012a)

	R_{TS} (AU)	solar latitude (deg)
Voyager 1	94.0	+ 34.3
Voyager 2	83.7	-27.5

Table 4.9: Voyager crossings of Termination Shock.

4.4 Heliospherical Size and Diffusion Parameter

In the past years the position of the Termination Shock was estimated through the observations of Voyager 1 and Voyager 2 spacecrafts(see Stone et al., 2005, 2008, and Table 4.9). In addition several authors (see Whang and Burlaga, 2000; Whang et al., 2004) suggest that the size of the heliosphere should change with the solar activity, following a quasi-periodic feature, roughly anti-correlated with the SSN. Following these results we evaluated the effect of stretched and compressed heliosphere on the Cosmic Ray intensities at the Earth introducing a dependence of the diffusion parameter on the heliosphere size. We note that for this preliminary study we used HelMod Code version 1.5 (described in Bobik et al., 2012a) and the results presented in this Section has been taken from Bobik et al. (2012c). We defined a new diffusion parameter K_0^*, introducing the parameter $R_c(r_{tm}, P)$ sensitive to the position of the Termination Shock:

$$K_0^*(R_{\rm tm}) = R_c(R_{\rm tm}, P) K_0(100 \text{ AU}) \tag{4.13}$$

where $K_0(100$ AU$)$ is the diffusion parameter defined in Eq. (3.32) and

$$R_c(R_{\rm tm}, P) = 1 + f(P)\left[\frac{R_{\rm tm} - 100}{99}\right] \tag{4.14}$$

$R_c(r_{tm}, P)$ allows to modify the value of the diffusion parameter adapting it to a different volume of the heliosphere, determined by $R_{\rm tm} \cdot R_c(R_{\rm tm}, P)$ is fully effective below a rigidity limit P_1. We also defined a transition function $f(P)$:

$$f(P) = \begin{cases} 0, & \text{for } P \geq P_2 \\ (P_2 - P)/(P_2 - P_1), & \text{for } P_1 < P < P_2 \\ 1, & \text{for } P \leq P_2 \end{cases} \tag{4.15}$$

For rigidity higher than P_2, the dependence on $R_{\rm tm}$ can be neglected. Here the diffusion parameter is still defined for an heliosphere dimension of 100 AU. In fact in Bobik et al. (2012a) we shown how within 2.3%, the simulated differential intensities for spherical heliospheres with radii of 80, 90, and 110 AU are compatible with that with a radius of 100 AU. The dependence on the heliosphere radius $R_{\rm tm}$ is then effective at rigidity lower than P_2. Using the novel diffusion parameter $K_0^*(R_{\rm tm}, P)$ we simulated the modulated spectra, for different values of $R_{\rm tm}$, P_1 and P_2, extending the modulated spectra down to a lower rigidity.

We compare our simulated spectra with proton data extended down to a kinetic energy of 200 MeV. Here we present results obtained using the following rigidity parameters: $P_2 = P_1 = 1.0GV$. We used the Local Interstellar Spectrum (LIS) described in Sect. 4.1 and compared it with the

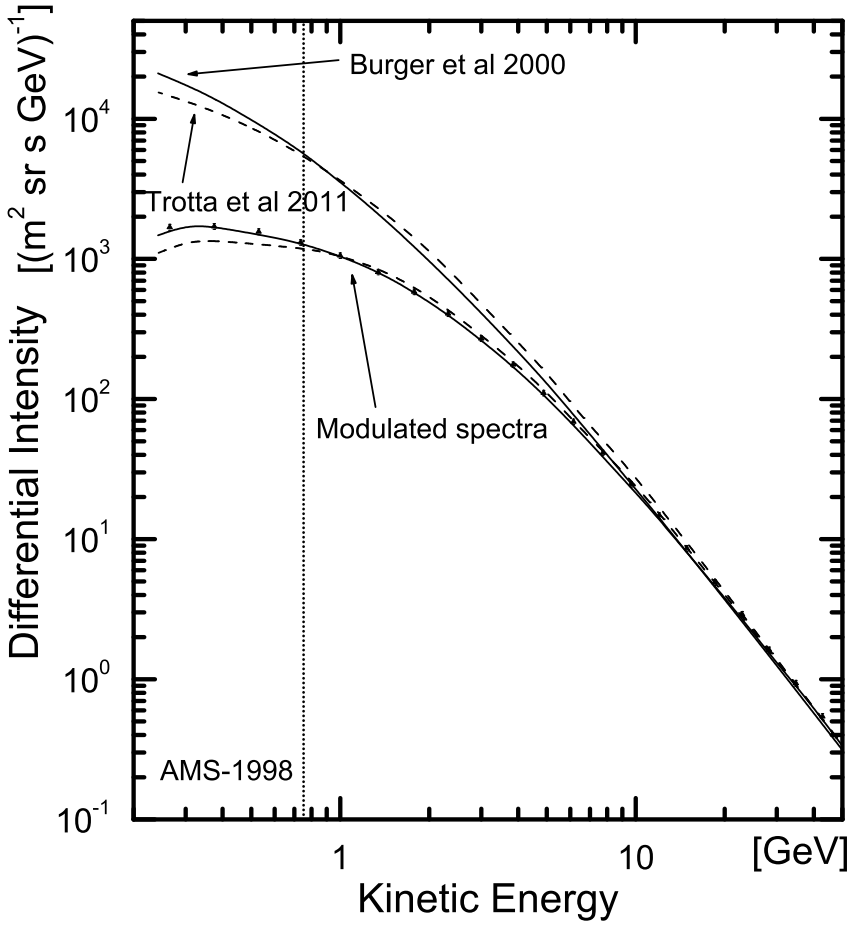

Figure 4.21: Modulated proton spectra and comparison with AMS–1998 data (Aguilar et al., 2002). LIS are taken form Burger et al. (2000) and GALPROP (Trotta et al., 2011). The vertical dotted line represents the lower limit of the sensitivity of the NM. Above this limit the two LIS are not significantly different. (figure from Bobik et al., 2012c)

LIS form GALPROP (Trotta et al., 2011). In Fig. 4.21 the results compared with AMS–1998 data (Aguilar et al., 2002) are shown, assuming $R_{\rm tm} = 120$ AU, as discussed later on. We estimated the best value of $R_{\rm tm}$, looking at the RMS differences ($\eta_{\rm rms}$) with experimental data using Eqs. (4.6) and (4.7). For each experimental spectrum we got the best values of $R_{\rm tm}$ shown in Table 4.10 together with the minimum value of $\eta_{\rm rms}$. Data from BESS flights are given in Shikaze et al. (2007), data from AMS–1998 are given in Aguilar et al. (2002). In Fig. 4.22 modulated spectra, obtained using values of $R_{\rm tm}^{best}$ reported in Table 4.10, are shown in comparison with BESS experimental data. Modulated spectrum compared with AMS–1998 data has been shown in Fig. 4.21. We did not use data measured by PAMELA 2006/08 because published spectra start from 400 MeV, while our analysis is more sensitive below this limit. In Table 4.10 we report the interval of values of $R_{\rm tm}$ where $\eta_{\rm rms}$ does not change by more than $\sim (2-3)\%$ from its minimum value, reported in the last column. This variation represents the uncertainty of the computation itself, estimated with the procedure described in Sect. 3.2.5. Results are shown in Fig. 4.23 in comparison with models (Whang et al., 2004) and Voyager measurements (Stone et al., 2005, 2008). Our results are not in contradiction with Voyager observations and models of TS distance as a function of solar activity.

	$R_{\rm tm}^{best}$ (AU)	$R_{\rm tm}^{min}$ (AU)	$R_{\rm tm}^{max}$ (AU)	$\eta_{\rm rms}$ (%)
BESS–1997	115	100	130	7.05
AMS–1998	120	110	135	4.86
BESS–1999	120	110	130	3.35
BESS–2000	140	125	150	10.00
BESS–2002	105	95	115	11.78

Table 4.10: Best values of $R_{\rm tm}^{best}$, its minimum and maximum values, and RMS differences between simulations and experimental data.

More over, as shown in Fig. 4.21 and 4.22, modulated spectra succeed to fit observing data, in particular during periods of low solar activity. For more accurate results we need more accurate experimental data. Current error bars are of the order of 5% or even larger. Moreover systematic deviations are present looking at different data sets at energy above (20–30) GV, where spectra are not affected by solar modulation. In addition current observation data, taken on board of stratospheric balloons or space orbiters, may be contaminated at low energy by secondaries produced inside the Earth magnetosphere. A LIS spectrum with a slightly different shape could be also preferred to fit better low energy data. Finally a refinement of our model could be requested, starting with a slightly different values of P_2 and P_1, in order to smooth the ripple present in some spectrum. In the future a model with a non spherical Heliosphere can be also developed.

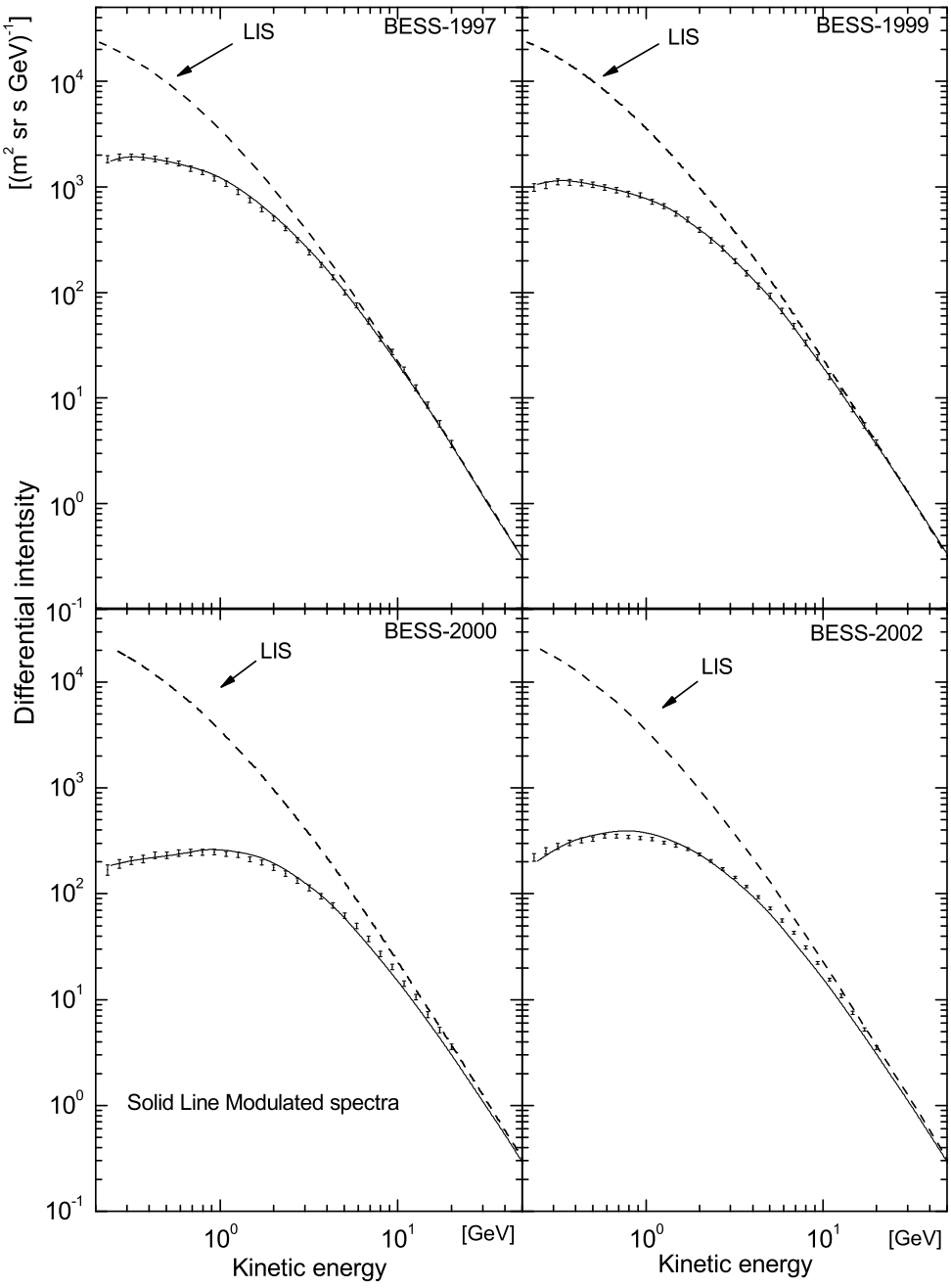

Figure 4.22: Modulated proton spectra and comparison with BESS-1997, BESS-1999, BESS- 2000, BESS-2002 observing data (Shikaze et al., 2007). (figure from Bobik et al., 2012c)

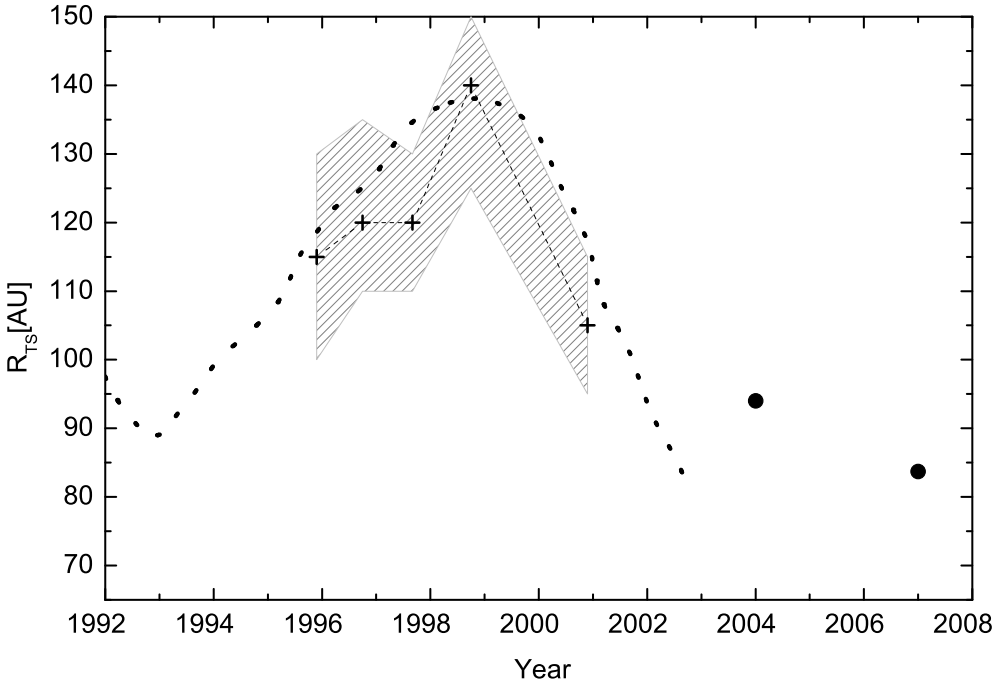

Figure 4.23: $R_{\rm tm}$ best value for the several experiments (crosses) in comparison with Voyager data (dots, Stone et al., 2005, 2008) and models (dashed line, Whang et al., 2004). The shadow represents the region between the minimum and maximum value, as reported in Table 4.10. (figure from Bobik et al., 2012c)

4.5 Conclusion and Remarks

In this work we focus our attention on the GCR Solar Modulation by mean of the HelMod Monte Carlo Model. This model is based on the Parker Equation, that consider the charged particles propagation through the interplanetary medium as a diffusive process with the contribute of convection, adiabatic energy loss and magnetic drift mechanism. This partial differential transport equation was solved with a Monte Carlo technique that use an equivalent set of ordinary stochastic differential equations to describe the time evolution of pseudo-particle inside the heliosphere. With the contribution of all simulated pseudo-particle trajectories we can obtain the modulated intensities, e.g. at Earth orbit, once known an external local interstellar spectrum. The model depends on various parameters like the diffusion coefficient, solar wind speed, heliospheric current sheet tilt angle, interplanetary magnetic field magnitude at Earth and his global polarity. As interplanetary magnetic field we propose an hybrid description that includes the Standard Parker field, experimentally established as the most convenient to reproduce the IMF on ecliptic plane, as well as a polar correction that increases the IMF magnitude at poles. The magnitude of this correction is related to a perturbation parameter δ_m which is explored in this work. We compare HelMod solutions with Proton GCR data observed during solar cycle 23 by AMS, BESS and PAMELA, with a separate analysis for periods of high and low solar activity. We found a set of parameters that is able to describe with good accuracy the observed intensities, leading to the conclusion that the present code is suitable to reproduce the whole solar cycle condition. We successfully applied

the model (optimized for protons down to 1GV) also for electrons and positrons. From the study of positron ratio at low energies we arrived to the conclusion that this is strongly affected by solar modulation during periods with $A < 0$ IMF (like those observed by PAMELA). A solar modulation model including drift effects is then able to explain the inconsistency between, e.g., AMS–01 and PAMELA (which collected data in periods of opposite IMF polarity), of observed positron ratio at energies $< 10 - 20$ GeV. Furthermore, the present model is able to reproduce data outside the ecliptic plane observed by Ulysses spacecraft. Although diffusion is the dominant process in the GCR propagation, current analysis remarks how drift mechanism have to be included in the solution in order to reproduce the large scale effects over a complete *hale cycle* ($\sim$ 22 years). Moreover the observation carried out by Ulysses through the latitudinal heliosphere during two successive solar activity minimum, could be again explained with the inclusion into the model of drift mechanism. So that observation at the same time of intensity of, e.g., protons and electrons, at different solar latitude position, reveal the presence of a latitudinal gradient from solar poles down to solar equator for period with $qA > 0$ and a more isotropic distribution during periods with $qA < 0$. This indication reveals as in the first case low energy particle reaching the inner heliosphere suffer a preferred transport toward higher latitudes, while in the latter case there are no special entry points at poles. Finally in this work we also explore how particle with rigidity lower than 1 GV suffer the Solar modulation in function of the extension of the heliosphere. We found that including into the model also a dynamic dimension of the heliosphere could reproduce low energy data observed at Earth. The time variation of heliosphere dimension, as obtained from the model as the one able to reproduce data, is in agreement with theoretical model.

Appendix A

Diffusion Tensor in Spherical Coordinates

The matrix (2.3) represent the diffusion tensor with with one axis parallel to the average magnetic field, i.e. $\mathbf{B} = B_0\mathbf{e}_1$, and the other two perpendicular to this; in a generic frame coordinate the diffusion tensor is written as:

$$K_{ik} = \begin{vmatrix} K_{rr} & K_{r\theta} & K_{r\phi} \\ K_{\theta r} & K_{\theta\theta} & K_{\theta\phi} \\ K_{\phi r} & K_{\phi\theta} & K_{\phi\phi} \end{vmatrix} \tag{A.1}$$

In a spherical coordinate system (r, θ, ϕ) the magnetic field vector $\mathbf{B}$ could be defined using the two angles Ψ and ζ defined in follow way (see Fig. A.1):

Ψ is the angle between $\mathbf{B}$ and the plane r,θ,

ζ is the angle between the ascending node of the vector $\mathbf{B}$ on the plane r,θ and the $\mathbf{e}_r$ unit vector.

So that,

$$\mathbf{B} = B[\cos(\Psi)\cos(\zeta)e_r + \cos(\Psi)\sin(\zeta)e_\theta - \sin(\Psi)e_\phi] \tag{A.2}$$

where $B = \sqrt{B_r^2 + B_\theta^2 + B_\phi^2}$ is the magnitude of the magnetic field $\mathbf{B}$, and e_r, e_θ, e_ϕ are the radial, polar and azimuthal unit vectors respectively.
From Eq. (A.2) is possible to get the angles Ψ and ζ as functions of the $\mathbf{B}$ components:

$$\sin(\Psi) = -\frac{B_\phi}{\sqrt{B_r^2 + B_\theta^2 + B_\phi^2}}; \qquad \cos(\Psi) = \frac{\sqrt{B_r^2 + B_\theta^2}}{\sqrt{B_r^2 + B_\theta^2 + B_\phi^2}}; \tag{A.3}$$

$$\sin(\zeta) = \frac{B_\theta}{\sqrt{B_r^2 + B_\theta^2}}; \qquad \cos(\zeta) = \frac{B_r}{\sqrt{B_r^2 + B_\theta^2}}; \tag{A.4}$$

$$\tan(\Psi) = \frac{-B_\phi}{\sqrt{B_r^2 + B_\theta^2}}; \qquad \tan(\zeta) = \frac{B_\theta}{B_r}. \tag{A.5}$$

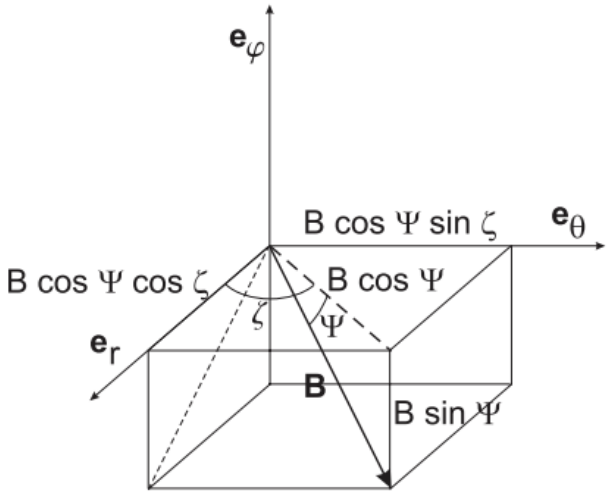

Figure A.1: Magnetic field vector projection in a spherical coordinates frame (figure from Burger et al., 2008).

From Eq. (A.2) it is also possible to get the expressions for the unit vectors in the frame with one axis parallel to the magnetic field (Engelbrecht, 2008).

$$\mathbf{e}_{||} = \cos(\Psi)\cos(\zeta)\mathbf{e}_r + \cos(\Psi)\sin(\zeta)\mathbf{e}_\theta - \sin(\Psi)\mathbf{e}_\phi \tag{A.6}$$

$$\mathbf{e}_{\perp_2} = -\sin(\zeta)\mathbf{e}_r + \cos(\zeta)\mathbf{e}_\theta \tag{A.7}$$

$$\mathbf{e}_{\perp_3} = \sin(\Psi)\cos(\zeta)\mathbf{e}_r + \sin(\Psi)\sin(\zeta)\mathbf{e}_\theta + \cos(\Psi)\mathbf{e}_\phi \tag{A.8}$$

The coordinates changing matrix M is than:

$$K_{ij}^S = MK_{ij}M^T; \qquad M = \begin{vmatrix} \cos(\zeta)\cos(\Psi) & -\sin(\zeta) & \cos(\zeta)\sin(\Psi) \\ \sin(\zeta)\cos(\Psi) & \cos(\zeta) & \sin(\zeta)\sin(\Psi) \\ -\sin(\Psi) & 0 & \cos(\Psi) \end{vmatrix} \tag{A.9}$$

that applied to the matrix (2.3) gives the Diffusion tensor representation in heliocentric spherical coordinates:

$$K_{rr} = K_{\perp,2}\,\sin^2\zeta + \cos^2\zeta\,(K_{||}\,\cos^2\Psi + K_{\perp,3}\,\sin^2\Psi), \tag{A.10}$$

$$K_{\theta\theta} = K_{\perp,2}\,\cos^2\zeta + \sin^2\zeta\,(K_{||}\,\cos^2\Psi + K_{\perp,3}\,\sin^2\Psi), \tag{A.11}$$

$$K_{\phi\phi} = K_{||}\sin^2\Psi + K_{\perp,3}\cos^2\Psi, \tag{A.12}$$

$$K_{r\theta} = -K_A\sin\Psi + \sin\zeta\cos\zeta\,(K_{||}\cos^2\Psi + K_{\perp,3}\,\sin^2\Psi - K_{\perp,2}), \tag{A.13}$$

$$K_{\theta r} = K_A\sin\Psi + \sin\zeta\cos\zeta\,(K_{||}\cos^2\Psi + K_{\perp,3}\,\sin^2\Psi - K_{\perp,2}), \tag{A.14}$$

$$K_{r\phi} = -K_A\cos\Psi\sin\zeta - (K_{||} - K_{\perp 3})\sin\Psi\cos\Psi\cos\zeta, \tag{A.15}$$

$$K_{\phi r} = K_A\cos\Psi\sin\zeta - (K_{||} - K_{\perp 3})\sin\Psi\cos\Psi\cos\zeta, \tag{A.16}$$

$$K_{\theta\phi} = K_A\cos\Psi\cos\zeta - (K_{||} - K_{\perp 3})\sin\Psi\cos\Psi\sin\zeta, \tag{A.17}$$

$$K_{\phi\theta} = -K_A\cos\Psi\cos\zeta - (K_{||} - K_{\perp 3})\sin\Psi\cos\Psi\sin\zeta. \tag{A.18}$$

Appendix B

Stochastic Differential Equations

B.1 General Treatment

The Monte Carlo resolution is based on the equivalence, as reported e.g. in Gardiner (1985), between a Fokker-Planck equation in the follow standard form:

$$\partial_t F = -\sum_i \partial_i [A_i(\mathbf{x},t)F] + \frac{1}{2}\sum_{i,j}\partial_i\partial_j\{[\tilde{\mathbf{D}}(\mathbf{x},t)]_{ij}F\} \tag{B.1}$$

and a generic Stochastic Differential Equation (SDE) as:

$$d\mathbf{x} = \mathbf{A}(\mathbf{x},t)dt + \tilde{\mathbf{L}}(\mathbf{x},t)d\mathbf{W}(t) \tag{B.2}$$

where $d\mathbf{W}(t)$ is a Wiener Process Gardiner (1985), $\mathbf{x}$ is a point in the phase-space, F is a probability distribution function associated to $\mathbf{x}$ (that usually is a particle distribution in the phase-space, e.g. Achterberg and Krulls (1992)), and finally $\tilde{\mathbf{D}} = \tilde{\mathbf{L}}\tilde{\mathbf{L}}^{\mathbf{T}}$. We can related $\mathbf{A}(\mathbf{x},t)dt$ to advective (e.g. drift or convection) process, while $\tilde{\mathbf{L}}(\mathbf{x},t)d\mathbf{W}(t)$ is the diffusion process. Achterberg and Krulls (1992) states that the equation (B.2) simulates a random walk, and a realization of this random walk obtained by (numerical) integration of the SDE can be thought of as a typical particle orbit in phase space. The distribution F can be obtained at any given time as the density of *pseudo-particles* in phase space by averaging over many realizations of the SDE.

We apply this approach to Cosmic Rays transport in the heliosphere, that is generally described by Parker's Equation for the particle's density U:

$$\frac{\partial U}{\partial t} = \nabla\cdot(\mathbf{K^S}\cdot\nabla U - \mathbf{V_{sw}}U - \mathbf{v_d}U) + \frac{1}{3}(\nabla\cdot\mathbf{V_{sw}})\frac{\partial}{\partial T}(\alpha_{\rm rel}TU) \tag{B.3}$$

In heliocentric spherical coordinates this could be rewritten as:

$$\begin{aligned}
\frac{\partial U}{\partial t} &= \frac{1}{r^2}\frac{\partial}{\partial r}\left(r^2 K_{rr}\frac{\partial}{\partial r}U + rK_{r\theta}\frac{\partial}{\partial \theta}U + \frac{r}{\sin\theta}K_{r\phi}\frac{\partial}{\partial \phi}U\right) + \\
&+\frac{1}{r\sin\theta}\frac{\partial}{\partial \theta}\left(\sin\theta K_{\theta r}\frac{\partial}{\partial r}U + \frac{\sin\theta}{r}K_{\theta\theta}\frac{\partial}{\partial \theta}U + \frac{1}{r}K_{\theta\phi}\frac{\partial}{\partial \phi}U\right) + \\
&+\frac{1}{r\sin\theta}\frac{\partial}{\partial \phi}\left(K_{\phi r}\frac{\partial}{\partial r}U + \frac{1}{r}K_{\phi\theta}\frac{\partial}{\partial \theta}U + \frac{1}{r\sin\theta}K_{\phi\phi}\frac{\partial}{\partial \phi}U\right) + \\
&-\frac{1}{r^2}\frac{\partial r^2 V_r U}{\partial r} - \frac{1}{r\sin\theta}\frac{\partial \sin\theta V_\theta U}{\partial \theta} - \frac{1}{r\sin\theta}\frac{\partial V_\phi U}{\partial \phi} + \\
&-\frac{1}{r^2}\frac{\partial r^2 v_{d_r} U}{\partial r} - \frac{1}{r\sin\theta}\frac{\partial \sin\theta v_{d_\theta} U}{\partial \theta} - \frac{1}{r\sin\theta}\frac{\partial v_{d_\phi} U}{\partial \phi} + \\
&+\frac{1}{3}\left(\frac{1}{r^2}\frac{\partial r^2 V_r}{\partial r} + \frac{1}{r\sin\theta}\frac{\partial \sin\theta V_\theta}{\partial \theta} + \frac{1}{r\sin\theta}\frac{\partial V_\phi}{\partial \phi}\right)\frac{\partial}{\partial T}(\alpha_{\rm rel} T U)
\end{aligned} \tag{B.4}$$

where to simplify the reader we denoted as $K_{ij}^S = K_{ij}$. Then Eq. (B.4) had to be rewritten into the standard form of Eq. (B.1) with $\mathbf{q} = \{r, \mu, \phi, T\}$: this could be done by replacing $\theta = \arccos(\mu)$, $\partial\theta = -(1-\mu^2)^{-0.5}\partial\mu$ and defining $F = Ur^2$;

$$\begin{aligned}
\frac{\partial F}{\partial t} &= -\frac{\partial}{\partial r}\left[\frac{F}{r^2}\frac{\partial}{\partial r}(r^2 K_{rr})\right] - \frac{\partial}{\partial r}\left[-F\frac{\partial}{\partial \mu}\left(\frac{K_{r\mu}\sqrt{1-\mu^2}}{r}\right)\right] - \frac{\partial}{\partial r}\left[\frac{F}{r^2}\frac{\partial}{\partial \phi}\left(\frac{rK_{r\mu}}{\sqrt{1-\mu^2}}\right)\right] \\
&-\frac{\partial}{\partial r}\left[F(V_{\rm sw} + v_{d_r})\right] - \frac{\partial}{\partial \mu}\left[-\frac{F}{r^2}\frac{\partial}{\partial r}\left(rK_{\mu r}\sqrt{1-\mu^2}\right)\right] - \frac{\partial}{\partial \mu}\left[F\frac{\partial}{\partial \mu}\left(K_{\mu\mu}\frac{1-\mu^2}{r^2}\right)\right] \\
&-\frac{\partial}{\partial \mu}\left[-\frac{F}{r^2}\frac{\partial}{\partial \phi}\left(K_{\mu\phi}\right)\right] - \frac{\partial}{\partial \mu}\left[-\frac{F}{r}v_{d_\mu}\sqrt{1-\mu^2}\right] - \frac{\partial}{\partial \phi}\left[\frac{F}{r^2}\frac{\partial}{\partial r}\left(\frac{rK_{\phi r}}{\sqrt{1-\mu^2}}\right)\right] \\
&-\frac{\partial}{\partial \phi}\left[\frac{F}{r^2}\frac{\partial}{\partial \mu}\left(-K_{\phi\mu}\right)\right] - \frac{\partial}{\partial \phi}\left[\frac{F}{r^2}\frac{\partial}{\partial \phi}\left(\frac{K_{\phi\phi}}{1-\mu^2}\right)\right] - \frac{\partial}{\partial \phi}\left[\frac{F}{r}\frac{v_{d_\phi}}{\sqrt{1-\mu^2}}\right] \\
&-\frac{\partial}{\partial T}\left[-F\frac{\alpha_{\rm rel}T}{3r^2}\frac{\partial V_{\rm sw} r^2}{\partial r}\right] + \frac{1}{2}\frac{\partial}{\partial r}\frac{\partial}{\partial r}[2K_{rr}F] + \frac{1}{2}\frac{\partial}{\partial r}\frac{\partial}{\partial \mu}\left[-\frac{2K_{r\mu}\sqrt{1-\mu^2}}{r}F\right] \\
&+\frac{1}{2}\frac{\partial}{\partial r}\frac{\partial}{\partial \phi}\left[\frac{2K_{r\phi}}{r\sqrt{1-\mu^2}}F\right] + \frac{1}{2}\frac{\partial}{\partial \mu}\frac{\partial}{\partial r}\left[-\frac{2K_{\mu r}\sqrt{1-\mu^2}}{r}F\right] \\
&+\frac{1}{2}\frac{\partial}{\partial \mu}\frac{\partial}{\partial \mu}\left[\frac{2K_{\mu\mu}(1-\mu^2)}{r^2}F\right] + \frac{1}{2}\frac{\partial}{\partial \mu}\frac{\partial}{\partial \phi}\left[\frac{-2K_{\mu\phi}}{r^2}F\right] + \frac{1}{2}\frac{\partial}{\partial \phi}\frac{\partial}{\partial r}\left[\frac{2K_{\phi r}}{r\sqrt{1-\mu^2}}F\right] \\
&+\frac{1}{2}\frac{\partial}{\partial \phi}\frac{\partial}{\partial \mu}\left[\frac{-2K_{\phi\mu}}{r^2}F\right] + \frac{1}{2}\frac{\partial}{\partial \phi}\frac{\partial}{\partial \phi}\left[\frac{2K_{\phi\phi}}{r^2(1-\mu^2)}F\right].
\end{aligned} \tag{B.5}$$

Where we additionally supposed a pure radial outward Solar Wind.
From a comparison between Eq. (B.1) and Eq. (B.5) is possible define:

$$\mathbf{A} = \begin{bmatrix}
\frac{1}{r^2}\frac{\partial}{\partial r}(r^2 K_{rr}) - \frac{\partial}{\partial \mu}\left(\frac{K_{r\mu}\sqrt{1-\mu^2}}{r}\right) + \frac{1}{r^2}\frac{\partial}{\partial \phi}\left(\frac{rK_{r\theta}}{\sqrt{1-\mu^2}}\right) + V_{\rm sw} + v_{d_r} \\
-\frac{1}{r^2}\frac{\partial}{\partial r}\left(rK_{\mu r}\sqrt{1-\mu^2}\right) + \frac{\partial}{\partial \mu}\left(K_{\mu\mu}\frac{1-\mu^2}{r^2}\right) - \frac{1}{r^2}\frac{\partial}{\partial \phi}\left(K_{\mu\phi}\right) - \frac{1}{r}v_{d_\mu}\sqrt{1-\mu^2} \\
\frac{1}{r^2}\frac{\partial}{\partial r}\left(\frac{rK_{\phi r}}{\sqrt{1-\mu^2}}\right) + \frac{\partial}{\partial \mu}\left(-K_{\phi\mu}\right) + \frac{1}{r^2}\frac{\partial}{\partial \phi}\left(\frac{K_{\phi\phi}}{1-\mu^2}\right) + \frac{1}{r}\frac{v_{d_\phi}}{\sqrt{1-\mu^2}} \\
-\frac{\alpha_{\rm rel}T}{3r^2}\frac{\partial V_{\rm sw} r^2}{\partial r}
\end{bmatrix} \tag{B.6}$$

$$\tilde{\mathbf{D}} = \begin{bmatrix} 2K_{rr} & -\frac{2K_{r\mu}\sqrt{1-\mu^2}}{r} & \frac{2K_{r\phi}}{r\sqrt{1-\mu^2}} \\ -\frac{2K_{\mu r}\sqrt{1-\mu^2}}{r} & \frac{2K_{\mu\mu}(1-\mu^2)}{r^2} & \frac{-2K_{\mu\phi}}{r^2} \\ \frac{2K_{\phi r}}{r\sqrt{1-\mu^2}} & \frac{-2K_{\phi\mu}}{r^2} & \frac{2K_{\phi\phi}}{r^2(1-\mu^2)} \end{bmatrix} \tag{B.7}$$

Note that, since the second order acceleration mechanism are not considered, the 4$^{\text{rd}}$ column and row – that are related to $q_4 = T$ – are omitted (Pei et al., 2010b);

B.2 2-D Approximation

To reduce the Eq. (B.2) to a 2-D (radius and polar angle) approximation we simply neglect the ϕ component in the parameter $\mathbf{A}$ and $\tilde{\mathbf{D}}$ defined by Eqs. (B.6)–(B.7)

Because matrix $\tilde{\mathbf{D}}$ is symmetric (i.e. $K_{\mu r} = K_{r\mu}$) and positive definite is possible to obtain a matrix $\tilde{\mathbf{L}}$ that satisfy the relation $\tilde{\mathbf{D}} = \tilde{\mathbf{L}}\tilde{\mathbf{L}}^{\mathbf{T}}$ (Gardiner, 1985). In this work we apply the simplest way so solve the system

$$\tilde{\mathbf{D}} = \begin{bmatrix} a & c \\ c & b \end{bmatrix} = \begin{bmatrix} v & w \\ x & y \end{bmatrix} \begin{bmatrix} v & x \\ w & y \end{bmatrix} = \tilde{\mathbf{L}}\tilde{\mathbf{L}}^{\mathbf{T}} \tag{B.8}$$

choosing the solution where $w = 0$:

$$\tilde{\mathbf{L}} = \begin{bmatrix} (2K_{rr})^{1/2} & 0 \\ \frac{-2K_{r\mu}}{r}\left(\frac{1-\mu^2}{2K_{rr}}\right)^{1/2} & \frac{1}{r}\left((1-\mu^2)\frac{K_{\mu\mu}K_{rr}-K_{r\mu}^2}{0.5K_{rr}}\right)^{1/2} \end{bmatrix} \tag{B.9}$$

note that this procedure is equivalent to use a the Cholesky–Banachiewicz or Cholesky–Crout algorithms. As pointed out in appendix B of Pei et al. (2010b), the matrix $\tilde{\mathbf{L}}$ is not unique, in fact, e.g., Bobik et al. (2012a) use a different solution with $x = 0$. The two solutions are stochastic equivalent (see e.g. Kopp et al., 2012) but Eq. B.9 allow to simpler formulas in the computation algorithm. The SDE implemented in Helmod 2.0 are then:

$$dr = \frac{1}{r^2}\frac{\partial}{\partial r}(r^2 K_{rr})dt - \frac{\partial}{\partial \mu}\left(\frac{K_{r\mu}\sqrt{1-\mu^2}}{r}\right)dt + (V_{\text{sw}} + v_{d_r})dt + (2K_{rr})^{1/2}R_r\sqrt{dt} \tag{B.10}$$

$$\begin{aligned} d\mu = &-\frac{1}{r^2}\frac{\partial}{\partial r}\left(rK_{\mu r}\sqrt{1-\mu^2}\right)dt + \frac{\partial}{\partial \mu}\left(K_{\mu\mu}\frac{1-\mu^2}{r^2}\right)dt - \frac{1}{r}v_{d_\mu}\sqrt{1-\mu^2}dt \\ &+ \frac{-2K_{r\mu}}{r}\left(\frac{1-\mu^2}{2K_{rr}}\right)^{1/2}R_r\sqrt{dt} + \frac{1}{r}\left((1-\mu^2)\frac{K_{\mu\mu}K_{rr}-K_{r\mu}^2}{0.5K_{rr}}\right)^{1/2}R_\mu\sqrt{dt} \end{aligned} \tag{B.11}$$

$$dT = -\frac{\alpha_{\text{rel}}T}{3r^2}\frac{\partial V_{\text{sw}}r^2}{\partial r}dt \tag{B.12}$$

B.3 Random Numbers Probability Distribution

The Monte Carlo technique require the use of random numbers. Usually computer architecture provides a default pseudo-random numbers ξ with a uniform generation probability $g(\xi)$ in a

defined interval $[a, b]$.

$$g(\xi) = \begin{cases} 0 & \text{for } \xi < 0 \text{ or } \xi > 1 \\ 1 & \text{otherwise} \end{cases} \tag{B.13}$$

In general it is possible use the variable ξ, to calculate a new random number T distributed with a generic probability distribution $p(T)$. Since the probability distribution $p(T)$ is, by definition within the range $[a, b]$, normalized to 1:

$$\int_a^b f(T)dT = 1, \tag{B.14}$$

we need a procedure that generate a sequence of T values with the requirement that in each subrange Ω is

$$P\{T_k \in \Omega\} = \int_\Omega p(T)dT \leq 1 \tag{B.15}$$

that, for small range $b - a = dx$, is equivalent to

$$P\{T_k \in \Omega\} = p(T)dT. \tag{B.16}$$

The relation between the uniform generation probability $g(\xi)$ and a generic probability distribution $p(T)$ gives to a differential equation (cap 3.1 pag. 36–37 of Kalos and Whitlock, 2009),

$$g(\xi) \left| \frac{d\xi}{dT} \right| = p(T), \tag{B.17}$$

which solution contains all the possible transformation between the two variables ξ and T. Usually, in practical application, is easier get the probability distribution once chosen the transformation function between ξ and T. For example if we consider a random number that is uniform in logarithmic scale, the transformation is:

$$T = 10^{\log_{10} T_{min} + \xi(\log_{10} T_{max} - \log_{10} T_{min})} = Tmin \cdot \left(\frac{T_{max}}{T_{min}} \right)^{\xi}, \tag{B.18}$$

or equivalently,

$$\xi = \frac{\log_{10} T - \log_{10} T_{min}}{\log_{10} T_{max} - \log_{10} T_{min}}. \tag{B.19}$$

Solving Eq. (B.17) is possible to get the probability distribution:

$$p(T) = \left| \frac{d\xi}{dT} \right| g(\xi) = \left| \frac{1}{T} \log_{10}^{-1} \left(\frac{T_{max}}{T_{min}} \right) \right| \tag{B.20}$$

An other example could be presented using the transformation function:

$$T = \frac{T_{min}}{\xi} \rightarrow p(T) = \left| \frac{T_{min}}{T^2} \right|. \tag{B.21}$$

Both example presented here increase the statistic precision at low energy, decreasing the probability to generate high energy pseudo-particles, but experience on simulations shown that Eq. (B.18)

allow to better results since better balance the low and high energy generation, which are respectively the modulated part of the spectrum and energy range used to normalize the modulated spectra to LIS.

Appendix C

Additional Energy Loss in the Heliosphere

As described in Sect. 2.2.3, we improve our model taking into account also the additional energy losses experienced by Cosmic Rays during the propagation in Heliosphere. In the case of protons (or nuclei) these energy losses can be neglected, while for electrons this assumption is no more valid, due to their small mass. In the following Sections we describe several processes producing energy losses in Cosmic Rays. For a better look into this study see Brianza (2011); Rozza (2011). The description presented in this Section follow the approach close to Bobik et al. (2011a).

C.1 Collision

Electrons moving in a region containing gas or plasma lost energy by means of Plasma ionization and excitation processes. This happens when electrons move across the interstellar medium as well as inside the solar cavity. Since Plasma is already Ionized, during a collision only excitation process could realize. Inside electron plasma could take place some collective phenomena called Plasma Excitation where all particles moves together as one, called plasma oscillation. Plasma Excitation energy losses are proportional to the logarithm of the electron energy and, in the case of neutral plasma (i.e. ion density equal to electron density, $n_{ion} \sim n_e$), can be described by the following relation (Gould, 1975):

$$\left.\frac{dT}{dt}\right|_{coll} = -\frac{3}{4}\sigma_T c(mc^2)n_e\Big[\ln\Big(\frac{T}{mc^2}\Big) + 2\ln\Big(\frac{mc^2}{h\nu_{pl}}\Big)\Big] \tag{C.1}$$

where T is the energy of electrons, n_e is the atoms density in the ISM (or in the Heliosphere), $\sigma_T = \dfrac{e^4}{6\pi\epsilon_0^2 m^2 c^4}$ is the cross Section of the process, and $\nu_{pl} = \dfrac{e}{2\pi}\sqrt{\dfrac{n_e}{\epsilon_0 m}}$ is the plasma frequency.

C.2 Bremsstrahlung

Bremsstrahlung energy loss is due to acceleration (or actually deceleration) of electrons interacting with charged particles. When a charged particle is able to pass through the Coulomb shield of

the atom than it is able to interact with the electric field of the nuclei. In this case the incident particle experience a strong deceleration with consequent photon emission (the Bremsstrahlung radiation). In the heliosphere the interplanetary medium is supposed to be completely ionized and so a relativistic Bremsstrahlung, in which the impact parameter is of the same order of magnitude of nuclear scale, could be experienced by electrons.

It is proportional to the energy of the particle T and, in the case of neutral plasma with generic density n_{pl}, could be represented by (Blumenthal and Gould, 1970):

$$\left.\frac{dT}{dt}\right|_{brems} = -\frac{3}{8\pi}\sigma_T c \alpha_{FS} T n_{pl} 2.42 \left(4 \ln \frac{2T}{mc^2} - \frac{4}{3}\right) \tag{C.2}$$

where σ_T is the Thompson cross Section, c is the speed of light, α_{FS} is the fine-structure constant.

C.3 Synchrotron

Synchrotron radiation forms when a charged particle moves in a magnetic field; due to Lorentz interaction the particle do a circular path emitting electromagnetic radiation. The energy loss is proportional to T^2 and could parametrize as (Longair, 1994):

$$\left.\frac{dT}{dt}\right|_{sync} = -2\, c\, \sigma_T\, U_{mag}\, \beta^2\, \gamma_{rel}^2\, \sin^2 \theta_{obs} \tag{C.3}$$

where $U_{mag} = \frac{B^2}{2\mu_0}\left[\frac{eV}{m^3}\right]$ is the magnetic field density, $\gamma_{rel} = \frac{T}{mc^2}$ is the Lorentz factor and finally θ_{obs} is the angle between the direction of the particle and line of view of the observer. In the case of ultra-relativistic particle and integrating over the all θ_{obs} directions, the Synchrotron energy loss become:

$$\left.\frac{dT}{dt}\right|_{sync} = -\frac{4}{3} c\, \sigma_T\, U_{mag}\, \gamma_{rel}^2 \tag{C.4}$$

C.4 Inverse-Compton

The Inverse-Compton energy loss is due to the interaction of ultra-relativistic electrons with the soft background radiation. This process could be described by two cases: Thomson approximation or Klein-Nishina regime. Thomson approximation is valid at low energies. In this case the Compton cross Section is used, and the energy loss rate is proportional to T^2. Klein-Nishina is an extreme case where both the energy of the photons and of the particles are very high (e.g. $\frac{4\varepsilon\gamma}{m_e c^2} \gg 1$, where ε is the photon energy, γ is the Lorentz relativistic factor, and $m_e c^2$ is the rest mass of the particle).

Defining $\xi = \frac{\gamma k_b T}{m_e c^2}$ (with k_b Boltzmann constant) the Inverse-Compton energy loss in presence of a black body radiation is (Delahaye et al., 2010):

$$-\left.\frac{dT}{dt}\right|_{IC} = \begin{cases} \frac{4}{3}\sigma_T c U_{ph}\left[\left(\frac{T}{mc^2}\right)^2 - 1\right] & \xi < 3.8\cdot 10^{-4} \\ 10^{-45}\frac{T^2(k_bT)^4}{\xi} e^{\sum_{i=0}^{6} c_i (\ln\xi)^i} & 3.8\cdot 10^{-4} \le \xi \le 1.8\cdot 10^{3} \\ \frac{\sigma_T}{16}\frac{(m_e c k_b T)^2}{\hbar^3}\ [\ln(4\xi) - 1.9805] & \xi > 1.8\cdot 10^{3} \end{cases} \tag{C.5}$$

where $c_i = \{74.77, -0.1953, -0.0997, 0.004352, 0.0003546, -0.0000301\}$ and U_{ph} is the photon energy density.

C.5 Energy Loss in the Heliosphere

The heliosphere dynamics is strongly related to the Sun activity. While in the intergalactic medium it is possible to account for average quantities, in the solar cavity we need to evaluate them locally, as a function of the distance from the Sun. The plasma density measured at $r_0 = 1$ AU is $n_{pl}(1\text{AU}) \approx 8-9$ protons/cm^3. Using the continuity equation it is possible to estimate the plasma density in the Heliosphere at every distance from the Sun:

$$n_{pl} = n_{pl}(1\text{AU})\left(\frac{r_0}{r}\right)^2. \tag{C.6}$$

Moreover, assuming that the electromagnetic emission of the Sun has a black body behavior, we can estimate the photon density inside the Heliosphere:

$$U_{ph} = \frac{L_\theta}{4\pi c}\left(\frac{r_0}{r}\right)^2 \tag{C.7}$$

where $L_\theta = 3.846\cdot 10^{26}$ W.

As IMF we used a modified Parker field, according to Eq. (1.14), that enhanced the magnitude of IMF in the polar regions. A comparison among the several energy loss processes inside the Heliosphere at 1 AU is shown in Fig. C.1. We found that Inverse-Compton is the dominant process, due to the large quantity of photons emitted by the Sun.

We estimated the importance of these energy loss processes inside the Heliosphere, in comparison with the adiabatic energy losses. We used our Monte Carlo simulation code of the Heliosphere (described in Sect. 3) and adapted it to take into account these processes. We first estimated the average time of permanence of GCR leptons inside the Heliosphere, considering only particles reaching the Earth. From the time spent in the Heliosphere by these particles, we estimated the total energy loss due to the Inverse-Compton process (ΔT_{IC}), neglecting other losses. We compared ΔT_{IC} with the total energy lost by the same particles in the Heliosphere. We estimated the adiabatic energy loss (ΔT_{FF}) by using the Force Field approach described in Sect. 2.3(Gleeson and Axford, 1968a). Using a typical modulation potential occurring in periods of medium solar activity ($\Phi = 550$ MV), we estimated an adiabatic energy loss $\Delta T_{FF} = 0.55$ GeV, roughly constant at all energies. In Table C.5 we compare the two energy losses. The Inverse-Compton one is always several order of magnitude lower than the total energy loss. At energies around 10 GeV the Inverse-Compton energy loss is 0.19% of the adiabatic one. This confirm that also for leptons

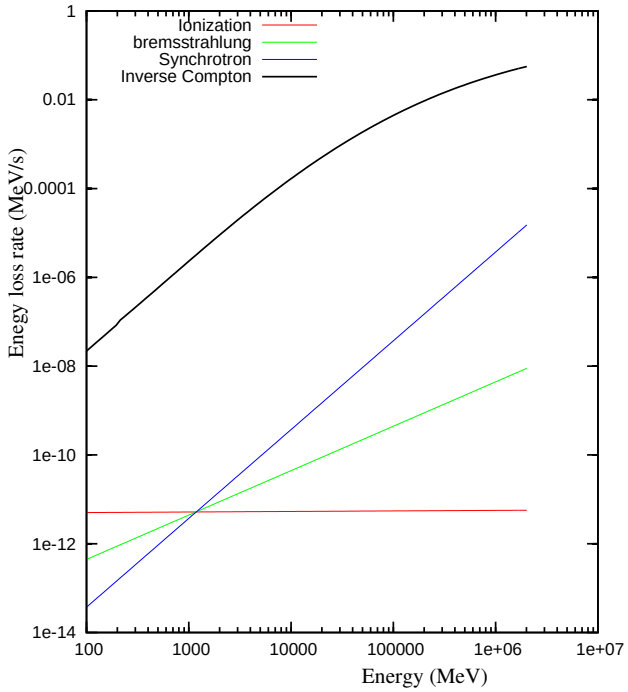

Figure C.1: Energy loss rate of electrons inside the heliosphere at 1 AU, which is due to several processes. (figure from Bobik et al., 2011a)

the adiabatic process is dominant within the heliosphere (Bobik et al., 2011a).

T_0 (GeV)	ΔT_{IC} (GeV) $\times 10^{-3}$	$\Delta T_{IC}/T_0$ %	ΔT_{FF} (GeV)	$\Delta T_{FF}/T_0$ %	$\Delta T_{IC}/\Delta T_{FF}$ %
1	0.145	0.014	0.55	55	0.025
10	1.056	0.010	0.55	5.5	0.192
10^2	2.335	0.0023	0.55	0.55	0.42
10^3	1.815	0.00018	0.55	0.055	0.33

Table C.1: Energy loss estimation for different initial energy of the particle. (Bobik et al., 2011a)

Appendix D

Comparison with Data - All Results

D.1 Low Activity

In follow tables are reported the computed $\eta_{\rm rms}(\%)$ For BESS–1997,AMS–1998, PAMELA–2006/08, obtained from Eq. (4.6) using "R" and "L" Models for the tilt angle, No Drift Approximation for several values of ρ_E, $\delta_m =$ and ρ_k; the differential intensities were calculated accounting for particles inside two heliospheric regions where solar latitudes are lower than $|5.7°|$.

$\rho_k = 0.10$; $\rho_E = 1$

	$\delta_m = 0.0 \times 10^{-5}$			$\delta_m = 1.0 \times 10^{-5}$		
	"R" Model	"L" Model	No Drift	"R" Model	"L" Model	No Drift
BESS-97	22.4	10.7	32.2	19.3	6.8	35.0
AMS-98	12.6	12.2	34.6	8.6	10.6	31.5
PAMELA	7.1	10.0		7.3	8.6	
Average	14.1	11.0	33.4	11.7	8.7	33.2
	$\delta_m = 2.0 \times 10^{-5}$			$\delta_m = 3.0 \times 10^{-5}$		
	"R" Model	"L" Model	No Drift	"R" Model	"L" Model	No Drift
BESS-97	17.9	6.5	34.7	19.4	6.5	35.0
AMS-98	8.7	8.4	32.8	10.0	12.1	32.1
PAMELA	8.2	9.9		7.6	10.6	
Average	11.6	8.3	33.7	12.3	9.7	33.5

$\rho_k = 0.11$; $\rho_E = 1$

	$\delta_m = 1.0 \times 10^{-5}$			$\delta_m = 2.0 \times 10^{-5}$		
	"R" Model	"L" Model	No Drift	"R" Model	"L" Model	No Drift
BESS-97	7.0	6.4	30.4	8.0	7.3	31.2
AMS-98	5.5	10.1	27.1	9.1	7.7	28.4
PAMELA	6.7	10.3	25.5	6.4	12.1	25.3
Average	6.4	9.0	27.7	7.8	9.0	28.3

$\delta_m = 3.0 \times 10^{-5}$

	"R" Model	"L" Model	No Drift
BESS-97	7.4	8.3	31.6
AMS-98	8.6	7.9	29.5
PAMELA	6.5	10.2	26.5
Average	7.5	8.8	29.2

$\rho_k = 0.12$; $\rho_E = 1$

	$\delta_m = 1.0 \times 10^{-5}$			$\delta_m = 2.0 \times 10^{-5}$		
	"R" Model	"L" Model	No Drift	"R" Model	"L" Model	No Drift
BESS-97	7.4	7.7	26.0	7.7	8.0	27.8
AMS-98	6.2	7.1	24.8	5.5	7.1	24.9
PAMELA	5.1	6.5	19.5	5.6	6.6	21.4
Average	6.3	7.1	23.5	6.3	7.3	24.7

$\delta_m = 3.0 \times 10^{-5}$

	"R" Model	"L" Model	No Drift
BESS-97	7.9	7.9	25.7
AMS-98	7.6	6.7	25.6
PAMELA	5.6	6.2	21.9
Average	7.1	6.9	24.4

$\rho_k = 0.13$; $\rho_E = 1$

	$\delta_m = 1.0 \times 10^{-5}$			$\delta_m = 2.0 \times 10^{-5}$		
	"R" Model	"L" Model	No Drift	"R" Model	"L" Model	No Drift
BESS-97	7.8	8.3	22.8	8.4	8.3	24.1
AMS-98	5.2	5.3	21.9	5.9	8.9	21.3
PAMELA	5.9	5.6	15.6	5.5	5.7	15.8
Average	6.3	6.4	20.1	6.6	7.6	20.4

$\delta_m = 3.0 \times 10^{-5}$

	"R" Model	"L" Model	No Drift
BESS-97	8.4	10.0	23.5
AMS-98	6.2	8.0	22.0
PAMELA	5.5	5.1	16.1
Average	6.7	7.7	20.5

$\rho_k = 0.14$; $\rho_E = 1$

	$\delta_m = 1.0 \times 10^{-5}$			$\delta_m = 2.0 \times 10^{-5}$		
	"R" Model	"L" Model	No Drift	"R" Model	"L" Model	No Drift
BESS-97	8.7	8.9	17.6	9.6	10.3	19.
AMS-98	5.4	5.2	18.0	5.4	5.4	17.8
PAMELA	7.9	7.0	12.1	6.8	5.9	11.8
Average	7.3	7.0	15.9	7.3	7.2	16.4

$\delta_m = 3.0 \times 10^{-5}$

	"R" Model	"L" Model	No Drift
BESS-97	8.4	8.7	18.3
AMS-98	5.3	5.3	19.3
PAMELA	7.8	5.5	12.8
Average	7.2	6.5	16.8

$\rho_k = 0.10$; $\rho_E = 8$

	$\delta_m = 1.0 \times 10^{-5}$			$\delta_m = 2.0 \times 10^{-5}$		
	"R" Model	"L" Model	No Drift	"R" Model	"L" Model	No Drift
BESS-97	23.8	22.7	34.1	9.4	10.2	35.1
AMS-98	25.4	29.4	34.2	21.3	23.4	33.4
PAMELA				33.6	34.1	30.4
Average	24.6	26.0	34.1	21.4	22.6	33.0

$\delta_m = 3.0 \times 10^{-5}$

	"R" Model	"L" Model	No Drift
BESS-97	9.1	9.3	33.3
AMS-98	18.9	19.1	32.3
PAMELA	29.6	30.7	27.9
Average	19.2	19.7	31.1

$\rho_k = 0.11$; $\rho_E = 8$

	$\delta_m = 0.0 \times 10^{-5}$			$\delta_m = 1.0 \times 10^{-5}$		
	"R" Model	"L" Model	No Drift	"R" Model	"L" Model	No Drift
BESS-97	9.4	9.0	33.0	10.5	9.7	30.1
AMS-98	14.5	16.0	32.8	18.4	19.6	28.8
PAMELA	28.7	29.7	24.8	26.8	28.0	23.7
Average	17.5	18.2	30.2	18.6	19.1	27.5
	$\delta_m = 2.0 \times 10^{-5}$			$\delta_m = 3.0 \times 10^{-5}$		
	"R" Model	"L" Model	No Drift	"R" Model	"L" Model	No Drift
BESS-97	11.1	7.3	29.6	7.3	8.8	29.9
AMS-98	16.2	17.2	29.2	13.3	13.2	28.1
PAMELA	25.7	27.2	22.3	23.9	25.1	20.1
Average	17.7	17.2	27.1	14.8	15.7	26.0

$\rho_k = 0.12$; $\rho_E = 8$

	$\delta_m = 1.0 \times 10^{-5}$			$\delta_m = 2.0 \times 10^{-5}$		
	"R" Model	"L" Model	No Drift	"R" Model	"L" Model	No Drift
BESS-97	10.5	8.2	25.9	7.5	9.9	24.6
AMS-98	14.4	16.5	24.9	11.4	13.2	24.4
PAMELA	22.4	22.9	18.9	21.3	21.9	16.6
Average	15.8	15.9	23.3	13.4	15.0	21.9

$\delta_m = 3.0 \times 10^{-5}$

	"R" Model	"L" Model	No Drift
BESS-97	7.1	9.1	25.0
AMS-98	10.1	11.3	25.0
PAMELA	19.6	21.4	15.3
Average	12.3	13.9	21.8

$\rho_k = 0.13$; $\rho_E = 8$

	$\delta_m = 1.0 \times 10^{-5}$			$\delta_m = 2.0 \times 10^{-5}$		
	"R" Model	"L" Model	No Drift	"R" Model	"L" Model	No Drift
BESS-97	7.6	7.1	20.6	6.9	11.4	21.1
AMS-98	12.2	13.3	20.7	10.2	10.7	21.3
PAMELA	17.5	19.0	14.8	16.2	17.6	11.6
Average	12.5	13.1	18.7	11.1	13.2	18.0

$\delta_m = 3.0 \times 10^{-5}$

	"R" Model	"L" Model	No Drift
BESS-97	8.8	7.7	20.8
AMS-98	9.2	12.1	20.1
PAMELA	16.5	16.8	11.0
Average	11.5	12.2	17.3

$\rho_k = 0.14$; $\rho_E = 8$

	$\delta_m = 1.0 \times 10^{-5}$			$\delta_m = 2.0 \times 10^{-5}$		
	"R" Model	"L" Model	No Drift	"R" Model	"L" Model	No Drift
BESS-97	7.6	6.8	17.2	7.7	6.3	18.2
AMS-98	9.9	11.5	18.6	9.0	9.4	17.4
PAMELA	13.6	14.8	10.4	12.9	13.0	8.8
Average	10.4	11.0	15.4	9.9	9.6	14.8

$\delta_m = 3.0 \times 10^{-5}$

	"R" Model	"L" Model	No Drift
BESS-97	8.4	9.0	17.5
AMS-98	6.5	7.9	17.3
PAMELA	12.5	12.8	7.4
Average	9.1	9.9	14.1

$\rho_k = 0.10$; $\rho_E = 10$

	$\delta_m = 0.0 \times 10^{-5}$			$\delta_m = 1.0 \times 10^{-5}$		
	"R" Model	"L" Model	No Drift	"R" Model	"L" Model	No Drift
BESS-97	23.1	23.0	33.7	13.6	12.2	33.1
AMS-98	27.6	26.4	32.9	21.8	24.6	32.9
PAMELA	35.7		29.6	33.2	34.2	27.7
Average	28.8	24.7	32.1	22.9	23.7	31.2

	$\delta_m = 2.0 \times 10^{-5}$			$\delta_m = 3.0 \times 10^{-5}$		
	"R" Model	"L" Model	No Drift	"R" Model	"L" Model	No Drift
BESS-97	11.2	9.2	33.4	9.1	7.8	32.4
AMS-98	17.8	20.4	31.8	16.4	17.2	31.3
PAMELA	31.4	32.8	28.1	30.4	31.2	25.2
Average	20.1	20.8	31.1	18.6	18.7	29.6

$\rho_k = 0.11$; $\rho_E = 10$

	$\delta_m = 1.0 \times 10^{-5}$			$\delta_m = 2.0 \times 10^{-5}$		
	"R" Model	"L" Model	No Drift	"R" Model	"L" Model	No Drift
BESS-97	12.7	8.7	30.0	10.8	10.0	28.9
AMS-98	18.7	19.6	29.1	14.9	17.3	28.0
PAMELA	28.2	29.0	23.4	26.8	27.9	21.6
Average	19.9	19.1	27.5	17.5	18.4	26.2

$\delta_m = 3.0 \times 10^{-5}$

	"R" Model	"L" Model	No Drift
BESS-97	9.6	8.5	29.0
AMS-98	12.8	14.0	27.7
PAMELA	26.2	26.0	19.2
Average	16.2	16.2	25.3

$\rho_k = 0.12$; $\rho_E = 10$

	$\delta_m = 1.0 \times 10^{-5}$			$\delta_m = 2.0 \times 10^{-5}$		
	"R" Model	"L" Model	No Drift	"R" Model	"L" Model	No Drift
BESS-97	11.3	10.1	24.6	9.2	8.5	24.0
AMS-98	18.0	18.3	25.9	14.0	14.2	24.6
PAMELA	24.4	24.1	19.4	21.8	22.5	17.9
Average	17.9	17.5	23.3	15.0	15.1	22.1

$\delta_m = 3.0 \times 10^{-5}$

	"R" Model	"L" Model	No Drift
BESS-97	8.2	6.8	23.7
AMS-98	10.6	13.1	25.0
PAMELA	19.9	21.1	15.6
Average	12.9	13.7	21.4

$\rho_k = 0.13$; $\rho_E = 10$

	$\delta_m = 1.0 \times 10^{-5}$			$\delta_m = 2.0 \times 10^{-5}$		
	"R" Model	"L" Model	No Drift	"R" Model	"L" Model	No Drift
BESS-97	9.1	10.3	22.3	7.8	8.2	22.0
AMS-98	13.8	13.9	20.9	10.5	11.8	20.7
PAMELA	18.9	19.6	15.0	19.0	18.5	13.2
Average	13.9	14.6	19.4	12.5	12.9	18.6

$\delta_m = 3.0 \times 10^{-5}$

	"R" Model	"L" Model	No Drift
BESS-97	7.6	9.0	20.7
AMS-98	8.8	9.9	21.9
PAMELA	16.0	17.3	11.0
Average	10.8	12.1	17.9

$\rho_k = 0.14$; $\rho_E = 10$

	$\delta_m = 1.0 \times 10^{-5}$			$\delta_m = 2.0 \times 10^{-5}$		
	"R" Model	"L" Model	No Drift	"R" Model	"L" Model	No Drift
BESS-97	8.1	5.8	17.9	7.8	9.5	17.5
AMS-98	10.5	12.4	18.2	9.2	9.3	17.5
PAMELA	15.5	15.0	11.3	13.9	13.8	8.3
Average	11.4	11.1	15.8	10.3	10.9	14.4

$\delta_m = 3.0 \times 10^{-5}$

	"R" Model	"L" Model	No Drift
BESS-97	7.2	7.9	16.3
AMS-98	6.7	10.4	16.8
PAMELA	11.0	11.2	7.2
Average	8.3	9.8	13.4

D.2 High Activity

In follow tables are reported the computed $\eta_{\rm rms}(\%)$ For BESS–1999,BESS–2000, BESS–2002 obtained from Eq. (4.6) using "R" and "L" Models for the tilt angle, No Drift Approximation for several values of ρ_E, $\delta_m =$ and ρ_k; the differential intensities were calculated accounting for particles inside two heliospheric regions where solar latitudes are lower than $|5.7°|$.

$\rho_k = 0.10$; $\rho_E = 1$

	$\delta_m = 0.0 \times 10^{-5}$			$\delta_m = 1.0 \times 10^{-5}$		
	"R" Model	"L" Model	No Drift	"R" Model	"L" Model	No Drift
BESS–1999	12.6	12.0	24.3	11.7	10.9	25.1
BESS–2000	13.4	14.0	14.8	14.0	12.1	14.9
BESS–2002	7.4	6.3	7.2	7.3	7.4	7.5
Average	11.2	10.8	15.4	11.0	10.1	15.8
	$\delta_m = 2.0 \times 10^{-5}$			$\delta_m = 3.0 \times 10^{-5}$		
	"R" Model	"L" Model	No Drift	"R" Model	"L" Model	No Drift
BESS–1999	9.3	10.6	25.7	8.5	9.7	25.4
BESS–2000	12.5	12.6	16.7	12.4	13.3	15.2
BESS–2002	6.9	6.7	7.7	7.0	7.4	8.1
Average	9.6	10.0	16.7	9.3	10.1	16.2

$\rho_k = 0.11$; $\rho_E = 1$

	$\delta_m = 1.0 \times 10^{-5}$			$\delta_m = 2.0 \times 10^{-5}$		
	"R" Model	"L" Model	No Drift	"R" Model	"L" Model	No Drift
BESS–1999	6.9	7.4	19.5	6.6	6.7	18.1
BESS–2000	22.1	22.1	10.7	20.9	21.5	9.8
BESS–2002	11.3	9.7	17.9	10.5	10.4	18.3
Average	13.4	13.1	16.0	12.7	12.9	15.4

$\delta_m = 3.0 \times 10^{-5}$

	"R" Model	"L" Model	No Drift
BESS–1999	6.7	7.5	20.3
BESS–2000	21.1	20.3	10.4
BESS–2002	10.2	9.8	18.0
Average	12.7	12.5	16.2

$\rho_k = 0.12$; $\rho_E = 1$

	$\delta_m = 1.0 \times 10^{-5}$			$\delta_m = 2.0 \times 10^{-5}$		
	"R" Model	"L" Model	No Drift	"R" Model	"L" Model	No Drift
BESS–1999	7.4	6.6	15.5	6.8	6.8	14.6
BESS–2000	32.4	31.0	13.3	31.3	29.9	12.2
BESS–2002	16.4	15.5	11.3	16.6	14.1	11.5
Average	18.7	17.7	13.4	18.3	16.9	12.8

$\delta_m = 3.0 \times 10^{-5}$

	"R" Model	"L" Model	No Drift
BESS–1999	7.1	6.7	14.8
BESS–2000	30.9	30.9	12.4
BESS–2002	16.3	14.4	11.2
Average	18.1	17.3	12.8

$\rho_k = 0.13$; $\rho_E = 1$

	$\delta_m = 1.0 \times 10^{-5}$			$\delta_m = 2.0 \times 10^{-5}$		
	"R" Model	"L" Model	No Drift	"R" Model	"L" Model	No Drift
BESS–1999	9.1	8.2	10.3	10.6	9.1	9.6
BESS–2000	38.5	40.7	22.6	40.4	41.1	20.5
BESS–2002	22.3	21.7	10.1	23.9	23.8	9.8
Average	23.3	23.5	14.3	25.0	24.7	13.3

$\delta_m = 3.0 \times 10^{-5}$

	"R" Model	"L" Model	No Drift
BESS–1999	9.3	8.8	9.8
BESS–2000	39.6	42.1	20.4
BESS–2002	24.0	21.8	9.3
Average	24.3	24.2	13.1

$\rho_k = 0.14$; $\rho_E = 1$

	$\delta_m = 1.0 \times 10^{-5}$			$\delta_m = 2.0 \times 10^{-5}$		
	"R" Model	"L" Model	No Drift	"R" Model	"L" Model	No Drift
BESS–1999	11.8	11.0	7.3	13.7	12.2	6.9
BESS–2000	51.9	51.9	32.3	52.4	51.0	29.8
BESS–2002	33.3	29.1	14.5	32.2	29.2	14.5
Average	32.3	30.7	18.0	32.8	30.8	17.1

$\delta_m = 3.0 \times 10^{-5}$

	"R" Model	"L" Model	No Drift
BESS–1999	12.2	12.3	6.8
BESS–2000	50.8	50.1	32.1
BESS–2002	31.6	29.5	14.8
Average	31.5	30.7	17.9

$\rho_k = 0.10$; $\rho_E = 8$

	$\delta_m = 0.0 \times 10^{-5}$			$\delta_m = 1.0 \times 10^{-5}$		
	"R" Model	"L" Model	No Drift	"R" Model	"L" Model	No Drift
BESS–1999		20.8	26.5		20.7	25.1
BESS–2000	25.7	27.0	18.7	22.6	22.3	17.3
BESS–2002	32.5	33.8		29.8	30.4	27.2
Average	29.1	27.2	22.6	26.2	24.5	23.2
	$\delta_m = 1.0 \times 10^{-5}$			$\delta_m = 3.0 \times 10^{-5}$		
	"R" Model	"L" Model	No Drift	"R" Model	"L" Model	No Drift
BESS–1999		18.9	24.9			
BESS–2000	21.3	20.0	15.0	18.4	17.9	12.3
BESS–2002	28.2	30.0	25.7	26.4	26.6	22.6
Average	24.7	23.0	21.9	22.4	22.3	17.4

$\rho_k = 0.11$; $\rho_E = 8$

	$\delta_m = 1.0 \times 10^{-5}$			$\delta_m = 2.0 \times 10^{-5}$		
	"R" Model	"L" Model	No Drift	"R" Model	"L" Model	No Drift
BESS–1999	14.8	14.7	20.2	10.8	12.8	18.7
BESS–2000	15.8	14.5	10.5	12.6	12.3	9.5
BESS–2002	23.9	22.9	18.4	21.1	21.5	18.4
Average	18.2	17.4	16.4	14.8	15.5	15.5

$\delta_m = 3.0 \times 10^{-5}$

	"R" Model	"L" Model	No Drift
BESS–1999	10.3	11.5	18.5
BESS–2000	10.9	10.9	10.6
BESS–2002	19.4	19.8	15.1
Average	13.5	14.0	14.7

$\rho_k = 0.12$; $\rho_E = 8$

	$\delta_m = 1.0 \times 10^{-5}$			$\delta_m = 2.0 \times 10^{-5}$		
	"R" Model	"L" Model	No Drift	"R" Model	"L" Model	No Drift
BESS–1999	10.7	13.2	14.8	7.0	10.1	15.2
BESS–2000	10.2	10.0	11.8	10.6	10.7	14.8
BESS–2002	15.5	17.2	12.7	14.9	16.7	11.2
Average	12.1	13.5	13.1	10.8	12.5	13.7

$\delta_m = 3.0 \times 10^{-5}$

	"R" Model	"L" Model	No Drift
BESS–1999	7.3	6.5	12.8
BESS–2000	12.1	12.1	17.9
BESS–2002	13.2	13.7	10.2
Average	10.9	10.8	13.6

$\rho_k = 0.13$; $\rho_E = 8$

	$\delta_m = 1.0 \times 10^{-5}$			$\delta_m = 2.0 \times 10^{-5}$		
	"R" Model	"L" Model	No Drift	"R" Model	"L" Model	No Drift
BESS–1999	6.5	7.4	11.1	6.6	7.4	9.2
BESS–2000	13.6	13.7	19.4	16.2	16.5	22.9
BESS–2002	11.4	11.3	9.9	10.6	11.0	10.4
Average	10.5	10.8	13.5	11.1	11.7	14.2

$\delta_m = 3.0 \times 10^{-5}$

	"R" Model	"L" Model	No Drift
BESS–1999	7.0	6.2	8.7
BESS–2000	19.5	19.2	27.9
BESS–2002	10.5	10.2	11.0
Average	12.3	11.9	15.9

$\rho_k = 0.14$; $\rho_E = 8$

	$\delta_m = 1.0 \times 10^{-5}$			$\delta_m = 2.0 \times 10^{-5}$		
	"R" Model	"L" Model	No Drift	"R" Model	"L" Model	No Drift
BESS–1999	7.1	6.5	7.4	8.3	7.1	7.1
BESS–2000	24.3	23.5	30.9	25.9	25.8	32.4
BESS–2002	10.7	10.8	13.2	11.3	11.7	15.3
Average	14.0	13.6	17.2	15.2	14.9	18.3

$\delta_m = 3.0 \times 10^{-5}$

	"R" Model	"L" Model	No Drift
BESS–1999	9.1	8.4	6.3
BESS–2000	29.6	28.2	40.3
BESS–2002	13.7	12.9	18.3
Average	17.5	16.5	21.6

$\rho_k = 0.10$; $\rho_E = 10$

	$\delta_m = 0.0 \times 10^{-5}$			$\delta_m = 1.0 \times 10^{-5}$		
	"R" Model	"L" Model	No Drift	"R" Model	"L" Model	No Drift
BESS–1999		22.0	26.2		21.0	25.5
BESS–2000	27.4	28.4	18.7	24.0	23.7	18.7
BESS–2002	34.7	34.9	27.9	31.3	33.0	27.9
Average	31.1	28.4	24.2	27.6	25.9	24.0
	$\delta_m = 2.0 \times 10^{-5}$			$\delta_m = 3.0 \times 10^{-5}$		
	"R" Model	"L" Model	No Drift	"R" Model	"L" Model	No Drift
BESS–1999		19.5	25.8		16.5	22.9
BESS–2000	21.1	21.0	14.8	16.6	19.5	11.5
BESS–2002	29.4	29.7	25.8	27.0	26.8	22.2
Average	25.2	23.4	22.1	21.8	20.9	18.9

$\rho_k = 0.11$; $\rho_E = 10$

	$\delta_m = 1.0 \times 10^{-5}$			$\delta_m = 2.0 \times 10^{-5}$		
	"R" Model	"L" Model	No Drift	"R" Model	"L" Model	No Drift
BESS–1999	14.7	13.4	20.4	12.4	13.7	19.1
BESS–2000	15.2	15.1	10.5	13.1	13.8	9.8
BESS–2002	24.3	24.8	19.3	21.9	22.3	17.0
Average	18.1	17.8	16.7	15.8	16.6	15.3

$\delta_m = 3.0 \times 10^{-5}$

	"R" Model	"L" Model	No Drift
BESS–1999	10.1	10.1	17.0
BESS–2000	11.1	11.3	11.1
BESS–2002	21.3	21.3	15.2
Average	14.2	14.2	14.4

$\rho_k = 0.12$; $\rho_E = 10$

	$\delta_m = 1.0 \times 10^{-5}$			$\delta_m = 2.0 \times 10^{-5}$		
	"R" Model	"L" Model	No Drift	"R" Model	"L" Model	No Drift
BESS–1999	10.5	10.9	15.5	9.1	9.1	14.5
BESS–2000	10.0	10.4	11.9	10.3	10.6	15.1
BESS–2002	18.2	16.1	11.6	16.2	15.7	10.5
Average	12.9	12.5	13.0	11.8	11.8	13.4

$\delta_m = 3.0 \times 10^{-5}$

	"R" Model	"L" Model	No Drift
BESS–1999	8.2	6.5	11.1
BESS–2000	11.8	12.1	18.1
BESS–2002	14.5	13.3	9.5
Average	11.5	10.6	12.9

$\rho_k = 0.13$; $\rho_E = 10$

	$\delta_m = 1.0 \times 10^{-5}$			$\delta_m = 2.0 \times 10^{-5}$		
	"R" Model	"L" Model	No Drift	"R" Model	"L" Model	No Drift
BESS–1999	7.5	7.8	9.9	5.7	6.7	9.8
BESS–2000	14.0	12.8	19.2	15.4	16.3	24.2
BESS–2002	13.9	11.2	9.5	10.5	11.2	10.3
Average	11.8	10.6	12.8	10.5	11.4	14.7

$\delta_m = 3.0 \times 10^{-5}$

	"R" Model	"L" Model	No Drift
BESS–1999	5.6	6.3	8.3
BESS–2000	20.2	19.7	29.4
BESS–2002	9.6	11.0	11.4
Average	11.8	12.3	16.4

$\rho_k = 0.14$; $\rho_E = 10$

	$\delta_m = 1.0 \times 10^{-5}$			$\delta_m = 2.0 \times 10^{-5}$		
	"R" Model	"L" Model	No Drift	"R" Model	"L" Model	No Drift
BESS–1999	6.4	6.7	6.4	7.7	7.6	7.0
BESS–2000	22.4	22.2	31.0	24.7	25.3	33.2
BESS–2002	9.9	10.6	13.7	11.4	10.9	15.0
Average	12.9	13.1	17.1	14.6	14.6	18.4

$\delta_m = 3.0 \times 10^{-5}$

	"R" Model	"L" Model	No Drift
BESS–1999	9.9	9.2	6.6
BESS–2000	29.0	29.0	40.7
BESS–2002	13.0	12.7	17.5
Average	17.3	17.0	21.6

Appendix E

Coordinate Analysis for AMS-02 Experiment

The AMS-02 experiment was installed on-board of the International Space Station (ISS) on May 19^{th} 2011, to provide high precision study of cosmic rays of energies from GeV to TeV. The ISS follows a Low Earth Orbit at about 400km of altitude from the Earth surface, far enough to observe cosmic radiation before it interacts with the high levels of the atmosphere. This makes the ISS one of the best environment to perform Cosmic Rays physic. Thanks to the high acceptance of the instrument and to the long duration of the mission, AMS-02 will reach high statistic and great precision measurements. Since this is a space-born experiment, additional variables compared to the ground based observations, have to be taken into account as, for example, the position of the Sun respect to the payload (i.e. AMS-02). Sun light in facts can affect the thermal of the instrument that, in turn, affect the stability and the efficiency. Furthermore the position relative to the Earth and attitude of the instrument is important in order, e.g., to consider geomagnetic effects (see e.g. Bobik et al., 2006) or to perform study of anisotropy (see e.g. Ackermann et al., 2010). In this Section we present how it is possible to get the AMS-02 pointing direction and Sun position once know telemetry data about ISS (or AMS attitude). The discussion in this Section follow the approach close to Della Torre et al. (2012b).

E.1 Reference Frames

A reference frame is defined at a given time (epoch) by an origin and three orthogonal axis $(\hat{X}, \hat{Y}, \hat{Z})$ fixed with respect to a given body (e.g. Earth, Shuttle, ISS...). For the purpose of this work we focus our attention on *Earth Centered* and *Orbit Object* reference frames; in the formers the origin are located in the center of the Earth and they differ one with the other in the orientation of the $\hat{X}\hat{Y}$ plane which can be parallel to the real (or mean) equator or to ecliptic plane. In *Orbit Object* frames, instead, the center is located inside the fling object (e.g., ISS), and each frame requires its own definition.

E.1.1 Earth Centered Coordinates

In this work we consider three *Earth Centered* reference frames: the *Ecliptic* frame for the evaluation of Sun Motion (with respect the Earth) while the *Earth Centered Inertial* and the *Greenwich True of Date* frames are used for compute the orbit of ISS.

In the ***Ecliptic*** frame the origin is located in the center of the Earth and the main axis ($\hat{X}$) is directed toward the Vernal Equinox (also called first point of Aries or Υ); this direction lies along the line of intersection between the plane of the Earth's equator and the Ecliptic one[1]. These two planes form an angle called Obliquity of the ecliptic (ε, see e.g. figure 19 of Duffett-Smith and Zwart, 2011). If we neglect the effects of Precession and Nutation[2] the Υ point can be considered fixed respect to the Stars. Now the **ecliptic longitude** (λ), of a V point in the Sky, is defined to be the angle subtended by the Υ point and the F point, where F is the perpendicular interSection between the Ecliptic Plane and the imaginary line passing through V (Duffett-Smith and Zwart, 2011). The **ecliptic latitude** (β_e) is the angle subtended by F and V (Duffett-Smith and Zwart, 2011). The latitude is positive if the object is above (i.e. north of) the Ecliptic Plane; the longitude increases along the eastward Ecliptic direction. Throughout the year, the Sun moves eastward along the trace of the Ecliptic. By definition the Sun ecliptic latitude is always zero. This frame is often used to display satellite trajectories, interplanetary magnetic field observations and solar wind velocity data (Bhavnani and Vancour, 1991).

The ***Earth Centered Inertial*** (ECI) reference, also known as Geocentric Celestial Inertial or Equatorial coordinates, is an Inertial Cartesian right-handed system referred to the plane of the Earth Equator. The main axis $\hat{X}$ points in the direction of the first point of Aries. The $\hat{Z}$ axis overlaps with the Earth rotational axis and it is defined positive toward the north. The $\hat{Y}$ axis lies on the equatorial plane and completes the right-handed orthogonal set ($\hat{Y} = \hat{Z} \times \hat{X}$, Bhavnani and Vancour, 1991; NASA, 2001). A given epoch defines the direction for the Vernal Equinox (Bhavnani and Vancour, 1991): in the **Aries True of Date (ATD)** the $\hat{X}$ axis points towards the first point of Aries for the true-of-date, for **Aries Mean of 1950 (M50)** is considered the Epoch 1950 while for **Aries Mean of 2000 (J2000)** the reference Aries point was for Epoch 2000 (1st January 2000). The celestial longitude, of an object in the Sky, is called **right ascension** (α). It is the angle from the $\hat{X}$ axis to the $\hat{Y}$ direction and it is usually expressed in hours and minutes, with 24h to complete the circle of 360 degrees. The celestial latitude, called **declination** (δ), is the angular distance of the object from the celestial equator and it is positive in the north direction. The ECI frame is usually used in astronomy and for satellite orbit calculations (Bhavnani and Vancour, 1991).

Finally the ***Greenwich True of Date*** (GTOD) system is a Geocentric, Earth-fixed frame, i.e. it is co-moving with the Earth. The main axis points toward the Greenwich True of Date

[1] The Ecliptic is the plane containing the Earth's orbit around the Sun.

[2] The combined gravitational field of the Sun and the Moon, acting on the non-spherical Earth, are responsible for the slow gyration of the rotational Earth's axis which changes its direction with a period of about 25800 years. This phenomena is called Precession. Superimposed on this regular motion there are also small additional periodic terms which are caused by the variation of distances and relative directions of the Moon and the Sun. This slight wobbling motion, which continuously modify the strength and the direction of the gravitational field, is called Nutation (Lang, 1999; Duffett-Smith and Zwart, 2011).

Meridian and it lies on the Earth equatorial plane. The $\hat{Z}$ axis overlaps with the Earth rotational axis and it is positive toward the north pole. The $\hat{Y}$ axis, placed on the equatorial plane, completes the right-handed orthogonal set ($\hat{Y} = \hat{Z} \times \hat{X}$, Bhavnani and Vancour, 1991; NASA, 2001). The **Longitude** is the angle defined positive from the $\hat{X}$ axis to the $\hat{Y}$ direction, while the **Latitude** is the angular distance from the True of Date Equator, and it is positive in the north direction. The GTOD is a convenient system to relate the coordinates of a co-moving Earth object with the inertial and quasi-inertial systems (Bhavnani and Vancour, 1991). The velocity vectors, expressed in this system, are relative to this rotating frame fixed with the Earth (NASA, 2001).

E.1.2 Object Centered Coordinates

It is possible to define a local frame for each object, in particular for this work we consider three frame centered on ISS instantaneous orbit position, ISS structure and AMS-02 detector, respectively.

The ***Local Vertical Local Horizontal*** (LVLH) frame is a quasi-inertial, right-handed Cartesian system with the origin located in the center of mass of the orbital object (i.e. ISS). In this frame $\hat{X}\hat{Z}$ plane defines the instantaneous orbit plane at the time of interest. The $\hat{Z}$ axis lies along the geocentric radius vector to the vehicle and it is positive toward the center of the Earth (Bhavnani and Vancour, 1991; NASA, 2001). The $\hat{Y}$ axis is normal to the orbit plane and opposite to the orbit momentum vector $\hat{H}$. The $\hat{X}$ axis completes the right-hand orthogonal system; it is tangent to the orbital plane and positive toward the direction of the vehicle motion. The LVLH is useful to transform a fixed Earth orientation to an orbital orientation (Bhavnani and Vancour, 1991).

The ***Space Station Coordinate Systems*** (also called *Body frame*) are Body–Fixed Right–handed Cartesian systems. If the origin is located at the geometric center of Integrated Truss Segment (ITS) S0 of the ISS, the coordinate system is called *Space Station Analysis Coordinate System* (SSACS). If the origin is in the center of mass of the ISS the system is called *Space Station Body Coordinate System* (SSBCS) (NASA, 2001). In both cases, the $\hat{X}_A$ axis is parallel to the longitudinal axis of the module cluster; the $\hat{Y}_A$ axis is parallel to the axis of module cluster, and positive in the starboard direction; the $\hat{Z}_A$ axis completes the right handed Cartesian System and it is positive in the nadir direction. The forward direction ($+\hat{X}_A$) is called Ram Side, the backward ($-\hat{X}_A$) is called Wake Side; the ($+\hat{Y}_A$) direction is called Starboard, while the opposite one ($-\hat{Y}_A$) is called Port. AMS-02 is located on the Starboard side of the ISS. The SSACS (or SSBCS) coordinate system is derived using the LVLH flight orientation. To define the relationship between this reference frame and another it is necessary to give three attitude angles called Yaw, Pitch and Roll. This are also called Euler angle, and are right-handed rotations around the $\hat{Z}_A$, $\hat{Y}_A$, and $\hat{X}_A$ axes respectively (NASA, 2001). They globally represent the attitude of the flight object. To pass from the LVLH reference system to SSACS (or SSBCS), the sequence that one have to apply to the components of the object is: Yaw, Pitch and Roll.

Finally also ***AMS-02*** has its own Cartesian right-handed coordinate system. The origin of this system is located at (-85.598, 2136.390, -388.112) cm from the origin of SSACS, which corresponds to the geometric center of tracker detector. The $\hat{X}_{ams}$ axis points toward the Port direction, the

$\hat{Z}_{ams}$ axis is directed toward the Zenith direction (i.e. the top part of the detector). the $\hat{Y}_{ams}$ axis is directed to the Wake side. The structure of the detector is tilted of about 12° with respect to the axis perpendicular the ISS structure (see Fig. E.1).

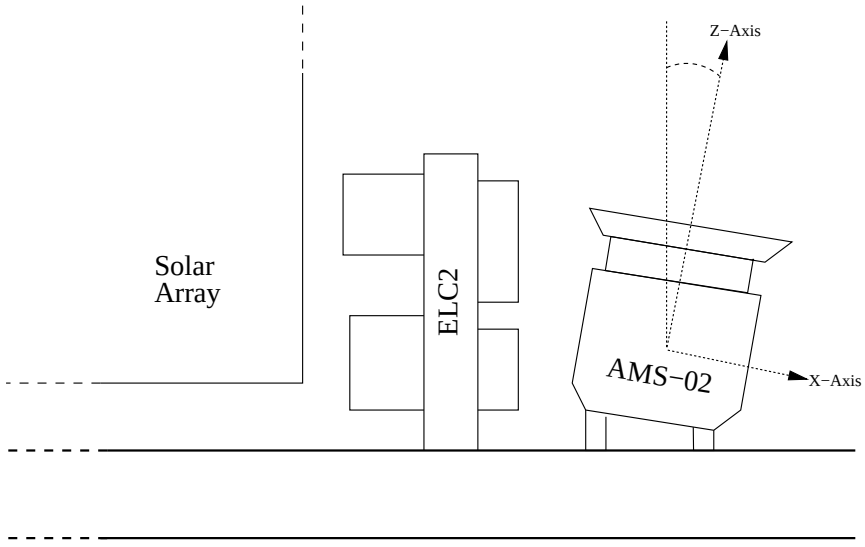

Figure E.1: The AMS coordinate system on the Starboard side of ISS, left side is toward the starboard direction (figure from Della Torre et al., 2012b).

E.2 Sun Ephemeris

During the year, the Earth moves on an elliptical orbit around the Sun, making a complete revolution in 365.2422 days (Duffett-Smith and Zwart, 2011). Viewed from the Earth, it seems that the Sun is moving in an orbit around our planet so it is convenient to refer to this case when one has to calculate the apparent motion of the Sun. Another convenient assumption is to calculate the Sun position in term of the ecliptic longitude. The procedure described afterward can be found in Duffett-Smith and Zwart (2011). In literature it is possible to find other algorithms (see e.g. Blanco-Muriel et al., 2001; Meuss, 2000) that differ from this one on the precision with which the secular functions are evaluated and depend on second order perturbation effects that can be included or neglected.

For simplicity, we introduce a *Mean Sun* which moves in a circle around the Earth at a constant speed, rather than along the ellipse that it actually traces. The angle between this *Mean Sun* and the perigee [3] is called *Mean Anomaly* ($M_\odot$). This angle can be obtained using the angles ε_g and ϖ_g, which are the Sun's mean ecliptic longitude at the Epoch [4] and the longitude of the Sun at perigee respectively.

$$M_\odot = \varepsilon_g - \varpi_g \tag{E.1}$$

[3]The perigee is the point of closest approach between the Sun and the Earth.

[4]The Sun's mean ecliptic longitude is the position that the Sun would have got if it were moving in a circular orbit rather than on an ellipse.

with

$$\varepsilon_g = 279.6966778^\circ + 360^\circ \cdot (A - Ai) + 0.0003025^\circ \cdot T_s^2; \tag{E.2}$$

$$\varpi_g = 281.2208444^\circ + 1.719175^\circ \cdot T + 0.000452778^\circ \cdot T_s^2; \tag{E.3}$$

where $A = 100.0021359 \cdot T_s$, Ai is the integer part of A and $T_s = (JD - 2415020.0)/36525.$ is the number of Julian Centuries since 1900 Jan 0.5. The *Eccentricity Anomaly* (E) can be obtained by the solution of Kepler's equation

$$E - e \sin E = M_\odot \tag{E.4}$$

where e is the eccentricity of the Sun-Earth orbit given by

$$e = 0.01675104 - 0.0000418 \cdot T_s - 0.000000126 \cdot T_s^2. \tag{E.5}$$

The Kepler's equation (E.4) is not easy to solve, but it is possible to use a simple recursive routine described in Duffett-Smith and Zwart (2011). Having the solution of the Kepler's equation, we can find the *True Anomaly* (ν), which is employed in the true elliptic motion of the Sun,

$$\tan\left(\frac{\nu}{2}\right) = \sqrt{\frac{1+e}{1-e}} \tan\frac{E}{2} \tag{E.6}$$

The Sun Longitude ($\lambda_\odot$), in Ecliptic Coordinates, is given by

$$\lambda_\odot = \nu + \varpi_g \tag{E.7}$$

With the true anomaly (ν), we can easily calculate the Sun-Earth distance (r):

$$r = r_0 \frac{1 - e^2}{1 + e \cos\nu} \tag{E.8}$$

where $r_0 = 1.495985 \times 10^{13}$ cm is the semi-major axis of the Earth-Sun Orbit.

E.3 Frame Transformations

In general a transformation between two reference systems may be performed using an arithmetic matrix (Hapgood, 1992). For each transformation we define a matrix $\mathbf{T}$ such that $\mathbf{q}_2 = \mathbf{T}\mathbf{q}_1$, where $\mathbf{q}_1$ is the Old vector and $\mathbf{q}_2$ is the New vector in cartesian coordinates:

$$\mathbf{q}_2 = \begin{bmatrix} x_2 \\ y_2 \\ z_2 \end{bmatrix} = \begin{bmatrix} t_{11} & t_{12} & t_{13} \\ t_{21} & t_{22} & t_{23} \\ t_{31} & t_{32} & t_{33} \end{bmatrix} \begin{bmatrix} x_1 \\ y_1 \\ z_1 \end{bmatrix} = \mathbf{T}\mathbf{q}_1 \tag{E.9}$$

Thus the problem reduces to the determination of the nine components t_{ij} of the matrix $\mathbf{T}$ for each specific transformation; these t_{ij} can be seen as the components of the New principal axes in the Old reference system. Thus each row of the matrix $\mathbf{T}$ in equation (E.9), are the coordinates,

in the Old coordinate system, of New $\hat{X}$, $\hat{Y}$, $\hat{Z}$ unit vectors axes:

$$\hat{X} = (t_{11}, t_{12}, t_{13}) \tag{E.10}$$

$$\hat{Y} = (t_{21}, t_{22}, t_{23}) \tag{E.11}$$

$$\hat{Z} = (t_{31}, t_{32}, t_{33}) \tag{E.12}$$

As remarked in Hapgood (1992), this approach has several advantages: (a) a transformation $\mathbf{T}$ may be reversed applying the inverse matrix $\mathbf{T}^{-1}$ which is simply the transposed of $\mathbf{T}$; (b) a transformation from a system $\mathbf{A}$ to the system $\mathbf{C}$ may be performed by first transforming to an intermediate system $\mathbf{B}$ and then to the system $\mathbf{C}$, thus we may multiply the matrices to obtain the whole transformation:

$$\mathbf{T_{AC}} = \mathbf{T_{BC}}\mathbf{T_{AB}}. \tag{E.13}$$

This also means that it is possible to move from ecliptic to AMS-02 frame passing by intermediate frames or with an unique transformation obtained multiplying the respective transformation matrices. So that the coordinates transformation from the ECI frame (i.e. Right Ascension and declination coordinates) to AMS-02 could be summarized with the sequence

$$\mathbf{T}_{ECI \to AMS-02} = \mathbf{T}_{LVLH \to AMS-02}\mathbf{T}_{ECI \to LVLH} \tag{E.14}$$

Some times the position of and orbit object (the so called State Vector) is given in GTOD Longitude and Latitude. To convert the state vector into ECI Right Ascension and Declination a simple rotation of the Cartesian coordinates around the $\hat{Z}$ axis is required,

$$\mathbf{q}_{ECI} = \mathbf{T}_{GTOD \to ECI}\mathbf{q}_{GTOD} \tag{E.15}$$

the rotation matrix is (Bhavnani and Vancour, 1991; Hapgood, 1992; Franz and Harper, 2002):

$$\mathbf{T}_{GTOD \to ECI} = \begin{bmatrix} \cos(\theta_{GMST}) & -\sin(\theta_{GMST}) & 0 \\ \sin(\theta_{GMST}) & \cos(\theta_{GMST}) & 0 \\ 0 & 0 & 1 \end{bmatrix}, \tag{E.16}$$

where θ_{GMST}, expressed in radians, is the Greenwich Mean Sidereal Time, defined by the angle between the Greenwich Meridian and the Aries Point of Date, measured eastward from the Aries Point in the equatorial plane (Meuss, 2000; Franz and Harper, 2002):

$$\theta_{GMST} \approx 280.46061837^\circ + 360.98564736629^\circ \cdot d_J + T_J^2 \cdot (0.000387933^\circ - T_J \cdot (1/38710000.0)^\circ) \tag{E.17}$$

where T_J is the number of Julian centuries since epoch J2000, and d_J is the number of Julian Days from J2000. Note that for very high precision measurements, correction for nutation and precession should be applied as well. The global effect is a Precession of the Equinox of about $12''$ per century and a decrease in the obliquity of about $47''$ per century (see page 15 of Lang, 1999)

Then to pass to the LVLH reference frame, one remind that it is defined by means of the Orbital

Object radial position vector $\mathbf{R}$ and its velocity vector $\mathbf{V}$ given in ECI coordinates. By definition, the $\hat{Z}$ axis is collinear with the position vector (from the vehicle to the geographic center of the Earth) and they have opposite sign; moreover $\hat{Z}$ and $\hat{X}$ form the instantaneous orbit plane of the orbital object, thus (Bhavnani and Vancour, 1991; Suter, 1998):

$$\hat{Z} = \frac{-\mathbf{R}}{|\mathbf{R}|}, \tag{E.18}$$

$$\hat{Y} = \frac{\hat{Z} \times \mathbf{V}}{|\hat{Z} \times \mathbf{V}|}, \tag{E.19}$$

$$\hat{X} = \hat{Y} \times \hat{Z}. \tag{E.20}$$

which corresponds to a rotation of the axis, according to the instantaneous position of the flight object. In addition we have to take into account a translation of coordinates of the origin ($\mathbf{P}$) from the center of the Earth to the Orbital Object:

$$\mathbf{q}_{LVLH} = \mathbf{T}_{ECI \to LVLH} \left(\mathbf{q}_{ECI} + \mathbf{P}_{Earth \to Orbit} \right) \tag{E.21}$$

$$\mathbf{T}_{ECI \to LVLH} = \begin{bmatrix} \hat{X} \\ \hat{Y} \\ \hat{Z} \end{bmatrix}; \qquad \mathbf{P}_{Earth \to Orbit} = \begin{bmatrix} -R_x \\ -R_y \\ -R_z \end{bmatrix} \tag{E.22}$$

where $\hat{X}$, $\hat{Y}$ and $\hat{Z}$ are the unity LVLH vectors defined by Eqs.(E.18)–(E.20). Here we neglect any small eccentricity of the Orbit which makes $\mathbf{R}$ and $\mathbf{V}$ not exactly perpendicular to each other. We remark that, if the Orbital Object radial position vector $\mathbf{R}$ and its velocity vector $\mathbf{V}$ are given directly in the GTOD frame, one should convert the position and velocity vector using Eq. (E.15) with thenprocedure described in Figure 4-1 of (GREEN BOOK, 2010).

Finally the last term in Eq. (E.14) consider the attitude of the Orbital Object with respect the orbital plane ($\mathbf{T}_{LVLH \to ISS}$), the displacement of the Payload on it ($\mathbf{P}_{ISS \to AMS\,Origin}$), and the inclination of Payload frame ($\mathbf{T}_{AMS\,Origin \to AMS\,frame}$).

$$\mathbf{q}_{AMS-02} = \mathbf{T}_{AMS\,Origin \to AMS\,frame} \left(\mathbf{T}_{LVLH \to ISS}\, \mathbf{q}_{LVLH} + \mathbf{P}_{ISS \to AMS\,Origin} \right) \tag{E.23}$$

The attitude determination is exclusively concerned with the definition of the angular or rotational orientation of the object (which is usually the observer) with respect to the LVLH coordinate system (Bhavnani and Vancour, 1991). Usually this rotation is given by a sequence of Euler angles called, Yaw, Pitch and Roll[5]. Each rotation takes place around the specified axis in the intermediate reference frame which is defined by the previous rotation. In addition they are non-commutative, i.e. the angles used to reach a final orientation depend on the sequence of the specific axes (Bhavnani and Vancour, 1991). The ISS attitude is given by rotations from LVLH in the order Yaw (φ_Y), Pitch (φ_P) and Roll (φ_R) (NASA, 2001), so the transformation matrix is (Wisniewski,

[5]They are the rotation around $\hat{Z}$, $\hat{Y}$ and $\hat{X}$ axis respectively.

2000; Suter, 1998):

$$\mathbf{T}_{LVLH\to ISS} = \begin{bmatrix} 1 & 0 & 0 \\ 0 & \cos\varphi_R & \sin\varphi_R \\ 0 & -\sin\varphi_R & \cos\varphi_R \end{bmatrix} \begin{bmatrix} \cos\varphi_P & 0 & -\sin\varphi_P \\ 0 & 1 & 0 \\ \sin\varphi_P & 0 & \cos\varphi_P \end{bmatrix} \begin{bmatrix} \cos\varphi_Y & \sin\varphi_Y & 0 \\ -\sin\varphi_Y & \cos\varphi_Y & 0 \\ 0 & 0 & 1 \end{bmatrix} \tag{E.24}$$

where we neglected the difference origin position between SSBCS and SSACS. The translation of the origin to the Payload position can be performed using the vector :

$$\mathbf{P}_{ISS\to AMS\,Origin} = \begin{bmatrix} +85.598 \\ -2136.390 \\ +388.112 \end{bmatrix} \tag{E.25}$$

with distances expressed in cm. Finally to convert to AMS-02 reference frame one first have to apply an intermediate transformation that rotate the axis from ISS to AMS directions:

$$\begin{bmatrix} \hat{X}_{int.} \\ \hat{Y}_{int.} \\ \hat{Z}_{int.} \end{bmatrix} = \begin{bmatrix} 0 & -1 & 0 \\ -1 & 0 & 0 \\ 0 & 0 & -1 \end{bmatrix} \begin{bmatrix} \hat{X} \\ \hat{Y} \\ \hat{Z} \end{bmatrix} = \begin{bmatrix} -\hat{Y} \\ -\hat{X} \\ -\hat{Z} \end{bmatrix} \tag{E.26}$$

then the frame is tilted of an angle ϑ_A respect to the ISS Starboard segment. The rotation matrix has to be applied around the intermediate axis $\hat{Y}_{int.}$ axis:

$$\mathbf{T}_{AMS\,Origin\to AMS\,frame} = \begin{bmatrix} \cos\vartheta_A & 0 & -\sin\vartheta_A \\ 0 & 1 & 0 \\ \sin\vartheta_A & 0 & \cos\vartheta_A \end{bmatrix} \begin{bmatrix} 0 & -1 & 0 \\ -1 & 0 & 0 \\ 0 & 0 & -1 \end{bmatrix}. \tag{E.27}$$

Eq. (E.14) is then obtained neglecting the translations of the origin. This procedure could be applied to any kind of sources that one to project into AMS-02 frame. The opposite transformation (e.g. to obtain ECI coordinates of an High Energy event observed by AMS-02) can be performed using the inverse matrix of (E.14), i.e.:

$$\mathbf{T}_{AMS-02\to ECI} = \mathbf{T}^{-1}_{ECI\to AMS-02} \tag{E.28}$$

E.3.1 Sun from AMS-02

A special case applied for AMS-02 was to evaluate the Sun position as seen by the detector. As seen in Sect. E.2 the Sun Ephemeris could be easily calculate in Ecliptic frame.

The Ecliptic longitude (λ), and the ecliptic latitude (β) may be converted into Right Ascension (α) and Declination (δ) directly by (Lang, 1999; Duffett-Smith and Zwart, 2011):

$$\alpha = \arctan\left(\frac{\sin\lambda\cos\varepsilon - \tan\beta_e\sin\varepsilon}{\cos\lambda}\right) \tag{E.29}$$

$$\delta = \arcsin(\sin\beta_e\cos\varepsilon + \cos\beta_e\sin\varepsilon\sin\lambda) \tag{E.30}$$

where ε is the obliquity of the ecliptic, i.e. the angle between the equator and the ecliptic planes. This angle, that at epoch J2000 has a mean value of $23°26'21.448''$ (Lang, 1999; Alan, 2000), changes slowly with time and for more precise calculation the appropriate value should be used. The Mean Obliquity of the ecliptic for any date is given by the equation (Duffett-Smith and Zwart, 2011):

$$\varepsilon = 23.43929167^{\circ} + \left(\frac{46.815}{3600}\right)^{\circ} \cdot T_J + \left(\frac{0.0006}{3600}\right)^{\circ} \cdot T_J^2 - \left(\frac{0.00181}{3600}\right)^{\circ} \cdot T_J^3; \tag{E.31}$$

where T_J is the number of Julian centuries since epoch J2000, i.e 12h00m UT of 1st January 2000 ($JD_J = 2451545.0$). To increase the accuracy of the calculation, the nutation has to be taken into account as well. The nutation is a small periodic motion caused by the variation of distances and relative directions of the Moon and Sun. Daily values for the nutation in longitude and obliquity are given in Alan (2000) for the specific year with a precision of about $1''$. Approximate expressions for the nutation, with the same precision of about $1''$, can be found in Lang (1999) and Duffett-Smith and Zwart (2011).

Once known the coordinates of the Sun in ECI frame, it is possible to get the same in AMS-02 using Eq. (E.14). The position, the velocity vector in the GTOD frame as well the attitude of the ISS with respect LVLH frame are obtained by ISS telemetry, available to AMS-02 collaboration. In fig E.2 it is possible to see the typical example of the Sun position that one can obtain by applying this sequence of transformations.

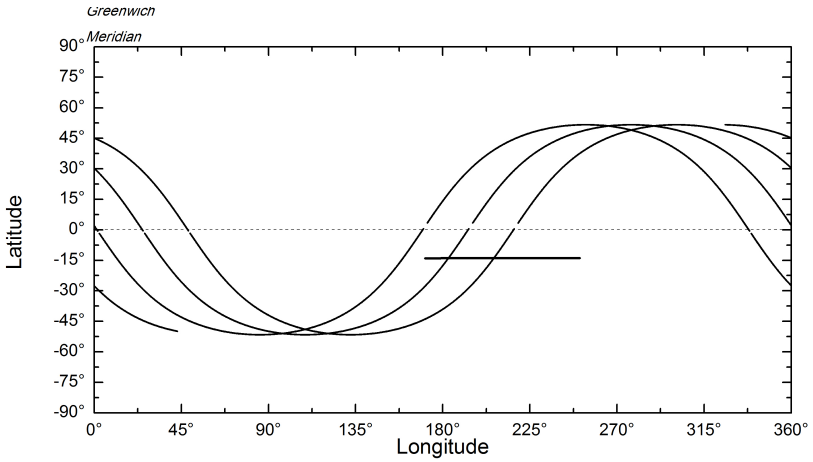

(a) ISS (dotted line) and Sun (solid line) Position in GTOD coordinates; dashed line is the Earth equator;

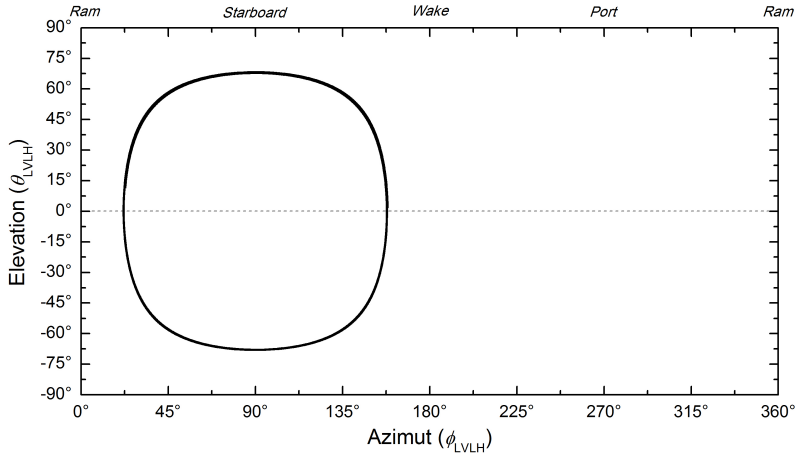

(b) Sun (solid line) Position in LVLH coordinates; dashed line is the instantaneous plane of the orbit;

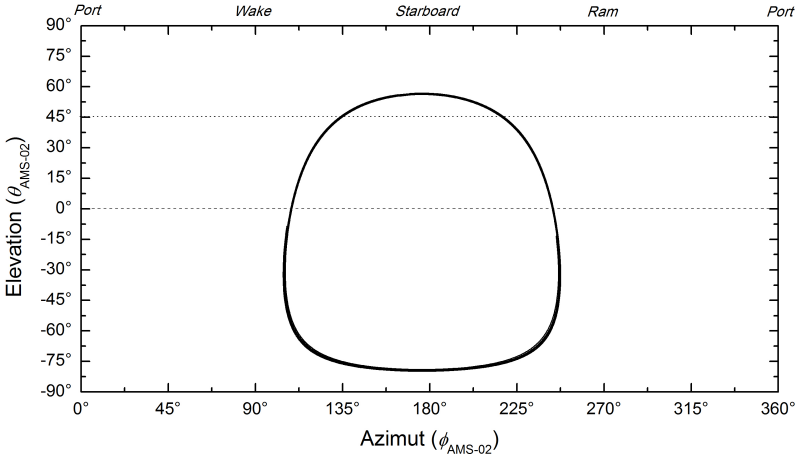

(c) Sun (solid line) Position in AMS-02 coordinates; dashed line is the $\hat{X}\hat{Y}$ plane, the region above the dotted line (45°-90°) is the geometrical field of view of AMS-02

Figure E.2: Sun Position calculate from 18h01m UTC 30th October 2011 to 00h21m UTC 31th October 2011 in (a) GTOD, (b) LVLH and (c) AMS-02 coordinates

Bibliography

Abbasi, R. U., Abu-Zayyad, T., Amann, J. F., and HiRes Collaboration (2004). Measurement of the Flux of Ultrahigh Energy Cosmic Rays from Monocular Observations by the High Resolution Fly's Eye Experiment. *Phys. Rev. Lett.*, 92(15):151101.

Abe, K., Sanuki, T., Anraku, K., and Collaboration, B. (2003). Measurements of proton, helium and muon spectra at small atmospheric depths with the BESS spectrometer. *Phys. Lett. B*, 564:8–20.

Abraham, J., Aglietta, M., Aguirre, I. C., and The Pierre Auger Collaboration (2004). Properties and performance of the prototype instrument for the Pierre Auger Observatory. *Nucl. Instrum. Meth. A*, 523:50–95.

Achterberg, A. and Krulls, W. M. (1992). A fast simulation method for particle acceleration. *Astron. Astrophys.*, 265:L13–L16.

Ackermann, M., Ajello, M., Atwood, W. B., and FERMI Collaboration (2010). Searches for cosmic-ray electron anisotropies with the Fermi Large Area Telescope. *Phys. Rev. D*, 82(9):092003.

Adriani, O., Barbarino, G. C., Bazilevskaya, G. A., and PAMELA Collaboration (2009). An anomalous positron abundance in cosmic rays with energies 1.5-100 GeV. *Nature*, 458(7238):607–609.

Adriani, O., Barbarino, G. C., Bazilevskaya, G. A., and PAMELA Collaboration (2010). PAMELA Results on the Cosmic-Ray Antiproton Flux from 60 MeV to 180 GeV in Kinetic Energy. *Phys. Rev. Lett.*, 105(12):121101.

Adriani, O., Barbarino, G. C., Bazilevskaya, G. A., and PAMELA Collaboration (2011). PAMELA Measurements of Cosmic-Ray Proton and Helium Spectra. *Science*, 332:69.

Aguilar, M., Alcaraz, J., Allaby, J., and AMS Collaboration (2002). The Alpha Magnetic Spectrometer (AMS) on the International Space Station: Part I - results from the test flight on the space shuttle. *Phys. Rep.*, 366:331–405.

Aguilar, M., Alcaraz, J., Allaby, J., and AMS Collaboration (2007). Cosmic-ray positron fraction measurement from 1 to 30 GeV with AMS-01. *Phys. Lett. B*, 646(4):145–154.

Aguilar, M., Alcaraz, J., Allaby, J., and AMS Collaboration (2010). Relative Composition and Energy Spectra of Light Nuclei in Cosmic Rays: Results from AMS-01. *Astrophys. J.*, 724:329–340.

Aguilar, M., Alcaraz, J., Allaby, J., and AMS Collaboration (2011). Isotopic Composition of Light Nuclei in Cosmic Rays: Results from AMS-01. *Astrophys. J.*, 736:105.

Alan, F. (2000). *Astronomical Almanac*. check it!

Alania, M. V. (2002). Stochastic Variations of Galactic Cosmic Rays. *Acta. Phys. Pol. A*, 33:1149.

Alanko-Huotari, K., Usoskin, I. G., Mursula, K., and Kovaltsov, G. A. (2007a). Cyclic variations of the heliospheric tilt angle and cosmic ray modulation. *Adv. Space Res.*, 40:1064–1069.

Alanko-Huotari, K., Usoskin, I. G., Mursula, K., and Kovaltsov, G. A. (2007b). Stochastic simulation of cosmic ray modulation including a wavy heliospheric current sheet. *J. Geophys. Res.*, 112(A8).

Alcaraz, J., Alpat, B., Ambrosi, G., and AMS Collaboration (2000). Leptons in near earth orbit. *Phys. Lett. B*, 484:10–22.

Alfvén, H. (1942). Existence of Electromagnetic-Hydrodynamic Waves. *Nature*, 150:405–406.

Alfvén, H. (1977). Electric currents in cosmic plasmas. *Rev. Geophys. Space Ge.*, 15:271–284.

Antoni, T., Apel, W. D., Badea, A. F., and KASCADE Collaboration (2005). KASCADE measurements of energy spectra for elemental groups of cosmic rays: Results and open problems. *Astropart. Phys.*, 24:1–25.

Armstrong, T. P., Pesses, M. E., and Decker, R. B. (1985). Shock drift acceleration. *Washington DC American Geophysical Union Geophysical Monograph Series*, 35:271–285.

Asaoka, Y., Abe, K., Yoshimura, K., Ishino, M., Fujikawa, M., and Orito, S. (1998). Development of a large-area aerogel Cherenkov counter onboard BESS. *Nucl. Instrum. Meth. A*, 416:236–242.

Aschwanden, M. J. (2006). *The Sun, Encyclopedia of the Solar System*. San Diego, CA: Academic Press.

Ave, M., Boyle, P. J., Gahbauer, F., Höppner, C., Hörandel, J. R., Ichimura, M., Müller, D., and Romero-Wolf, A. (2008). Composition of Primary Cosmic-Ray Nuclei at High Energies. *Astroph. J.*, 678:262–273.

Axford, W. I. (1981). Acceleration of cosmic rays by shock waves. In *International Cosmic Ray Conference*, volume 12, pages 155–203.

Babcock, H. W. and Babcock, H. D. (1955). The Sun's Magnetic Field, 1952-1954. *Astroph. J.*, 121:349.

Balogh, A., Marsden, R. G., and Smith, E. J. (2001). *The heliosphere near solar minimum. The Ulysses perspective*. Springer-Praxis Books in Astrophysics and Astronomy.

Balogh, A., Smith, E. J., Tsurutani, B. T., Southwood, D. J., Forsyth, R. J., and Horbury, T. S. (1995). The Heliospheric Magnetic Field Over the South Polar Region of the Sun. *Science*, 268:1007–1010.

Battiston, R. (2010). The Anti Matter Spectrometer (AMS-02):. a Particle Physics Detector in Space. In Leroy, C., Rancoita, P.-G., Barone, M., Gaddi, A., Price, L., and Ruchti, R., editors, *Astroparticle, Particle and Space Physics, Detectors and Medical Physics Applications*, pages 741–750.

Bhavnani, K. H. and Vancour, R. P. (1991). Coordinate system for space and geophysical applications. Technical report, US Air Force Systems Command - PL-TR-91-229.

Bieber, J. W. and Matthaeus, W. H. (1997). Perpendicular Diffusion and Drift at Intermediate Cosmic-Ray Energies. *Astrophys. J.*, 485:655.

Biermann, L. (1951). Kometenschweife und solare Korpuskularstrahlung. *Zeitschrift für Astrophysik*, 29:274.

Biermann, L. (1957). Solar Corpuscular Radiation and the Interplanetary Gas. *Observatory*, 77:109–110.

Biermann, L. (1961). The Solar Wind and the Interplanetary Media. In Liller, W., editor, *Space Astrophysics*, page 150. McGraw-Hill.

Blanco-Muriel, M., Alarcòn-Padilla, D., Lòpez-Moratalla, T., and Lara-Coira, M. (2001). Computing the solar vector. *Solar Energy*, 70(5):431–441.

Blandford, R. D. and Ostriker, J. P. (1980). Supernova shock acceleration of cosmic rays in the Galaxy. *Astroph. J.*, 237:793–808.

Blumenthal, G. R. and Gould, R. J. (1970). Bremsstrahlung, Synchrotron Radiation, and Compton Scattering of High-Energy Electrons Traversing Dilute Gases. *Rev. Mod. Phys.*, 42:237–271.

Bobik, P., Boella, G., Boschini, M. J., Consolandi, C., Della Torre, S., Gervasi, M., Grandi, D., Elmo, M., Kudela, K., Memola, E., Pensotti, S., Rancoita, P. G., Rozza, D., and Tacconi, M. (2011a). Energy Loss for Electrons in the Heliosphere and Local Interstellar Spectrum for Solar Modulation. In Giani, S., Leroy, C., and Rancoita, P. G., editors, *Cosmic Rays for Particle and Astropart. Phys.*, pages 482–489.

Bobik, P., Boella, G., Boschini, M. J., Consolandi, C., Della Torre, S., Gervasi, M., Grandi, D., Kudela, K., Pensotti, S., Rancoita, P. G., and Tacconi, M. (2012a). Systematic Investigation of Solar Modulation of Galactic Protons for Solar Cycle 23 Using a Monte Carlo Approach with Particle Drift Effects and Latitudinal Dependence. *Astrophys. J.*, 745:132.

Bobik, P., Boella, G., Boschini, M. J., Gervasi, M., Grandi, D., Kudela, K., Pensotti, S., and Rancoita, P. G. (2006). Magnetospheric transmission function approach to disentangle primary from secondary cosmic ray fluxes in the penumbra region. *J. Geophys. Res.-Space*, 111:5205.

Bobik, P., Boschini, M. J., Consolandi, C., Della Torre, S. Gervasi, M., Grandi, D., Kudela, K., Noventa, F., Pensotti, S., Rancoita, P. G., and Rozza, D. (2012b). Cosmic Rays propagation in the Heliosphere. In S. Giani, C. Leroy, L. Price, P.-G. Rancoita & R. Ruchti, editor, *Astroparticle, Particle, Space Physics, and Detectors for Physics Applications - Vol. 7*, pages 226–231. World Scientific.

Bobik, P., Boschini, M. J., Consolandi, C., Della Torre, S., Gervasi, M., Grandi, D., Kudela, K., Noventa, F., Pensotti, S., Rancoita, P. G., and Rozza, D. (2012c). Heliosphere Dimension and Cosmic Ray Modulation. In S. Giani, C. Leroy, L. Price, P.-G. Rancoita & R. Ruchti, editor, *Astroparticle, Particle, Space Physics, and Detectors for Physics Applications - Vol. 7*, pages 249–257. World Scientific.

Bobik, P., Boschini, M. J., Consolandi, C., Della Torre, S., Gervasi, M., Grandi, D., Kudela, K., Pensotti, S., and Rancoita, P. G. (2011b). Antiproton modulation in the Heliosphere and AMS-02 antiproton over proton ratio prediction. *Astrophys. Space Sci. Trans.*, 7(3):245–249.

Bobik, P., Boschini, M. J., Consolandi, C., Della Torre, S., Gervasi, M., Grandi, D., Kudela, K., Pensotti, S., Rancoita, P. G., Rozza, D., and Tacconi, M. (2012d). Polar Interplanetary Magnetic Field Correction for the Heliosphere cosmic ray modulation Monte Carlo model. *Submitted to Advances in Astronomy.*

Bobik, P., Boschini, M. J., Della Torre, S., Gervasi, M., Grandi, D., Kudela, K., and Rancoita, P. G. (2010). Galactic Cosmic Rays Modulation and Prediction for the AMS-02 Mission. In Leroy, C., Rancoita, P.-G., Barone, M., Gaddi, A., Price, L., and Ruchti, R., editors, *Astroparticle, Particle and Space Physics, Detectors and Medical Physics Applications*, pages 210–219.

Bobik, P., Kudela, K., Boschini, M., Grandi, D., Gervasi, M., and Rancoita, P. G. (2008). Solar modulation model with reentrant particles. *Adv. Space Res.*, 41:339–342.

Boella, G., Gervasi, M., Mariani, S., Rancoita, P., and Usoskin, I. (2001). Evidence for charge drift modulation at intermediate solar activity from the flux variation of protons and alpha particles. *J. Geophys. Res. A21*, 106:29355.

Boezio, M., Carlson, P., Francke, T., and CAPRICE Collaboration (1999). The Cosmic-Ray Proton and Helium Spectra between 0.4 and 200 GV. *Astroph. J.*, 518:457–472.

Boezio, M., Pearce, M., Picozza, P., and PAMELA Collaboration (2009). PAMELA and indirect dark matter searches. *New J. Phys.*, 11(10):105023.

Brajsa, R., Vrsnak, B., Ruzdjak, V., Rosa, D., Hrzina, D., Wöhl, H., Clette, F., and Hochedez, J.-F. (2001). An Analysis of the Solar Rotation Velocity by Tracing Coronal Features. In Brekke, P., Fleck, B., and Gurman, J. B., editors, *Recent Insights into the Physics of the Sun and*

Heliosphere: Highlights from SOHO and Other Space Missions, volume 203 of *IAU Symposium*, page 377.

Brianza, L. (2011). *Modulazione di elettroni e positroni in eliosfera con AMS-02.* Bachelor's thesis, Department of Physics, University of Milano-Bicocca, Milano, Italy.

Burger, R. A., Ferreira, S. E. S., Bieber, J. W., Engel, R., Gaisser, T. K., and Stanev, T. (2001). The antiproton to proton ratio over a 22-year cycle: a time dependent approach. In *International Cosmic Ray Conference*, volume 9, page 3661.

Burger, R. A. and Hattingh, M. (1995). Steady-State Drift-Dominated Modulation Models for Galactic Cosmic Rays. *Astroph. and Sp. Sc.*, 230:375–382.

Burger, R. A. and Hattingh, M. (2001). Effect of Fisk-type heliospheric magnetic fields on the latitudinal transport of cosmic rays. In *International Cosmic Ray Conference*, volume 9, page 3698.

Burger, R. A., Krüger, T. P. J., Hitge, M., and Engelbrecht, N. E. (2008). A Fisk-Parker Hybrid Heliospheric Magnetic Field With a Solar-Cycle Dependence. *Astrophys. J.*, 674:511–519.

Burger, R. A., Moraal, H., and Webb, G. M. (1985). Drift theory of charged particles in electric and magnetic fields. *Astrophys. Space Sci.*, 116:107–129.

Burger, R. A. and Potgieter, M. S. (1989). The calculation of neutral sheet drift in two-dimensional cosmic-ray modulation models. *Astrophys. J.*, 339(1):501–511.

Burger, R. A., Potgieter, M. S., and Heber, B. (2000). Rigidity dependence of cosmic ray proton latitudinal gradients measured by the Ulysses spacecraft: Implications for the diffusion tensor. *J. Geophys. Res.*, 105:27447–27456.

Burger, R. A. and Visser, D. J. (2010). Reduction of Drift Effects due to Solar Wind Turbulence. *Astrophys. J.*, 725:1366–1372.

Burlaga, L. F. and Ness, N. F. (1993). Large-scale distant heliospheric magnetic field: Voyager 1 and 2 observations from 1986 through 1989. *J. Geophys. Res.*, 98:17451–17460.

Büsching, I. and Potgieter, M. S. (2008). The variability of the proton cosmic ray flux on the Sun's way around the galactic center. *Adv. Space Res.*, 42:504–509.

Caballero-Lopez, R. A. and Moraal, H. (2004). Limitations of the force field equation to describe cosmic ray modulation. *J. Geophys. Res.-Space*, 109:1101.

Casolino, M., Picozza, P., Altamura, F., and PAMELA Collaboration (2008). Launch of the space experiment PAMELA. *Adv. Space Res.*, 42:455–466.

CDAweb (2012). Coordinated data analysis web database http://cdaweb.gsfc.nasa.gov/istp_public/.

Chandrasekhar, S. (1943). Stochastic Problems in Physics and Astronomy. *Rev. Mod. Phys.*, 15:1–89.

Chang, J., Adams, J. H., Ahn, H. S., and ATIC Collaboration (2008). An excess of cosmic ray electrons at energies of 300-800GeV. *Nature*, 456:362–365.

Clem, J. M. and Dorman, L. I. (2000). Neutron Monitor Response Functions. *Space Sci. Rev.*, 93:335–359.

Cliver, E. W. (2000). Solar energetic particles: Acceleration and transport. In Dingus, B. L., Kieda, D. B., and Salamon, M. H., editors, *26th International Cosmic Ray Conference, ICRC XXVI*, volume 516 of *American Institute of Physics Conference Series*, pages 103–119.

Cranmer, S. R., Kohl, J. L., Noci, G., and Collaborators (1999). An Empirical Model of a Polar Coronal Hole at Solar Minimum. *Astroph. J.*, 511:481–501.

Cravens, T. E. (1997). *Physics of solar system plasmas*. Cambridge : Cambridge University Press, 1997. QB 529 C72 1997. DA.

Crooker, N. U., Siscoe, G. L., Shodhan, S., Webb, D. F., Gosling, J. T., and Smith, E. J. (1993). Multiple heliospheric current sheets and coronal streamer belt dynamics. *J. Geophys. Res.*, 98:9371–9381.

Davis, Jr., L. (1972). The Interplanetary Magnetic Field. *NASA Special Publication*, 308:93.

De Simone, N., Di Felice, V., Gieseler, J., Boezio, M., Casolino, M., Picozza, P., Heber, B., and PAMELA Collaboration (2011). Latitudinal and radial gradients of galactic cosmic ray protons in the inner heliosphere - PAMELA and Ulysses observations. *Astrophys. Space Sci. Trans.*, 7:425–434.

Decker, R. B., Krimigis, S. M., Roelof, E. C., Hill, M. E., Armstrong, T. P., Gloeckler, G., Hamilton, D. C., and Lanzerotti, L. J. (2005). Voyager 1 in the Foreshock, Termination Shock, and Heliosheath. *Science*, 309:2020–2024.

Delahaye, T., Lavalle, J., Lineros, R., Donato, F., and Fornengo, N. (2010). Galactic electrons and positrons at the Earth: new estimate of the primary and secondary fluxes. *Astron. Astrophys.*, 524:A51.

Della Torre, S., Bobik, P., Boschini, M. J., Consolandi, C., Gervasi, M., Grandi, D., Kudela, K., Pensotti, S., Rancoita, P. G., Rozza, D., and Tacconi, M. (2012a). Effects of solar modulation on the cosmic ray positron fraction. *Adv. Space Res.*, 49:1587–1592.

Della Torre, S., Consolandi, C., and Grandi, D. (2012b). AMS Note 2012-02-01 - Coordinates and Sun Position for AMS-02. Internal note, AMS Collaboration.

Dröge, W. (2005). Probing heliospheric diffusion coefficients with solar energetic particles. *Adv. Space Res.*, 35:532–542.

Dröge, W., Kartavykh, Y. Y., Klecker, B., and Kovaltsov, G. A. (2010). Anisotropic Three-Dimensional Focused Transport of Solar Energetic Particles in the Inner Heliosphere. *Astroph. J.*, 709:912–919.

Duffett-Smith, P. and Zwart, J. (2011). *Pratical Astronomy with your Calculator or spreadsheet.* Cambrige University Press.

Dunzlaff, P., Kopp, A., and Heber, B. (2010). Propagation of Jovian electron jets in heliospheric flux tube structures. *J. Geophys. Res.-Space*, 115:10106.

Engelbrecht, N. (2008). On the heliospheric diffusion tensor and its effect on 26 day recurrent cosmic rays variation. *Ph.D. Thesis, Potchestroom Campus of North-West University.*

Engelbrecht, N. E. and Burger, R. A. (2010). Effects of various dissipation range onset models on the 26-day variations of low-energy galactic cosmic-ray electrons. *Adv. Space Res.*, 45:1015–1025.

Fermi, E. (1949). On the Origin of the Cosmic Radiation. *Phys. Rev.*, 75:1169–1174.

Ferrando, P., Raviart, A., Haasbroek, L. J., Potgieter, M. S., Droege, W., Heber, B., Kunow, H., Mueller-Mellin, R., Sierks, H., Wibberenz, G., and Paizis, C. (1996). Latitude variations of $\approx$7MeV and >300MeV cosmic ray electron fluxes in the heliosphere: ULYSSES COSPIN/KET results and implications. *Astron. Astrophys.*, 316:528–537.

Ferreira, S. E., Potgieter, M. S., Burger, R. A., Heber, B., and Fichtner, H. (2001a). Modulation of Jovian and galactic electrons in the heliosphere: 1. Latitudinal transport of a few MeV electrons. *J. Geophys. Res.*, 106:24979–24988.

Ferreira, S. E. S. (2005). The transport of galactic and jovian cosmic ray electrons in the heliosphere. *Adv. Space Res.*, 35:586–596.

Ferreira, S. E. S. and Potgieter, M. S. (2003). Modulation over a 22-year cosmic ray cycle: On the tilt angles of the heliospheric current sheet. *Adv. Space Res.*, 32:657–662.

Ferreira, S. E. S. and Potgieter, M. S. (2004). Long-Term Cosmic-Ray Modulation in the Heliosphere. *Astrophys. J.*, 603:744–752.

Ferreira, S. E. S., Potgieter, M. S., Burger, R. A., Heber, B., Fichtner, H., and Lopate, C. (2001b). Modulation of Jovian and galactic electrons in the heliosphere: 2. Radial transport of a few MeV electrons. *J. Geophys. Res.*, 106:29313–29322.

Ferreira, S. E. S., Potgieter, M. S., and Scherer, K. (2007). Transport and acceleration of anomalous cosmic rays in the inner heliosheath. *J. Geophys. Res.-Space*, 112:11101.

Fichtner, H., Le Roux, J. A., Mall, U., and Rucinski, D. (1996). On the transport of pick-up ions in the heliosphere. *Astron. Astrophys.*, 314:650–662.

Fichtner, H., Potgieter, M., Ferreira, S., and Burger, A. (2000). On the propagation of Jovian electrons in the heliosphere: transport modelling in 4-D phase space. *Geophys. Res. Lett.*, 27:1611.

Fichtner, H. and Scherer, K. (2000). The heliosphere: a brief overview. In Scherer, K., Fichtner, H., and Marsch, E., editors, *The Outer Heliosphere: Beyond the Planets*, pages 1–12.

Fichtner, H., Sreenivasan, S. R., and Fahr, H. J. (1996). Cosmic ray modulation and a non-spherical heliospheric shock. *Astron. Astrophys.*, 308:248–260.

Fisk, L. A. (1971). Solar modulation of galactic cosmic rays, 2. *J. Geophys. Res.*, 76:221.

Fisk, L. A. (1996). Motion of the footpoints of heliospheric magnetic field lines at the Sun: Implications for recurrent energetic particle events at high heliographic latitudes. *J. Geophys. Res.*, 101:15547–15554.

Fisk, L. A. and Gloeckler, G. (2009). The acceleration of Anomalous Cosmic Rays by stochastic acceleration in the heliosheath. *Adv. Space Res.*, 43:1471–1478.

Fisk, L. A., Kozlovsky, B., and Ramaty, R. (1974). An Interpretation of the Observed Oxygen and Nitrogen Enhancements in Low-Energy Cosmic Rays. *Astroph. J. Letter*, 190:L35.

Flückiger, E. O., Moser, M. R., Pirard, B., and et al. (2008). A parameterized neutron monitor yield function for space weather applications. In *International Cosmic Ray Conference*, volume 1, pages 289–292.

Forbush, S. E. (1946). Three Unusual Cosmic-Ray Increases Possibly Due to Charged Particles from the Sun. *Phys. Rev.*, 70:771–772.

Fransson, C. and Epstein, R. I. (1980). Acceleration and propagation of cosmic rays. *Astroph. J.*, 242:411–415.

Franz, M. and Harper, D. (2002). Heliospheric coordiante system. *Planet. Space Sci.*, (50):217–233.

Freier, P., Lofgren, E. J., Ney, E. P., Oppenheimer, F., Bradt, H. L., and Peters, B. (1948). Evidence for Heavy Nuclei in the Primary Cosmic Radiation. *Phys. Rev.*, 74:213–217.

Gaensler, B. M. and Slane, P. O. (2006). The Evolution and Structure of Pulsar Wind Nebulae. *Annu. Rev. Astron. Astr.*, 44:17–47.

Garcia-Munoz, M., Mason, G. M., and Simpson, J. A. (1973). A New Test for Solar Modulation Theory: the 1972 May-July Low-Energy Galactic Cosmic-Ray Proton and Helium Spectra. *Astroph. J. Letter*, 182:L81.

Garcia-Munoz, M., Meyer, P., Pyle, K. R., Simpson, J. A., and Evenson, P. (1986). The dependence of solar modulation on the sign of the cosmic ray particle charge. *J. Geophys. Res.*, 91:2858–2866.

Gardiner, C. (1985). *Handbook of stochastic methods: for physics, chemistry and natural sciences.* Springer Edition.

Gazis, P. R., Barnes, A., Mihalov, J. D., and Lazarus, A. J. (1992). The structure of the inner heliosphere from Pioneer Venus and IMP observations. In Marsch, E. and Schwenn, R., editors, *Solar Wind Seven Colloquium*, pages 183–186.

Gazis, P. R., Barnes, A., Mihalov, J. D., and Lazarus, A. J. (1994). Solar wind velocity and temperature in the outer heliosphere. *J. Geophys. Res.*, 99:6561–6573.

Gervasi, M., Rancoita, P. G., Usoskin, I. G., and Kovaltsov, G. A. (1999). Monte-Carlo approach to Galactic Cosmic Ray propagation in the Heliosphere. *Nucl. Phys. B - Proc. Sup.*, 78:26–31.

Gleeson, L. J. and Axford, W. I. (1967). Cosmic rays in the interplanetary medium. *Astrophys. J. Lett.*, 149:L115.

Gleeson, L. J. and Axford, W. I. (1968a). Solar Modulation of Galactic Cosmic Rays. *Astrophys. J.*, 154:1011.

Gleeson, L. J. and Axford, W. I. (1968b). The Compton-Getting Effect. *Astrophys. Space Sci.*, 2:431–437.

Gleeson, L. J. and Urch, I. H. (1971). Energy losses and modulation of galactic cosmic rays. *Astrophys. Space Sci.*, 11:288–308.

Gleeson, L. J. and Urch, I. H. (1973). A Study of the Force-Field Equation for the Propagation of Galactic Cosmic Rays. *Astrophys. Space Sci.*, 25:387–404.

Gloeckler, G. and Jokipii, J. R. (1966). Low-Energy Cosmic-Ray Modulation Related to Observed Interplanetary Magnetic Field Irregularities. *Phys. Rev. Lett.*, 17:203–207.

Golian, S., Krause, E., and Perlow, G. (1946). Cosmic radiation above 40 miles. *Phys. Rev.*, 70:223–224.

Gombosi, T. I. (1998). *Physics of the space environment.* Cambridge ; New York : Cambridge University Press, 1998. (Cambridge atmospheric and space science series).

Gould, R. J. (1975). Energy loss of relativistic electrons and positrons traversing cosmic matter. *Astroph. J.*, 196:689–694.

Grasso, D., Profumo, S., Strong, A., and Collaborators (2009). On possible interpretations of the high energy electron–positron spectrum measured by the Fermi Large Area Telescope. *Astropart. Phys.*, 32(2):140 – 151.

GREEN BOOK (2010). Navigation data—definitions and conventions - 500.0-g-3. Technical report, CCSDS.

Haasbroek, L. J. and Potgieter, M. S. (1995). The Modulation of Cosmic Rays in the High Latitude Heliosphere: A Computer Simulation. *Space Sci. Rev.*, 72:385–390.

Haasbroek, L. J., Potgieter, M. S., and Le Roux, J. A. (1995). A computer simulation of large cosmic ray decreases and their effects on the declining modulation cycle. *Adv. Space Res.*, 16:209–.

Haino, S., Sanuki, T., Abe, K., and BESS Collaboration (2004). Measurements of primary and atmospheric cosmic-ray spectra with the BESS-TeV spectrometer. *Phys. Lett. B*, 594:35–46.

Hapgood, M. (1992). Space physic coordinate transformations: A user guide. *Planet. Space Sci.*, 40(5):711–717.

Harvey, K. L. and Recely, F. (2002). Polar Coronal Holes During Cycles 22 and 23. *Sol. Phys.*, 211:31–52.

Hathaway, D. H. (2010). The Solar Cycle. *Living Rev. Sol. Phys.*, 7:1.

Hattingh, M. and Burger, R. A. (1995). A new simulated wavy neutral sheet drift model. *Adv. Space Res.*, 16(9):213–216.

Heber, B., Bothmer, V., Dröge, W., and Collaborators (1998). Latitudinal distribution of greater than 106 MeV protons and its relation to the ambient solar wind in the inner southern and northern heliosphere - ULYSSES Cosmic and Solar Particle Investigation Kiel Electron Telescope results. *J. Geophys. Res.*, 103:4809.

Heber, B., Droege, W., Ferrando, P., Haasbroek, L. J., Kunow, H., Mueller-Mellin, R., Paizis, C., Potgieter, M. S., Raviart, A., and Wibberenz, G. (1996). Spatial variation of >40MeV/n nuclei fluxes observed during the ULYSSES rapid latitude scan. *Astron. Astrophys.*, 316:538–546.

Heber, B., Gieseler, J., Dunzlaff, P., Gómez-Herrero, R., Klassen, A., Müller-Mellin, R., Mewaldt, R. A., Potgieter, M. S., and Ferreira, S. E. S. (2008). Latitudinal Gradients of Galactic Cosmic Rays during the 2007 Solar Minimum. *Astrophys. J.*, 689:1443–1447.

Heber, B. and Potgieter, M. (2007). In Balogh, A., Lanzerotti, L., and Suess, S., editors, *The Heliosphere through the Solar Activity Cycle*, page 195.

Heber, B. and Potgieter, M. S. (2006). Cosmic Rays at High Heliolatitudes. *Space Sci. Rev.*, 127:117–194.

Heber, B., Potgieter, M. S., and Ferrando, P. (1997). Solar modulation of galactic cosmic rays: the 3D heliosphere. *Adv. Space Res.*, 19:795–804.

Herbst, K., Kopp, A., Heber, B., Steinhilber, F., Fichtner, H., Scherer, K., and Matthiä, D. (2010). On the importance of the local interstellar spectrum for the solar modulation parameter. *J. Geophys. Res.-Space*, 115:0.

Hess, V. (1912). Über Beobachtungen der durchdringenden Strahlung bei sieben Freiballonfahrt. *Phys. Zeits*, 13:1084–1091.

Higham, D. J. (2001). An Algorithmic Introduction to Numerical Simulation of Stochastic Differential Equations. *SIAM Review*, 43:525–546.

Hillas, A. M. (2006). Cosmic Rays: Recent Progress and some Current Questions. *ArXiv Astrophysics e-prints*.

Hitge, M. and Burger, R. A. (2010). Cosmic ray modulation with a Fisk-type heliospheric magnetic field and a latitude-dependent solar wind speed. *Adv. Space Res.*, 45:18–27.

Hoeksema, J. T. (1995). The Large-Scale Structure of the Heliospheric Current Sheet During the ULYSSES Epoch. *Space Sci. Rev.*, 72:137–148.

Hundhausen, A. J. (1977). An interplanetary view of coronal holes. In Zirker, J. B., editor, *Coronal Holes and High Speed Wind Streams*, pages 225–329.

Isenberg, P. A. and Jokipii, J. R. (1979). Gradient and curvature drifts in magnetic fields with arbitrary spatial variation. *Astrophys. J.*, 234:746–752.

Jokipii, J. R. (1966). Cosmic-Ray Propagation. I. Charged Particles in a Random Magnetic Field. *Astrophys. J.*, 146:480.

Jokipii, J. R. (1971). Propagation of cosmic rays in the solar wind. *Rev. Geoph. Space Phys.*, 9:27–87.

Jokipii, J. R. (1989). The physics of cosmic-ray modulation. *Adv. Space Res.*, 9:105–119.

Jokipii, J. R. and Kopriva, D. A. (1979). Effects of particle drift on the transport of cosmic rays. III - Numerical models of galactic cosmic-ray modulation. *Astrophys. J.*, 234:384–392.

Jokipii, J. R. and Kota, J. (1989). The polar heliospheric magnetic field. *Geophys. Res. Lett.*, 16:1–4.

Jokipii, J. R. and Kóta, J. (1995). Three-DImensional Cosmic-Ray Simulations: Heliographic Latitude and Current-Sheet Tilt. *Space Sci. Rev.*, 72:379–384.

Jokipii, J. R. and Kóta, J. (1997). Galactic and Anomalous Cosmic Rays in the Heliosphere. In *International Cosmic Ray Conference*, volume 8, page 151.

Jokipii, J. R. and Kóta, J. (2008). Particle Acceleration at Shocks: Effects of Spatial Variations Along the Shock Face. In Li, G., Hu, Q., Verkhoglyadova, O., Zank, G. P., Lin, R. P., and Luhmann, J., editors, *American Institute of Physics Conference Series*, volume 1039, pages 390–396.

Jokipii, J. R., Kóta, J., Giacalone, J., Horbury, T. S., and Smith, E. J. (1995). Interpretation and consequences of large-scale magnetic variances observed at high heliographic latitude. *Geophys. Res. Lett.*, 22:3385–3388.

Jokipii, J. R. and Levy, E. H. (1977). Effects of particle drifts on the solar modulation of galactic cosmic rays. *Astrophys. J. Lett.*, 213:L85–L88.

Jokipii, J. R., Levy, E. H., and Hubbard, W. B. (1977). Effect of particle drift on cosmic-ray transport. i. general properties, application to solar modulation. *Astrophys. J.*, (213):861–868.

Jokipii, J. R. and Owens, A. J. (1975). Implications of observed charge states of low-energy solar cosmic rays. *J. Geophys. Res.*, 80:1209–1212.

Jokipii, J. R. and Parker, E. N. (1970). on the Convection, Diffusion, and Adiabatic Deceleration of Cosmic Rays in the Solar Wind. *Astroph. J.*, 160:735.

Jokipii, J. R. and Thomas, B. (1981). Effects of drift on the transport of cosmic rays. IV - Modulation by a wavy interplanetary current sheet. *Astrophys. J.*, 243:1115–1122.

Jones, G. H., Balogh, A., and Smith, E. J. (2003). Solar magnetic field reversal as seen at Ulysses. *Geophys. Res. Lett.*, 30(19):190000–1.

Kallenrode, M.-B. (2004). *Space physics : an introduction to plasmas and particles in the heliosphere and magnetospheres*. Advanced texts in physics. Berlin: Springer.

Kalos, M. and Whitlock, P. (2009). *Monte Carlo Methods*. John Wiley & Sons.

Kasper, J. C. (2002). *Solar wind plasma: Kinetic properties and micro- instabilities*. PhD thesis, Massachusetts Institute of Technology.

King, J. H. and Papitashvili, N. E. (2005). Solar wind spatial scales in and comparisons of hourly Wind and ACE plasma and magnetic field data. *J. Geophys. Res.-Space*, 110:A02104.

Klöden, P. E. and Platen, E. (1999). *Numerical Solution of Stochastic Differential Equations*. Springer Edition.

Kobylinski, Z. (2001). Comparison of the fisk magnetic field with the standard parker IMF: consequences for diffusion coefficients. *Adv. Space Res.*, 27:541–546.

Kojima, M., Washimi, H., Misawa, H., and Hakamada, K. (1992). Solar wind observed within 0.3 AU with interplanetary scintillation. In Marsch, E. and Schwenn, R., editors, *Solar Wind Seven Colloquium*, pages 201–204.

Kopp, A., Büsching, I., Strauss, R. D., and Potgieter, M. S. (2012). A stochastic differential equation code for multidimensional Fokker-Planck type problems. *Comput. Phys. Commun.*, 183:530–542.

Kota, J. and Jokipii, J. R. (1983). Effects of drift on the transport of cosmic rays. VI - A three-dimensional model including diffusion. *Astrophys. J.*, 265:573–581.

Kota, J. and Jokipii, J. R. (1991). The role of corotating interaction regions in cosmic-ray modulation. *Geophys. Res. Lett.*, 18:1797–1800.

Kóta, J. and Jokipii, J. R. (1997). 3-D simulation of heliospheric transport: A comparison of models. In *International Cosmic Ray Conference*, volume 2, pages 25–28.

Kóta, J. and Jokipii, J. R. (1999). Cosmic ray modulation and the structure of the heliospheric magnetic field. In *International Cosmic Ray Conference*, volume 7, pages 9–12.

Kota, J. and Jokipii, J. R. (2001). Recurrent Depressions of Galactic Cosmic Rays in CIRs: 22-Year Cycle. In *International Cosmic Ray Conference*, volume 9 of *International Cosmic Ray Conference*, page 3577.

Kota, J. and Owens, A. J. (1980). Energy-dependent diffusion of cosmic rays in the dynamical halo model. *Astroph. J.*, 237:814–818.

Krieger, A. S., Timothy, A. F., and Roelof, E. C. (1973). A Coronal Hole and Its Identification as the Source of a High Velocity Solar Wind Stream. *Sol. Phys.*, 29:505–525.

Kruells, W. M. and Achterberg, A. (1994). Computation of cosmic-ray acceleration by Ito's stochastic differential equations. *Astron. and Astrophys*, 286:314–327.

Krüger, H. and Moraal, H. (2010). A calibration neutron monitor: Statistical accuracy and environmental sensitivity. *Adv. Space Res.*, 46:1394–1399.

Krüger, H., Moraal, H., Bieber, J. W., Clem, J. M., Evenson, P. A., Pyle, K. R., Duldig, M. L., and Humble, J. E. (2008). A calibration neutron monitor: Energy response and instrumental temperature sensitivity. *J. Geophys. Res.-Space*, 113:8101.

Lang, K. (1999). *Astrophysical Formulae*, volume II. Springer.

Lange, D., Fichtner, H., and Kissmann, R. (2006). Time-dependent 3D modulation of Jovian electrons. Comparison with Ulysses/KET observations. *Astron. Astrophys.*, 449:401–410.

Langner, U. (2004). *Effect of termination shock acceleraion on cosmic ray in the helisphere*. PhD thesis, Potchestroom University, Potchestroom.

Langner, U. W. and Potgieter, M. S. (2004). Solar wind termination shock and heliosheath effects on the modulation of protons and antiprotons. *J. Geophys. Res.-Space*, 109:1103.

Langner, U. W. and Potgieter, M. S. (2005). Modulation of Galactic Protons in an Asymmetrical Heliosphere. *Astrophys. J.*, 630:1114–1124.

Langner, U. W., Potgieter, M. S., and Webber, W. R. (2003). Modulation of cosmic ray protons in the heliosheath. *J. Geophys. Res.-Space*, 108:8039.

Lazarian, A. and Opher, M. (2009). A Model of Acceleration of Anomalous Cosmic Rays by Reconnection in the Heliosheath. *Astroph. J.*, 703:8–21.

Leroy, C. and Rancoita, P.-G. (2009). *Principles of Radiation Interaction in Matter and Detection, 2nd Edition*. World Scientific Publishing Co.

Leroy, C. and Rancoita, P.-G. (2011). *Principles of Radiation Interaction in Matter and Detection, 3rd Edition*. World Scientific Publishing Co.

Levy, E. H. (1976). The interplanetary magnetic field structure. *Nature*, 261:394.

Li, G., Webb, G., Le Roux, J., Wiedenbeck, M., Florinski, V., and Zank, G. (2009). Modeling the transport of cosmic ray due to long term variation using a stochastic differential method. In *Proceeding of the 31st ICRC, 7–15 July, Lodz*, International Cosmic Ray Conference.

Longair, M. S. (1990). Cosmic rays and the Galactic radio background emission. In Kassim, N. E. and Weiler, K. W., editors, *Low Frequency Astrophysics from Space*, volume 362 of *Lecture Notes in Physics, Berlin Springer Verlag*, pages 227–236.

Longair, M. S. (1994). *High energy astrophysics. Vol.2: Stars, the galaxy and the interstellar medium*. Cambridge: Cambridge University Press, 2nd ed.

Marsch, E. (1991). Kinetic Physics of the Solar Wind Plasma. *Phys. Chem. Space*, 21:45–133.

Marsch, E., Axford, W. I., and McKenzie, J. F. (2003). Solar wind. In Dwivedi, B. N., editor, *Dynamic Sun*, pages 374–402.

Marsden, R. G. (2001). The 3-D Heliosphere at Solar Maximum. *The Publications of the Astronomical Society of the Pacific*, 113:129–130.

Matthaeus, W. H., Qin, G., Bieber, J. W., and Zank, G. P. (2003). Nonlinear Collisionless Perpendicular Diffusion of Charged Particles. *Astrophys. J. Letter*, 590:L53–L56.

McComas, D. J., Alexashov, D., Bzowski, M., Fahr, H., Heerikhuisen, J., Izmodenov, V., Lee, M. A., Möbius, E., Pogorelov, N., Schwadron, N. A., and Zank, G. P. (2012). The Heliosphere's Interstellar Interaction: No Bow Shock. *Science*, 336:1291.

McComas, D. J., Allegrini, F., Bochsler, P., and Collaborators (2009). Global Observations of the Interstellar Interaction from the Interstellar Boundary Explorer (IBEX). *Science*, 326:959.

McComas, D. J., Bame, S. J., Barker, P., Feldman, W. C., Phillips, J. L., Riley, P., and Griffee, J. W. (1998). Solar Wind Electron Proton Alpha Monitor (SWEPAM) for the Advanced Composition Explorer. *Space Sci. Rev.*, 86:563–612.

McComas, D. J., Barraclough, B. L., Funsten, H. O., Gosling, J. T., Santiago-Muñoz, E., Skoug, R. M., Goldstein, B. E., Neugebauer, M., Riley, P., and Balogh, A. (2000). Solar wind observations over Ulysses' first full polar orbit. *J. Geophys. Res.*, 105:10419–10434.

McComas, D. J., Ebert, R. W., Elliott, H. A., Goldstein, B. E., Gosling, J. T., Schwadron, N. A., and Skoug, R. M. (2008). Weaker solar wind from the polar coronal holes and the whole Sun. *Geophys. Res. Lett.*, 35:18103.

McCracken, K. G., McDonald, F. B., Beer, J., Raisbeck, G., and Yiou, F. (2004). A phenomenological study of the long-term cosmic ray modulation, 850-1958 AD. *J. Geophys. Res.-Space*, 109:12103.

McDonald, F. B., Ferrando, P., Heber, B., Kunow, H., McGuire, R., Müller-Mellin, R., Paizis, C., Raviart, A., and Wibberenz, G. (1997). A comparative study of cosmic ray radial and latitudinal gradients in the inner and outer heliosphere. *J. Geophys. Res.*, 102:4643–4652.

McMurdo (2012). The data from McMurdo were provided by the University of Delaware with support from the U.S. National Science Foundation under grant ANT-0739620.

Meuss, J. (2000). *Astronomical Algorithms, 2nd Edition*. Willman-Bell, Richmond,VA.

Minnie, J., Bieber, J. W., Matthaeus, W. H., and Burger, R. A. (2007). Suppression of Particle Drifts by Turbulence. *Astrophys. J.*, 670:1149–1158.

Moraal, H. (1990). Proton Modulation Near Solar Minimim Periods in Cosecutive Solar Cycles. In *International Cosmic Ray Conference*, volume 6, page 140.

Moses, D. (1987). Jovian electrons at 1 AU - 1978-1984. *Astrophys. J.*, 313:471–486.

Moskalenko, I. V. and Strong, A. W. (1998). Production and Propagation of Cosmic-Ray Positrons and Electrons. *Astroph. J.*, 493:694.

Moskalenko, I. V., Strong, A. W., Ormes, J. F., and Potgieter, M. S. (2002). Secondary Antiprotons and Propagation of Cosmic Rays in the Galaxy and Heliosphere. *Astroph. J.*, 565:280–296.

Nakamura et al. (2010). The review of particle physics (particle data group). *J. Phys. G: Nucl. Part. Phys.*

NASA (2001). Space station reference coordinate systems. Technical report, International Space Station Program.

NASA-COHOweb (2012). online database http://cohoweb.gsfc.nasa.gov/cw.html.

NASA-OMNIweb (2012). online database http://omniweb.gsfc.nasa.gov/form/dx1.html.

Ness, N. F., Scearce, C. S., and Seek, J. B. (1964). Initial Results of the Imp 1 Magnetic Field Experiment. *J. Geophys. Res.*, 69:3531–3569.

NMDB (2012). Data provided by NMDB database (www.nmdb.eu), founded under the European Union's FP7 programme (contract no. 213007).

Odstrcil, D. (2003). Modeling 3-D solar wind structure. *Adv. Space Res.*, 32:497–506.

Orito, S., Maeno, T., Matsunaga, H., and BESS Collaboration (2000). Precision Measurement of Cosmic-Ray Antiproton Spectrum. *Phys. Rev. Lett.*, 84:1078–1081.

Palmer, I. D. (1982). Transport coefficients of low-energy cosmic rays in interplanetary space. *Rev. Geophys. Space Ge.*, 20:335–351.

Parker, E. N. (1957). Newtonian Development of the Dynamical Properties of Ionized Gases of Low Density. *Phys. Rev.*, 107:924–933.

Parker, E. N. (1958). Dynamics of the interplanetary gas and magnetic fields. *Astrophys. J.*, 128:664.

Parker, E. N. (1960). The Hydrodynamic Theory of Solar Corpuscular Radiation and Stellar Winds. *Astrophys. J.*, 132:821.

Parker, E. N. (1961). Sudden Expansion of the Corona Following a Large Solar Flare and the Attendant Magnetic Field and Cosmic-Ray Effects. *Astrophys. J.*, 133:1014.

Parker, E. N. (1963). *Interplanetary dynamical processes.* New York, Interscience Publishers, 1963.

Parker, E. N. (1964). The Scattering of Charged Particles by Magnetic Irregularities. *J. Geophys. Res.*, 69:1755–1758.

Parker, E. N. (1965). The passage of energetic charged particles through interplanetary space. *Plan. Space Sci.*, 13:9.

Pei, C., Bieber, J. W., Breech, B., Burger, R. A., Clem, J., and Matthaeus, W. H. (2010a). Cosmic ray diffusion tensor throughout the heliosphere. *J. Geophys. Res.-Space*, 115:3103.

Pei, C., Bieber, J. W., Burger, R. A., and Clem, J. (2010b). A general time-dependent stochastic method for solving Parker's transport equation in spherical coordinates. *J. Geophys. Res.-Space*, 115:12107.

Pei, C., Bieber, J. W., Burger, R. A., and Clem, J. (2012). Three-dimensional Wavy Heliospheric Current Sheet Drifts. *Astrophys. J.*, 744:170.

Pei, C., Jokipii, J. R., and Giacalone, J. (2006). Effect of a Random Magnetic Field on the Onset Times of Solar Particle Events. *Astrophys. J.*, 641:1222–1226.

Perko, J. S. (1987). Solar modulation of galactic antiprotons. *Astron. and Astrophys.*, 184:119–121.

Pesses, M. E., Eichler, D., and Jokipii, J. R. (1981). Cosmic ray drift, shock wave acceleration, and the anomalous component of cosmic rays. *Astroph. J. Letter*, 246:L85–L88.

Phillips, J. L., Bame, S. J., Barnes, A., Barraclough, B. L., Feldman, W. C., Goldstein, B. E., Gosling, J. T., Hoogeveen, G. W., McComas, D. J., Neugebauer, M., and Suess, S. T. (1995). Ulysses solar wind plasma observations from pole to pole. *Geophys. Res. Lett.*, 22:3301–3304.

Pommois, P., Zimbardo, G., and Veltri, P. (2001). A Monte Carlo simulation of magnetic field line tracing in the solar wind. *Nonlinear. Proc. Geoph.*, 8:151–158.

Potgieter, M. S. (1997). Implications of Enhanched Perpendicular Diffusion in the Heliospheric Modulation of Cosmic Rays. In *25th International Cosmic Ray Conference*, volume 2.

Potgieter, M. S. (1998). The Modulation of Galactic Cosmic Rays in the Heliosphere: Theory and Models. *Space Sci. Rev.*, 83:147–158.

Potgieter, M. S. (2000). Heliospheric modulation of cosmic ray protons: Role of enhanced perpendicular diffusion during periods of minimum solar modulation. *J. Geophys. Res.*, 105:18295–18304.

Potgieter, M. S. (2008). Solar cycle variations and cosmic rays. *J. Atmos. Sol.-Terr. Phy.*, 70:207–218.

Potgieter, M. S. and Ferreira, S. E. S. (2002). Effects of the solar wind termination shock on the modulation of Jovian and galactic electrons in the heliosphere. *J. Geophys. Res.-Space*, 107:1089.

Potgieter, M. S. and Langner, U. W. (2004). Heliospheric Modulation of Cosmic-Ray Positrons and Electrons: Effects of the Heliosheath and the Solar Wind Termination Shock. *Astrophys. J.*, 602:993–1001.

Potgieter, M. S. and Le Roux, J. A. (1994). The Long-Term Heliospheric Modulation of Galactic Cosmic Rays according to a Time-dependent Drift Model with Merged Interaction Regions. *Astrophys. J.*, 423:817.

Potgieter, M. S., Le Roux, J. A., Burlaga, L. F., and McDonald, F. B. (1993a). The role of merged interaction regions and drafts in the heliospheric modulation of cosmic rays beyond 20 AU - A computer simulation. *Astrophys. J.*, 403:760–768.

Potgieter, M. S., Le Roux, J. A., Burlaga, L. F., and McDonald, F. B. (1993b). The role of merged interaction regions and drafts in the heliospheric modulation of cosmic rays beyond 20 AU - A computer simulation. *Astrophys. J.*, 403:760–768.

Potgieter, M. S. and Moraal, H. (1985). A drift model for the modulation of galactic cosmic rays. *Astrophys. J.*, 294(part 1):425–440.

Potgieter, M. S. and Moraal, H. (1988). Acceleration of cosmic rays in the solar wind termination shock. I - A steady state technique in a spherically symmetric model. *Astroph. J.*, 330:445–455.

Richardson, J. D., Wang, C., and Paularena, K. I. (2001). The solar wind: from solar minimum to solar maximum. *Adv. Space Res.*, 27:471–479.

Rochester, G. D. and Turver, K. E. (1981). Cosmic rays of ultra-high energy. *Contemp. Phys.*, 22:425–450.

Rozza, D. (2011). Studio di elettroni e positroni galattici con lo spettrometro AMS-02. Master's thesis, University of Milano-Bicocca, Milano, Italy.

Ruffolo, D., Chuychai, P., Wongpan, P., Minnie, J., Bieber, J. W., and Matthaeus, W. H. (2008). Perpendicular Transport of Energetic Charged Particles in Nonaxisymmetric Two-Component Magnetic Turbulence. *Astrophys. J.*, 686:1231–1244.

Ruždjak, D., Brajša, R., Sudar, D., and Wöhl, H. (2005). The Influence of the Evolution of Sunspot Groups on the Determination of the Solar Velocity Field. *Sol. Phys.*, 229:35–43.

Sanderson, T. R., Appourchaux, T., Hoeksema, J. T., and Harvey, K. L. (2003). Observations of the Sun's magnetic field during the recent solar maximum. *J. Geophys. Res.-Space*, 108:1035.

Sanderson, T. R., Marsden, R. G., Wenzel, K.-P., Balogh, A., Forsyth, R. J., and Goldstein, B. E. (1995). High-Latitude Observations of Energetic Ions During the First ULYSSES Polar Pass. *Space Sci. Rev.*, 72:291–296.

Sanuki, T., Motoki, M., Matsumoto, H., and BESS Collaboration (2000). Precise Measurement of Cosmic-Ray Proton and Helium Spectra with the BESS Spectrometer. *Astrophys. J.*, 545:1135–1142.

Sasaki, M., Matsumoto, H., Nozaki, M., and BESS Collaboration (2002). Progress in search for antihelium with BESS. *Nucl. Phys. B - Proc. Sup.*, 113:202–207.

Schein, M., Jesse, W. P., and Wollan, E. O. (1941). The nature of the primary cosmic radiation and the origin of the mesotron. *Phys. Rev.*, 59:615–615.

Scherer, K., Fichtner, H., Strauss, R. D., Ferreira, S. E. S., Potgieter, M. S., and Fahr, H.-J. (2011). On Cosmic Ray Modulation beyond the Heliopause: Where is the Modulation Boundary? *Astrophys. J.*, 735:128.

Schlaepfer, H. (2003). Cosmic ray. *SPATIUM, published by Association Pro ISSI*, (11).

Schlickeiser, R. (1989). Cosmic-ray transport and acceleration. I - Derivation of the kinetic equation and application to cosmic rays in static cold media. II - Cosmic rays in moving cold media with application to diffusive shock wave acceleration. *Astrophys. J.*, 336:243–293.

Schulz, M. (1973). Interplanetary sector structure and the helliomagnetic equator. *Astrophys. Space Sci.*, 24:371–383.

Schwenn, R. (1983). The average solar wind in the inner heliosphere: Structures and slow variations. In *NASA Conference Publication*, volume 228, pages 489–507.

Shalchi, A., editor (2009). *Nonlinear Cosmic Ray Diffusion Theories*, volume 362 of *Astrophys. Space Sci. Library*.

Shalchi, A. and Schlickeiser, R. (2004). The Parallel Mean Free Path of Heliospheric Cosmic Rays in Composite Slab/Two-dimensional Geometry. I. The Damping Model of Dynamical Turbulence. *Astrophys. J.*, 604:861–873.

Sheeley, Jr., N. R., Wang, Y.-M., Hawley, S. H., Brueckner, G. E., Dere, K. P., Howard, R. A., Koomen, M. J., Korendyke, C. M., Michels, D. J., Paswaters, S. E., Socker, D. G., St. Cyr, O. C., Wang, D., Lamy, P. L., Llebaria, A., Schwenn, R., Simnett, G. M., Plunkett, S., and Biesecker, D. A. (1997). Measurements of Flow Speeds in the Corona between 2 and 30 R sub sun. *Astroph. J.*, 484:472.

Shikaze, Y., Orito, S., Mitsui, T., and BESS Collaboration (2007). Measurements of 0.2 20 GeV/n cosmic-ray proton and helium spectra from 1997 through 2002 with the BESS spectrometer. *Astrop. Phys.*, 28:154–167.

Shikaze, Y., Orito, S., Mitsui, T., Yoshimura, K., Matsumoto, H., Matsunaga, H., Nozaki, M., Sonoda, T., Ueda, I., and Yoshida, T. (2000). Large-area scintillator hodoscope with 50 ps timing resolution onboard BESS. *Nucl. Instrum. Meth. A*, 455:596–606.

SIDC-team (1900-2012). The International Sunspot Number. *Monthly Report on the International Sunspot Number, online catalogue.*

Simpson, J. A. (1983). Elemental and Isotopic Composition of the Galactic Cosmic Rays. *Annu. Rev. Nucl. Part. S.*, 33:323–382.

Simpson, J. A. (1996). Ulysses cosmic-ray investigations extending from the south to the north polar regions of the Sun and heliosphere. *Nuovo Cimento C*, 19:935–943.

Simpson, J. A. (1997). The Cosmic Radiation: Reviewing the Present and Future. In *International Cosmic Ray Conference*, volume 8, page 4.

Simpson, J. A., Anglin, J. D., Balogh, A., and Collaborators (1992). The ULYSSES Cosmic Ray and Solar Particle Investigation. *Astron. Astrophys. Supplement Series*, 92:365–399.

Simpson, J. A., Zhang, M., and Bame, S. (1996). A solar polar north-south asymmetry for cosmic-ray propagation in the heliosphere: The ulysses pole-to-pole rapid transit. *Astrophys. J. Lett.*, 465(1):L69.

Smith, C. W. and Bieber, J. W. (1991). Solar cycle variation of the interplanetary magnetic field spiral. *Astroph. J.*, 370:435–441.

Smith, E. J. (2001). The heliospheric current sheet. *J. Geophys. Res.*, 106:15819–15832.

Smith, E. J. and Marsden, R. G. (2003). Ulysses Observations at Solar Maximum: Introduction. *Geophys. Res. Lett.*, 30(19):190000–1.

Smith, J. E. (1989). Interplanetary magnetic field over two solar cycles and out to 20 AU. *Adv. Space Res.*, 9:159–169.

Snodgrass, H. B. (1983). Magnetic rotation of the solar photosphere. *Astrophys. J.*, 270:288–299.

Stawicki, O. (2003). *On Solar Wind Magnetic Fluctuations and Their Influence on the Transport of Charged Particles in the Heliosphere.* PhD thesis, Institut fur Theoretische Physik IV, Ruhr-Universitat Bochum.

Stephens, A. S. and Golden, L. R. (1990). The Effect of Reacceleration on Cosmic Ray Proton and Helium Nuclei. In *International Cosmic Ray Conference*, volume 3, page 353.

Stone, E. C., Cohen, C. M. S., Cook, W. R., and Collaborators (1998). The Solar Isotope Spectrometer for the Advanced Composition Explorer. *Space Sci. Rev.*, 86:357–408.

Stone, E. C., Cummings, A. C., McDonald, F. B., Heikkila, B. C., Lal, N., and Webber, W. R. (2005). Voyager 1 Explores the Termination Shock Region and the Heliosheath Beyond. *Science*, 309:2017–2020.

Stone, E. C., Cummings, A. C., McDonald, F. B., Heikkila, B. C., Lal, N., and Webber, W. R. (2008). An asymmetric solar wind termination shock. *Nature*, 454:71–74.

Stone, E. C., Cummings, A. C., and Webber, W. R. (1996). The distance to the solar wind termination shock in 1993 and 1994 from observations of anomalous cosmic rays. *J. Geophys. Res.*, 101:11017–11026.

Strauss, R. D. and Potgieter, M. S. (2010). Modeling anomalous cosmic ray oxygen gradients over successive solar cycles. *J. Geophys. Res.-Space*, 115:12111.

Strauss, R. D., Potgieter, M. S., Büsching, I., and Kopp, A. (2011). Modeling the Modulation of Galactic and Jovian Electrons by Stochastic Processes. *Astrophys. J.*, 735:83.

Strauss, R. D., Potgieter, M. S., Büsching, I., and Kopp, A. (2012a). Modelling heliospheric current sheet drift in stochastic cosmic ray transport models. *Astrophys. Space Sci.*, 339:223–236.

Strauss, R. D., Potgieter, M. S., and Ferreira, S. E. S. (2012b). Modeling ground and space based cosmic ray observations. *Adv. Space Res.*, 49:392–407.

Strauss, R. D., Potgieter, M. S., Ferreira, S. E. S., and Hill, M. E. (2010). Modelling anomalous cosmic ray oxygen in the heliosheath. *Astron. Astrophys.*, 522:A35.

Strong, A. W. and Moskalenko, I. V. (2001). Models for galactic cosmic-ray propagation. *Adv. Space Res.*, 27:717–726.

Strong, A. W., Moskalenko, I. V., and Reimer, O. (2004). Diffuse Galactic Continuum Gamma Rays: A Model Compatible with EGRET Data and Cosmic-Ray Measurements. *Astroph. J.*, 613:962–976.

Suter, H. (1998). Space shuttle flight parameters for mission sts-91. Internal Report.

Takahashi, Y. and JEM-EUSO Collaboration (2009). The JEM-EUSO mission. *New J. Phys.*, 11(6):065009.

Teegarden, B. J., McDonald, F. B., Trainor, J. H., Webber, W. R., and Roelof, E. C. (1974). Interplanetary Mev electrons of Jovian origin. *J. Geophys. Res.*, 79:3615.

Thomas, B. T. and Smith, E. J. (1981). The structure and dynamics of the heliospheric current sheet. *J. Geophys. Res.*, 86:11105–11110.

Trotta, R., Jóhannesson, G., Moskalenko, I. V., Porter, T. A., Ruiz de Austri, R., and Strong, A. W. (2011). Constraints on Cosmic-ray Propagation Models from A Global Bayesian Analysis. *Astroph. J.*, 729:106.

Usoskin, I. G., Alanko-Huotari, K., Kovaltsov, G. A., and Mursula, K. (2005). Heliospheric modulation of cosmic rays: Monthly reconstruction for 1951-2004. *J. Geophys. Res.-Space*, 110:12108.

Usoskin, I. G., Bazilevskaya, G. A., and Kovaltsov, G. A. (2011). Solar modulation parameter for cosmic rays since 1936 reconstructed from ground-based neutron monitors and ionization chambers. *J. Geophys. Res.-Space*, 116:2104.

Vladimirov, A. E., Digel, S. W., Jóhannesson, G., Michelson, P. F., Moskalenko, I. V., Nolan, P. L., Orlando, E., Porter, T. A., and Strong, A. W. (2011). GALPROP WebRun: An internet-based service for calculating galactic cosmic ray propagation and associated photon emissions. *Comput. Phys. Commun.*, 182:1156–1161.

Webb, G. M. and Gleeson, L. J. (1977). Green's theorem and Green's functions for the steady-state cosmic-ray equation of transport. *Astrophys. Space Sci.*, 50:205–223.

Webber, W. R., Cummings, A. C., McDonald, F. B., Stone, E. C., Heikkila, B., and Lal, N. (2008). Galactic cosmic ray H and He nuclei energy spectra measured by Voyagers 1 and 2 near the heliospheric termination shock in positive and negative solar magnetic polarity cycles. *J. Geophys. Res.-Space*, 113:10108.

Weisstein, E. W. (2012). Central limit theorem. From MathWorld–A Wolfram Web Resource. http://mathworld.wolfram.com/CentralLimitTheorem.html.

Wenzel, K.-P. (1993). Ulysses - Its status and prospects. *Adv. Space Res.*, 13:275–280.

Whang, Y. C. and Burlaga, L. F. (2000). Anticipated Voyager crossing of the termination shock. *Geophys. Res. Lett.*, 27:1607.

Whang, Y. C., Burlaga, L. F., Wang, Y.-M., and Sheeley, N. R. (2004). The termination shock near 35° latitude. *Geophys. Res. Lett.*, 31:3805.

Whang, Y. C., Burlaga, L. F., Wang, Y.-M., and Sheeley, Jr., N. R. (2003). Solar Wind Speed and Temperature Outside 10 AU and the Termination Shock. *Astrophys. J.*, 589:635–643.

Wilcox, J. M. and Ness, N. F. (1965). Quasi-Stationary Corotating Structure in the Interplanetary Medium. *J. Geophys. Res.*, 70:5793–5805.

Wisniewski, R. (2000). Lectures notes on modelling of a spacecraft.

WSO (2012). Wilcox Solar Observatory; http://wso.stanford.edu/.

Yamada, Y., Yanagita, S., and Yoshida, T. (1998). A stochastic view of the solar modulation phenomena of cosmic rays. *Geophys. Res. Lett.*, 25:2353–2356.

Yamamoto, A., Anraku, K., Golden, R., Haga, T., Higashi, Y., Imori, M., Inaba, S., Kimbell, B., Kimura, N., and Makida, Y. (1994). Balloon-borne experiment with a superconducting solenoidal magnet spectrometer. *Adv. Space Res.*, 14:2.

Yin, P.-f., Yuan, Q., Liu, J., Zhang, J., Bi, X.-j., Zhu, S.-h., and Zhang, X. (2009). Pamela data and leptonically decaying dark matter. *Phys. Rev. D*, 79:023512.

Yoon, Y. S., Ahn, H. S., Allison, P. S., and CREAM Collaboration (2011). Cosmic-ray Proton and Helium Spectra from the First CREAM Flight. *Astroph. J.*, 728:122.

Yoshimura, K., Orito, S., Ueda, I., and Collaborators (1995). Observation of cosmic-ray antiprotons at energies below 500 MeV. *Phys. Rev. Lett.*, 75:3792–3795.

Zhang, M. (1999). A Markov Stochastic Process Theory of Cosmic-Ray Modulation. *Astrophys. J.*, 513:409–420.

Zhang, L. and Cheng, K. S. (2001). Cosmic-ray positrons from mature gamma-ray pulsars. *Astron. Astrophys.*, 368:1063–1070.

Zirker, J. B. (1977). Coronal holes - an overview. In Zirker, J. B., editor, *Coronal Holes and High Speed Wind Streams*, pages 1–26.

Zurbuchen, T. H., Schwadron, N. A., and Fisk, L. A. (1997). Direct observational evidence for a heliospheric magnetic field with large excursions in latitude. *J. Geophys. Res.*, 102:24175–24182.

Acknowledgments

This thesis is the arrival point of a long journey started many years ago when I met for the first time the AMS02-MiB group. The topic of the cosmic radiation to probe the interplanetary medium catch me from the first time I heard about it. Many difficulties arose during the last years but, thanks to the support and the expertise of this group, we were able to improve the model and provide answer to (almost) all the questions. I would like to first acknowledge the whole AMS02-MiB group and collaborators: Cristina, Davide, Davidino, Massimo, Matteo, Mauro, Pavol, Pier-Giorgio, rigorously in alphabetic order, as well as the students and fellows who works with us in the past three years. In particular I am grateful to Davide, for his friendship and continuous encouragement, and to Francesco, that with his thoroughness spur me to see in more details the Fokker-Planck and SDE theory (if the reader don't understand what are these acronyms, please start to read the thesis from the beginning!!).

Special thanks are for my family (Fio, Isa, Cri, Tata, uncles and cousins of all orders) that always support and believe in me in this crazy journey through the continents, maths, particles and stars: it is important to know that, regardless how far you are, there is a place that you can call "Home" , where someone is waiting for you.

Thanks also to special friends of my life (Matteo, Cla, Davide, Guido, Enzo, Marica). Their friendship, discussion and good company allow me to see the life beyond physics, and to be (I hope) a better person and scientist.

I am grateful to the scout brothers of CNGEI Cernobbio. I have no words to describe how their smiles, laughs and adventures helped me in the difficult moments.

I would like to acknowledge all friends met during the missions, shifts and meetings of AMS-02 collaboration, too many people to be listed in this page, but always available to help and teach me new things about the experiment. In particular the closer friends I have met during the last year I have spent at CERN (Kun, Alberto, Gaia, Nicola, Eleni, Thobias) who made this year one of the special years of my life.

Finally the last *but not least* acknowledgements are for two special old/new friends (Serena and Manuela) that with their presence remind to me a part of myself that I was forgetting and now I recover gained of new experiences, emotions and pictures for my memory book (special edition).